Structure and rheology of anisotropic colloids

Vincent Labalette

To cite this version:

Vincent Labalette. Structure and rheology of anisotropic colloids. Chemical and Process Engineering. Institut National Polytechnique de Toulouse - INPT, 2020. English. NNT : 2020INPT0068 . tel-04169741

HAL Id: tel-04169741

https://theses.hal.science/tel-04169741

Submitted on 24 Jul 2023

HAL is a multi-disciplinary open access archive for the deposit and dissemination of scientific research documents, whether they are published or not. The documents may come from teaching and research institutions in France or abroad, or from public or private research centers.

L'archive ouverte pluridisciplinaire **HAL**, est destinée au dépôt et à la diffusion de documents scientifiques de niveau recherche, publiés ou non, émanant des établissements d'enseignement et de recherche français ou étrangers, des laboratoires publics ou privés.

THÈSE

En vue de l'obtention du

DOCTORAT DE L'UNIVERSITÉ DE TOULOUSE

Délivré par :
Institut National Polytechnique de Toulouse (Toulouse INP)

Discipline ou spécialité :
Génie des Procédés et de l'Environnement

Présentée et soutenue par :
M. VINCENT LABALETTE
le vendredi 24 juillet 2020

Titre :

Structure and rheology of anisotropic colloids

Ecole doctorale :
Mécanique, Energétique, Génie civil, Procédés (MEGeP)

Unité de recherche :
Laboratoire de Génie Chimique (LGC)

Directeur(s) de Thèse :
M. YANNICK HALLEZ

Rapporteurs :
M. HUGUES BODIGUEL, INP GRENOBLE
Mme EMANUELA BIANCHI, UNIVERSITE DE VIENNE

Membre(s) du jury :
M. ERIC CLIMENT, TOULOUSE INP, Président
M. JEFFREY MORRIS, CITY COLLEGE OF NEW YORK, Membre
Mme MARTINE MEIRELES, CNRS TOULOUSE, Invité
M. SETO RYOHEI, CHINESE ACADEMY OF SCIENCES, Membre
M. YANNICK HALLEZ, UNIVERSITE TOULOUSE 3, Membre

Abstract

Colloidal clays are hydrous magnesium phyllosilicates (sometimes aluminum), usually bearing a negative structural charge coming from isomorphic substitution compensated by the presence of cations in the basal spacing or on the surface of the colloid. These nanoparticles have a platelet shape with an aspect ratio going from 20 to 100. When immersed in water, clays hydrate and swell, leading to the release of the cations. The hydroxyl group presents on the edge of the particles are sensitive to the pH (titrable sites) resulting in an amphoteric edge charge. At low pH the rim is positively charged and becomes neutral or negative at pH 11. Therefore, suspensions of colloidal clays have both charge and shape anisotropies. Thanks to these features, clay dispersions exhibit interesting optical properties (ochreous clays), mechanical properties (tile manufacturing, surface coating) and even cleaning properties (grease-removing). Although studied for decades, the behavior of colloidal clays remains controversial. In this manuscript, we propose a coarse-grained model to simulate particles with both structural and charge anisotropy. This model allows studying the behavior of colloidal suspensions at equilibrium and under shear flow. Contrary to the Monte-Carlo method usually employed to model the equilibrium behavior of anisotropic particles, the model presented in this thesis takes into account hydrodynamic interactions, allowing the dynamics of the system to be studied. The particles are coarse-grained as clusters of spheres bound by springs or constrained to a rigid body motion thanks to solid mechanics equations. The dynamics of the particles are computed using the Accelerated Stokesian Dynamics code (ASD), and the electrostatic interactions are computed in a pairwise additive fashion with a Yukawa potential. The implementation of this coarse-grained model in the ASD method allows studying the microstructure of anisotropic particles presenting similar features than Laponite, a 2:1 synthetic smectite clay widely studied experimentally and numerically in the literature. Several studies are presented here while varying the volume fraction and the range of electrostatic interactions. The dynamics of formation of the observed structures (Wigner glass, gel, overlapping coin, etc.) and their structural evolution behavior are then discussed. Finally, the rheological response of the different structures to a start-up shear has been studied, highlighting the importance of the ratio between the electrostatic and the hydrodynamic forces. For initially percolated systems, it has been shown that the stress response on the applied strain depends on the initial microstructure at short times, and exhibits shear-thinning and final viscous response independent of the initial structure.

Résumé

Les argiles colloïdalles sont des phillosilicates d'hydrure de magnésium (ou d'aluminium) pouvant, de part des substitutions isomorphiques, acquérir une charge négative structurale compensée par la présence de cations au niveau de l'espace interfoliaire ou en surface même du colloïde. Ces nanoparticules ont une forme de palet avec un rapport de forme pouvant varier entre 20 et 100. Lors de leur mise en suspension, les colloïdes s'hydratent provoquant ainsi leur gonflement et le relargage des cations. Les groupements hydroxyles présents en bordure des argiles sont extrêmement dépendants du pH et peuvent ainsi générer une charge de bord positive à bas pH, ou négative à pH élevé. Ainsi les argiles colloïdales en suspension présentent à la fois une anisotropie de forme et de charge. Ces caractéristiques confèrent aux dispersions d'argile des propriétés optiques (argiles ocreuses), mécaniques (fabrication de tuile, enduit) ou même nettoyantes (pouvoir dégraissant) intéressantes. Bien qu'étudié depuis de nombreuses années, le comportement des argiles en suspension reste controversé. C'est dans ce contexte que s'inscrit cette thèse dont l'objectif est de proposer un modèle de simulation « gros-grains » de particules présentant une anisotropie à la fois structurale et de charge et ainsi d'étudier le comportement à l'équilibre et hors équilibre d'une suspension de particules anisotropes. Contrairement au modèle Monte-Carlo habituellement utilisé pour modéliser le comportement à l'équilibre d'une suspension de particules anisotropes, le modèle présenté ici tient compte des interactions hydrodynamiques et permet ainsi d'étudier la dynamique du système, que ce soit lors de la formation de structures à l'équilibre ou suite à l'application de force de cisaillement. Les particules sont modélisées à l'aide d'agrégats de sphères liées entre elles par des ressorts, ou contraintes à un mouvement de corps rigide via les équations de la mécanique du solide. La dynamique des agrégats est étudiée à l'aide du code de simulations de type Accelerated Stokesian Dynamics (ASD) et les interactions électrostatiques modélisées suivant le principe d'additivité de paires avec un potentiel de Yukawa. L'implémentation du modèle à « gros-grain » de particules anisotropes dans le code ASD a ainsi permis d'étudier les structures à l'équilibre et sous écoulement de particules présentant des caractéristiques communes avec la Laponite, une smectite de type 2:1 largement étudiée expérimentalement et numériquement dans la littérature. Dans ce manuscrit, des études concernant ces particules anisotropes sont présentées pour différentes fraction volumique et portées d'interactions électrostatiques. La dynamique de formation des structures au repos (Wigner glass, gel, overlapping coin...) ainsi que leurs évolutions sont discutées. Enfin, la réponse rhéologique de ces structures lors de l'application d'un écoulement cisaillant est étudiée, mettant en lumière l'importance du ratio entre les forces électrostatiques et hydrodynamiques au sein de la dynamique du système. Pour des structures initialement percolées, la réponse du stress à la déformation du système dépend de la microstructure initiale aux temps courts, et possède un comportement rhéofluidifiant ainsi qu'une viscosité finale indépendants de la microstructure initiale.

Contents

List of Figures

List of Tables

Introduction

A colloidal suspension refers to a heterogeneous mixture composed of small particles considered as the dispersed phase in a continuous phase. Particles of the dispersed phase are sensitive to the thermal fluctuations of the molecules belonging to the continuous phase. Such particles have a typical diameter ranging from $1\ \mathrm{nm}$ to $1\ \mathrm{\mu m}$ and are called colloids. The suspending fluid, the continuous phase, can be gaseous (fog, clouds, aerosol), liquid (ink, milk, paints) or solid (butter, cranberry glass, aerogel).

Colloids originate either from the natural environment or can also be synthesized in laboratories. Natural colloids are everywhere, and where used well before even the word colloid existed. One of the first traces of the use of colloidal suspensions goes back to ancient Egypt and China several thousand years ago. In those ancient times, humans were using an ink mainly composed of soot (dispersed phase) mixed with vegetable oils or animal glue (suspending medium) [1]. One can also cite the Lycurgus cup from the 4th century AD, which is certainly, among the oldest applications, the most famous. The glass of this cup presents a dichroic effect due to the presence of gold and silver nanoparticles: when the cup is front lighted, it has a green color, whereas a reflected light produces a red color. Although the colloids were widely used in everyday life (yogurt, wiped cream, etc.), one had to wait for the end of $19th$ century to attend the first use of the term colloid, from the Greek "Kolla" meaning glue, by Thomas Graham in 1861. This author used this term to describe a suspension that cannot diffuse through a membrane [2]. Since, one has realized that colloids were responsible for numerous physico-chemical phenomena, such as the beautiful color of a colloidal crystal of silica (SiO_2) also known as opal, or the "ouzo effect" [3] in the pastis [4] due to the natural colloidal droplets of anethole, a flavoring substance which can be extracted from licorice. Natural colloids are also part of the human body, as viruses, bacterias, or thrombocytes (these small platelets are one of the blood component that clump blood vessel injured). Finally, to conclude this non-exhaustive list of examples, one can cite the family of clays as colloids. Clays are platelets with a thickness of the order of a nanometer and a radius of several dozen to several hundreds of nanometers. These particles bear negative charges on the faces and a rim charge, which can be either positive or negative, depending on the pH of the suspension. Under specific conditions, clays can form a gel, or a glass, well below the classic isotropic to nematic transition. Indeed, due to the edge to face interactions, clay particles can, for instance, generate a house of card structure spanning the totality of the system. Such a structure provides rheological characteristics to the suspension close to a solid state. For uncharged disk-shaped particles, the transition from a liquid-like to a solid-like state normally occurs when particles do not have a positional order, but are on average aligned which correspond to the nematic state mentioned earlier. These hallmarks make clay particles an exciting candidate, for example, as a rheology-modifier in technological applications as a surface coating. However, to really optimize their use, one should be able to predict the macroscopic behavior of clay suspensions, which is strongly related to the interactions at the microscopic scale. Due to the polydispersity and the complex chemical heterogeneity of natural clays, researchers sometimes investigate the role of physico-chemical parameters, such as the pH or the ionic strength on simpler systems such as synthesized model clays.

Non-natural colloids can either be synthesized chemically or through self-assembly and are interesting for studying and understanding the behavior of natural particles, but are also used to provide specific properties to other systems owing to their well defined characteristics. Among them, one can cite the use of metallic colloids such as silver nanodisk for the detection of organic species using Surface Enhanced Raman Spectroscopy (SERS) [5], the use of lignin colloidal spheres prepared by self-assembly in sunscreens [6], the use of fumed silica for its strong thickening effect in the plastic industry and the use of Laponite, a synthesized clay in numerous applications such as paints, household cleaners, and personal care product.

To summarize colloids are everywhere, and their technological applications seem limitless. Therefore, it is essential to understand the behavior of colloidal suspensions in order to use them wisely. If the macroscopic behavior of a suspension is relatively easy to observe, it cannot be foreseen unless the microscopic interactions between colloidal particles are known and understood. For a given set of particles, the microscopic interactions can generate complex microstructures, which will tremendously influence the flow of the suspension. The study of this flow in the response of an applied force is called rheology. Due to the small size of the colloids and the complex physico-chemical parameters involved in a colloidal suspension, the experimental study of the microstructure requires measuring statistical quantities, which could be difficult to interpret. That is why researchers often try to model the system to carry-out numerical simulations. The difficulty of modeling a system of interacting particles lies in the fact that a too complex model can be impossible to simulate due to a tremendous computational time or a lack of knowledge, while a too simple model might not be able to capture the correct physics. Consequently, the researcher's work is to propose the simplest model to correctly capture both the microscopic and macroscopic behavior of the colloidal suspension.

In this Ph.D. thesis, we propose a coarse-grained model to simulate the suspension of particles with both charge and structural anisotropy. Such particles are quite close to clays, and so they will be called "clay-like" particles in this work. We have thus decided to compare our results with a synthetic clay particle already mentioned, Laponite. However, we emphasize that the model can be used for any other anisotropic particle.

This thesis is composed of four chapters and is organized as follows.

In the first chapter, the basic theoretical concepts in colloidal sciences are introduced. The forces and the equations governing the colloidal suspensions are presented. These forces drive the spatial arrangement of the particles, referred to as the microstructure of the suspension. The complexity of the study of colloidal suspensions lies in the fact that the microstructure is influenced by the forces and the forces by the microstructure. Changing the concentration in particles or the concentration in salt of a suspension of repulsive spheres can induce a drastic change of the microstructure and consequently influence its mechanical response to an applied shear. Owing to the relation between microscopical behavior and spatial arrangement, it is common to define a phase diagram to illustrate the effect of parameters such as concentration, temperature or ionic strength on both microstructure and macroscopically behavior. To give an insight into the different existing phases, relatively simple phase diagrams are presented for isotropic colloids, and the difficulty of producing a phase diagram for complex systems such as clay is discussed. Then, the most common rheological behaviors of non-Newtonian suspensions are described.

In the second chapter, numerical methods used to simulate anisotropic particles are presented. These methods comprise many-body hydrodynamic interactions using the Accelerated Stokesian Dynamics (ASD) developed by Sierou & Brady [7] and Banchio & Brady [8]. As the ASD method was originally designed for suspensions of spheres, two different models are presented to generate anisotropic rigid objects: the first one relies on the coupling of spheres using springs, and the second one mathematically constrains the motions of a cluster of spheres arranged in a hexagonal close-packed fashion to enforce the rigid body motion. Then, validations of these coarse-graining methods are carried out, and their limitations are discussed.

In the third chapter, the structure of suspensions of clay-like particles without any background flow is studied. Such a study is commonly realized with Monte Carlo (MC) simulations. The main goal of this chapter is to prove that despite the limitations of the numerical method developed in the second chapter and the coarse-graining of the particles, the approach developed in this work is able to produce phase diagrams for clay-like suspensions similar to the ones obtained with Monte Carlo methods. The limitations essentially come from a CPU cost much higher than that of MC methods, but such a cost is the price to pay to obtain accurate hydrodynamic interactions. If these hydrodynamic interactions are not necessary to study the phases of a suspension without background flow (MC method), they cannot be neglected to predict the dynamics and the rheology of a suspension. Thus, obtaining similar phases diagram using the method developed in the second chapter validates its use for suspension under shear.

Finally, in the fourth chapter, these new simulation capabilities are exploited to study the dynamics of suspensions of clay-like particles with and without shear flow. The analysis of the kinetics of aggregation at rest and under flow allowed us to better understand the physical phenomena involved. For example, despite the complexity introduced by the shape and the charge anisotropy of the particles, aggregation under shear is well described by orthokinetic arguments using a particular effective volume fraction. Then, the dependence of the rheological properties of a suspension of clay-like particles is investigated as a function of the ratio between the viscous forces arising from the shear flow and the electrostatic forces. This balance of forces drastically influences the microstructure of the suspensions, as well as mechanisms with significant effects on suspensions properties. The clay-like suspensions can exhibit an elastic regime, overshoot stress, behave as a thixotropic material, or even formed a two-dimensional hexagonal crystalline structure with strings aligned to the flow direction, with both positional and oriental correlations observed. To our knowledge, this last phenomenon has been observed previously neither experimentally nor using simulations. The dependence of the structure and rheology of clay-like suspensions on the balance of forces and the different mechanisms involved in the numerous behaviors observed are explained in this last chapter.

References

[1] Hiroshi Kimura, Yasushi Nakayama, Akira Tsuchida, and Tsuneo Okubo. Rheological properties of deionized Chinese ink. *Colloids and Surfaces B: Biointerfaces*, 56(1-2):236–240, April 2007.

[2] T. Graham. Liquid Diffusion Applied to Analysis. *Proceedings of the Royal Society of London*, 11(0):243–247, January 1860.

[3] Steven A. Vitale and Joseph L. Katz. Liquid Droplet Dispersions Formed by Homogeneous Liquid-Liquid Nucleation: "The Ouzo Effect". *Langmuir*, 19(10):4105–4110, May 2003.

[4] Isabelle Grillo. Small-angle neutron scattering study of a world-wide known emulsion: Le Pastis. *Colloids and Surfaces A: Physicochemical and Engineering Aspects*, 225(1-3):153–160, September 2003.

[5] Cecilia Gestraud. *Synthèse, fonctionnalisation et assemblage de nanodisques d'argent*. PhD thesis, 2019.

[6] Yong Qian, Xiaowen Zhong, Ying Li, and Xueqing Qiu. Fabrication of uniform lignin colloidal spheres for developing natural broad-spectrum sunscreens with high sun protection factor. *Industrial Crops and Products*, 101:54–60, July 2017.

[7] Asimina Sierou and John F. Brady. Accelerated Stokesian Dynamics simulations. *Journal of Fluid Mechanics*, 448, December 2001.

[8] Adolfo J. Banchio and John F. Brady. Accelerated Stokesian dynamics: Brownian motion. *The Journal of Chemical Physics*, 118(22):10323–10332, June 2003.

Introduction to colloidal suspensions

1

As mentioned in the introduction, a colloidal suspension refers to a heterogeneous mixture of fine particles, in a suspending medium. One particularity of these particles is that they are small enough to have their motions influenced by the thermal fluctuations arising from the surrounding continuous medium. As for any multiphasic system, the phases interact, and the study of a colloidal suspension requires to determine the physic of each phase and to relate these physics through a coupling relation.

It has been proved that these microscopic interactions between particles and between the fluid and the particles drive the macroscopic behavior of a colloidal dispersion. Interactions generate physical and physico-chemical forces, which lead to the spatial arrangement of the colloids, known as the microstructure of the suspension, and has a ubiquitous role in the macroscopic behavior. Broadly speaking, the microscopic interactions influence the structure, and the structure influence the microscopic interactions.

In this first chapter, the theoretical concepts used to describe colloidal suspensions are introduced. Firstly the equations describing both the particles and the fluid motions are presented. Then the forces at play in colloidal suspensions are developed. Finally, some macroscopic behaviors of colloidal suspensions are enumerated.

1 Flow of a colloidal suspension

A colloidal suspension is composed of particles embedded in a viscous fluid. The interactions between particles and between the fluid and the particles drive the macroscopic behavior of the suspension. In this section, we introduce the basic properties and equations used to study the fluid behavior of a colloidal suspension.

1.1 Low-Reynolds-number hydrodynamics

Consider a suspension of rigid (non-deformable) particles in an incompressible fluid. This suspension can be considered as an effective monophasic viscous fluid governed by the Navier-Stokes equations, *i.e.* the continuity equation for an incompressible fluid:

$$\nabla \cdot \mathbf{u} = 0 \tag{1.1}$$

and the equation of the conservation of the momentum:

$$\rho \frac{\partial \mathbf{u}}{\partial t} = \mathbf{f} + \nabla \cdot \boldsymbol{\sigma} \tag{1.2}$$

where **u** is the fluid velocity, ρ the density of the suspension, **f** the external body force per unit volume, and $\boldsymbol{\sigma}$ the Cauchy stress tensor. This tensor is symmetric and can be split into a diagonal part representative of the hydrostatic pressure and a deviatoric part related to the distortion of the system. For a Newtonian fluid, the Cauchy stress tensor is given by:

$$\boldsymbol{\sigma} = -P\boldsymbol{I} + 2\eta \mathbf{E}^{\infty} \tag{1.3}$$

with $P = (-1/3)\mathbf{tr}(\boldsymbol{\sigma})$, $\boldsymbol{I}$ the identity matrix, η the fluid viscosity and $\mathbf{E}^{\infty}$ the rate-of-strain tensor defined as:

$$\mathbf{E}^{\infty} = \frac{1}{2}\left(\nabla\mathbf{u} + \nabla\mathbf{u}^{T}\right) \tag{1.4}$$

where $\nabla\mathbf{u}$ is the velocity gradient, and $\nabla\mathbf{u}^{T}$ its transpose.

One should keep in mind that the fluid is a mixture between a Newtonian fluid and particles. Thus, as in any multiphase flow, each phase has a direct effect on the behavior of the other. Therefore, $\boldsymbol{\sigma}$ needs to account for a so-called particle stress tensor described later. With a view to simplification, particles are considered spherical, rigid (as noted above), and with a radius a. The following dimensionless numbers are defined, to characterize the consequences of the presence of particles on the system:

- $Re = Ua/\nu$ - the Reynolds number, characterizing the relative importance of inertial and viscous forces. U is the velocity of the flow, $\nu = \eta/\rho$ the kinematic viscosity and η the dynamic viscosity. Given that colloids have a typical length scale between 1 nm to 1 µm, it is correct to consider $Re << 1$.

- $St = a^2/(T\nu)$ - the Stokes number, characterizing the ratio between the particle's motion intrinsic time-scale and the characteristic time for momentum transport by viscous diffusion. In other words, this number characterizes the capacity of the particle to follow the streamlines of the fluid. For the same reason as for the Reynolds number, the Stokes number of a colloidal suspension is small $(St << 1)$.

- $Pe = Ua/D$ - the Péclet number, characterizing in that study the ratio of viscous forces and Brownian forces exerted on the colloids. D is the diffusion coefficient from the Stokes-Einstein law which for hard spheres equals to $k_bT/(6\pi\eta a)$ where k_b is the Boltzmann constant and T the absolute temperature.

In this manuscript, both the Reynolds and the Stokes number are considered small. Only the influence of the Péclet number is studied.

1.2 The Stokes equations

At low Reynolds and Stokes numbers, the Navier-Stokes equations become the Stokes equations:

$$\begin{aligned} \nabla \cdot \mathbf{u} &= 0, \\ \nabla \cdot \boldsymbol{\sigma} + \mathbf{f} &= 0 \end{aligned} \tag{1.5}$$

Some properties of flows verifying the Stokes equations, called creeping flows, are enumerated hereafter (more detail can be found in [3, 5]):

- the linearity principle: let a force f_1 be applied on a particle and U_1 the particle's velocity induced by this force. Doubling the force, *i.e.*, $f_2 = 2f_1$ doubles the velocity of the particle $U_2 = 2U_1$. This property leads to the following two principles.
- the superposition principle: the sum of the solutions satisfying the Stokes equations satisfies the Stokes equations too. A general flow field, for example a shear flow, can be split into two simpler flows: a rotational and a strain flow.
- the reversibility principle: due to the impossibility of crossing flow lines, the application of identical successive forces with opposite sign brings particles back to their starting point. If the same protocol is applied one, ten or one hundred times, particles always go back to their initial positions.
- the instantaneity principle: in the Stokes equations, time is not present, and the flow can be considered as quasi-static, *i.e.*, the flow's history has no role to play.

Due to the superposition principle, any flow can be defined as a sum of a translational, rotational and straining flow:

$$\mathbf{u}^{\infty}(\mathbf{x}) = \mathbf{U}^{\infty} + \mathbf{\Omega}^{\infty} \cdot \mathbf{x} + \mathbf{E}^{\infty} \cdot \mathbf{x} \tag{1.6}$$

with

$$\Omega_{ij}^{\infty} = \frac{1}{2}\left[\frac{\partial u_i}{\partial x_j} - \frac{\partial u_j}{\partial x_i}\right] \quad \text{and} \quad E_{ij}^{\infty} = \frac{1}{2}\left[\frac{\partial u_i}{\partial x_j} + \frac{\partial u_j}{\partial x_i}\right] \tag{1.7}$$

where $\mathbf{\Omega}^{\infty}$ and $\mathbf{E}^{\infty}$ are respectively the rotational and rate of strain tensors. In this manuscript, Stokes equations are always valid for any boundary conditions, and from the uniqueness corollary, each boundary condition (*e.g.*, set of forces on colloids) corresponds to one Stokes flow.

The fundamental solution of the Stokes equations is called the Stokeslet. It represents a tensorial relation between point forces and the velocities of the points. Let's consider a spherical particle of radius a translating in a Stokes flow with an effective external force $\mathbf{F}^e$ acting on its center of gravity. Far from the particle, points on its surface cannot be distinguished from its center of gravity. Then, forces acting on its surface can be relocalized to its center. The disturbance field in $\mathbf{x}$ created by the presence of the particle can be assimilated to the disturbance field of a point force or any superior moments (multipole expansion). The Stokeslet can be written using the Green's function $\mathcal{G}$:

$$\mathbf{u}^{PF}(\mathbf{x}) = \frac{\mathbf{F}^e(0)}{8\pi\eta} \cdot \mathcal{G}(\mathbf{x}) \tag{1.8}$$

where $\mathbf{u}^{PF}$ is the fluid flow field induced by the particle motion. The Green's function for a translating sphere in an infinite medium (no rotation nor stresslet) is called the Oseen-Burgers tensor and is equal to:

$$\mathcal{G} = \frac{\mathbf{I}}{r} + \frac{\mathbf{xx}}{r^3} \tag{1.9}$$

with r the distance to the center of gravity, $\mathbf{I}$ the identity matrix and $\mathbf{x}$ the position vector of the particle.

Let us now consider several interacting particles. The flow field acting on one particle is equal to the background flow field, plus the sum of the disturbance flows generated by the neighbors of the particle studied. Given the fact that disturbance flows can also be represented as forces, knowing the initial spatial arrangement of the spheres allows computing the forces and the dynamic behavior of the particles at any time using the Langevin equation.

1.3 The Langevin equation

Whereas the fluid velocity field is calculated using the Stokes equations, the trajectories of particles embedded in a fluid are governed by the Newtonian physics:

$$\begin{aligned} \mathbf{m} \cdot \frac{d\mathbf{U}}{dt} &= \mathbf{F}^h + \mathbf{F}^b + \mathbf{F}^p \\ \mathbf{i} \cdot \frac{d\boldsymbol{\Omega}}{dt} &= \mathbf{T}^h + \mathbf{T}^b + \mathbf{T}^p \end{aligned} \tag{1.10}$$

where **m** and **i** represent the mass and moment of inertia of the particles respectively, **U** and **Ω** the particle translational and rotational velocity vectors, **F** the forces and **T** the torques applied to the particles. The superscript h stands for hydrodynamic and corresponds to the force/torque on a particle due to its motion relative to the ambient fluid, b corresponds to the Brownian term and comes from the thermal agitation of the fluid. Finally, p stands for interparticle forces acting on the particles. One should be aware that external forces such as gravity can also be captured in this term. In this manuscript, particles are considered as inertialess. Thus, the left-hand parts of the previous equations vanish, leading to the "overdamped Langevin" equation:

$$\mathbf{0} = \mathbf{F}^h + \mathbf{F}^b + \mathbf{F}^p \tag{1.11}$$

where we have used the combined force/torque expression $\mathbf{F} = (\mathbf{F}, \mathbf{T})$. To understand how this equation can help us to compute the trajectories of the colloids numerically, we first need to describe the different forces.

2 Forces in a colloidal suspension

The microstructure of colloidal suspensions depends on the forces between particles, fluid and particles, and any forces coming from an external potential (magnetic field, gravitation). In a colloidal suspension, the volume fraction and characteristics of the colloids (shape, charge, density) determine the complexity and the amplitude of the forces, and ultimately the microstructure. At equilibrium and really low volume fraction, particles act like they are alone, and therefore interparticle forces are insignificant. The only remaining forces come from external potentials, thermal disturbances (Brownian motion), and interactions with confining walls. In the next paragraphs, the usual forces involved in a suspension are presented.

2.1 Gravity

A uniform gravitational field **g** acting on a particle generates the following force:

$$\mathbf{F}_g = \rho_p \mathbf{g} V_p \tag{1.12}$$

with V_p the volume of the particle and ρ_p its density. For immersed particles, Archimedes' principle indicates that a buoyance force associated with the pressure field acts in the opposite direction and the resultant of both forces is:

$$\mathbf{F}_r = \mathbf{F}_A + \mathbf{F}_g = (\rho_p - \rho_f)\mathbf{g}V_p \tag{1.13}$$

where ρ_f is the density of the fluid, $\mathbf{F}_r$ the resultant force and $\mathbf{F}_A$ the buoyancy force. The ratio $R_{A/g} = \mathbf{F}_A/\mathbf{F}_g$ determines the behavior of the colloids. If $R_{A/g} < 1$, colloids settle down, while if $R_{A/g} > 1$, the buoyancy is the most important force and the colloids move toward the surface and float. Finally, if $R_{A/g} = 1$, both buoyancy and gravity are equal ($\mathbf{F}_r = \mathbf{0}$) and do not have any effect on the motion of the colloids. In this work, we assume $R_{A/g} = 1$. Based on these facts, the behavior of colloids only depends on all the other forces applied, such as the hydrodynamic force.

2.2 The hydrodynamic force, torque and stresslet

In a suspension, the fluid stress field $\boldsymbol{\sigma}$ exerts a traction $\boldsymbol{f} = \boldsymbol{\sigma} \cdot \mathbf{n}$ ($\mathbf{n}$ the surface normal made precise below) on immersed particles. The integral of this traction over the surface of the particles results in the hydrodynamic force $\mathbf{F}^{\mathrm{h}}$, torque $\mathbf{T}^{\mathrm{h}}$ and the complete first moment $\mathbf{M}$. The definitions of the hydrodynamic force, torque and first moment are given below for rigid and spherical particles. For soft and anisotropic particles (spheroids), the reader is referred to the book from Kim & Karilla [5]. The force corresponds to the integral of the surface tractions on the particle's surface:

$$\mathbf{F}^{\mathrm{h}} = \int_{S_p} \boldsymbol{\sigma} \cdot \mathbf{n}\, dS = \int_{S_p} \boldsymbol{f} dS \tag{1.14}$$

where S_p is the surface of the particle, $\boldsymbol{f} = \boldsymbol{\sigma} \cdot \mathbf{n}$ is the surface traction and $\mathbf{n}$ the normal surface vector pointing in the fluid's direction. The torque generates angular momentum on particles and can be written using the Einstein notation:

$$T_k^{\mathrm{h}} = -\epsilon_{ijk} \int_{S_p} f_i x_j dS \tag{1.15}$$

where ϵ_{ijk} is the Levi-Civita tensor and $\boldsymbol{x}$ the position vector. Lastly, the complete first moment is a second rank tensor given by:

$$M_{ij} = \int_{S_p} f_i x_j dS \tag{1.16}$$

The first moment can be split into a symmetric and anti-symmetric part $M_{ij} = A_{ij} + S_{ij}$. The anti-symmetric part and the torque are directly related through the relation:

$$A_{ij} = \frac{1}{2} \int_{S_p} (\sigma_{ik} x_j - \sigma_{jk} x_i) n_k dS = -\frac{1}{2} \epsilon_{ijk} T_k^h \tag{1.17}$$

As the stress tensor is symmetric and the particle spherical, it clearly appears that in the absence of any external torque $A_{ij} = 0$. The symmetric part, commonly named stresslet is defined as [1]:

$$S_{ij} = \frac{1}{2} \int_{S_p} (\sigma_{ik} x_j + \sigma_{jk} x_i) n_k dS \tag{1.18}$$

The hydrodynamic force, torque and stresslet are the mainstays of the method used to solve the Langevin equation. Indeed, as the Stokes equations are linear, the resulting velocity fields and tractions are linear functions of the boundary conditions. Maybe the most useful result of this fact is the existence of a mobility matrix coupling all the moments of the hydrodynamic force density on the particle surface (force, torque and stresslet) to the moments of the particle velocities (translational, rotational and rate of deformation):

$$\begin{pmatrix} \mathbf{U}-\mathbf{u}^{\infty}(\mathbf{x}) \\ \boldsymbol{\omega}-\boldsymbol{\omega}^{\infty}(\mathbf{x}) \\ \mathbf{E}-\mathbf{E}^{\infty}(\mathbf{x}) \end{pmatrix} = -\begin{pmatrix} \mathcal{M}_{\mathrm{UF}} & \mathcal{M}_{\Omega\mathrm{F}} & \mathcal{M}_{\mathrm{EF}} \\ \mathcal{M}_{\mathrm{UT}} & \mathcal{M}_{\Omega\mathrm{T}} & \mathcal{M}_{\mathrm{ET}} \\ \mathcal{M}_{\mathrm{US}} & \mathcal{M}_{\Omega\mathrm{S}} & \mathcal{M}_{\mathrm{ES}} \end{pmatrix} \cdot \begin{pmatrix} \mathbf{F}^{h} \\ \mathbf{T}^{h} \\ \mathbf{S}^{h} \end{pmatrix} \tag{1.19}$$

where $\mathbf{U}$ and $\boldsymbol{\omega}$ are, respectively, the particle translational and rotational velocities, $\mathbf{E}$ the particle rate of strain which is equal to zero for rigid particles, $\mathbf{u}^{\infty}(\mathbf{x})$ the ambient fluid velocity field in the absence of any disturbance due to the particles, $\boldsymbol{\omega}^{\infty} = (1/2)\nabla \times \mathbf{u}^{\infty}$ the ambient rotational fluid velocity and finally $\mathbf{E}^{\infty}(\mathbf{x})$ the rate of strain of the ambient fluid (see equation (1.7)). The grand mobility tensor $\mathcal{M}$ is positive-definite and symmetric. Due to its symmetry, the grand mobility tensor can be inverted which gives the grand resistance tensor denoted:

$$R = \begin{pmatrix} \mathcal{R}_{\mathrm{FU}} & \mathcal{R}_{\mathrm{F}\omega} & \mathcal{R}_{\mathrm{FE}} \\ \mathcal{R}_{\mathrm{TU}} & \mathcal{R}_{\mathrm{T}\omega} & \mathcal{R}_{\mathrm{TE}} \\ \mathcal{R}_{\mathrm{SU}} & \mathcal{R}_{\mathrm{S}\omega} & \mathcal{R}_{\mathrm{SE}} \end{pmatrix} \tag{1.20}$$

The switch between the resistance and mobility formulation can be really helpful in numerical algorithms, but one must be careful of the fact that $\mathcal{M}_{\mathrm{UF}}^{-1} \neq \mathcal{R}_{\mathrm{FU}}$. The grand resistance and grand mobility tensors take into account the totality of the interactions of the particles, *i.e.*, the near and the far-field many-body interactions. The detail about the functions used for the construction of both the grand mobility and grand resistance tensors of spheres and axisymmetric particles can be found in the book from Kim & Karrila [5]. However, the resistance and the mobility tensors remain unknown for particles with complex shapes.

2.3 The Brownian force

The fluid constitutive of the continuum medium is composed of molecules in motion. This motion is due to the thermal disturbances of the molecules, which is related to the temperature of the fluid: the lower the temperature is, the slower the molecules move. While molecules are discovering the surrounding space, they hit colloids and transfer some kinetic energy to them. For small colloidal particles, this energy is important enough to generate a random displacement, the Brownian motion. The word random refers to the fact that the average displacement over a long period of time must be equal to zero. The Brownian displacement depends on the shape of the particle, the temperature, and on the local concentration of colloids.

For a dilute suspension of hard spheres, Einstein and Smoluchowski gave at the beginning of the 20^{th} century the expression of the mean square displacement $\left\langle (\Delta \boldsymbol{r}(t))^2 \right\rangle$ using the diffusion coefficient D :

$$\lim_{t\to\infty} \left\langle (\Delta \boldsymbol{r}(t))^2 \right\rangle = 6Dt \tag{1.21}$$

where t is the time, $\mathbf{r}$ the displacement vector of the particles, and with the surrounding brackets $<>$ standing for the ensemble average. For an isolated hard spheres, $D = k_bT/(6\pi\eta a)$.

When the concentration of hard spheres is high enough to not allow considering the suspension as dilute, self-diffusion is commonly split into a short and a long time part. The short time self-diffusion coefficient is determined by the average instantaneous mobility of an individual particle as $D_0^s = k_b T < \mathcal{M}_{11} >$. In contrast, the long time self-diffusion stands for a more complex behavior where the colloid interacts with other colloids under conditions of interest.

A few years after the discovery of Einstein and Smoluchowski, Langevin proposed a microscopic model of the Brownian motion using a Brownian force applied directly to the particles. This force must have a zero average and a non-zero temporal correlation approximated by white noise. In other words, the Brownian force must satisfy:

$$\left\langle \mathbf{F}^b(t) \right\rangle = 0 \quad \text{and} \quad \left\langle \mathbf{F}^b(0)\mathbf{F}^b(t) \right\rangle = \mathbf{F}^c \delta(t) \tag{1.22}$$

where $\mathbf{F}^c$ is the correlation force amplitude and $\delta(t)$ the Dirac delta function[1]. The value of $\mathbf{F}^c$ is determined from the equipartition principle (at thermal equilibrium, the kinetic energy of a particle is $k_b T/2$ for each degree of freedom). The correlation force is related to the drag force on the particle which is a clear demonstration of the fluctuation-dissipation theorem:

$$\mathbf{F}^c = 2 k_b T \boldsymbol{\mathcal{R}}_{\text{FU}} \tag{1.23}$$

The entire demonstration can be found on page 121 in the book of Guazzelli & Morris [3].

2.4 Van der Waals forces

Van der Waals (vdW) forces are electrodynamic forces between atoms and molecules. These forces act on every atom and molecule, even uncharged ones, and are effective from interatomic spacing ($\sim 0.2\text{nm}$) to long-range distances ($\sim 10\text{nm}$ in water) and depend on both the material properties of the particle and the surrounding medium. Between two permanent dipoles, the forces are called the Keesom forces, between one permanent and one induced dipole the Debye forces, and finally, the forces between two induced dipoles are called the London forces. The free energy of each of these forces varies in function of the distance between the two atoms as $1/r^6$. For a monodisperse suspension of colloids, these forces are generally attractive but remain cumbersome to calculate. Indeed, the principle of additivity is not correct for many-body system. One can understand this by considering two molecules. The vdW on the first molecule are simply due to the presence of its neighbor. If a third molecule is now added, it will generate an instantaneous field coming from the differences between the exact positions of the electrons compared with the positions of the protons, which will polarize the two other molecules and then modify the electrodynamic forces. To overcome this problem, Lifshitz suggested a theory where the atomic structure of the particles is not taken into account. Then particles are considered as a continuum medium, and the interparticle forces only depend on the dielectric constant and the refractive index of the volume studied. For a complete description of the vdW forces, and for the description of the Lifshitz theory, the reader may refer to the book of Parsegian [8]. Van der Waals forces are not taken into account in the hydrodynamic code used in this thesis (see section 1.1) as we will consider them to be negligible compared to electrostatic forces.

---

[1] In equation 1.22, $\delta(t)$ has the dimension of s^{-1}

2.5 Electrostatic forces

Surface charges of colloids can exist due to reactions on the surface of the colloid (*e.g.* (de)protonation of surface groups), or the adsorption of ions (replacement of an ion from the crystal with another ion with a different valence for example). Most colloids have a surface charge, which has the effect of modifying the local distribution of ions in the solution. Indeed, counterions are attracted by the opposite charges on the surface of the colloid (Coulomb's forces) and can form a dense layer known as the Stern layer. Thermal agitation tends to restore a uniform concentration of ions in the solution. A second layer where both Coulomb's attraction and thermal diffusion compete appears: the Gouy-Chapman or diffuse layer. If the ions can be assimilated to uncorrelated diffuse charges and the potential of the mean force is equal to the mean of the local potentials, then the repartition of ions in the diffuse layer follows the Boltzmann distribution:

$$n_k = n_k^\infty exp\left(-\frac{ez_k\psi}{k_bT}\right) \tag{1.24}$$

where z_k is the valence of the ionic species k, n_k the local number density of ions, n_k^∞ the number density of ions far away from the surface of the colloid where $\psi = 0$, ψ the electrostatic potential, and e the elementary charge of an electron (-1.605×10^{-19} C). Charges on colloids produce an electric field $\boldsymbol{E}$ given by the Maxwell-Gauss equation reduced for electrostatics:

$$\nabla \cdot (\varepsilon \boldsymbol{E}) = \rho \tag{1.25}$$

with ε the permittivity of the medium, ρ the density of charges defined as

$$\begin{cases} \rho = 0 & \text{in particles} \\ \rho = \displaystyle\sum_{k=1}^{N} ez_k n_k & \text{in the fluid} \end{cases} \tag{1.26}$$

where N is the number of different ionic species in the solution. The electric field $\boldsymbol{E}$ derives from the electrostatic potential ψ:

$$\boldsymbol{E} = -\nabla\psi \tag{1.27}$$

If we insert equations (1.24), (1.26) and (1.27) in equation (1.25), we obtain the Laplace and Poisson-Boltzmann equations:

$$\begin{cases} \nabla \cdot (-\varepsilon\nabla\psi) = 0 & \text{in particles} \\ \nabla \cdot (-\varepsilon\nabla\psi) = \displaystyle\sum_{k=1}^{N} ez_k n_k^\infty e^{-\frac{ez_k\psi}{k_BT}} & \text{in the fluid} \end{cases} \tag{1.28}$$

These equations allow calculating the electrostatic potential of a charged particle in an electrolyte. This theory is mostly valid only for monovalent ions ($z_+ = 1$ and $z_- = -1$) which allows considering the number densities of the two ionic species where $\psi = 0$ as equal: $n^\infty = n_+^\infty = n_-^\infty$. If ε is constant, it is straightforward to show:

$$\Delta\psi = \frac{2en^\infty}{\varepsilon} \sinh\left(\frac{e\psi}{k_BT}\right) \tag{1.29}$$

with Δ the Laplacian. To obtain a non-dimensional equation, we introduce the characteristic thickness of the double layer, the Debye length $\kappa^{-1} = \left[(\varepsilon k_B T)/(2e^2 n^\infty)\right]^{1/2}$, the dimensionless operator $\Delta^* = 1/\kappa^2 \Delta$ and the non-dimensional electrostatic potential ($\psi^* = \frac{e\psi}{k_B T}$). Finally the previous equation can be written in a non-dimensional form:

$$\Delta^* \psi^* = \sinh \psi^* \tag{1.30}$$

The excess of ions in the double layer and the electric field generate a stress field on the colloids. The resulting stress tensor can be written with the Einstein notation as:

$$\sigma_{ij} = -\Pi \delta_{ij} + M_{ij} \qquad i, j \in \{1, 2, 3\} \tag{1.31}$$

with M_{ij} the Maxwell tensor defined as:

$$M_{ij} = \varepsilon \left(E_i E_j - \frac{1}{2} E^2 \delta_{ij} \right) \tag{1.32}$$

and Π the local osmotic pressure due the ions equal to:

$$\Pi = 2n^\infty k_B T \left(\cosh \psi^* - 1\right) \tag{1.33}$$

As the electric field derives from the electrostatic potential, solving the PB (see equation (1.30)) allows calculating the full stress tensor. From this definition of the osmotic stress tensor, electrostatic forces, torques and first moments can be derived as in equations (1.14) to (1.16).

In this section, we have presented the forces driving the spatial arrangement of the particles. These microscopic interactions are responsible for the microstructure and influence the macroscopic behavior of the suspension. The microstructure can have specific hallmarks allowing the introduction of the idea of the existence of phases of a suspension.

3 Phase behavior

The forces described above have the effect of driving the spatial arrangement of the particles referred to as the microstructure. This microstructure depends on the particle shape, polydispersity, volume fraction, and the forces applied to the system. Microscopic interactions have an impact on the macroscopic behavior of the suspension, which is often characterized by different phases. To have an insight into the different existing phases and the complexity of some colloidal systems, we will start with the easiest system and make it progressively more complex.

Let us first consider a monodisperse suspension of hard spheres without background flow. We assume the resulting structure to be independent of the temperature, and with an infinite interaction potential between two spheres if the particles are in contact, else zero. Then, the phase diagram only depends on the volume fraction. At low volume fraction, $\phi < 0.494$, the suspension is in a fluid state, and particles are uniformly distributed due to Brownian motion. Increasing the volume fraction, $0.494 \lesssim \phi < 0.58$, leads to a glassy state where the amorphous suspension is solid with no large distance order. Finally, above $\phi = 0.58$ the suspension becomes a crystal, *i.e.*, with long-range order, and reaches its maximal compact fraction (Face-Centered Crystal, FCC) at $\phi = 0.74$. The transition between two states is not instantaneous, and the coexistence of two phases is observed, *e.g.*, the liquid to solid transition occurs for $0.494 \lesssim \phi < 0.54$. Even for the simplest suspension, the phase diagram is not easily predictable as shown in Figure 1.1.

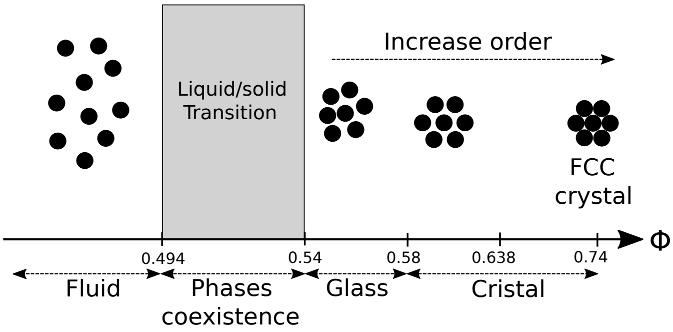

Figure 1.1: Hard sphere suspension phase diagram

Let us now make the system more complicated by considering a suspension of spheres with electrostatic interactions. If the interactions are repulsive, the transition from the liquid state to a solid-like phase occurs at a smaller volume fraction. When this transition occurs at a very low volume fraction due to strong and long-range repulsive electrostatic interactions the phase is called a Wigner glass. In an attractive system, sticky spheres with attractive short-range interactions can percolate and form a floc even at low volume fraction. The formation of the floc mainly depends on the ratio between the attraction forces and the Brownian forces. The dynamics of a floc depend on its size: the bigger the floc is, the slower it diffuses, but the faster it settles due to gravitation if present. The settling often leads to a phase separation between flocs, with a phase rich in colloids and a liquid state poor in colloids. When the flocs span the available space, they form a gel. As the range of electrostatic interactions can be tuned through the addition of salt, the characteristics of the final gel such as its density depend on both the volume fraction of particles and on the salt concentration [9].

One should keep in mind that many colloids exhibit a shape anisotropy, which drastically increases the number of possible phases. For example, Jabbari-Farouji et al. count no less than eight different phases for infinitely thin repulsive hard disks modeled with Monte-Carlo [4]. When colloidal particles have both shape and charge anisotropy, and if at the same time, the suspension is sensitive to experimental protocols, establishing the phase diagram of the colloidal suspension can be challenging. That is why, even after years of research, some discrepancies still exist concerning the phase diagram of the Laponite as shown in Figure 1.2. Laponite is a synthetic hectorite-type smectite clay with a platelet shape and an aspect ratio of approximately 30. Its faces are negatively charged while the rim bears a positive charge. Therefore, Laponite has both shape and charge anisotropy.

To describe the phases of such a complex suspension, researchers often need to make use of several measured quantities (see Figure 1.2) obtained using Dynamic Light Scattering (DLS), Static Light Scattering (SLS) and Small Angle-X ray Scattering (SAXS) [6]. Thanks to these experimental methods, it is possible to determine the spatial arrangement of the particles, their diffusion, the existence of arrested states, etc.

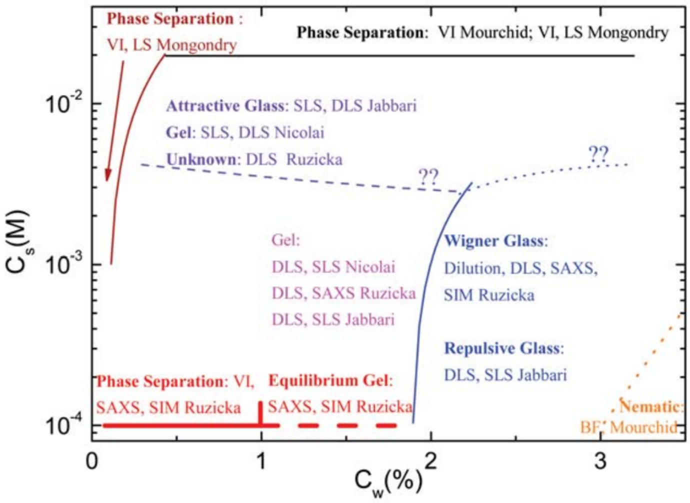

Figure 1.2: Laponite phase diagram proposed by Ruzicka and coworkers in [9].

In this section, we have only presented some phases of suspensions without background flow. However, different structures can be observed when a flow is applied to the suspension. Indeed, the microstructure depends on the forces applied to the suspension, and therefore the hydrodynamic stresses coming from the flowing fluid can modify the structure. The study of the flow of a colloidal suspension when stress is applied is called rheology.

4 Rheology of colloidal suspensions

Knowledge of microscopic interactions allows pushing further the comprehension of the macroscopic behavior of colloidal suspensions, especially its rheological behavior. The flowing behavior of colloidal suspensions is usually not Newtonian due to the numerous and complex interactions between particles and between fluid and particles. Some of these behaviors are interesting for industrial processes and in everyday life. That is why non-Newtonian suspensions are so common, *e.g.*, the toothpaste has yield stress, the mix of cornstarch with water undergoes a shear-thickening behavior, and the tomato ketchup is a thixotropic fluid. The suspension behavior is determined using experiments carried out with rheometers and allows measuring the response of the material to applied forces. Numerous types of rheometers exist depending on the flow applied (shear or extensional) and on the geometry (plate-plate, cylindrical, cone-plate, etc.). In this manuscript, we will only study the simple shear flow (Couette flow). The latter is easily obtained by confining a suspension between two parallels plates (see Figure 1.3). The application of a tangential force on the top plate generates its motion while the bottom plate is kept motionless. Then, considering no-slip conditions, the first layer of particles near the moving plate goes to the same velocity as the plate itself, dragging at its turn through viscous effects the other streamlines of the system and creating a velocity gradient in the y-direction. If the velocity is low enough to avoid turbulence, the fluid flows parallel to the plates, and the velocity gradient in the y-direction is constant. The strain rate is then defined as:

$$\dot{\gamma} = \frac{v_{plate}}{h} \tag{1.34}$$

where v_{plate} is the velocity of the moving plate and h the distance between the two plates. The shear stress is simply the force applied to the upper plate (**F** in blue in Figure 1.3), divided by the surface of contact between the fluid and the plate. In this study, calculations are realized at an imposed shear rate in an infinite medium which means that we simulate the case that the plates are far enough to have negligible effects on the flow (red box on the Figure 1.3).

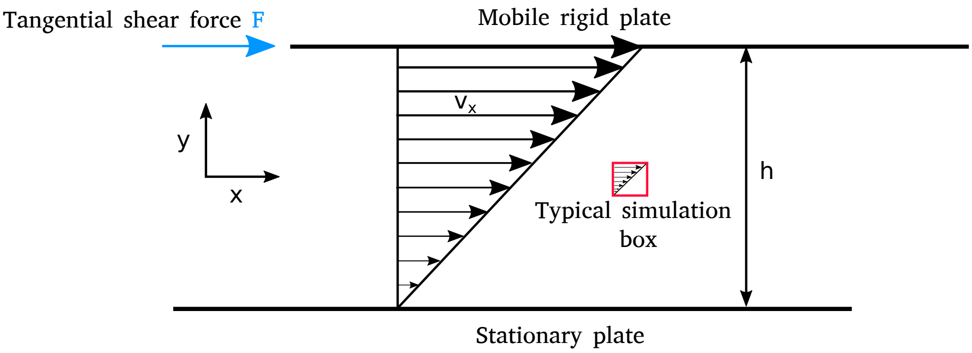

Figure 1.3: Simple shear flow between a moving and a stationary plate.

The relation between the shear stress and the shear rate defines the fluid behavior. A few classical examples are provided in the following paragraphs.

4.1 Newtonian fluids

The most simple fluids are Newtonian and are omnipresent in everyday life (water, olive oil, fruit juice, wine). In such fluids, the shear rate $\dot{\gamma}$ is linearly related to the shear stress σ through the constant viscosity of the fluid η:

$$\sigma = \eta\dot{\gamma} \tag{1.35}$$

Colloidal suspensions usually undergo more complex behavior even if the pure fluid phase is Newtonian.

4.2 Shear thinning and shear thickening fluids

The viscosity of some fluids increases (shear thickening) or decreases (shear thinning) with the shear rate. When the relation between the shear rate and the shear stress is a power law, those fluids are referred to as "generalized Newtonian fluids":

$$\sigma = k\dot{\gamma}^n \tag{1.36}$$

with k a constant depending on the fluid and n the power-law index. When n is equal to 1, one can recognize the Newtonian behavior described earlier. In such a case, k is simply the viscosity of the suspension. If $0 < n < 1$, shear-thinning is observed, *i.e.* the viscosity decreases when the shear stress increases. For $1 < n$ one can observe a shear-thickening fluid: the more the shear rate increases, the more the viscosity increases. The behavior of a colloidal suspension depends on its microstructure and of the shear stress applied. The same suspension can behave as a shear-thinning fluid, a Newtonian fluid and a shear-thickening fluid while varying the shear stress and the shear rate. Such a behavior is quite prevalent for colloidal suspensions and is reported for a suspension of latex spheres embedded in a

Newtonian fluid in Figure 1.4.

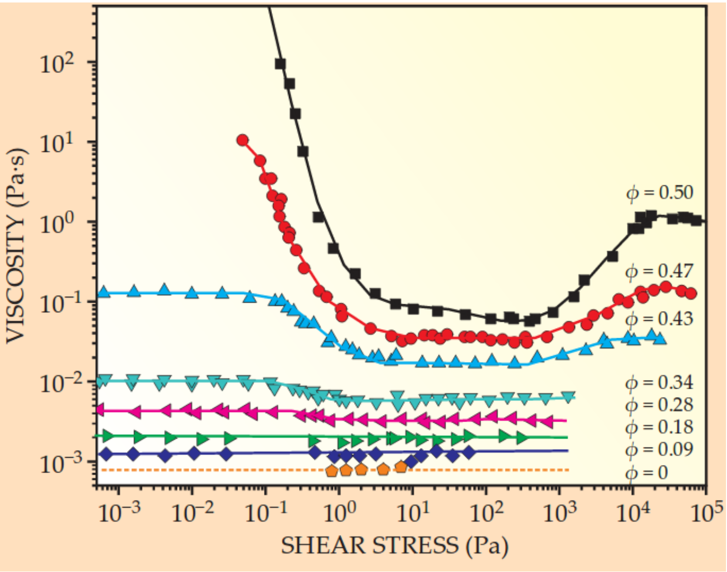

Figure 1.4: Viscosity of colloidal latex dispersions in function of the shear stress from [10].

At relatively low volume fraction ($\phi < 0.2$) the suspension is Newtonian: the viscosity remains constant whatever the shear stress (orange, purple and green curves). Increasing the volume fraction leads to shear thinning at low shear stress (curves in pink and cyan) and shear thickening at high shear stress (blue, red and black curves). At high volume fractions ($\phi > 0.43$), the suspension does not flow if the shear stress is not beyond a critical shear stress ($\sigma \sim 10^{-1}$ Pa for the red curve corresponding to a suspension with a volume fraction of $\phi = 0.47$). This critical stress is called the yield stress of the suspension.

4.3 Yield stress fluids

A yield stress fluid requires a critical stress to flow. The corresponding force to reach this critical value corresponds to the energy needed by the system to break enough inter-particular bonds to allow flow. Once this energetic threshold is crossed, the fluid can undergo a Newtonian behavior (Bingham model), shear-thinning or shear-thickening (Herschel-Bulkley models). The shear stress and the shear rate are frequently related through the following law:

$$\sigma = \sigma_y + k\dot{\gamma}^n \tag{1.37}$$

where σ_y is the yield stress. The viscosity of an ideal yield stress fluid diverges at the vicinity of the critical stress. Nevertheless, this divergence is never observed in a real fluid as shown in Figure 1.5.

4.4 Thixotropic fluids

Let us consider a colloidal suspension without any background flow. The final microstructure is reached once the Helmholtz free energy of the system is minimized, and could be trapped in a local minimum as in a gel. The application of a shear stress, referred to later as the first shear, can break bonds with

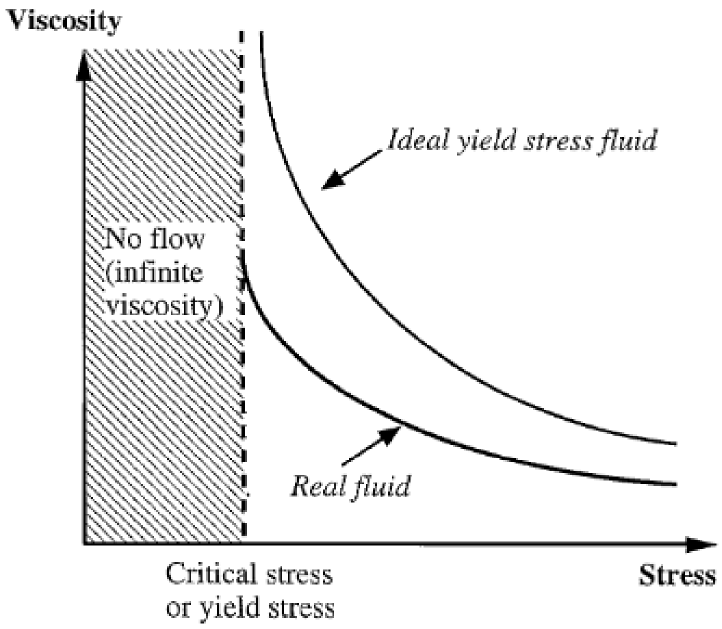

Figure 1.5: Viscosity of an ideal and a real yield stress fluid [2].

the smallest energy, and therefore modify the microstructure of the suspension leading to the reduction of the viscosity in a time-dependent fashion. Stopping the flow allows the microstructure to tend back to an energy minimum, which can be the same as the original one, or different. During this period of rest of the suspension, the viscosity increases. When a new shear is applied, if the suspension undergoes the same behavior as during the first shear, *i.e.*, the time-dependent viscosity and the same final viscosity after a long shear period of time, the suspension is then considered as thixotropic [7]. For example, one can cite tomato ketchup, latex paints, and Laponite suspensions as thixotropic fluids.

5 Conclusion

In this first chapter, the basic theoretical concepts of colloidal suspensions have been introduced. It has been highlighted that the microscopic interactions drive the spatial arrangement of particles that influence the macroscopic behavior of the suspension. A better understanding of the microscopic scale is crucial to define the phases of a suspension and to foresee their behaviors under stress.

Due to the small size of the colloids, the direct observation of the microstructure is often not possible. Moreover, the tremendous number of parameters in a colloidal suspension is really challenging to monitor (*e.g.*, polydispersity, ionic strength, pH, volume fraction, etc.). That is why experimental studies are not always suited to the microscopic study of a colloidal suspension. To overcome this difficulty, researchers have modeled colloids numerically and to study the influence of specific parameters such as the size or the polydispersity on the microstructure. In the next chapter, numerical models used to simulate suspensions of particles with both shape and charge anisotropy are presented.

References

[1] G. K. Batchelor. The stress system in a suspension of force-free particles. *Journal of Fluid Mechanics*, 41(3):545–570, April 1970.

[2] Philippe Coussot, Q. D. Nguyen, H. T. Huynh, and Daniel Bonn. Avalanche Behavior in Yield Stress Fluids. *Phys. Rev. Lett.*, 88(17):175501, April 2002.

[3] Elisabeth Guazzelli, Jeffrey F. Morris, and Sylvie Pic. *A Physical Introduction to Suspension Dynamics*. Cambridge University Press, Cambridge, 2011.

[4] Sara Jabbari-Farouji, Jean-Jacques Weis, Patrick Davidson, Pierre Levitz, and Emmanuel Trizac. Interplay of anisotropy in shape and interactions in charged platelet suspensions. *The Journal of Chemical Physics*, 141(22):224510, December 2014.

[5] S. Kim and S.J. Karrila. *Microhydrodynamics: Principles and Selected Applications*. Dover Civil and Mechanical Engineering. Dover Publications, 2013.

[6] Tao Li, Andrew J. Senesi, and Byeongdu Lee. Small Angle X-ray Scattering for Nanoparticle Research. *Chemical Reviews*, 116(18):11128–11180, September 2016.

[7] Jan Mewis and Norman J. Wagner. *Colloidal Suspension Rheology*. Cambridge Series in Chemical Engineering. Cambridge University Press, Cambridge, 2011.

[8] V. Adrian Parsegian. *Van der Waals Forces: A Handbook for Biologists, Chemists, Engineers, and Physicists*. Cambridge University Press, 2005. Library Catalog: www.researchgate.net.

[9] Barbara Ruzicka and Emanuela Zaccarelli. A fresh look at the Laponite phase diagram. *Soft Matter*, 7(4):1268, 2011.

[10] Norman J Wagner and John F Brady. Shear thickening in colloidal dispersions. 62:7, 2009.

Numerical models of colloidal suspensions

2

Experimental study of colloidal suspensions is a complicated task due to numerous parameters affecting the behavior of the particles. Among them, one can cite the difficulty of having a perfectly monodisperse suspension with the desired shape (aspect ratio) or the same instantaneous charge on every particle. Other difficulties, such as monitoring the local pH affecting the surface charge, the aging of the suspension, and broadly speaking a modification of the experimental protocol used to prepare and study the colloidal suspension can lead to discrepancies between groups of research concerning the behavior of the "same" colloidal suspension. Moreover, it is challenging to study the influence of only one parameter experimentally, as most of them are interdependent.

One alternative is to carry out numerical simulations resolving the dynamics of the colloidal suspension. Numerical simulations are especially useful to study colloidal suspensions of particles with both shape and charge anisotropy. Indeed, the simulations allow fixing some parameters such as the charges and the shape of the particles while focusing the study of only one parameter, *e.g.*, the electrostatic interaction range. However, a lot of assumptions and simplifications are often considered to model this kind of colloidal suspension due to the lack of theories concerning anisotropic particles. The model used to describe the colloids, their interactions with other particles and with the surrounding fluid can be more or less complicated and time-consuming, depending on the accuracy required for the study. For example, the more accurate way to compute the hydrodynamic stress tensor on the particles is to mesh the system and then to solve in every point of space Stokes equations using direct numerical simulations (DNS). The negative side of this method lies in its tremendous computational cost coming from the three-dimensional resolution of the Stokes equations. Moreover, the Brownian motion is difficult to compute – *e.g.* using fluctuating hydrodynamic (see Landau & Lifshitz [23]); that is why DNS is rarely used to model colloidal suspensions. An alternative way to compute the dynamics of a colloidal suspension is to coarse-grain the system into elementary objects for which the theory is known and relatively "easy" to compute. Disregard this highlighting, in the first chapter, it has been stated that the mobility tensor of spherical objects is known, which makes evident the use of spheres as elementary objects to coarse-grain anisotropic colloids. To illustrate the coarse-graining of a particle, let us consider a rod-shaped colloid. Instead of considering the rod as a unique object, it can be described by a stack of spheres as shown on the middle rod in Figure 2.1 or even coarse-grained in a finner way, as shown for the right-most rod in the same figure. Of course, using a fine description increases the computational cost. That is why the principle of this kind of simulation is to coarse-grain the system as much as possible while keeping the physics unchanged. In practice the dynamics of interconnected spheres will be considered instead of that of the original rods.

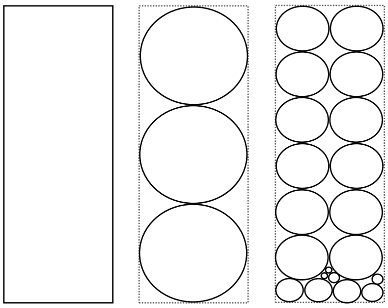

Figure 2.1: Coarse grain examples of a rod shaped colloid.

Although this coarse-graining of the particles allows computing hydrodynamics, studies from literature are mainly focused on the behavior of suspensions without background flow and have been carried out using Monte-Carlo (MC) or Brownian Dynamics (BD) simulations. Given that the rheology of a suspension is the study of its flow in response to an applied force, the hydrodynamic interactions can be taken into account in the model to compute rheological quantities such as the viscosity or the normal stress differences. We will present in this chapter a numerical method allowing the computation of the rheological quantities for a suspension of particles with both shape and charge anisotropy.

To this end, the numerical method used to compute the spherical colloidal dynamics is first presented. Then, the explanation of how this method is used to coarse-grain anisotropic particles with both structural and charge anisotropy is described. Finally, the two different models implemented in this thesis are described and compared with results from the literature.

1 Numerical simulation of suspensions of spherical colloidal

Although the dynamics of spherical colloids including many-body interactions can be computed using different methods such as the force coupling method (FCM) or even using DNS, the oldest method in our knowledge is the one introduced in the early 1980s by Bossis and Brady [7]. In their method, these authors proposed to numerically compute the Langevin equation in writing the hydrodynamic force using the grand resistance matrix (see Chapter 1 section 2.2). This method is known as the Stokesian Dynamics.

1.1 Stokesian Dynamics

We note that due to the linearity of the Stokes equations the hydrodynamic force and torque on a particle are coupled with the disturbance flow $\mathbf{F}^h = -\boldsymbol{\mathcal{R}}^{FU}(\mathbf{U}_p - \mathbf{u}^\infty) + \boldsymbol{\mathcal{R}}^{FE}\mathbf{E}^\infty$ where we have used the force/torque notation $\mathbf{F}^h = (\mathbf{F}^h, \mathbf{T}^h)$, the translational/rotational velocity notation $\mathbf{U}_p = (\mathbf{U}_p, \boldsymbol{\Omega}_p)$, and where $\boldsymbol{\mathcal{R}}^{FU}$ and $\boldsymbol{\mathcal{R}}^{FE}$ are part of the grand resistance tensor. The resistance expression of the hydrodynamic force can be inserted into equation (1.11), giving the final expression of the overdamped Langevin equation used by Bossis & Brady [7] for the calculation of the dynamical behavior of a sheared suspension of spheres:

$$0 = -\boldsymbol{\mathcal{R}}^{FU}(\mathbf{U}_p - \mathbf{u}^\infty) + \boldsymbol{\mathcal{R}}^{FE}\mathbf{E}^\infty + \mathbf{F}^p \tag{2.1}$$

where $\mathbf{F}^p$ represents interparticle forces, $\mathbf{U}_p$ the velocity of the colloids and $\mathbf{E}^\infty$ the bulk rate-of-strain tensor. In the following equations, the net interparticle force on the suspension is assumed to vanish: $\sum \mathbf{F}^p = 0$. To compute the velocity and therefore solve equation (2.1), we need to generate the grand resistance tensor $\boldsymbol{\mathcal{R}}$ and invert $\boldsymbol{\mathcal{R}}^{FU}$. One should remember that the grand resistance matrix must take into account both the near- and far-field many-body interactions. In their first work Bossis & Brady [7, 9], did not consider the stresslet for the computation of the grand resistance matrix. In order to decrease the leading error of such an assumption, Durlofsky and Brady [12] proposed a new method where the resistance tensor is computed in two steps. To develop this method, we first need to explain how the velocity and the forces are linked through the grand mobility matrix. Let us now consider N rigid particles in an ambient flow $\mathbf{u}^\infty$. The integral equation of the velocity field at any point $\boldsymbol{x}$ in the fluid or within the particles is given by [22]:

$$u_i(\boldsymbol{x}) - u_i^\infty(\boldsymbol{x}) = -\frac{1}{8\pi\eta}\sum_{\alpha=1}^{N}\int_{S_\alpha} \mathcal{G}_{ij}(\boldsymbol{x}-\boldsymbol{y}) f_i \, dS_y \tag{2.2}$$

where S_α represents the surface of the particle α, and $\boldsymbol{y}$ the point on the particle surface. Expanding $\mathcal{G}_{ij}(\boldsymbol{x}-\boldsymbol{y})$ about $\boldsymbol{y} = 0$ and introducing the definitions of the zeroth (the hydrodynamic force) and first moment of the surface traction $\boldsymbol{f}$ given respectively by equations (1.15) and (1.16), we obtain the multipole expansion:

$$u_i(\boldsymbol{x}) - u_i^\infty(\boldsymbol{x}) = \sum_{\alpha=1}^{N}\left\{-F_j^h\left(1+\frac{a^2}{6}\nabla^2\right)\frac{\mathcal{G}_{ij}(\boldsymbol{x})}{8\pi\eta} + M_{jk}\left(1+\frac{a^2}{10}\nabla^2\right)\frac{\partial}{\partial x_k}\frac{\mathcal{G}_{ij}(\boldsymbol{x})}{8\pi\eta} + ...\right\} \tag{2.3}$$

The exact solution requires the full Taylor expansion, corresponding to the addition of higher moments symbolized by the "..." in the equation (2.3). In what follows the expansion is truncated up to the "dipole version" as only the first two moments (zeroth and first order) are considered. Then we define the disturbance velocity field $\mathbf{u}_i^\alpha(\boldsymbol{x})$ generated by all the particles except the particle α, without taking into account the background flow:

$$u_i^\alpha(\boldsymbol{x}) = \sum_{\beta=1,\beta\alpha}^{N}\left\{-F_j^h\left(1+\frac{a^2}{6}\nabla^2\right)\frac{\mathcal{G}_{ij}(\boldsymbol{x})}{8\pi\eta} + M_{jk}\left(1+\frac{a^2}{10}\nabla^2\right)\frac{\partial}{\partial x_k}\frac{\mathcal{G}_{ij}(\boldsymbol{x})}{8\pi\eta}\right\} \tag{2.4}$$

The Faxén laws for spheres [4] allow writing the motion $\mathbf{U}^\alpha$ of the particle α as a function of the disturbance velocity field given in equation (2.4):

$$\begin{aligned}
U_i^\alpha - u_i^\infty(\boldsymbol{x}^{\boldsymbol{\alpha}}) &= -\frac{F_i^{h,\alpha}}{6\pi\eta a} + \left(1+\frac{a^2}{6}\boldsymbol{\nabla}^2\right)u_i^\alpha\left(\boldsymbol{x}^{\boldsymbol{\alpha}}\right)\\
\omega_i^\alpha - \omega_i^\infty(\boldsymbol{x}^{\boldsymbol{\alpha}}) &= -\frac{T_i^{h,\alpha}}{8\pi\eta a^3} + \frac{1}{2}\boldsymbol{\nabla}\times u_i^\alpha\left(\boldsymbol{x}^\alpha\right)\\
-E_{ij}^\infty(\boldsymbol{x}^{\boldsymbol{\alpha}}) &= -\frac{3}{20\pi\eta a^3}S_{ij}^{h,\alpha} + \frac{1}{2}\left(1+\frac{a^2}{10}\boldsymbol{\nabla}^2\right)\left[\frac{\partial u_i^\alpha}{\partial x_j^\alpha} + \frac{\partial u_j^\alpha}{\partial x_i^\alpha}\right]
\end{aligned} \tag{2.5}$$

Introducing equation (2.4) into equation (2.5) allows writing the velocity of particle α as a function of the zeroth and first moment. If we write equation (2.5) for each particle, the tensorial relation between the velocities and the hydrodynamic force, torque, and stresslet of the particles correspond to the far-field approximation of the grand mobility matrix $\mathcal{M}^{\infty}$:

$$\begin{bmatrix} \mathbf{U}_p - \mathbf{u}^{\infty}(\boldsymbol{x}) \\ \boldsymbol{\omega_p} - \boldsymbol{\omega}^{\infty}(\boldsymbol{x}) \\ -\mathbf{E}^{\infty}(\boldsymbol{x}) \end{bmatrix} = -\mathcal{M}^{\infty} \cdot \begin{bmatrix} \mathbf{F}^h \\ \mathbf{T}^h \\ \mathbf{S}^h \end{bmatrix} \tag{2.6}$$

One should notice that $\mathcal{M}^{\infty}$ is a purely geometric tensor and only depends on the position of the particles. Moreover, emphasize on the fact that $\mathcal{M}^{\infty}$ must be defined as symmetric and positive definite, and special attention must be paid to the signs of the forces. The terms "approximation" and "far-field" are used to represent the fact that the multipole expansion was truncated to the dipole order. Due to that truncation, the lubrication interactions are not taken into account. That is why, after the inversion of the grand resistance matrix to form $(\boldsymbol{\mathcal{M}}^{\infty})^{-1}$, Durlofsky and Brady [12] proposed to introduce in a second step and in a pairwise additive fashion a two-body resistance tensor[1] $\boldsymbol{\mathcal{R}}_{2B}$. However as the far-field two-body interaction $\boldsymbol{\mathcal{R}}_{2B}^{\infty}$ was already taken into account into $(\boldsymbol{\mathcal{M}}^{\infty})^{-1}$, it must be subtracted, which lead to the final equation for the grand resistance matrix:

$$\boldsymbol{\mathcal{R}} = (\boldsymbol{\mathcal{M}}^{\infty})^{-1} + \boldsymbol{\mathcal{R}}_{2B} - \boldsymbol{\mathcal{R}}_{2B}^{\infty} \tag{2.7}$$

where the last two terms depict near-field interactions for a distance within a cutoff radius generally equals to 4 particle radii. For larger distance, the entry is simply zero, and therefore we obtain a sparse near-field lubrication matrix $\boldsymbol{\mathcal{R}}_{nf} = \boldsymbol{\mathcal{R}}_{2B} - \boldsymbol{\mathcal{R}}_{2B}^{\infty}$.

The same year Durlofsky et al. developed this method, Bossis & Brady worked on adding the Brownian force to equation (2.1) while respecting the fluctuation-dissipation theorem [5]. With the Brownian force, the Langevin equation becomes:

$$\begin{bmatrix} \mathbf{0} \\ \mathbf{S} \end{bmatrix} = -\boldsymbol{\mathcal{R}} \cdot \begin{bmatrix} \mathbf{U}_p - \mathbf{u}^{\infty} \\ -\mathbf{E}^{\infty} \end{bmatrix} + \begin{bmatrix} \mathbf{F}^b + \mathbf{F}^p \\ -\mathbf{r}\mathbf{F}^p \end{bmatrix} \tag{2.8}$$

where $\mathbf{r}$ is the center to center vector for a pair of spheres and $-\mathbf{r}\mathbf{F}^p$ the stress known in molecular dynamics as the "pressure tensor". It is important to emphasize that all the forces, torques, and stresslets are applied to the centers of gravity of the spheres. Particles are considered as "overlapping" each other if the distance between two centers is inferior to the sum of the radii. Lubrication forces are sometimes not sufficient to avoid such non-physical behavior without use of a very small time step not suitable for numerical simulations. To overcome this difficulty, a repulsive short-range force is added and corresponds to one of the interparticle forces $\mathbf{F}^p$ as first described in early work by Brady and coworkers [7]. The integration of the first line of equation (2.8) twice over a time step Δt (smaller than the time needed by the microstructure to change, and larger than the relaxation time) leads to the displacement $\Delta \mathbf{x}$ of the particle [6, 7, 9, 12, 14]:

$$\left.\begin{aligned} \Delta \mathbf{x} = (\mathbf{u}^{\infty} + \boldsymbol{\mathcal{R}}_{\text{FU}}^{-1} \cdot [\boldsymbol{\mathcal{R}}_{\text{FE}} : \mathbf{E}^{\infty} + \mathbf{F}^p])\Delta t + k_b T \nabla \cdot \boldsymbol{\mathcal{R}}_{\text{FU}}^{-1} \Delta t + \mathbf{X}(\Delta t) \\ \textit{with } \langle \mathbf{X} \rangle = 0 \quad \textit{and} \quad \langle \mathbf{X}(\Delta t)\, \mathbf{X}(\Delta t) \rangle = 2 k_b T \boldsymbol{\mathcal{R}}_{\text{FU}}^{-1} \Delta t \end{aligned}\right\} \tag{2.9}$$

---

[1] The exact formulation of the two spheres resistance tensor is given in the book of Kim & Karrila [20].

with $\mathbf{X}(\Delta t)$ the random displacement of the particle due to Brownian motion, and $k_b T \nabla \cdot \boldsymbol{\mathcal{R}}_{\text{FU}}^{-1}$ a mean drift term coming from the simple forward time-stepping (displacement due to the configuration space divergence of the N-particle diffusivity). Most of the numerical cost of the resolution of this equation stems from the generation of the far-field mobility matrix $\boldsymbol{\mathcal{M}}^{\infty}$ involving $O(N_s^2)$ operations, its inversion $O(N_s^3)$ and in the inversion of $\boldsymbol{\mathcal{R}}_{\text{FU}}$, a $(6N_s \times 6N_s)$ tensor where N_s represents the number of individual spheres in the suspension. It clearly appears that this method is not adequate for the computation of a large system with hundreds of particles. That is the reason why a new method with a more favorable scaling was developed in the early 2000s referred to as Accelerated Stokesian Dynamics.

1.2 Accelerated Stokesian Dynamics

The ASD method was developed by Sierou et al. [35] to reduce the computational cost. Sierou & Brady proposed to compute the far-field hydrodynamic force and stresslet directly, thus avoiding the calculation of $\mathcal{M}^{\infty}$ and its inversion. The expression of the hydrodynamic force is given by

$$\mathbf{F}^h = -\boldsymbol{\mathcal{R}}_{\text{FU},nf} \cdot (\mathbf{U}_p - \mathbf{u}^{\infty}) + \boldsymbol{\mathcal{R}}_{\text{FE},nf} : \mathbf{E}^{\infty} + \mathbf{F}_{ff}^h, \tag{2.10}$$

where the subscript "nf" means near-field and "ff" far-field. It is important to emphasize that the far-field force also refers to many-body interactions. Its computation is realized in an iterative fashion in $O(N_s^{1.25})$ operations. We stress that $\boldsymbol{\mathcal{R}}_{\text{FU},nf}$ is a sparse matrix and its inversion can be done using an iterative solver such as the conjugate gradient method scaling as $O(N_s)$ if implemented with a Cholesky preconditioner. For a complete explanation of the computation of the far-field hydrodynamic force, torque and stresslet, the reader may refer to Sierou's article [35] and thesis [34]. In a few words, the computation of $\mathbf{F}_{ff}^h$ is based on the work from Hasimoto [16]. The author wrote the periodic fundamental solutions of the Stokes equations for point forces (recall that spheres can be approximated by point forces at a large distance, see Chapter 1 section 1.2). Next, Hasimoto used the Ewald's summation technique to write the velocity of a sphere as a sum of both a real space and a wave space part: $\mathbf{u}_{ff} = \mathbf{u}^{RS} + \mathbf{u}^{WS}$ where the superscript RS and WS stand for respectively the real space and the wave space sum part. Comparing this expression of the velocity with the point force solution leads to the expressions for the periodic Stokeslet in the real ($\boldsymbol{\mathcal{G}}^{RS}$) and in the Fourier space ($\boldsymbol{\mathcal{G}}^{WS}$). The real sum contribution to the velocity is straightforward using multipole expansions with the successive derivatives of the Stokeslet $\boldsymbol{\mathcal{G}}^{RS}$. The wave sum contribution to the velocity is more complex and is computed in three steps. Firstly, the moments of the particle (force, doublet, quadrupole and octupole) are distributed on the nodes of a grid and described by point forces. Secondly, the application of the Fourier transform of the point forces allows writing the wave part velocity in the Fourier space $\hat{\mathbf{u}}^{WS}$. Finally, the inverse Fourier transform of $\hat{\mathbf{u}}^{WS}$ gives $\mathbf{u}^{WS}$, the wave-space contribution to the total velocity. Concerning the nodes on which the moments are distributed, Sierou and Brady have shown that the moments conservation requires 125 nodes per spheres. However, it will be demonstrated later in this manuscript that for anisotropic particles, the use of a coarser grid does not change the results significantly (see Chapter 2 section 3). Thanks to the far-field velocity $\mathbf{u}_{ff}$ Sierou and Brady were able to calculate the far-field hydrodynamic force, torque, and stresslet using the Faxén laws:

$$\begin{aligned}
\boldsymbol{F}_{ff}^{h,\alpha} &= -6\pi\eta a \left(\mathbf{U}^{\alpha} - \mathbf{u}^{\infty}(\boldsymbol{x}^{\boldsymbol{\alpha}})\,\right) + 6\pi\eta a \left(1 + \frac{a^2}{6}\boldsymbol{\nabla}^2\right)\mathbf{u}_{ff}^{\alpha}\left(\boldsymbol{x}^{\boldsymbol{\alpha}}\right)\\
\boldsymbol{T}_{ff}^{h,\alpha} &= -8\pi\eta a^3\left(\boldsymbol{\omega}_i^{\alpha} - \boldsymbol{\omega}_i^{\infty}(\boldsymbol{x}^{\boldsymbol{\alpha}})\right) + 4\pi\eta a^3\boldsymbol{\nabla}\times\mathbf{u}_{ff}^{\alpha}(\boldsymbol{x}^{\boldsymbol{\alpha}}) \qquad (2.11)\\
\boldsymbol{S}_{ff}^{h,\alpha} &= \frac{20\pi\eta a^3}{3}\left[\mathbf{E}^{\infty}(\boldsymbol{x}^{\boldsymbol{\alpha}}) + \left(1 + \frac{a^2}{10}\boldsymbol{\nabla}^2\right)\mathbf{e}_{ff}(\boldsymbol{x}^{\boldsymbol{\alpha}})\right]
\end{aligned}$$

One should note the similarities with the equation (2.6). Thus, introducing the grand mobility matrix the previous equation becomes:

$$\begin{bmatrix}\mathbf{F}_{ff}^{h}\\ \mathbf{T}_{ff}^{h}\\ \mathbf{S}_{ff}^{h}\end{bmatrix} = -(\boldsymbol{\mathcal{M}}^{\infty})^{-1}\cdot\begin{bmatrix}\mathbf{U}_p - \mathbf{u}^{\infty}\\ \boldsymbol{\omega}_p - \boldsymbol{\omega}^{\infty}\\ -\mathbf{E}^{\infty}\end{bmatrix} \qquad (2.12)$$

The hydrodynamic far-field forces, torques and stresslets are computed in an iterative fashion involving $O(N_s^{1.25})$. We have reported in Appendix 1 the flow chart given by Sierou [34]. Finally equation (2.8) becomes in the Accelerated Stokesian Dynamics (ASD) developed by Sierou and Brady:

$$\begin{bmatrix}\mathbf{0}\\ \mathbf{S}\end{bmatrix} = -\widetilde{\mathcal{R}}_{nf}\cdot\begin{bmatrix}\mathbf{U}_p - \mathbf{u}^{\infty}\\ -\mathbf{E}^{\infty}\end{bmatrix} + \begin{bmatrix}\mathbf{F}^{p} + \mathbf{F}_{ff}^{h} - \lambda(\mathbf{U}_p - \mathbf{u}^{\infty})\\ -\mathbf{r}\mathbf{F}^{p} + \mathbf{S}_{ff}^{h}\end{bmatrix} \qquad (2.13)$$

with the near-field resistance matrix:

$$\widetilde{\mathcal{R}}_{nf} = \begin{bmatrix}\widetilde{\boldsymbol{\mathcal{R}}}_{\text{FU},nf} & \boldsymbol{\mathcal{R}}_{\text{FE},nf}\\ \boldsymbol{\mathcal{R}}_{\text{SU},nf} & \boldsymbol{\mathcal{R}}_{\text{SE},nf}\end{bmatrix} \qquad (2.14)$$

where a diagonal tensor $\lambda\mathbf{I}$ was added the $\boldsymbol{\mathcal{R}}_{\text{FU,nf}}$ to ensure its positiveness and its invertibility: $\widetilde{\boldsymbol{\mathcal{R}}}_{\text{FU}} = \boldsymbol{\mathcal{R}}_{\text{FU}} + \lambda\mathbf{I}$. Following Swan [37], a value of 1 for λ is always sufficient.

The method developed by Sierou was only for non-Brownian particles. The Brownian part was added by Banchio & Brady who proposed two methods to extend the ASD to suspensions with Brownian motion. The authors used the linearity of the Stokes flows to superimpose effects and to split $\mathbf{U}_p - \mathbf{u}^{\infty}$ into a hydrodynamic velocity $\mathbf{U}^h$, an interparticle velocity $\mathbf{U}^p$ and a Brownian velocity $\mathbf{U}^b$. Thus, the authors obtained two equations, the first one including the hydrodynamic and interparticle parts, and a second one including only the Brownian part written as:

$$\begin{bmatrix}\mathbf{0}\\ \mathbf{S}^h + \mathbf{S}^p\end{bmatrix} = -\widetilde{\mathcal{R}}_{nf}\cdot\begin{bmatrix}\mathbf{U}^h + \mathbf{U}^p\\ -\mathbf{E}^{\infty}\end{bmatrix} + \begin{bmatrix}\mathbf{F}^{p} + \mathbf{F}_{ff}^{h} - \lambda(\mathbf{U}^h + \mathbf{U}^p)\\ -\mathbf{r}\mathbf{F}^{p} + \mathbf{S}_{ff}^{h}\end{bmatrix} \qquad (2.15)$$

$$\begin{bmatrix}\mathbf{0}\\ \mathbf{S}^b\end{bmatrix} = -\left[(\boldsymbol{\mathcal{M}}^{\infty})^{-1} + \boldsymbol{\mathcal{R}}_{2B} - \boldsymbol{\mathcal{R}}_{2B}^{\infty}\right]\cdot\begin{bmatrix}\mathbf{U}^b\\ \mathbf{0}\end{bmatrix} + \begin{bmatrix}\mathbf{F}^b\\ \mathbf{0}\end{bmatrix} \qquad (2.16)$$

where we have used the developed form of the grand resistance matrix given in equation (2.7). The first method consists in replacing the Brownian far-field mobility matrix $\boldsymbol{\mathcal{M}}^{\infty}$ by a diagonal matrix with effective values depending on the volume fraction. These values are the translational and rotational short-time self-diffusivity for spheres at equilibrium without any interparticle interactions, equivalent to a sphere in an infinite medium. Concerning the computation of the Brownian motion for anisotropic particles, we have made the choice of considering the far-field mobility matrix as a diagonal matrix, even if it can have the consequence of slightly violating the fluctuation-dissipation theorem. Naturally, identifying the diffusion coefficients with those of plate-like particles is non-sense. Thus, we decided to consider those parameters as free parameters to mimic the theoretical average diffusion coefficient of the desired particle in an infinitely dilute system. If this method is not physically rigorous it drastically decreases the computational cost. Indeed, the inverse of a diagonal matrix is trivial to compute and can easily be added to the near-field resistance matrix before being inverted using the conjugate gradient method. The key step in the second method consists in replacing $(\boldsymbol{\mathcal{M}}^{\infty})^{-1}$ by its Chebyshev polynomial approximation. The details can be found in Banchio & Brady's paper [1].

The ASD method was widely used in the last decade. For example, one can cite the study of repulsive electrostatic interactions by Nazockdast et al. [29], oscillatory flows by Marenne and coworkers [24, 25], self-propelled particles by Swan et al. [37] who also adapted the ASD to confined geometry in his thesis [36]. Recently, Brady's group developed a far-field computation of a polydisperse suspension [41] which could allow using polydisperse spheres to coarse grain anisotropic particles.

1.3 Summary

The Stokesian Dynamics (SD) method was originally designed to compute the dynamics of a small number of spheres (64 spheres). The limitation concerning the latter lies in the important computation cost for the construction of the grand resistance matrix and its inversion. Indeed, its computation requires the formation of the far-field approximation of the mobility matrix $\boldsymbol{\mathcal{M}}$ of size $(11N_s \times 11N_s)$ and its inversion scaling respectively as $O(N_s^2)$ and $O(N_s^3)$. Then, solving the velocities of the spheres requires the inversion of the grand resistance matrix $\mathcal{R}$ of size $(11N_s \times 11N_s)$ scaling also as $O(N_s^3)$. Given the fact that a typical simulation carried out in the current study comprises 2220 spheres, computing then inverting $\mathcal{M}$ of size (24420×24420) is too expensive, and therefore this method will not be used for systems with such a high number of spheres. Nonetheless, one should keep in mind that this method is the reference, and the ASD method was developed only for the purpose of decreasing the computational cost. This accelerated version avoids computing directly the far-field approximation of the grand mobility matrix, and therefore the grand resistance matrix. The far-field hydrodynamic force, torque, and stresslet are computed in an iterative fashion. The Brownian motion is either computed using a diagonal matrix instead of $\boldsymbol{\mathcal{M}}$ or using the Chebyshev decomposition of the latter. In this work we have made the choice to use a diagonal matrix in the ASD method to simulate anisotropic coarse-grained particles.

Using the ASD method allows reducing the scaling of the code from $O(N_s^3)$ for the SD version to $O(N_s^{1.25})$. However, attention should be paid to the way the Brownian motion is computed in ASD, and the SD method should always be used to validate the physical behavior of the suspensions, especially at low Péclet number due to the approximate treatment of Brownian effects in ASD. In order to study the dynamics of coarse-grained anisotropic particles, we have extended these methods to model the dynamics of rigid-bodies composed of spherical particles.

2 Coarse-grained model of anisotropic particles

Now that we have introduced the SD and ASD methods to compute the dynamics of spherical particles, we will present two different approaches to generate particles with both shape and charge anisotropy using spheres as elementary objects. The coarse-grained particles will also be called clay-like particles as it refers to a plate-like shape with some anisotropic charge distribution but we emphasize that the method developed allows simulating any shape. In this section, we will first describe how the coarse-grained particles are generated. Then two different methods used to keep a particle rigid are presented. Finally, the way to implement the charge anisotropy is developed.

2.1 Generation of a coarse-grained particle

The first step of the coarse-graining consists in the generation of a 2D hexagonal compact crystal of spheres, as shown in Figure 2.2 (a). The centers of gravity of three touching spheres form an equilateral triangle, which is the optimal way to place spheres to reach the maximum sphere packing fraction. Then, this hexagon is duplicated and stacked to form multiple layers, as shown in Figure 2.2 (b) and (c). Layers are stacked in a hexagonal close-packing (HCP) lattice to maintain the highest density. Finally, spheres are taken off from the crystal using a level-set method to obtain the final shape.

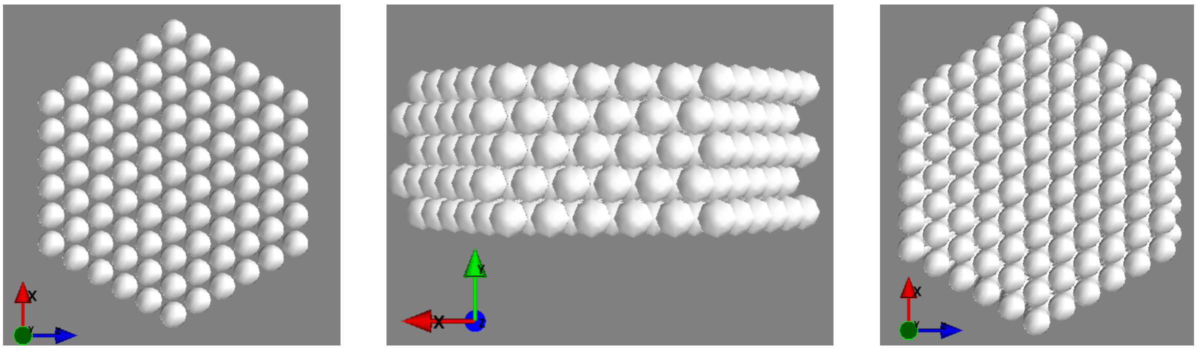

(a) Hexagonal sphere packing (b) HCP: z direction (c) HCP: y direction

Figure 2.2: Generation of a HCP crystal.

In this work, as the desired shape is a plate-like particle, the level-set function of an ellipsoid is used (in red in Figure 2.3): the distance between the center of each sphere and the surface of the ellipsoid is computed following the equations given by Eberly [13]. A positive distance means that the sphere is outside the ellipsoid and must be removed, whereas a negative distance means the sphere is inside the ellipsoid and has to be kept. Depending on the desired shape, the characteristics of the ellipsoid (semi-minor and semi-major axis) can be changed, and one can choose between an oblate or a prolate spheroid as shown in Figure 2.3.

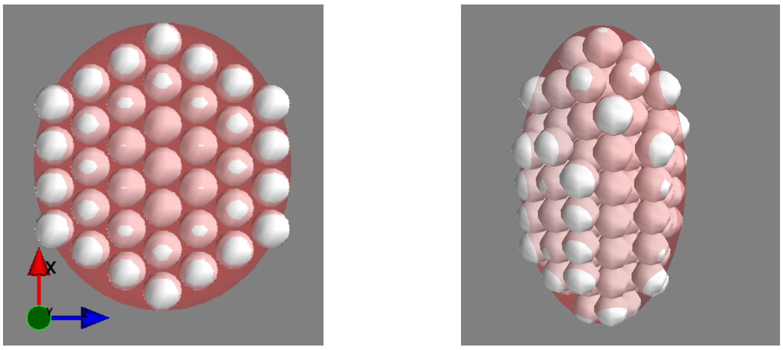

(a) Oblate particle (b) Prolate particle

Figure 2.3: Oblate and prolate spheroids generated from an HCP crystal and a level-set method. The oblate particle (a) will be considered as the coarse-graining of a plate-like particle.

The oblate spheroid in Figure 2.3 (a) is composed of 37 spheres and will be considered as the coarse-graining of the clay-like particle studied in this thesis. It will be referred to as $AR7$ particle in this manuscript due to its Aspect Ratio close to 7 (7.3 exactly due to small interparticle spacing). The prolate spheroid will be used as a validation test of the hydrodynamic behavior of the coarse-grained model at infinite Péclet number. We recall once again that the ASD code is originally designed for free spheres. To keep the object rigid, we developed two different methods. The first one consists in adding forces acting like springs between spheres of the same object. The second method consists of constraining the system by reducing the number of degrees of freedom for spheres of the same object using solid mechanics equations.

2.2 Spheres bound with springs - (A)SD-SBS

Binding spheres with springs to form a rigid coarse-grained object is quite common in the literature [8, 33]. The tied points of the springs on the surface of the spheres will be referred to as binding points. The number of binding points determines the number of springs for a pair of spheres. The computation of the positions of the N binding points for a pair of spheres is realized in two steps:

1. Firstly a reference point C_1^m is created at the intersection between the surface of the sphere m and the center to center line between the two particles. This point is considered as the pole in a spherical coordinates frame.

2. Then $N-1$ points are created around C_1^m. These points C_i^m with $1 \leq i \leq N$ are set, such as keeping both the latitude between C_1^m and C_i^m constant and the difference of longitude between two consecutive points constant too.

To ensure the stiffness of the anisotropic particle, each pair of particles must be rigid, and we have found that five binding points are necessary to avoid rolling, bending and stretching between two spheres. The springs are represented in red in Figure 2.4.

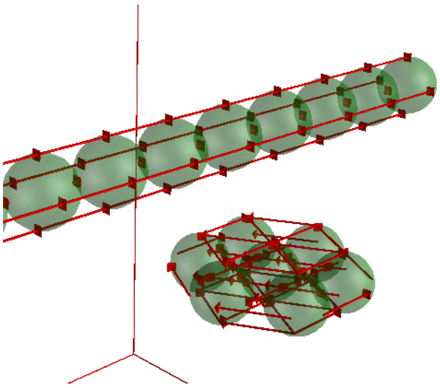

Figure 2.4: Rod and plate-like particle with springs binding spheres. Each red arrow represents a spring.

Using Hooke's law, the force on particle 1 due to a spring between particle 1 and particle 2 is equal to:

$$\mathbf{F}^1 = k\left(\left\|\mathbf{C}^2 - \mathbf{C}^1\right\| - L_0\right) \cdot \frac{\left(\mathbf{C}^2 - \mathbf{C}^1\right)}{\left\|\mathbf{C}^2 - \mathbf{C}^1\right\|} \tag{2.17}$$

where k is the spring constant, $\mathbf{C}^1$ and $\mathbf{C}^2$ the positions of the binding points on, respectively, particle 1 and 2 and L_0 is the length of the spring at rest. This force induces a torque on the particle 1:

$$\mathbf{T}^1 = \left(\mathbf{C}^1 - \mathbf{C}^1_g\right) \times \mathbf{F}^1 \tag{2.18}$$

where $\mathbf{C}^1_g$ is the center of gravity of the sphere and × stands for the cross-product. The total force and torque on a sphere are simply equal to the sum of the forces and torques generated by the springs tied on the particle. As the forces and the torques are applied to the center of the spheres in (A)SD, the sum of the spring forces is also applied to the center and can be considered as an interparticle force. This method will be referred to as the (A)SD-SBS (Spring-Bound Spheres) method. The advantage of this method is that almost no development is required in the code. Indeed, the force and the torque due to the springs on each pair of particles are simply added to the existing interparticle force $\mathbf{F}^p$.

Unfortunately, the (A)SD-SBS method has numerous weaknesses concerning numerical computation and computational time consumption. To illustrate the negative points of this method, let us first consider a pair of particles bound with springs. The springs react to the perturbations: they push back if they are compressed or pull back if stretched. From a numerical point of view, the objective is to keep a spring close to its rest length and to avoid any relative internal motions of the particles. Thus, the translational and rotational motions of the pair of spheres must be small enough to modify the length of the spring by only a few percent. Perfect rigidity is reached for an infinite spring constant k, requiring a time step going to zero. In practice, the object cannot be perfectly rigid, and the spring constant must be adapted to have a characteristic relaxation time much smaller than the time needed by the spheres to move by a few percent of their radius. It appears clearly that the spring constant depends on both the time step and the regime used for the simulation (Brownian or not). A bad set of the time step and spring constant can lead to the overlap between particles or massive oscillation. For example, let us consider a dumbbell with only translational Brownian motion. At the time step (i) the Brownian motion moves spheres further apart, then at the next time step $(i+1)$, springs are stretched and create a force to bring back the spheres to their original positions. If the Brownian motion at the time step $(i+1)$ moves particles closer with the same direction as the restoring force, the two forces (Brownian and spring) can generate a motion resulting in the overlap of the two spheres at the end of the time step $(i+1)$. The easiest solution could have been to reduce the time step. Nonetheless, it may not be sufficient as there always exists a probability, to generate an overlap coming from the addition of the displacements due to the springs and the Brownian motion. The time step should be reduced in an adaptive fashion to avoid any overlap. However, one should recall that the spheres are always close-packed in a particle, and therefore only a very small time step could avoid overlap to happen. Given the fact that in the condition of the simulations carried out in this manuscript (number of particles and time step), 1 iteration is realized in approximatively 10 seconds, reducing the time step drastically or iterating the same time step multiple times would blow up the computational time. Consequently, the use of spring to bind particles together does not seem adapted to the Brownian regime.

2.3 Rigid body motion - (A)SD-RBM

The principle of the second method was first described by Meng & Higdon [27, 28]. These authors added constraints to the Langevin equation to force the spheres making up a plate-like particle to move as a rigid body (no relative translational and rotational motion between spheres of the same object). They applied a rigid body constraint implicitly, *i.e.* by relating the motion of each sphere of the anisotropic particle, also called a cluster, with the motion of the cluster itself defined by three translational and three rotational velocities. In the following equations, the subscript s and c relate respectively to spheres and clusters, N_c refers to the number of clusters in the system and N_s to the number of spheres. From solid mechanics, the translational and angular velocities of points (spheres) belonging to a rigid body (cluster) are expressed as:

$$\mathbf{U}_s - \mathbf{u}_s^\infty = (\mathbf{U}_c - \mathbf{u}_c^\infty) + (\boldsymbol{\omega}_c - \boldsymbol{\Omega}_c^\infty) \times (\mathbf{x}_s - \mathbf{x}_c) - \mathbf{E}^\infty \cdot (\mathbf{x}_s - \mathbf{x}_c) \tag{2.19}$$

$$\boldsymbol{\omega}_s - \boldsymbol{\Omega}_s^\infty = \boldsymbol{\omega}_c - \boldsymbol{\Omega}_c^\infty \tag{2.20}$$

where $\mathbf{u}_s^\infty$ and $\mathbf{u}_c^\infty$ are the background velocities at, respectively, the center of the sphere $\mathbf{x}_s$ and the center of gravity of the cluster $\mathbf{x}_c$. These equations can be written in a compact $(6N_c \times 6N_s)$ matrix form:

$$\mathbf{U}_s - \mathbf{u}_s^\infty = \boldsymbol{\Sigma}^T \cdot (\mathbf{U}_c - \mathbf{u}_c^\infty) - \mathbf{E}^\infty \cdot (\mathbf{x}_s - \mathbf{x}_c) \tag{2.21}$$

where $\mathbf{U}_s$ is now a $(6N_s)$ vector and take into account both translational and rotational velocities, $\mathbf{E}^\infty \cdot (\mathbf{x}_s - \mathbf{x}_c)$ is also a $(6N_s)$ vector with terms corresponding to rotational velocity set to 0, and $\boldsymbol{\Sigma}^T$ the transpose of the rigid body tensor $\boldsymbol{\Sigma}$. The latter is composed of N_c blocks of size $(6 \times 6N_s)$ which can be split in N_s blocks of size (6×6), *i.e.*, one block per sphere. If the sphere does not belong to the cluster, the block is simply filled with 0, whereas if the sphere belongs to the cluster, the corresponding block $\boldsymbol{\Sigma}^T_{s\in c}$ is given by:

$$\boldsymbol{\Sigma}^T_{s\in c} = \begin{bmatrix} 1 & 0 & 0 & 0 & (\mathbf{x}_s-\mathbf{x}_c)_3 & -(\mathbf{x}_s-\mathbf{x}_c)_2 \\ 0 & 1 & 0 & -(\mathbf{x}_s-\mathbf{x}_c)_3 & 0 & (\mathbf{x}_s-\mathbf{x}_c)_1 \\ 0 & 0 & 1 & (\mathbf{x}_s-\mathbf{x}_c)_2 & -(\mathbf{x}_s-\mathbf{x}_c)_1 & 0 \\ 0 & 0 & 0 & 1 & 0 & 0 \\ 0 & 0 & 0 & 0 & 1 & 0 \\ 0 & 0 & 0 & 0 & 0 & 1 \end{bmatrix} \tag{2.22}$$

Note that the force and the torque on a cluster $\mathbf{F}_c$ are directly related to the forces and the torques on its constituent spheres. The relation between these values is made through the $(6\mathbf{N}_c \times 6\mathbf{N}_s)$ tensor $\boldsymbol{\Sigma}$:

$$\mathbf{F}_c = \boldsymbol{\Sigma}\cdot\mathbf{F}_s \tag{2.23}$$

Inserting equation (2.21) into the equations for spheres used in the (A)SD methods gives new equations involving the cluster velocities $\mathbf{U}_c$ as unknowns.

2.3.1 SD-RBM

The insertion of equation (2.21) into equation (2.8) gives:

$$\begin{bmatrix}\mathbf{0}\\ \mathbf{S}\end{bmatrix} = -\boldsymbol{\mathcal{R}}\cdot\begin{bmatrix}\boldsymbol{\Sigma}^T\cdot(\mathbf{U}_c-\mathbf{u}^\infty_c)-\mathbf{E}^\infty\cdot(\mathbf{x}_s-\mathbf{x}_c)\\ -\mathbf{E}^\infty\end{bmatrix}+\begin{bmatrix}\mathbf{F}^b_s+\mathbf{F}^p_s\\ -\mathbf{r}\mathbf{F}^p_s\end{bmatrix}, \tag{2.24}$$

Then, the matrix $\boldsymbol{\Sigma}$ can be applied on the first line of the previous equation (force and torque) to constrain the system. This line becomes in a non-compact form:

$$0 = -\boldsymbol{\Sigma}\cdot\boldsymbol{\mathcal{R}}_{\text{FU}}\cdot\left[\boldsymbol{\Sigma}^T\cdot(\mathbf{U}_c-\mathbf{u}^\infty_c)-\mathbf{E}^\infty\cdot(\mathbf{x}_s-\mathbf{x}_c)\right]+\boldsymbol{\Sigma}\cdot\boldsymbol{\mathcal{R}}_{\text{FE},nf}:\mathbf{E}^\infty+\boldsymbol{\Sigma}\cdot(\mathbf{F}^o) \tag{2.25}$$

where $\mathbf{F}^o_s$ stands for other forces and is equal to $\mathbf{F}^o_s = \mathbf{F}^b_s + \mathbf{F}^p_s$. As in the original code used for spheres, the Brownian part is computed in a second step and therefore $\mathbf{F}^o_s = \mathbf{F}^p_s$. Solving equation (2.25) consists in inverting the square $(6N_c \times 6N_c)$ and positive matrix $\left(\boldsymbol{\Sigma}\cdot\boldsymbol{\mathcal{R}}_{\text{FU}}\cdot\boldsymbol{\Sigma}^T\right)$ representing the resistance tensor of the coarse-grained anisotropic particle. This is done using the DGETRS subroutine from the LAPACK library. Once the velocities of the clusters are calculated, the velocities of the constituent spheres are straightforward to obtain using equation (2.21). This method will be referred to as the SD-RBM. Note that in SD-RBM, the cluster velocity is not computed in an iterative fashion, no term is added to the diagonal of $\boldsymbol{\mathcal{R}}_{\text{FU}}$ and the system to solve is much smaller.

Concerning the Brownian motion, the velocities $\mathbf{u}^b_s$ of individual unconstrained spheres are first computed as described by Banchio [1]. Then the corresponding Brownian forces are calculated using the grand resistance matrix $\mathbf{F}^b_s = \boldsymbol{\mathcal{R}}_{\text{FU}}\cdot\mathbf{u}^b_s$. Finally, using equation (2.23) and the mechanical velocity definition $\mathbf{u}^b_s = \boldsymbol{\Sigma}^T\cdot\mathbf{u}^b_c$ we compute the Brownian cluster velocity: $\mathbf{u}^b_c = \left(\boldsymbol{\Sigma}\cdot\boldsymbol{\mathcal{R}}_{\text{FU}}\cdot\boldsymbol{\Sigma}^T\right)^{-1}\cdot\mathbf{u}^b_s$.

2.3.2 ASD-RBM

The same reasoning can be applied to the ASD method. Considering the split of the hydrodynamic force into a near and a far-field contribution, equation (2.25) becomes:

$$0 = -\boldsymbol{\Sigma}\cdot\widetilde{\boldsymbol{\mathcal{R}}}_{\text{FU},nf}\cdot\left[\boldsymbol{\Sigma}^T\cdot(\mathbf{U}_c-\mathbf{u}^\infty_c)-\boldsymbol{\Sigma}\cdot\mathbf{E}^\infty\cdot(\mathbf{x}_s-\mathbf{x}_c)\right]+\boldsymbol{\mathcal{R}}_{\text{FE},nf}:\mathbf{E}^\infty+\boldsymbol{\Sigma}\cdot\left(\mathbf{F}^h_{ff}+\mathbf{F}^o\right) \tag{2.26}$$

where $\mathbf{F}_s^o = \left[\mathbf{F}_s^b + \mathbf{F}_s^p - \lambda(\mathbf{U}_s - \mathbf{u}_s^\infty)\right]$. As in the original code, a term λ is added to the diagonal of the resistance tensor in order to ensure it is positive definite and allow the quick inversion of the square $(6N_c \times 6N_c)$ matrix $\left(\mathbf{\Sigma} \cdot \widetilde{\boldsymbol{\mathcal{R}}}_{\text{FU},nf} \cdot \mathbf{\Sigma}^T\right)$. However, we noticed that a value of 1 is not enough for the system of clusters, and λ was finally set to 2. As with the SD-RBM method, the Brownian velocity is computed in a second step. Based on this, in the code $\mathbf{F}_s^o = [\mathbf{F}_s^p - \lambda(\mathbf{U}_s - \mathbf{u}_s^\infty)]$. The translational and rotational hydrodynamic velocities of the cluster are obtained by solving equation (2.26). This is the ASD-RBM method:

$$\begin{aligned}\mathbf{U}_c - \mathbf{u}_c^\infty = &\left(\mathbf{\Sigma} \cdot \widetilde{\boldsymbol{\mathcal{R}}}_{\text{FU},nf} \cdot \mathbf{\Sigma}^T\right)^{-1} \cdot \\ &\left[\widetilde{\boldsymbol{\mathcal{R}}}_{\text{FU},nf} \cdot \{\mathbf{E}^\infty \cdot (\mathbf{x}_s - \mathbf{x}_c)\} + \boldsymbol{\mathcal{R}}_{\text{FE},nf} : \mathbf{E}^\infty + \mathbf{\Sigma} \cdot \left(\mathbf{F}_{ff,s}^h + \mathbf{F}_s^o\right)\right]\end{aligned} \tag{2.27}$$

One should notice the simple dot used before the tensor $\{\mathbf{E}^\infty \cdot (\mathbf{x}_s - \mathbf{x}_c)\}$. The latter is in reality a $(6N_s)$ vector where the terms corresponding to rotational velocity are set to 0. The hydrodynamic far-field force, torque and stresslet are computed as in the code of Sierou [35], but instead of satisfying equation (2.12) they must satisfy:

$$\begin{aligned}&-\left(\boldsymbol{\mathcal{M}}^\infty + \begin{bmatrix} \mathbf{\Sigma}^T \cdot \left(\mathbf{\Sigma} \cdot \widetilde{\boldsymbol{\mathcal{R}}}_{\text{FU},nf} \cdot \mathbf{\Sigma}^T\right)^{-1} \cdot \mathbf{\Sigma} & 0 \\ 0 & 0 \end{bmatrix}\right) \cdot \begin{bmatrix} \mathbf{F}_{ff}^h \\ \mathbf{S}_{ff}^h \end{bmatrix} = \\ &\begin{bmatrix} \mathbf{\Sigma}^T \cdot \left(\mathbf{\Sigma} \cdot R_{nf}^{FU} \cdot \mathbf{\Sigma}^T\right)^{-1} \cdot \mathbf{\Sigma} \cdot \left[R_{nf}^{FU} \cdot \{\mathbf{E}^\infty \cdot (\mathbf{x}_s - \mathbf{x}_c)\} + R_{nf}^{FE} : \mathbf{E}^\infty\right] - \mathbf{E}^\infty \cdot (\mathbf{x}_s - \mathbf{x}_c) \\ -\mathbf{E}^\infty \end{bmatrix}\end{aligned} \tag{2.28}$$

The hydrodynamic far-field force, torque, and stresslet are solved using an iterative method following the same algorithm as the one described by Sierou. We implemented a bi-conjugate gradient stabilized method (BiCG-stab [39]) to replace the conjugate gradient method as recommended by Ichicki [17] when solving problems with particles moving as a rigid body.

2.3.3 Summary of the RBM methods

The SD-RBM and ASD-RBM methods are supposed to give similar results. However, one could expect some differences in the Brownian motion as the grand mobility matrix used to compute the Brownian velocity of the spheres is not computed in the same way. We emphasize on the fact that the SD-RBM method is the method of reference. The ASD-RBM is only used to reduce the computational cost.

Even if the RBM methods require more development than the SBS, they possess several advantages. The first positive point concerns the lower computational cost for the inversion of $\mathbf{\Sigma} \cdot \widetilde{\boldsymbol{\mathcal{R}}}_{\text{FU},nf} \cdot \mathbf{\Sigma}^T$ than $\widetilde{\boldsymbol{\mathcal{R}}}_{\text{FU},nf}$ due to its lower dimension :$(6N_c \times 6N_c)$ vs. $(6N_s \times 6N_s)$. For example, in this work, a typical calculation will involve 60 plate-like clusters with 37 spheres each, which requires solving (360×360) systems with the presented method instead of (13320×13320) systems. The second advantage of the RBM methods stems from the impossibility of the spheres of the same cluster to undergo relative translational or rotational motion whatever the time step and the regime (Brownian or not): the particle is perfectly rigid. As a consequence, this method is not adapted to compute the dynamical behavior of non-rigid particles (*e.g.* blood cell). In such case, the spring method, or a mix between springs and rigid body can be used. For example, Swan & Brady [37] applied a combination of both methods in a Stokesian dynamics code to model many rigid assemblies (dumbbells) with linear springs representing a self-propelled non-Brownian particle and to study their dynamics. For the reader information, the difference between our RBM method and the one from Meng & Higdon lies in the fact that these authors solved both the far-field hydrodynamics and the velocity of the constrained particles at the same time, which leads to a larger number of iterations to invert the matrix.

Now that the different methods to create a rigid anisotropic object composed of spheres and to compute hydrodynamic interactions between them have been presented, we will turn to the modeling of anisotropic electrostatic interactions.

2.4 Electrostatic forces

Electrostatic interactions are typically computed between liquid-suspended spheres in a pairwise additive fashion with a Yukawa potential whatever the volume fraction. Charge anisotropy is usually modeled considering point charges distributed on the surfaces of particles (site model). Some researchers started to study clay-like particles which can present, under specific chemical conditions, a charge anisotropy. Rim charges of Laponite, for example, are positively charged at pH ~ 10, and increasing the pH decreases the values of the charges [38]. The charges on the faces are always negative. Thus, the rim and the faces can have opposite charges, and the range of interactions between two charged clay particles depends on the salt concentration of the suspension coming from both the added salt and the counterions released by the particle. Therefore, the phase diagram of Laponite suspensions at equilibrium depends on the range of interactions, and various phases such as Wigner glasses, gel, or liquid states can be observed at the same volume fraction just by varying the salt concentration (see Figure 1.2). Kutter et al. [21] have used Monte-Carlo simulations of Laponite suspensions and have been able to reproduce some of the characteristic phases obtained experimentally. The authors modeled particles as plate-like with a finite number of point charges: 19, 37 and 61 sites. Following this work numerous Monte-Carlo simulations have been run considering the pairwise additive point charge model (site model) to investigate the state diagram of clay-like particles and the influence of both the charge anisotropy and the salt concentration [10, 11, 19, 32, 31]. In this study, we will also use a hard core Yukawa potential model to compute the electrostatic interactions between plate-like particles. However, we have to keep in mind that it might be quite far from reality, especially at a short distance, and only allows a qualitative insight on clay-like electrostatic interactions.

2.4.1 For a suspension of spheres

In both the ASD and SD code the electrostatic forces are referred to as the interparticles forces. Nazockdast & Morris [29] studied the effect of soft repulsive forces ($\mathbf{F}_y^p$) on the stress of suspensions of spheres and on their microstructure using a Yukawa potential. The expression of the electrostatic repulsive forces used in (A)SD is:

$$\mathbf{F}_y^p = -\left(\frac{k_b T}{a}\right) A \frac{e^{-(\kappa a)\ h}}{r/a} \left(\frac{1 + (\kappa a)\ r/a}{r/a}\right) \hat{\mathbf{r}} \tag{2.29}$$

where the superscript p refers to the interparticle forces, $h = (r/a - 2)$ to the distance between the surfaces, $\hat{\mathbf{r}} = \mathbf{r}_{ij}/r$ where $\mathbf{r}_{ij}$ is the center to center vector and r its norm, and with a the radius of the particle. κ^{-1} is the screening length, and A is the amplitude of the force. In their study, Nazockdast and Morris used $(\kappa a) = 3.8, 6, 12$ to compare the radial distribution function and the stress of the suspension obtained with the ASD code with theoretical developments. To understand the physical meaning of A, one should recall the original expression of the Yukawa force between two spheres in dimensional form:

$$\mathbf{F}_y^p = \frac{Z_1 Z_2 l_B e^{2\kappa a}}{a^2 (1+\kappa a)^2} e^{-\kappa a r/a} \frac{1+\kappa a\,(r/a)}{(r/a)^2} k_b T \hat{\mathbf{r}} \tag{2.30}$$

with Z_i the charge on the particle i. By identification, A is equal to:

$$A = Z_1 Z_2 \frac{e^2}{4\pi\varepsilon_0\varepsilon_r (1+\tau)^2 a^2} \tag{2.31}$$

So A is related to the charges of the colloids, to the range of electrostatic interactions, to the properties of the medium, and to the size of the colloid. The electrostatic forces of particles with both shape and charge anisotropy are also computed using a Yukawa potential.

2.4.2 Suspension of particles with charge anisotropy

As already mentioned, the centers and the rim of clay-like particles can bear opposite charges. To model in the (A)SD code the distribution of the anisotropic charges on the plate-like particles, we drew our inspiration from the work of Kutter [21]. The distribution is shown in Figure 2.5, where the faces of a plate-like particle are represented by the inner, red, negatively charged spheres, while the rim is represented by the external, green, positively charged spheres.

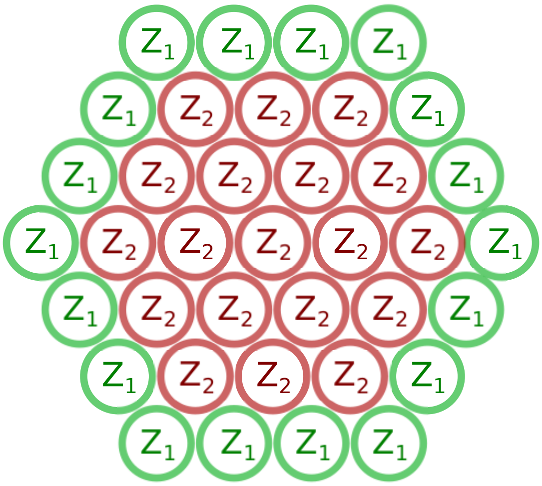

Figure 2.5: Charge anisotropy used in the ASD code to represent attractive and repulsive interactions between particles using hard core Yukawa potential.

Electrostatic interactions are turned off between the spheres of the same plate-like particle, and a repulsive Hard-Sphere (HS) force is added to avoid the interpenetration of the particles. The HS repulsive force used in the simulations is:

$$\mathbf{F}^{p}_{HS} = -\left(\frac{k_b T}{a}\right) 200 \frac{e^{-\kappa^{HS}\left(\tilde{r}-2a^{HS}\right)}}{1-e^{-\kappa^{HS}\left(\tilde{r}-2a^{HS}\right)}} \tag{2.32}$$

where κ^{HS} and a^{HS} are parameters slightly depending on the interaction range. Their effect is simply to decrease the occurrence of overlap between particles. Besides the two parameters κ^{HS} and a^{HS}, a buffer zone also depending on the interaction range is introduced. The buffer zone is a zone where electrostatic interactions, other than HS, are turned off if two surfaces are too close. All of these modifications must verify the following assertions to have no impact on the physical behavior of the suspension:

(i) the increase of the size of the radius is small compared with the actual radius of the sphere $\left(\frac{a^{HS}-a}{a} \ll 1\right)$,

(ii) the increase of the size of the radius is small compared with the double layer $\left(\frac{a^{HS}-a}{\kappa^{-1}} \ll 1\right)$,

(iii) the range of the HS repulsion force is small compared with the double layer $\left(\frac{\kappa a}{\kappa^{HS} a} \ll 1\right)$,

(iv) the range of the buffer zone d_{buff} is small compared to the double layer $(\kappa d_{buff} \ll 1)$.

2.4.3 Limitations of the electrostatic coarse-grained model

The site model used in this thesis to describe the electrostatic interactions between clay particles is a coarse-grained model, and therefore knowing its limitations is important for establishing the validity of the predictions of the simulations.

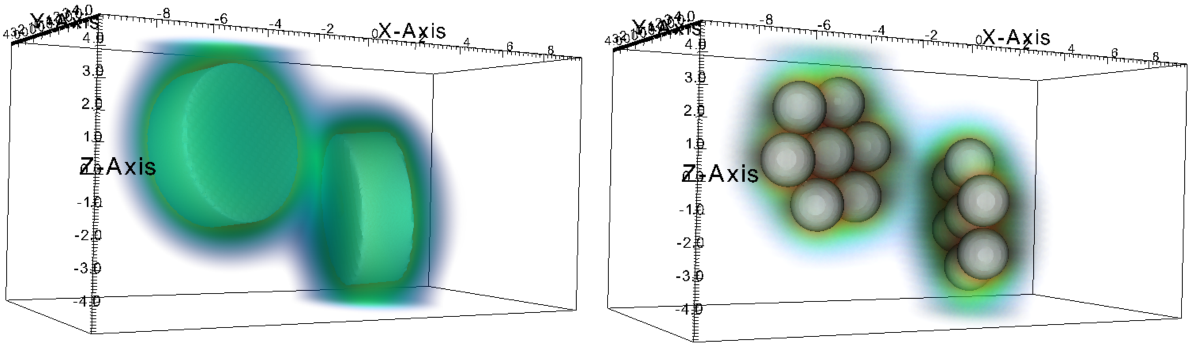

(a) Cylindrical particles

(b) Plate-like particles

Figure 2.6: Comparison of "exact" electrostatic potential between two anisotropic particles.

The first limitation is purely geometric and comes from the use of the spheres to coarse-grain a disk-shaped particle. Therefore, the distance between the surfaces of the particles is not the same as for real disk-shaped particles, implying a different charge distribution and dielectric constant. Moreover, the spheres belonging to the same object are close-packed, and many-body interactions involving the exclusion of ions from the double layers of one sphere due to the presence of its neighbor should in principle be taken into account. As many-body electrostatic interactions have no analytical expression, we have used the PoBoS code (Poisson-Boltzmann Solver) developed at Laboratoire de Génie Chimique (LGC) to compute the electrostatic many-body interactions between plate-like particles composed of spheres, as shown in Figure 2.6b and referred to as $AR3$ (aspect ratio $\approx$ 3). This code solves the full three-dimensional electric field using coupled Laplace and Poisson-Boltzmann equations for charges on the surface of particles of any shape (no pairwise additivity assumption) as presented in chapter 1 section 2.5. Using the PoBoS code, we have computed the electrostatic potential for repulsive plate-like particles with many-body interactions, which has been compared with the one obtained for the disk-shaped particles, as shown in Figure 2.6. Both the disk-shaped particles and the $AR3$ particles have the same diameter d. The charge of one true platelet was taken equal to Z_d, and the charge of one sphere was $Z_s = Z_d/N_s$ where N_s the number of spheres in one coarse-grained particle. It appears clearly that the potential in Figures 2.6a and 2.6b are not the same, and as the forces stem from these potentials, the forces will also be different. Thus, the coarse-graining of a disk as a cluster of spheres induces an error despite the use of many-body interactions.

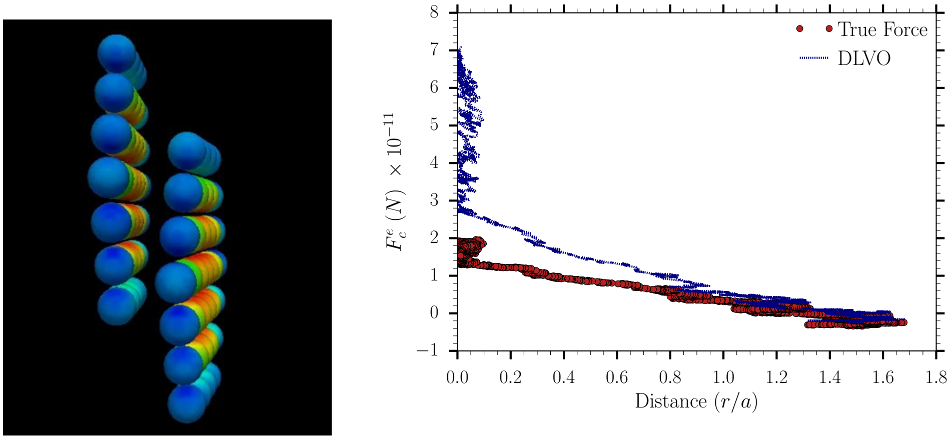

(a) Initial configuration

(b) Electrostatic forces

Figure 2.7: Initial configuration of two $AR7$ particles (a) and the different electrostatic forces (b) computed using the pairwise additivity of the DLVO theory and the Particle-field method of the PoBoS code also referred to as the "True force" in Figure (b). The colors in Figure (a) represent the value of the potential of the surfaces: the blue color is for a positive potential while the red for a negative potential. The distance in Figure (b) stands for the minimal distance between the surfaces of the two $AR7$.

The second limitation of the model is related directly to the pairwise additivity of the Yukawa potential. Indeed, this potential is valid for distant spheres interacting in an infinitely dilute medium. As already mentioned, even for two distant plate-like particles, spheres composing one cluster are in a close packed configuration, and their double layers interpenetrate strongly (see Figure 2.6b), which is outside of the validity domain of the DLVO theory. So in principle, the total interaction between two clusters cannot be modeled as a sum of sphere-sphere interaction, *i.e.*, $F^T_{MB} \neq \sum F^p_y$ where F^T_{MB} is the total force implying many-body interactions and $\sum F^p_y$ the total force computed using DLVO theory (see equation

(2.30)). To illustrate the importance of the many-body electrostatic interactions, let us considered two $AR7$ plate-like particles initialized in a face to face configuration as shown in Figure 2.7a. The charge of each sphere is set to obtain the electro-neutrality of the particle: $-22e$ and $23.22e$ respectively for the internal and the external spheres. The thickness of the Debye length is taken equal to $\kappa^{-1} = a$. The dynamical behaviors of the particles are computed using the SD-RBM method. The electrostatic forces used to compute the motion of the particles are calculated with both the Yukawa pairwise additive model and the PoBoS code. These options are referred to as "DLVO" and "True force" respectively in Figure 2.7b. The corresponding total forces applied to the centers of gravity of the particles F_c^e are reported in Figure 2.7b. The computation of these forces required the coupling of the PoBoS code with ASD. One can notice that both the "DLVO" and the "True Force" have similar behaviors as long as the minimal distance between the surfaces of the particles is larger than κ^{-1}. When particles are getting closer, the "DLVO" force increases more quickly than the force computed with PoBoS and is overestimated by approximatively a factor two at very short-range distances. As none of these methods are exact at contact, the force at a distance below $0.05a$ does not deserve to be commented. The difference concerning the electrostatic force amplitude provides the proof that the total interaction between two clusters cannot be modeled quantitatively as a sum of sphere-sphere interactions with a sphere charge being equal to the one used for many-body calculations.

To summarize, the site model used to model clay particles induces two kinds of limitations. The first one is purely geometric and is due to the coarse-graining of the shape of the particle from a disk-shaped to cluster of spheres. The second limitation lies in the use of the pairwise additivity of the Yukawa potential. To study electrostatic interactions between clay-like particles by a pairwise additive model, one should consider carefully the choice of the charges applied to the spheres. The charges must be set to generate a similar interaction force between two clusters like the one produced by two real clay particles. With this definition, the right choice of the charges should allow a good insight into the behavior of clay-like particles using the pairwise additive model of Yukawa potential. An example of the calculation of effective charges is given in the third chapter (see section 1.3.2).

2.5 Conclusion concerning the coarse-grained methods

In this section, we have first described a method to coarse-grain a particle with spheres. Then we have presented two different methods to keep the particle rigid. The first model consists in binding spheres with springs (SBS) and the second one in constraining the motion of the spheres to enforce rigid body motion (RBM). These models were implemented in both SD and ASD methods. We emphasize once again the fact that the SD method is more accurate as the grand resistance matrix is directly computed. However, this method is computationally too expensive and cannot be used for the study of suspensions of anisotropic particles. For this case we need to use the ASD method. Concerning the computation of the Brownian motion with the ASD method, we have chosen to approximate the grand mobility matrix by a diagonal matrix with two free parameters. The free parameters have been set to reproduce the Brownian diffusion of the particle studied using the SD-RBM. Finally, we have presented and discussed the coarse-graining of the electrostatics used in this manuscript.

The aim of the next section is to validate the numerical implementation of the models presented above.

3 Validation of the physical behavior of coarse-grained models

3.1 Hydrodynamic behavior

From the linearity of the Stokes flows, hydrodynamic effects can be superimposed. Therefore, if both the Brownian and non-Brownian behaviors are correct, the behavior at any intermediate Péclet is also correct, assuming only these effects are active. Consequently, only two different tests are required to verify the hydrodynamic behavior of anisotropic particles: one at infinite Péclet and the other at vanishing Péclet, *i.e.*, $Pe = \infty$ and $Pe = 0$.

3.1.1 Infinite Péclet number

The first test consists in studying the rotation period of an ellipsoid in an infinite Péclet number shear flow (non-Brownian system). In 1922, Jeffery described the dynamics of ellipsoidal particles in a viscous fluid and $Re = 0$ mathematically [18]. His theory is based on the fact that in the absence of external forces and torques, an ellipsoid translates at the velocity of the undisturbed fluid at the position of its center of gravity $\mathbf{u}^{\infty}(\mathbf{x})$. The director of the ellipsoid $\boldsymbol{p} = (p_x, p_y, p_z)$ corresponding to the unit vector in the direction of the symmetry axis (major axis for a prolate spheroid and minor axis for an oblate spheroid), describes periodic orbits also called Jeffery's orbits:

$$\begin{aligned} p_x &= \sin\theta_1 \sin\phi_1 \\ p_y &= \sin\theta_1 \cos\phi_1 \\ p_z &= \cos\theta_1 \end{aligned} \tag{2.33}$$

where angles θ_1 and ϕ_1 are time-dependent and equal to:

$$\begin{aligned} \phi_1 &= \arctan\left(r \tan\left[\frac{\dot{\gamma}t}{r + (1/r)}\right]\right) \\ \theta_1 &= \arctan\left(\frac{Cr}{\left(\sin^2\phi_1 + r^2\cos^2\phi_1\right)^2}\right) \end{aligned} \tag{2.34}$$

with $r = a/b$ the aspect ratio, a and b the semi-axis respectively parallel and perpendicular to the director, $\dot{\gamma}$ the rate of strain, t the time and C an integration constant depending on the initial configuration as shown in Figure 2.8b.

A prolate coarse-grained particle (see Figure 2.3b) is placed in an infinite shear flow with its director aligned with the y axis corresponding to a constant of integration $C = 0$. The norm of respectively, the semi-major and semi-minor axes are $9.4\ a$ and $4.63\ a$. The evolution of ϕ_1 and θ_1 is plotted in Figure 2.9 for the different numerical methods :ASD-RBM, SD-RBM and ASD-SBS. The values of the computed angles are compared with the theory in red on the figure, and referred to as "Jeffery". The theoretical rotation period is $15.85\ (1/\dot{\gamma})$ and is determined from equation (2.34).

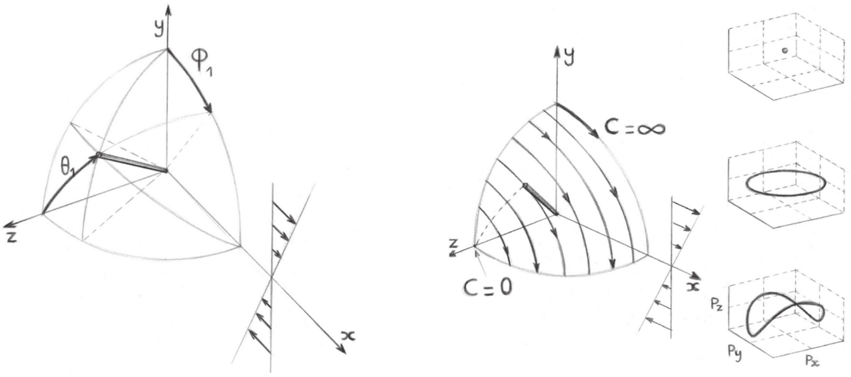

(a) Axis and polar angles

(b) Integration constant and Jeffery's orbits

Figure 2.8: Coordinate system (a) used for the computation of Jeffery's orbits (b), from the book of Guazzelli and Morris [15] p. 76.

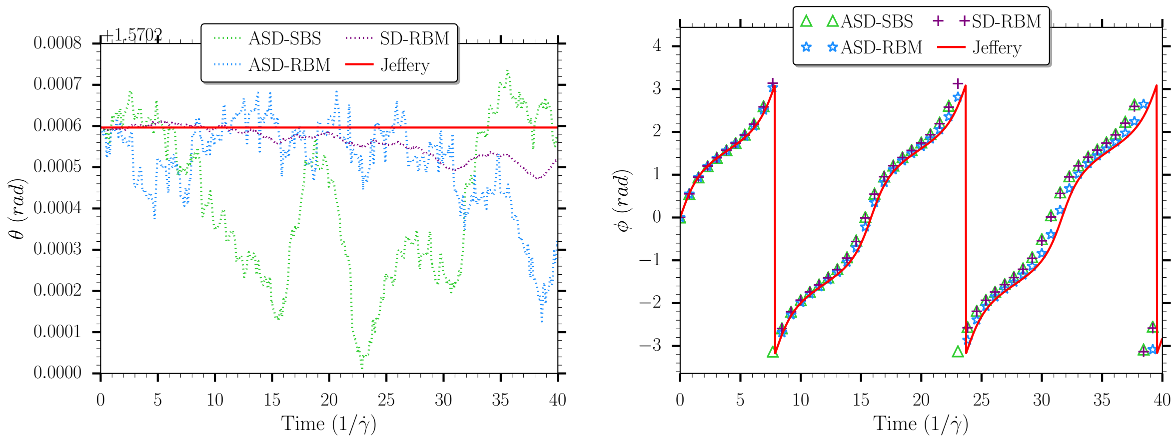

(a) Angle θ_1

(b) Angle ϕ_1

Figure 2.9: Comparison to theory of numerically computed θ_1 and ϕ_1 values for a prolate spheroid.

It appears clearly that angles θ_1 and ϕ_1 are in a good agreement with the theory. In Table 2.1, we compare the numerical methods quantitatively with the theory and with each other. The maximal error with the theory is below 4%. The ASD methods have less than 2% of difference with the SD method, which indicates a correct implementation of the far-field hydrodynamic force. One can notice that the ASD methods seem slightly more accurate than the SD on the prediction of the rotation period, but no conclusion can be drawn as the theory is known for true ellipsoids and not for the present coarse-grained ellipsoids. Moreover, ASD is an approximation of SD and is supposed to give the same results at best, in principle. The difference can be due to two numerical approximations canceling each other for example.

Some of the numerical parameters used for the calculations with the ASD methods must be detailed: while Sierou and coworkers [35] advised a mesh of 125 nodes per sphere for the computation of the

Methods Relative error	SD-RBM	ASD-RBM	SD-SBS	ASD-SBS
Theory	3.08%	1.19%	3.79%	2.98%
SD-RBM	$\diagdown$	1.96%	0.72%	$\diagdown$
SD-SBS	0.72%	$\diagdown$	$\diagdown$	0.84%

Table 2.1: Comparison of the theoretical rotation period of a prolate spheroid of aspect ratio equal to 2.027 (see Figure 2.3b) with different methods.

far-field hydrodynamics, we used here a coarse mesh of 17 nodes per sphere to reduce the computational time. A calculation realized with the advised number of nodes gives a rotation period of $15.42\,(1/\dot{\gamma})$ corresponding to a relative error with the theory of 2.71%. This rotation period is close to the one computed with the coarse grain mesh $15.65\,(1/\dot{\gamma})$. This surprisingly small difference could stem from the fact that the object is not a unique sphere, and even if one sphere has only 17 nodes, an ellipsoid is composed of 119 spheres, which involves no less than 2023 nodes for the entire particle. We consider acceptable the error induced by a coarser mesh for the computation of the many-body hydrodynamic interactions of coarse-grained particles.

3.1.2 Low Péclet number

The second test consists in validating the Brownian motion of an oblate spheroid with an aspect ratio of 7.3 corresponding to an $AR7$ particle. One should recall that the SD method computes the grand resistance matrix directly, and therefore the Brownian motion should be correctly calculated. Concerning the ASD method, we have chosen to consider the far-field mobility matrix as diagonal with two free parameters. These parameters are set to mimic the theoretical average diffusion coefficient of the real oblate spheroid.

In 1934 Perrin published an article about the Brownian motion of ellipsoidal particles [30] in which he gave the two translational frictional coefficients, *i.e.*, parallel and perpendicular to the director of the particle, and the rotational frictional coefficient of both the oblate and prolate spheroids. The diffusion coefficient D and the frictional coefficient f are linked through the Einstein-Smoluchowski relation $D = k_bT/f$. The theoretical and numerical diffusion coefficients of an oblate spheroid of radius 7.3 a are given in Table 2.2. They have been made non-dimensional using the translational and rotational diffusion coefficients of a sphere of radius a and given by the Stokes-Einstein equation, respectively $D_{t,0}$ and $D_{r,0}$. The theoretical rotational diffusion is small enough to be negligible. Thus, only translational coefficients are compared with computational results. In Table 2.2, $D_\perp$ and $D_\parallel$ are respectively the translational coefficients perpendicular and parallel to the direction vector of the particle, and $R_\perp$ and $R_\parallel$ are the rotational coefficients.

One can notice that the SD-RBM is in excellent agreement with the theory. It can reproduce the anisotropic diffusion behavior of an oblate spheroid. With the SD-SBS method, the translational diffusion coefficients are almost doubled compared to the theory. The presence of springs seems to increase the diffusion of the spheroid while raising the computational time drastically due to the necessity of a

	Theory	SD-RBM	SD-SBS	ASD-RBM
$D_{\perp}/D_{t,0}$	$2.17\ 10^{-1}$	$2.24\ 10^{-1}$	$4.14\ 10^{-1}$	$1.72\ 10^{-1}$
$D_{\|}/D_{t,0}$	$1.60\ 10^{-1}$	$1.44\ 10^{-1}$	$2.41\ 10^{-1}$	$1.75\ 10^{-1}$
$R_{\perp}/D_{r,0}$	$1.64\ 10^{-3}$	$\diagdown$	$\diagdown$	$\diagdown$
$R_{\|}/D_{r,0}$	$1.88\ 10^{-3}$	$\diagdown$	$\diagdown$	$\diagdown$

Table 2.2: Translational and rotational diffusion coefficients of an oblate spheroid of radius $7.3\ a$.

smaller time steps to allow the springs to react to the internal Brownian motion. That is one of the main reasons that made us choose the RBM method instead of the SBS. As the SD-SBS is not correct, the ASD-SBS method was not investigated.

Thanks to the tuned parameters, the ASD-RBM method generates the correct order of magnitude for the translational diffusion coefficients but is not able to reproduce their anisotropy properly. Retrieving a correct anisotropic diffusion coefficient is possible but requires the following developments. First, two different mobility matrices must be built, one for any perpendicular motion and the other for the parallel motion. Then, the Brownian force must also be split into two parts, one parallel to the direction vector of the platelet and the other perpendicular. Finally, two different motions should be computed (parallel and perpendicular) with the inversion of two different grand resistance tensors. Basically, it doubles the computational time required for one iteration. Moreover, the anisotropy of the diffusion coefficient for an oblate ellipsoid of aspect ratio 7.3 is $\sim 25\%$ and considering only the mean value of both the parallel and perpendicular coefficients already give a correct approximation of the Brownian motion. Therefore, the proposition to take into account the anisotropic diffusion was not implemented.

3.1.3 Summary of the hydrodynamic validation

To conclude this part, binding spheres with springs, *i.e.*, the SBS method, allows reproducing a correct behavior at infinite Péclet number but overestimates the Brownian motion, in addition to being time-consuming.

The RBM method is excellent at infinite Pe. Both the ASD and SD methods reproduce perfectly the Jeffery's period of rotation of an oblate spheroid. At a low Péclet number, the SD-RBM method retains the anisotropic diffusion behavior of the Brownian motion of an $AR7$ particle. The ASD-RBM method does not reproduce the anisotropic diffusion of the anisotropic particle but captures the correct average diffusion coefficient.

The hydrodynamic behavior of coarse-grained anisotropic particles has been validated for the RBM method, which is consequently the one chosen to carry out the rest of the simulations reported later in this manuscript.

3.2 Validation of the rheology of a suspension of platelets

Electrostatic, hydrodynamic, and Brownian interactions generate motions of particles and stresses. The stresses determine the viscosity of the suspension and the normal stress differences. The stress arises from interactions between particles and between fluid and particles and is the central quantity studied in the field of rheology. Validating its correct computation is essential for this work. As previously mentioned, Stokesian Dynamics already computes the bulk stress (average stress) of a suspension of spheres. However, the total stress on a cluster is not due simply to the sum of the stresses of the constituent spheres of the particle. Indeed, due to its particular shape, the cluster exhibits a second stress contribution related to the hydrodynamic force.

In this section, the physical description of the total stress on a coarse-grained particle is first given. Then, to validate the correct implementation of the stress calculation in the code, the bulk stress of dilute suspensions of spheroids is compared with theory. Finally, the bulk stress of concentrated suspensions of clusters is compared with results from the literature.

3.2.1 Average stress calculation for coarse-grained particles

The final formula of the stress for coarse-grained particles can be found in several papers [27, 33] but its origin is difficult to find described in detail. That is why, we have decided to dedicate a paragraph on its origin. Let us consider a suspension of non-Brownian perfectly rigid clusters composed of constrained spheres with no internal motion, in a Stokes flow. Such assumptions allow considering the clusters as both force and torque-free:

$$\mathbf{F}_c^h + \mathbf{F}_c^I = 0, \quad \text{and} \quad \mathbf{T}_c^h + \mathbf{T}_c^I = 0 \tag{2.35}$$

where the superscript h means hydrodynamic and I interparticle forces. The force on a cluster is equal to the sum of the forces on every one of its spheres. The torque on a cluster can be written as $\mathbf{T}_c = \sum_{s \in c} (\mathbf{T}_s + (\mathbf{x}_s - \mathbf{x}_c) \times \mathbf{F}_s)$, where $\sum_{s \in c}$ is the sum over the constituting spheres of the coarse-grained particle. One should remark that the internal constraints are not taken into account. Indeed, the mechanical picture of internal forces could be the cohesive forces between molecules or atoms of a rigid object acting like contact forces. Such forces sum to zero for each cluster and do not generate a bulk stress. As particles are considered inertialess, the equation of conservation of momentum is written:

$$\nabla \cdot \boldsymbol{\sigma}^h = -\mathbf{f}^{ext} \tag{2.36}$$

with $\mathbf{f}^{ext}$ the external force per unit volume. For a suspension of identical colloids in a linear shear flow, the average of the bulk stress can be written as:

$$\boldsymbol{\Sigma} = \boldsymbol{\Sigma}^h \equiv <\!\boldsymbol{\sigma}^h\!> = \frac{1}{V} \int_V \boldsymbol{\sigma}^h dV \tag{2.37}$$

The volume of integration can be split into a fluid (V_f) and a particle (V_p) part (see Batchelor [2]) equal to the sum of the volumes of all spheres s belonging to all clusters c: $V_p = \sum_c V_c = \sum_c \sum_{s \in c} V_s$:

$$\begin{aligned} \boldsymbol{\Sigma} \equiv <\!\boldsymbol{\sigma}^h\!> &= \frac{1}{V} \left[\int_{V_f} \boldsymbol{\sigma}^h dV + \sum_c \int_{V_c} \boldsymbol{\sigma}^h dV \right] \\ &= I.T. + 2\mu <\!\mathbf{e}^h\!> + \boldsymbol{\Sigma}^p \end{aligned} \tag{2.38}$$

where $I.T.$ is an isotropic term, $<\!\mathbf{e}^h\!>$ the mean rate of strain and $\boldsymbol{\Sigma}^p$ the stress arising from the presence of the particles. The definition of the stress of a Newtonian fluid was used to go from the first to the second line. For clarity, as only the local hydrodynamic stress tensor is considered, we replace $\boldsymbol{\sigma}^h$ by $\boldsymbol{\sigma}$. Then, using the relation $\partial x_j / \partial x_k = \delta_{jk}$ it is easy to demonstrate:

$$\sigma_{ij} = \frac{\partial}{\partial x_k}\left(\sigma_{ik} x_j\right) - \frac{\partial \sigma_{ik}}{\partial x_k} x_j \tag{2.39}$$

Inserting equation (2.39) in the particle stress ($\boldsymbol{\Sigma}^p$) gives the expression:

$$\boldsymbol{\Sigma}^p_{ij} = \frac{1}{V}\sum_c \int_{V_c}\left[\frac{\partial}{\partial x_k}\left(\sigma_{ik} x_j\right) - \frac{\partial \sigma_{ik}}{\partial x_k} x_j\right] dV \tag{2.40}$$

Using the divergence theorem on the first term of the right-hand side and inserting equation (2.36), it can be shown that:

$$\begin{aligned}
\boldsymbol{\Sigma}^p_{ij} &= \frac{1}{V}\sum_c \left[\int_{S_c} \sigma_{ik} x_j n_k dS + \int_{V_c} \left(\nabla\sigma\right)_i x_j dV\right] \\
&= \frac{1}{V}\sum_c \left[\int_{S_c} \sigma_{ik}\left(x_j - x_{c,j}\right) n_k dS + x_{c,j}\int_{S_c} \sigma_{ik} n_k dS - \int_{V_c} -\mathbf{f}^{ext} x_j dV\right] \\
&= \frac{1}{V}\sum_c \left[\int_{S_c} \sigma_{ik}\left(x_j - x_{c,j}\right) n_k dS - x_{c,j} F_i^{ext} + x_{c,j} F_i^{ext}\right] \\
&= \frac{1}{V}\sum_c \left[\int_{S_c} \sigma_{ik}\left(x_j - x_{c,j}\right) n_k dS\right] \\
&= \frac{1}{V}\sum_c \sum_{s\in c}\left[\int_{S_s} \sigma_{ik}\left(x_j - x_{s,j}\right) n_k dS + \int_{S_s} \sigma_{ik}\left(x_{s,j} - x_{c,j}\right) n_k dS\right] \\
&= \frac{1}{V}\sum_c \sum_{s\in c}\left[\int_{S_s} \sigma_{ik}\left(x_j - x_{s,j}\right) n_k dS + \left(x_{s,j} - x_{c,j}\right) F^h_{s,i}\right]
\end{aligned} \tag{2.41}$$

One can recognize the first term of the previous equation as the complete hydrodynamic traction first moment on a sphere s given by Batchelor [3]. We remind that this moment can be decomposed into a symmetric portion, the stresslet S_{ij}, and an antisymmetric portion A_{ij}, the rotlet:

$$\begin{aligned}
S^h_{ij} &= \frac{1}{2}\int_{S_s} \left[\sigma_{ik}(x_j - x_{s,j}) + \sigma_{jk}(x_i - x_{s,i})\right] n_k dS \\
A_{ij} &= \frac{1}{2}\int_{S_s} \left[\sigma_{ik}(x_j - x_{s,j}) - \sigma_{jk}(x_i - x_{s,i})\right] n_k dS = -\frac{1}{2}\varepsilon_{ijk} T^h_{s,k}
\end{aligned} \tag{2.42}$$

The sum of the torques for the cluster suspension is equal to:

$$\begin{aligned}
\sum_c \left(T^h_{c,k} + T^I_{c,k}\right) &= \sum_m \left[T^h_{s,k} + T^I_{s,k} + \varepsilon_{kij}\hat{x}_i(F^h_{s,j} + F^I_{s,j})\right] \\
&= \sum_m \left[T^h_{s,k} + \left(\hat{x}_i F^h_{s,j} - \hat{x}_j F^h_{s,i}\right) + \left(\hat{x}_i F^I_{s,j} - \hat{x}_j F^I_{s,i}\right)\right]
\end{aligned} \tag{2.43}$$

where we have introduced $\hat{\mathbf{x}} = \mathbf{x}_s - \mathbf{x}_c$. To go from the first to the second line, we used the fact that the interparticle forces sum to zero for each pair of spheres (equal but opposite direction). Then it is straightforward to write that the mean interparticle torque is equal to zero, $\sum_m \left(\hat{x}_i F^I_{s,j} - \hat{x}_j F^I_{s,i}\right) = 0$. Thus equation (2.43) can be simplified to:

$$T^h_{s,k} = -\left(\hat{x}_i F^h_{s,j} - \hat{x}_j F^h_{s,i}\right) \tag{2.44}$$

Using the definition of the first moment and the hydrodynamic torque, equation (2.41) becomes:

$$\begin{aligned}\Sigma_{ij}^{p} &= \frac{1}{V}\sum_{m}\left[S_{ij}^{h} + A_{ij} + \hat{x}_j F_{s,i}^{h}\right] \\ &= \frac{1}{V}\sum_{m}\left[S_{ij}^{h} - \frac{1}{2}\varepsilon_{ijk}T_{k}^{h} + \hat{x}_j F_{s,i}^{h}\right] \\ &= \frac{1}{V}\sum_{m}\left[S_{ij}^{h} + \frac{1}{2}\varepsilon_{ijk}\left(\hat{x}_i F_{s,j}^{h} - \hat{x}_j F_{s,i}^{h}\right) + \hat{x}_j F_{s,i}^{h}\right]\end{aligned} \tag{2.45}$$

Then the average bulk stress is equal to:

$$\Sigma_{ij} = I.T. + 2\mu{<}\mathbf{e}_{ij}{>} + \frac{1}{V}\sum_{m}\left[S_{ij}^{b} + S_{ij}^{I} + S_{ij}^{h} + \frac{1}{2}\left(\hat{x}_i F_{s,j}^{h} + \hat{x}_j F_{s,i}^{h}\right)\right] \tag{2.46}$$

To compute the bulk viscosity of a suspension under steady shear flow, the relative viscosity is only related to Σ_{12}, where 1 is the flow direction and 2 its gradient :

$$\eta_r = \frac{\Sigma_{12}}{2\eta_0 E_{12}^{\infty}} = 1 + \frac{1}{V}\sum_{m}\left[S_{12}^{b} + S_{12}^{I} + S_{12}^{h} + \frac{1}{2}\left(\hat{x}_1 F_{s,2}^{h} + \hat{x}_2 F_{s,1}^{h}\right)\right] \tag{2.47}$$

with η_0 the fluid viscosity and E^{∞} the bulk rate of strain tensor. This equation only differs from the one for spheres by the presence of the last terms between the parentheses and involving the hydrodynamic force.

3.2.2 Rheology of dilute suspensions

The theoretical stress of an oblate particle at infinite Péclet number shear flow is based on the fact that oblate spheroids follow Jeffery's orbit of period T. Thus, if the initial configuration is known, the spatial configuration, represented by the polar coordinates θ, ϕ, is also known at any time and described by the orientation distribution function $P(\theta, \phi_1, t)$. Moreover, as the stress generated by an oblate spheroid is known for a specific spatial configuration, the average stress of a dilute suspension can be calculated as:

$$\langle S\rangle = \frac{1}{T}\int_0^T\int_0^{2\pi}\int_0^{\pi} S(\theta,\phi_1)P(\theta,\phi_1,t)\,d\theta\, d\phi_1\, dt \tag{2.48}$$

Details on the computation of the stress can be found in Meng [26]. The author compared the theoretically and numerically obtained viscosity coefficients $(\eta_r - 1)/\phi$, where η_r is the relative viscosity and ϕ the volume fraction, of $AR3$, $AR5$ and $AR7$ plate-like particles (see Figure 2.10).

We have used the same coarse-grained model as Meng & Higdon for plate-like particles (see Figure 2.3a). This similarity allows us to compare our results directly with those of Meng & Higdon. The computation of the mean stress requires sampling distinct spatial configurations (θ, ϕ), and at least a simulation time of one Jeffery's period. The volume fraction of the suspension is set to 1% to avoid as much as possible interparticle interactions, and the particles are initialized randomly. At such a low volume fraction, particles do not interact with each other, *i.e.*, the lubrication and many-body terms vanish. Thus, the viscosity is only due to the influence of individual particles. To keep a constant number of spheres, we have carried out simulations with 12 $AR7$, 23 $AR5$ and 63 $AR3$ which corresponds to $\sim$ 440 spheres in each case. As the SD method is suitable only for the computation of less than a hundred of spheres due to its important computational cost, only the ASD methods were tested.

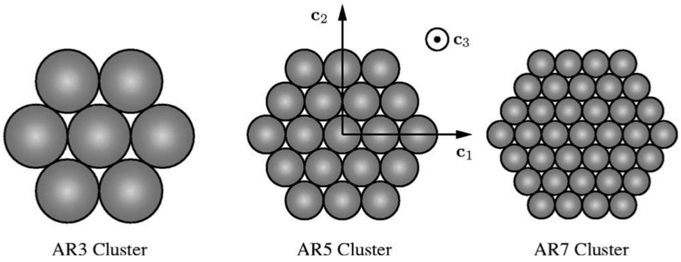

Figure 2.10: Model of plate-like particles used by Meng & Higdon [26, 27, 28] .

Concerning the case of spheres bound with springs (SBS), internal stresses generated by spring forces should sum to zero for each platelet. Due to the time-shifted scheme, springs react to perturbations at time $i+1$. Then, the sum of the stresses due to the hydrodynamic disturbances at time i and to springs at time $i+1$ should sum to zero. However, the hydrodynamic stress has a leading force term coming from the squeezing of two particles scaling as $1/r$, and summing numerically diverging forces rarely goes to 0. The internal stress was not observed to vanish in simulations, and the viscosity was miscalculated. Therefore viscosity coefficients for SBS are not reported in Table 2.3. This issue is the second main reason why we have chose to carry out our simulations of clay-like suspensions with the RBM method.

Relative viscosity results are given for the ASD-RBM on coarse and fine meshes, respectively 17 and 134 nodes per sphere. They are compared with the theory and with Meng & Higdon's results in Table 2.3. The agreement between RBM and Meng & Higdon's results is excellent in all cases.

Aspect ratio	3	5	7
Dilute theory	3.66	4.07	4.32
Meng & Higdon	3.89	4.32	4.80
ASD-RBM coarse	3.62	4.13	4.83
ASD-RBM fine	3.61	4.14	4.90

Table 2.3: Comparison of the viscosity coefficients obtained from theory with results from [27] and with the ASD-RBM method.

The refinement of the mesh used for the calculation of the far-field hydrodynamics does not improve the accuracy of the computed velocity of a dilute suspension of plate-like particles. As already mentioned this can be due to the fact than even for the smallest aspect ratio, the coarser mesh represents 17 nodes per sphere for the $AR3$, *i.e.* 119 nodes per anisotropic particle which is close to the 125 nodes per particle suggested by Sierou [35]. For aspects ratios 3 and 5, results from ASD are closer to the theory than the ones from Meng & Higdon. Both numerical simulations (ASD and M&H) overestimate the viscosity by $\sim 10\%$ for an aspect ratio of 7. This difference comes probably from the fact that simulations are carried out for a volume fraction of 1%. For particles with a high aspect ratio, a 1% volume fraction may not be small enough as particles can be dilute but touch each other nonetheless , and therefore generate an important stress. Thus, it is not surprising to slightly overestimate the stress when considering particles with a high aspect ratio. The consistency of the ASD results with those of M&H indicates that the drag force is correctly computed in our code. The calculation of the stress with equation (2.47) for anisotropic particles for the ASD-RBM method is therefore validated.

3.2.3 Rheology of concentrated suspensions

One should be aware that no theory exists for concentrated suspensions of plate-like particles. Thus results from ASD can only be compared with the ones obtained by M&H. From moderate to high volume fraction, the viscosity is mainly due to lubrication interactions. Treating the contacts, the lubrication term and the hard sphere repulsion in the same manner in ASD and M&H is essential to compare the two methods. The same repulsive force as the that used by Meng & Higdon [40] is implemented in the ASD code for this test:

$$\mathbf{F}^{Hig} = \begin{cases} \frac{4}{3}C^p\left(\frac{\delta_{min}}{r-2}\right)\left(\eta - \frac{1}{2}\eta^2\right)^3 \hat{\mathbf{r}} & \text{if } (r-2) < \delta_{min} \\ 0 & \text{if } \delta_{min} \leq (r-2) \end{cases} \tag{2.49}$$

Numerical models

where C^p is the strength of the repulsive force, r the distance between two particles with $\hat{\mathbf{r}}$ the corresponding vector, δ_{min} the minimum gap triggering the repulsive force and $\eta = 1-(r-2)/\delta_{min}$. For the present calculations, $C^p = 5$ and $\delta_{min} = 10^{-3}$. We have carried out simulations of suspensions of spheres and $AR3$ plate-like particles for different volume fractions with the ASD code using the repulsive force given in equation (2.49). The viscosities obtained for each of these calculations are compared with Meng and Higdon results [27] in Figure 2.11.

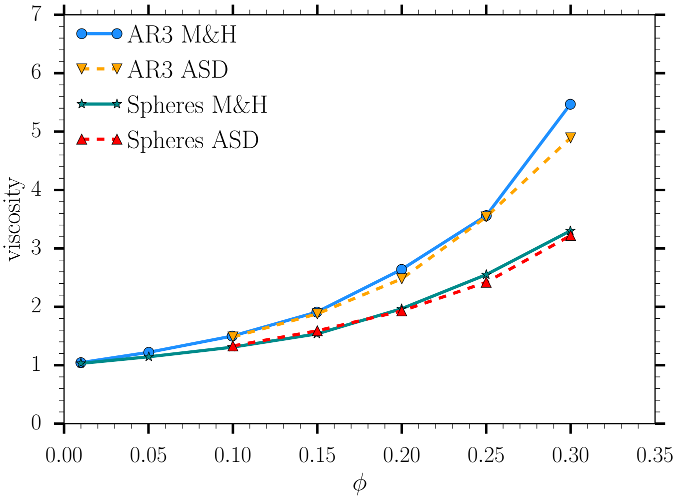

Figure 2.11: Evolution of the viscosity as a function of the volume fraction for suspensions of spheres and $AR3$. Dotted lines represent ASD calculation while full line represents Meng & Higdon calculations. Both methods are using the repulsive force given in the equation (2.49).

From low to moderate volume fraction ($\sim 20\%$), results are in a perfect agreement. At higher volume fraction, the calculations carried out with the ASD method have a viscosity slightly lower than the one obtained by Meng & Higdon. This difference can come from the use of a different time step (we do not know the value used by M&H), the different numerical schemes (ASD: simple forward time-stepping; M&H: Runge-Kutta 4) or any other small difference between the two codes.

One should be aware that the force F^{Hig} is extremely steep and requires a small time step to be triggered and to avoid the overlap between particles correctly. The comparison between the repulsive hard force initially used in the ASD code F^{HS} (see equation (2.32)) and the one used by Meng & Higdon F^{Hig} is given in Figure 2.12.

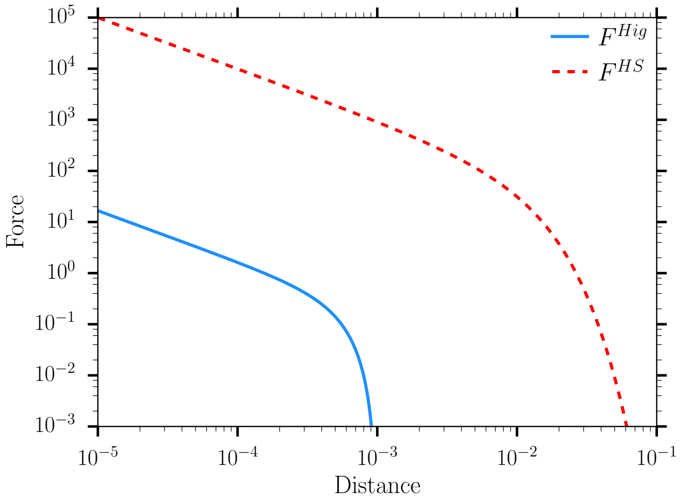

Figure 2.12: Comparison of the hard sphere repulsive force used by M&H F^{Hig} (full line) with the repulsive hard sphere force F^{HS} initially implemented in the ASD code (dotted line).

The repulsive hard force originally used in ASD is almost four orders of magnitude bigger than F^{Hig}. Moreover, at a distance of separation of $\sim 10^{-2}$, F^{HS} is already significant enough to avoid particles going closer. Consequently the particles are expected to approach more closely when using the Meng & Higdon force. In Figure 2.13 we have compared the viscosities of both $AR3$ and spheres suspensions computed for the two different forces, F^{Hig} and F^{HS}, as a function of the volume fraction. The calculations were carried out with the ASD code only while varying the model of the repulsive force.

The viscosity is slightly underestimated when using the repulsive force F^{HS}. However, the difference is only significant at high volume fraction ($\phi > 20\%$). As we will not launch any calculation with $\phi > 15\%$, and given the fact that F^{HS} allows using a larger time step, we have decided to carry out the simulations of anisotropic coarse-grained particles using F^{HS}. To conclude this section, comparisons with numerical results from M&H show that, at least for the range of volume fraction that we will investigate, the ASD-RBM method is validated for the computation of the rheology of suspensions of plate-like particles.

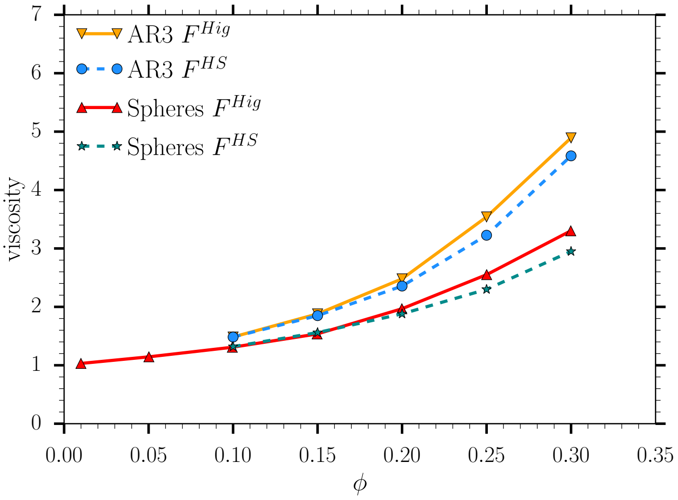

Figure 2.13: Evolution of the viscosity in the function of the volume fraction for suspensions of spheres and $AR3$. The calculations were carried out with the ASD code only.

4 Conclusion

In this chapter, the numerical methods used to compute the dynamics and the rheology of spherical colloidal suspensions, the Stokesian Dynamics (SD), and its approximate version the Accelerated Stokesian Dynamics (ASD) have been presented. These methods have been extended in this thesis to model coarse-grained particles with both shape and charge anisotropy. The charge anisotropy was introduced through the use of a site model based on a Yukawa potential. Two different methods were presented and implemented in the (A)SD code to keep the particles rigid. The first one consists in binding spheres with springs (SBS) represented in the code as forces and torques applied to the center of gravity of the particles. The second method consists in constraining the degrees of freedom of the spheres constituting the anisotropic colloids mathematically, to enforce the spheres belonging to the same cluster to move as a rigid body (RBM). Then, the hydrodynamic behavior of ellipsoids and plate-like particles was compared with the theory and results from the literature to be certain of the correct implementation of the methods and the physical behavior of the coarse-grained models. Due to the linearity of the Stokes flow, the hydrodynamic behavior can be studied as two distinct parts: the non-Brownian regime (high Péclet number) and the purely Brownian regime (low Péclet number, no background flow). At high Péclet number, Jeffery's orbits of prolate spheroids were studied at infinite dilution, and both methods, the SBS and RBM are in a perfect agreement with the theory. At low Péclet number, the SD of particles bound with springs overestimates the diffusion of plate-like colloids, contrary to the rigid body model. The latter is even able to reproduce the anisotropic diffusion behavior of an oblate spheroid. It is important to stress that the ASD is an approximation of the SD, and therefore if the SD is not able to reproduce a physical behavior, ASD can not be expected to do so. Therefore ASD-SBS was not studied at low Péclet. Due to the use of a diagonal matrix with free parameters to model the far-field Brownian mobility in the ASD code, the RBM model is not able to reproduce the anisotropic diffusion of an oblate spheroid. However, the mean diffusion coefficient can be tuned to match the theory. Finally, the rheological behavior of coarse-grained rigid body particles was studied in dilute and concentrate regimes for plate-like particles with different aspect ratios ($AR3$, $AR5$, $AR7$) to validate calculations of stresses, and in particular the shear stress. Concerning dilute suspensions, results from the RBM model used in this manuscript were compared with the theory and with the works from Meng and Higdon [26, 27, 28]. For particles with the lowest aspect ratio, results are in close agreement with both M&H's results and the theory. For particles with an aspect ratio equal to 7, the viscosity is slightly overestimated compared to the theory but matches well with M&H's results, which confirms the correct implementation of the model. As no theory exists for dense suspensions of anisotropic plate-like particles, the ASD results were compared with the ones from Meng and Higdon [27, 28] and appear once again in satisfactory agreement.

The rigid body model described in this chapter allows study of the microstructure of suspensions of particles with both structural and charge anisotropy. Moreover, using the extended ASD method, it is possible to explore numerically for the first time the dynamics of formation of this structure and the full rheological behavior of the suspension, including many-body hydrodynamics.

In the next chapter, we will focus on the final state of a suspension of clay-like particles without background flow and the dynamics of the formation of this structure. The last chapter will consist of the rheological study of a suspension of clay-like particles under shear flow.

References

[1] Adolfo J. Banchio and John F. Brady. Accelerated Stokesian dynamics: Brownian motion. *The Journal of Chemical Physics*, 118(22):10323–10332, June 2003.

[2] G. K. Batchelor. The stress system in a suspension of force-free particles. *Journal of Fluid Mechanics*, 41(3):545–570, April 1970.

[3] G. K. Batchelor and J. T. Green. The determination of the bulk stress in a suspension of spherical particles to order c 2. *Journal of Fluid Mechanics*, 56(03):401, December 1972.

[4] G. K. Batchelor and J. T. Green. The hydrodynamic interaction of two small freely-moving spheres in a linear flow field. *J. Fluid Mech.*, 56(2):375–400, November 1972.

[5] G. Bossis and J. F. Brady. Self-diffusion of Brownian particles in concentrated suspensions under shear. *The Journal of Chemical Physics*, 87(9):5437–5448, November 1987.

[6] G. Bossis and J. F. Brady. The rheology of Brownian suspensions. *The Journal of Chemical Physics*, 91(3):1866–1874, August 1989.

[7] G. Bossis and John F. Brady. Dynamic simulation of sheared suspensions. I. General method. *The Journal of Chemical Physics*, 80(10):5141–5154, May 1984.

[8] Robert Botet and Bernard Cabane. Scaling behaviors of colloidal aggregates under uniform pressure. *Physical Review E*, 70(3), September 2004.

[9] John F. Brady and Georges Bossis. The rheology of concentrated suspensions of spheres in simple shear flow by numerical simulation. *Journal of Fluid Mechanics*, 155:105, June 1985.

[10] Maxime Delhorme, Bo Jönsson, and Christophe Labbez. Gel, glass and nematic states of plate-like particle suspensions: charge anisotropy and size effects. *RSC Adv.*, 4(66):34793–34800, 2014.

[11] Maxime Delhorme, Christophe Labbez, and Bo Jönsson. Liquid Crystal Phases in Suspensions of Charged Plate-Like Particles. *The Journal of Physical Chemistry Letters*, 3(10):1315–1320, May 2012.

[12] L. Durlofsky, J. F. Brady, and G. Bossis. Dynamic simulation of hydrodynamically interacting particles. *Journal of Fluid Mechanics*, 180(-1):21, July 1987.

[13] David Eberly. Distance from a Point to an Ellipse, an Ellipsoid, or a Hyperellipsoid. *https://www.geometrictools.com/Documentation/DistancePointEllipseEllipsoid.pdf*, 2013.

[14] David R. Foss and John F. Brady. Structure, diffusion and rheology of Brownian suspensions by Stokesian Dynamics simulation. *Journal of Fluid Mechanics*, 407:167–200, March 2000.

[15] Elisabeth Guazzelli, Jeffrey F. Morris, and Sylvie Pic. *A Physical Introduction to Suspension Dynamics*. Cambridge University Press, Cambridge, 2011.

[16] H. Hasimoto. On the periodic fundamental solutions of the Stokes equations and their application to viscous flow past a cubic array of spheres. *Journal of Fluid Mechanics*, 5(02):317, February 1959.

[17] Kengo Ichiki and John F. Brady. Many-body effects and matrix inversion in low-Reynolds-number hydrodynamics. *Physics of Fluids*, 13(1):350–353, January 2001.

[18] G. B. Jeffery. The Motion of Ellipsoidal Particles Immersed in a Viscous Fluid. *Proceedings of the Royal Society A: Mathematical, Physical and Engineering Sciences*, 102(715):161–179, November 1922.

[19] Bo Jönsson, C. Labbez, and B. Cabane. Interaction of Nanometric Clay Platelets. *Langmuir*, 24(20):11406–11413, October 2008.

[20] S. Kim and S.J. Karrila. *Microhydrodynamics: Principles and Selected Applications*. Dover Civil and Mechanical Engineering. Dover Publications, 2013.

[21] S. Kutter, J.-P. Hansen, M. Sprik, and E. Boek. Structure and phase behavior of a model clay dispersion: A molecular-dynamics investigation. *The Journal of Chemical Physics*, 112(1):311–322, January 2000.

[22] O. A. Ladyzhenskaya. *The Mathematical Theory of Viscous Incompressible Flow*. Gordon & Breach, 1963.

[23] L. D. Landau and E. M. Lifshitz. *Fluid Mechanics*, volume 6. Second edition, 1987.

[24] Stéphanie Marenne and Jeffrey F. Morris. Nonlinear rheology of colloidal suspensions probed by oscillatory shear. *Journal of Rheology*, 61(4):797–815, July 2017.

[25] Stéphanie Marenne, Jeffrey F. Morris, David R. Foss, and John F. Brady. Unsteady shear flows of colloidal hard-sphere suspensions by dynamic simulation. *Journal of Rheology*, 61(3):477–501, May 2017.

[26] Qingjun Meng. *Large scale simulation of plate-like particle suspensions*. PhD thesis, University of Illinois, Urbana-Champaign, 2004.

[27] Qingjun Meng and Jonathan J. L. Higdon. Large scale dynamic simulation of plate-like particle suspensions. Part I: Non-Brownian simulation. *Journal of Rheology*, 52(1):1–36, January 2008.

[28] Qingjun Meng and Jonathan J. L. Higdon. Large scale dynamic simulation of plate-like particle suspensions. Part II: Brownian simulation. *Journal of Rheology*, 52(1):37–65, January 2008.

[29] Ehssan Nazockdast and Jeffrey F. Morris. Effect of repulsive interactions on structure and rheology of sheared colloidal dispersions. *Soft Matter*, 8(15):4223, 2012.

[30] Francis Perrin. Mouvement brownien d'un ellipsoide - I. Dispersion diélectrique pour des molécules ellipsoidales. *Journal de Physique et le Radium*, 5(10):497–511, 1934.

[31] Barbara Ruzicka and Emanuela Zaccarelli. A fresh look at the Laponite phase diagram. *Soft Matter*, 7(4):1268, 2011.

[32] Barbara Ruzicka, Emanuela Zaccarelli, Laura Zulian, Roberta Angelini, Michael Sztucki, Abdellatif Moussaïd, Theyencheri Narayanan, and Francesco Sciortino. Observation of empty liquids and equilibrium gels in a colloidal clay. *Nature Materials*, 10(1):56–60, January 2011.

[33] Ryohei Seto, Robert Botet, and Heiko Briesen. Hydrodynamic stress on small colloidal aggregates in shear flow using Stokesian dynamics. *Physical Review E*, 84(4), October 2011.

[34] Asimina Sierou. *Accelerated Stokesian dynamics development and application to sheared non-Brownian suspensions*. PhD thesis, California Institute of Technology, 2001.

[35] Asimina Sierou and John F. Brady. Accelerated Stokesian Dynamics simulations. *Journal of Fluid Mechanics*, 448, December 2001.

[36] James W Swan. *Colloids in confined geometries: hydrodynamics, simulation and rheology*. PhD thesis, California Institute of Technology, 2010.

[37] James W. Swan, John F. Brady, Rachel S. Moore, and ChE 174. Modeling hydrodynamic self-propulsion with Stokesian Dynamics. Or teaching Stokesian Dynamics to swim. *Physics of Fluids*, 23(7):071901, 2011.

[38] Santosh L. Tawari, Donald L. Koch, and Claude Cohen. Electrical Double-Layer Effects on the Brownian Diffusivity and Aggregation Rate of Laponite Clay Particles. *Journal of Colloid and Interface Science*, 240(1):54–66, August 2001.

[39] H. A. van der Vorst. Bi-CGSTAB: A Fast and Smoothly Converging Variant of Bi-CG for the Solution of Nonsymmetric Linear Systems. *SIAM J. Sci. and Stat. Comput.*, 13(2):631–644, March 1992.

[40] Marc Nathaniel Viera. *Large scale simulations of Brownian suspensions*. PhD thesis, University of Illinois, 2002.

[41] Mu Wang and John F. Brady. Spectral Ewald Acceleration of Stokesian Dynamics for polydisperse suspensions. *Journal of Computational Physics*, 306:443–477, February 2016.

Structure of suspensions of clay-like particles without background flow

3

Particles belonging to the clay family have both a structural and a charge anisotropy. These anisotropies are responsible for very complex behaviors leading to a rich phase diagram, highly sensitive to the experimental conditions, such as the volume fraction, the ionic strength, and the aging of the suspension. The macroscopic phases of clay suspensions are relatively "easy" to characterize experimentally. However, the study of the microstructure is more complex due to the small size of the particles and requires measuring some statistical quantities which could be difficult to interpret. For instance, the overlapping coin (OC) configuration between two clay-like particles has been observed for the first time numerically by Odriozola and coworkers [31] while authors were only expecting house-of-cards (HOC) configuration. Afterward, OC configuration has been observed experimentally thanks to cryo-SEM for Na-montmorillonite suspension, a natural clay, where OC and HOC configuration formed a honeycomb-like network in a wide range of salt concentration (10 to $100\ \mathrm{mM}$) [3]. Therefore, it is interesting to use a numerical model to study the effect of a varying parameter on the microstructure of suspensions of clay-like particles.

In this chapter, we focus on the behavior of plate-like particles with charge anisotropy without background flow. In such conditions, hydrodynamics are not supposed to modify the phase diagram [9], which has been classically studied with Monte Carlo simulations (MC). The final configuration (microstructure) is reached once the Helmholtz free energy is minimized and stabilized. This method is known to be efficiently analyzed by parallel methods, leading to a low numerical cost per iteration. Therefore, it allows carrying out simulations with a large number of particles (several thousands) and MC cycles. Consequently, simulations carried out with MC are able to reach equilibrium and are equivalent to an almost infinite aging time of the suspension. However, the kinetics of the formation of the microstructure and its rearrangement cannot be studied with MC as hydrodynamic interactions are ignored.

On the other hand, the ASD-RBM method solves the dynamics of the clay-like particles taking into account both the Brownian motion and many-body hydrodynamic interactions, and therefore, allows studying the formation of the microstructure. The ASD-RBM method is computationally expensive, and only a relatively small number of particles (commonly 60 platelets formed of 37 spheres, in this work) can be simulated over a short period of time. Thus, some structures requiring long aging are impossible to reach with this method. Moreover, the small number of particles can lead to unphysical structures related to the simulated size box.

Although the ASD method is certainly not the most effective method to study equilibrium structure, we have chosen to use it to provide a better understanding of the microstructure formation and to validate our model by comparing the results with the ones from MC simulations. The results from the ASD-RBM method for suspensions of clay-like particles without background flow will validate the method for its use for suspensions under shear.

The main goal of this chapter is, therefore, to prove that despite the limitations coming from the ASD-RBM method, suspensions of clay-like particles simulated with the method undergo similar behavior (phase diagram) as with MC simulations. As a first step, the system studied, and the numerical parameters are defined and placed in context with respect to results in the literature. Then, in a second step, the equilibrium structure is studied as a function of the range of electrostatic interactions and the volume fraction.

1 Models and simulations set up

When no flow is applied, a suspension of particles with both shape and charge anisotropy has a phase diagram depending on the excluded volume, and on the competition between electrostatic, Brownian, and van der Waals forces (see chapter 1). One should recall that the electrostatic forces depend on both the Debye length κ^{-1} and the surface charge of the particles Z_i. The Brownian force depends on the temperature of the system, as well as the size and the shape of the colloids. For a prescribed surface charge density distribution, the phase diagram of a suspension of anisotropic particles must be represented in a three-dimensional diagram with the range of interactions (involving the total ionic strength) compared to particle size, the volume fraction, and the temperature on different axes. In experiments and simulations, the temperature is most often considered to be at room temperature ($\sim$ 20 °C). Thus, the phase diagram is usually presented in two dimensions, volume fraction and ionic strength.

1.1 A model clay: Laponite

Colloidal clays are hydrous magnesium (sometimes aluminum) particles, usually bearing a negative structural charge coming from isomorphic substitution compensated by the presence of cations in the basal spacing or on the surface of the colloid. These nanoparticles have a platelet shape with an aspect ratio ranging from 20 to 100. When dispersed in water, clays hydrate and swell, leading to the release of the cations. Note that there are clays which swell a significantly ($> 100\%$, bentonite) and ones which do not swell much (0.05, kaolin). The hydroxyl groups present on the edge of the particle are sensitive to the pH (titratable sites), resulting in an amphoteric edge charge. At low pH, the rim is positively charged and becomes neutral or negative in basic solutions. Natural clays are often very complex to study due to their polydispersity and chemical heterogeneity. To understand the role of physicochemical parameters such as the pH or the ionic strength, researchers often focused their studies on a synthesized model clay particle with low polydispersity which is well-characterized chemically: Laponite.

Laponite is a hectorite-type smectite clay widely used in industrial processes as a rheology-modifier for paints, ceramic glazes, household cleaners, and surface coatings. Laponite is composed of rigid disc-shaped crystals with an aspect ratio of approximatively 28 and the empirical chemical formula

$Na^+_{0.7}\,[(Si_8Mg_{5.5}Li_{0.3})O_{20}(OH)_4]^{-0.7}$, where the exponent -0.7 comes from the fact that the sodium cation is shared in the interlayer region between adjacent crystals [30, 38]. Once dispersed in water, Laponite hydrates, swells, and releases a part of the Na^+ cations leading to a net structural negative charge. At pH ≤ 9, Laponite dissolves in water [38]. For pH ≥ 10, the protonation of the OH groups forms a positive rim charge, which slightly decreases while increasing the pH up to approximately 11. Above pH 11, the value of the charge is still debated as some authors consider the charge as neutralized [37] while others consider it negative [27] due to the formation of MgO_2^- on the rim.

To estimate the value of the positive rim charge at $10 \leq$ pH ≤ 11, Tawari and coworkers added Laponite to pure water in order to reach a concentration of $2\ \mathrm{g\,L^{-1}}$ [37]. The pH of the solution increased from 7 (pure water) up to a value of 9.97, which indicates a capture of H^+ ions to form $OH^{1/2+}$ groups on the rim. Given the density of Laponite equals to $2.2\ \mathrm{g\,cm^{-3}}$ and the mass of Laponite added to the solution, authors could calculate the corresponding OH^- concentration. Thus, the positive rim charge was found to be approximately $50\ e$ per particle. The authors also measured the negative charge of the Laponite, corresponding to the number of Na^+ released, by means of conductivity measurements and found a value of approximately $-500\ e$ per particle, that is 10 times the rim charge. This value must be compared to the structural charge obtained if all the Na^+ ions were dissociated from the colloid. The structural charge has a value depending directly on the number of unit cells in the composition of one Laponite platelet and on the elementary charge of a unit cell: $\simeq -0.7\,e$. The number of unit cells depends on the size of the particle and is between 1000 and 2000. Bipus and coworkers considered that Laponite RD (a type of Laponite) is composed of 1000 unit cells [6], Brunier and coworkers that Laponite is a crystal composed of about 1500 unit cells [7] and the supplier BYK gives the number of 2000 unit cells [8]. If we take the chemical formula $Na^+_{0.7}\,[(Si_8Mg_{5.5}Li_{0.3})O_{20}(OH)_4]^{-0.7}$, a thickness of a particle of $1\ \mathrm{nm}$ and an average diameter for the Laponite of $30\ \mathrm{nm}$, considering the density of the Laponite RD produced by Laporte Industries equals to $2.57\ \mathrm{g\,cm^{-3}}$ as given by Ruzicka [33], we find a number of unit cells of 1430 corresponding to a total structural charge of $-1000\ e$. From their all-atom model, Leote de Carvalho and Skipper [25] obtained a charge density of $0.25\ \mathrm{C\,m^{-2}}$ which would translate to $-1060\ e$ for Laponite with a $30\ \mathrm{nm}$ diameter. The same calculations with the data from Tawari give a structural charge of $-860\ e$. Various types of Laponite actually exist (including RD, XLG, XLS) with slightly different densities, which can explain some variability about structural charges reported in the literature.

For this study, the negative structural charge is considered equal to $\sim 1000\ e$. However, as a part of the Na^+ ions is never released, one can consider these ions as part of the colloid and reduce the charge accordingly. The corresponding reduced charge is equal to $-700\ e$, and is in agreement with Dijkstra et al. [13]. It will be referred to as the "net charge" which is actually necessary for practical force calculations and the charge on the rim must also be accounted for. The positive charge of the rim is taken equal to 10% of the negative charge in line with most of the literature [13, 24, 31, 37].

To provide the context of the study, we first describe some important numerical works from the literature about Laponite suspensions. These works will be used as references for the rest of this chapter and will be used as a comparison for our results.

1.2 Previous numerical works on Laponite suspension

A pioneering work on Laponite simulation is from Dijkstra and coworkers [13], who modeled Laponite particles as infinitely thin disks of diameter $\sigma = 25$ nm. The disks were not allowed to intersect each other, and the electrostatic interactions were reduced to quadrupolar interactions between fixed points in their centers. The interactions were tuned to favor the face to edge attractions compared to any other arrangement (e.g., stacking or edge to edge attraction). A repulsive Coulomb force was added to avoid the collapse of the disks for distances less than $\sigma/2$. Dijkstra and coworkers calculated the reduced osmotic pressure (Π^*) as a function of the reduced density (ρ^*) for different quadrupolar coupling constants, *i.e.*, for different ratios of electrostatic and Brownian forces. These authors observed a drastic increase of Π^* below the nematic transition obtained for bare disks by Eppenga and Frenkel [14], indicating a nearly incompressible phase, referred to as gel. If this model is at first sight very crude, it provides insight into how the formation of a gel phase at low Laponite concentration might occur. It also pointed out the importance of the electrostatic interactions on the structure of the suspension.

Some years later, Kutter and coworkers proposed a more complex electrostatic model [24] to reduce the errors induced by the quadrupolar interactions at short and long-ranges. Their approach consisted of modeling the Laponite as a rigid hexagonal disk with discrete charge sites, as shown in Figure 3.1a. The values of the charges were chosen to reach a total charge of $-700\ e$ for the plate-like particles, and the aspect ratio of the Laponite was conserved (thickness 1 nm, diameter 25 nm). These authors have made the assumption of pairwise additivity for the computation of the electrostatic interactions between two disks, and therefore the total interaction was simply the sum of the site-site screened Coulomb potential of the Yukawa form. This electrostatic interaction corresponds to the *site model* described in chapter 2 (see section 2.4). In their study, Kutter and coworkers used Monte-Carlo simulations to study the influence on the microstructure of the number of charged sites, the volume fraction, the range of electrostatic interactions, and the presence (model B) or absence (model A) of charges with an opposite sign on rim sites. They observed for the model B at high ionic strength and low particle concentration a phase separation with a phase rich in colloids (cluster phase) and a phase poor in colloids, a spanning network with a house of card structure at higher concentration, a fcc crystal phase (Face Centered Cubic) at low concentration and long interaction range for the model A. This study emphasized the importance of the model (A or B) on the final structure obtained.

In 2004, Odriozola and coworkers used a code based on Brownian Dynamics (BD) to simulate a suspension of platelets having the same aspect ratio as Laponite (1:25), and with 469 available charge sites [31]. However, as a first approach, these authors only considered the 61 sites represented in Figure 3.1b. Odriozola et al. considered as their predecessors two types of particles, *i.e.*, with (model A) and without (model B) opposite charges on the rim. In their simulations, these authors varied the volume fraction in the range 0.01 to 0.15, and the number of the charged sites from 61 to 469, allowing the comparison with Kutter and coworkers. All the calculations were realized with screening lengths (κ^{-1}) of 1 and 3 nm. For such interaction ranges, particles of model B (attractive particles) are expected to aggregate in a T-shape configuration following the work of Kutter et al. However, Odriozola and coworkers observed an unexpected spatial arrangement of particles, now referred to as the overlapping

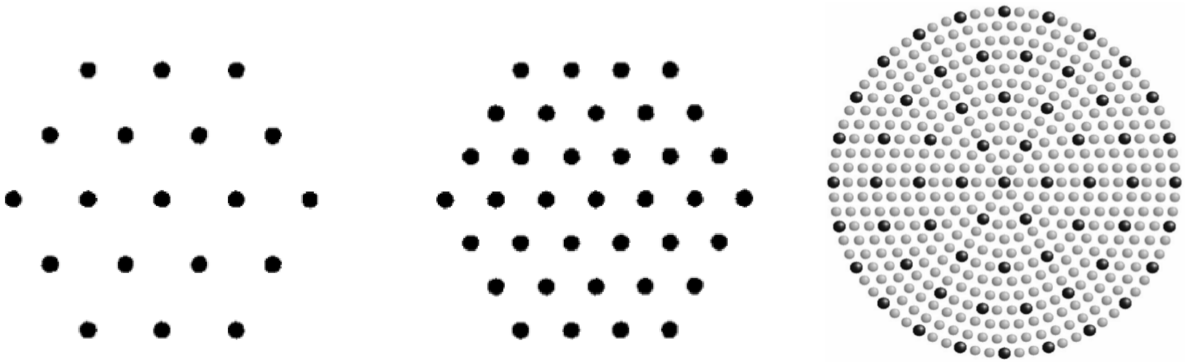

(a) Kutter's model [24] (b) Odriozola's model [31]

Figure 3.1: Charge sites model used by Kutter (left) and the bead model used by Odriozola (right) to compute electrostatic interactions. The dark spheres on the right picture interact through both Yukawa and Hard Sphere potentials, while the light ones only interact through Hard Sphere potential, which avoids the interpenetration of the particles.

coin configuration (OC). Kutter and coworkers did not observe such a spatial arrangement due to the fact that they considered spaces between charges allowing platelets to interpenetrate and facilitating at the same time the T-shape configuration.

The observation of both OC and HOC configurations by Odriozola and coworkers at high salinity ($\kappa^{-1} = 1$ nm and 3 nm) motivated the work from Jönsson et al. [23] in which they calculated the free energy of interaction for a pair of model clay particles. They used a model with 656 charged sites with 556 negative sites (faces) and 100 positive sites (rim), as shown in Figure 3.2a. These authors introduced the van der Waals forces in addition to the Coulomb screened potential to model the electrostatic interactions between particles and to be more representative of experimental conditions. These authors have defined the bond energy (free energy of interaction) by summing the totality of the potential acting on the particles. They have used MC simulations to generate the radial and random rotational displacements of the particles. These authors were able to determine the bond energy as a function of the distance between the centers of gravity of the particles. Jönsson and coworkers have found that vdW interactions play a minor role for a salinity less than 100 mM. Above this concentration, vdW interactions dominate the attraction phenomena and favor the OC configuration. These authors have also shown that at low salt concentration, 1 mM, the system is purely repulsive. However, they emphasized that such a low salinity cannot be reached experimentally just by immersing particles in pure deionized water, as the counterions released by Laponite particles lead to an increased ionic strength. At moderate salinity, the system becomes attractive and is best described by the overlapping coin configuration. Finally, at high salinity, electrostatic interactions are screened, and the vdW forces drive interactions. Therefore the microstructure at high salt concentration should mainly depend on the volume fraction and the temperature of the system. Indeed, increasing the temperature will increase the Brownian motion of the particles, and therefore increases the ratio between thermal energy and bond energy, *i.e.*, the reduced temperature T^*.

In 2010, Ruzicka and coworkers reported for the first time the experimental observation of empty

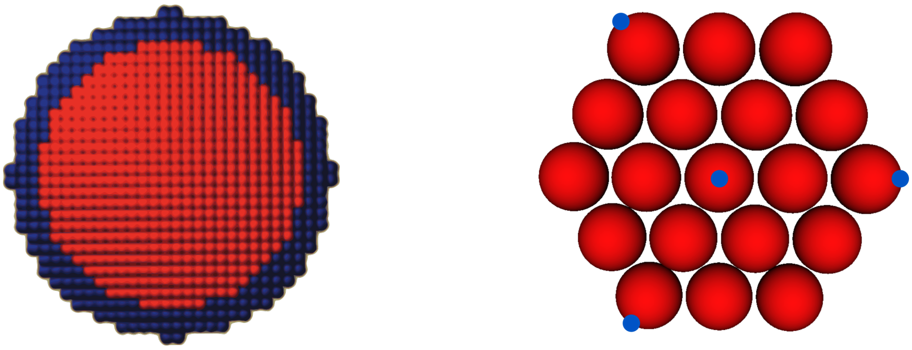

(a) Jönsson's model [23] (b) Ruzicka's model [35, 4]

Figure 3.2: Schematic picture of the clay-like particles used by Jönsson (left) and Ruzicka (right). In the left figure, the blue sites are positively charged, and the red sites are negatively charged. The patchy particle model used by Ruzicka and Angelini is composed of patches in blue in the right figure, and sites in red.

liquids and equilibrium gel in a colloidal clay suspension [35]. The empty liquid phase is described by Bianchi and coworkers as a spanning network with a high density fluctuation probability resulting in a very small overall density [5]. Such a phase is supposed to be favored for particles with a low valence number. The experiments of Ruzicka et al. consisted in the preparation of samples with a weight concentration in Laponite ranging from 0.1% to 1.2% immersed in pure deionized water, corresponding respectively to Debye lengths of 9 nm and 4.8 nm. These authors observed the suspension over 30 000 hours visually and measured the evolution of the structure factor as a function of the waiting time over $11\,000$ hours. For $C_w \leq 1\%$ the system undergoes a phase separation with a phase rich in colloids (a gel), and a phase poor in colloids (liquid). This phase separation is also indicated by the continuous increase of the static structure factor S reaching $S > 1$ at low scattering vector q. The residual turbidity of the gel phase, even after 30 000 hours, indicates the formation of large density fluctuations whose length scales are commensurate with the visible light providing the evidence of empty liquids. For a concentration $C_w = 1.2\%$, the system is totally percolated, and the sample remains transparent throughout the experimental time. The static structure factor at low wavenumber q saturates after one year, indicating that the system has reached its long time equilibrium structure. Its low q value remains below 1, indicating an important resistance to compression of the particle structure. Given that empty liquids are favored for particles with low coordination number [5], Ruzicka and coworkers tried to reproduce the static structure evolution inside and outside the phase separation using MC simulations of patchy-particles with low valence number. The patchy-particle has an aspect ratio equal to 1:5 (see Figure 3.2b) and is composed of 19 sites represented by the spheres in red, and five charged patches, three on the rim and two on the faces, represented in blue in Figure 3.2b. The sites interact only through a HS potential, while the patches interact through a short-range square-well potential acting only between the rim and the face patches. Ruzicka and coworkers have reported on a phase diagram the binodal and the percolation lines for a suspension of their patchy-particles as a function of both the reduced temperature T^* and the reduced density ρ^* (the number density scaled by the close-packed density). Such a diagram allows pointing out the importance of the accurate definition of the reduced temperature for simulations as the simple increase of T^* can lead to a phase transition from phase separation to an empty liquid or a liquid-like state. Ruzicka et al. carried out numerical simulations for reduced density inside ($\rho * < 0.114$) and outside ($\rho * > 0.114$) the phase separation region. The first step consisted in applying high reduced temperature to the suspensions to generate thermal energy larger than the bond energy and therefore, to preserve particles isolated and in a liquid-like state. In a second step, the suspensions were instantaneously quenched to low T^*, and the evolution of the static structure factor, $S(q)$ was tracked as a function of the number of MC cycles. The patchy-particle model was able to reproduce the low q continuous increase inside the phase separation region and its saturation outside, obtained experimentally. However, the numerical model drastically overestimates the values of $\lim_{q \to 0} S(q)$, certainly due to the numerous assumptions considered for the model. The aspect ratio of the patchy-particles model is, for instance, five time lower than for Laponite particles. Moreover, the patchy model only allows the creation of T-bonded structures, while Jönsson and al. have highlighted the importance of OC configurations [23].

Later, Angelini, Ruzicka, and coworkers observed a glass-glass transition of Laponite suspension experimentally at low ionic strength [4] and fixed weight fraction $C_w = 3\%$. The transition occurs approximately three days after the first arrested state is reached (Wigner glass) and leads to what the authors called a Disconnected House of Card glass (DHOC). During dilution experiments of the two arrested states, these authors observed that the first state fluidized with time, whereas the second remained solid, indicating attractive interactions between particles. To support the assumption of a DHOC spatial arrangement, these authors "upgraded" the patchy model: they added a Yukawa repulsive potential between the sites of different particles and a long-range orientational attraction between the patches in such a way that particles minimize their energy when they are orthogonal. These authors fixed the reduced temperature to one, and just by varying the screening length and the effective charges of the sites, they were able to reproduce the position of the first peak in experimental $S(q)$ of a Wigner glass. In such a case, the particles were randomly organized. Then, reducing T^*, Angelini et al. observed some DHOC arrangement of particles. However, they were not able to reproduce the aging behavior of a Wigner glass, as the continuous reduction of T^* leads to the shift of the peak in $S(q)$ to higher q, which is the opposite experimentally observed behavior.

The phase diagram of purely repulsive charged colloidal platelets was reported by Jabbari and coworkers [22]. Despite the lack of attractive interactions, this study can be representative of clay suspensions under specific conditions. Indeed, the rim charges of the Laponite are neutralized at pH $>$ 11 or with the addition of peptizers so that Laponite can act as repulsive disks. Many industrial processes using clays add polymers to neutralize the rim charges and therefore stabilize the suspension [28]. Although the totality of the phase diagram presented by Jabbari et al. is not representative of clay-like particles system at any pH, some similar behaviors should be observed with Laponite suspension, especially at long-range interactions where Laponite is supposed to act as a Wigner glass. These authors considered infinitely thin platelet particles (cf. Figure 3.3) with anisotropic charge interactions. Jabbari and coworkers used the model developed by Agra et al. [2], where two platelets interact through a modified screened Coulomb potential involving an anisotropic function taking into account the orientational dependence of the potential. The higher the salinity, the more sensitive the anisotropic function is to the angle between two platelets. This function avoids the implementation of the *site model* and only depends on the center to center distance between two platelets and their angle with the connecting centerline. The model used by Jabbari and coworkers requires less computational time than the *site models* mentioned before and accounts for surface charge renormalization. However, it is not able to distinguish all the possible configuration angles - *e.g.*, two platelets with the same angle of 45 degrees with respect to their connecting line can be parallel or can form a kind of right-angled triangle.

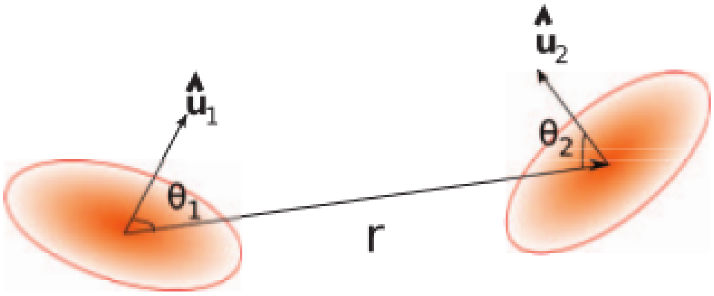

Figure 3.3: Schematic picture of two infinitely thin disks interacting through Yukawa potential with an orientational dependence developed by Agra et al. [2], and used by Jabbari and coworkers [21, 22].

One should keep in mind that decreasing the pH below 11 increases the rim charges. Then, the charge anisotropy of Laponite varies as a function of the pH. The influence of the charge anisotropy on the phase diagram of a dispersion of clay-like particles was investigated by Delhorme and coworkers [10]. These authors have studied the microstructure of platelet suspensions as a function of the added salt while varying both the charge anisotropy and the volume fraction. They have used a multi-level coarse-graining *site model* where site-site interactions are computed through a Yukawa potential (see Figure 3.4). A Lennard-Jones potential is applied between sites to avoid the interpenetration of the particles. Delhorme et al. have shown that the microstructure is sensitive to the details of the charge anisotropy and reported four different phases at strong charge anisotropy and three phases at lower charge anisotropy. In their work, Delhorme and coworkers varied the volume fraction based on the volume of the constituent spheres of one platelet from 0.01 to 0.105. They did not observe a Wigner glass, neither at high volume fraction (0.105) and low salinity as proposed by Ruzicka et al. at long waiting time [35] nor at low volume fraction and low ionic strength as reported experimentally for Laponite [26] and another kind of clay, Montmorillonite [36]. The authors also investigated the suspension behavior at higher volume fraction, ranging from 0.11 to 0.29, and proposed a phase diagram mostly composed of liquid crystal phases [12]. They observed different phases as a function of the added salt up to a volume fraction equal to 0.21. Above this threshold, both the high concentration of counterions driven by the release of Na^+ coming from the swelling of the Laponite, and the crowding effect, avoid the emergence of new phases and only an interpenetrated rectangular columnar phase is observed. Two years later, Delhorme and coworkers [11] studied the influence of the size and the charge anisotropy on the transition from an isotropic state to solid phases or nematic states using the multi-level coarse-graining mentioned earlier (see Figure 3.4). They have shown that large particles favored the liquid-gel transition with a strong charge anisotropy. In contrast, the liquid-glass transition is favored for small particles bearing only negative charges. The isotropic to nematic transition is favored for particles with a higher aspect ratio and a lower charge anisotropy.

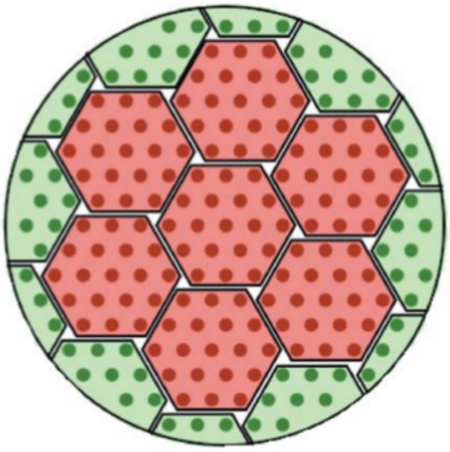

Figure 3.4: Schematic picture of the clay-like particles used by Delhorme [10, 11, 12]. The green sites are positively charged, and the red sites are negatively charged. The sites are used to compute electrostatic interactions at short range. At long range, the electrostatic interactions are computed between the patches composed of a group of sites (5 negative patches and 14 positive patches).

All of the models we have just presented were used to study disk-shaped particles with charge anisotropy using Monte Carlo simulations [10, 11, 12, 23, 22, 35] or Brownian Dynamics simulations [29, 31]. The relatively low computational cost of the MC and BD methods allowed the authors to model a large number of particles (from 100 for Odriozola et al. (BD) to more than 1000 for Jabbari et al. (MC)) with a relatively large aspect ratio (25 for Odriozola and coworkers, 15 for Delhorme and coworkers). All of these studies provide a good insight into the expected phases for clay-like particles suspensions as a function of the volume fraction and the interaction ranges.

1.3 System simulated

1.3.1 Description of a suspension of clay-like particles

As mentioned in the second chapter, we use $N_s^p = 37$ spheres to coarse-grain one clay-like particle (see Figure 3.5). This particle will be referred to as $AR7$ due to its aspect ratio of 7.3. Clearly, these model particles have a smaller aspect ratio than the smallest aspect ratio of 9 studied by Delhorme and coworkers [11], and they are one-fourth the ratio of Laponite. Therefore, we expect it to be more difficult to observe in the present work a transition from any isotropic to a nematic state at equilibrium [11]. Nevertheless, the aspect ratio is still larger than the one used by Ruzicka et al. or Angelini et al. (5 - [35, 4]), which did not prevent them from observing a complex phase diagram. Coming back to the system we choose to simulate, one should notice that in Figure 3.5 the center of gravity of the plate-like particle is also the center of gravity of the red sphere. The position and the orientation of a platelet are fully described by the position of the center of gravity and the vector director **n** of the platelet. The consideration of hydrodynamic interactions in the ASD method drastically increases the computational cost compared to MC and BD, and therefore we had to limit the number of platelets N_p to 60 for most of the simulations, which represents already 2220 spheres. Due to this small number of particles, statistical noise is sometimes important. Some simulations with the same volume fraction were carried out with twice as many particles to be sure not to observe structures correlated to the size of the box or to the low number of particles. Following Delhorme et al., the volume fraction is based on the volume of the spheres constituting the particle:

$$\phi = \frac{N_p V_p}{V_b} = \frac{4 N_p N_s^p \, \pi a^3}{3L^3} \tag{3.1}$$

where L is the length of the simulation box, V_b its volume, and V_p is the volume of an $AR7$ particle. We have decided to vary the volume fraction from $\phi = 0.05$ to $\phi = 0.124$ to be able to compare our results with the paper from Delhorme and coworkers [10]. Note that these volume fractions correspond respectively to the reduced densities $\rho^* = 6.75$ and $\rho^* = 16.71$, which allows also comparison with the work from Ruzicka and coworkers [35]. Since we want to study the phases without background flow, we set $Pe = 3\pi\eta R^3\dot{\gamma}/(k_b T) \ll 1$, taking $3.89\ 10^{-3}$. All the simulations are carried out over a time $\tau = 50\ a^2/(2D_0)$, where D_0 is the diffusion coefficient of one individual sphere. By considering the mean translational diffusion coefficient of a plate-like particle, the center of gravity of an $AR7$ can only cover a distance of $0.49R$ in nondimensional time of $\tau = 50$ if thermal effects are the only source of motion. Because this distance is small, we can only compute systems with high volume fraction to generate significant interactions between particles in the time window of the simulation. One should know that $50\ a^2/(2D_0)$ corresponds to approximately 74 ns. Although this real time is extremely low, the suspensions of $AR7$ undergo similar behaviors to the ones obtained with Monte-Carlo and presented in section 1.2.

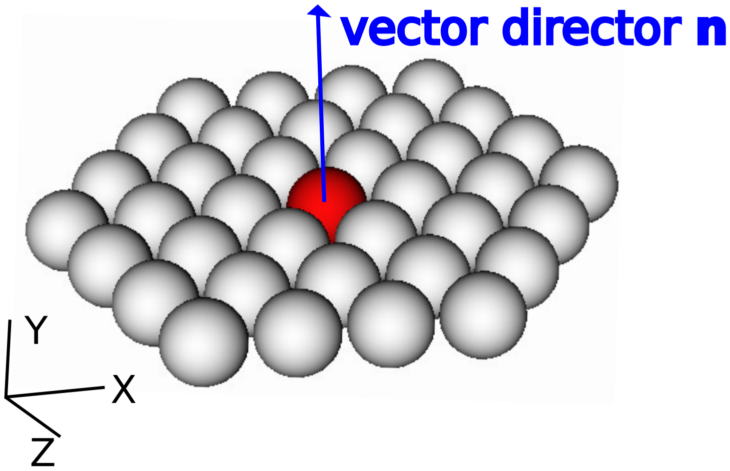

Figure 3.5: Clay-like particle coarse-grained with 37 individual spheres referred to as $AR7$.

1.3.2 Set up of the particles charges

As previously explained, due to the high computational cost of the ASD method we are not able to carry out simulations with plate-like particles having the same aspect ratio as Laponite. One should also remember that Ruzicka and coworkers [35] have pointed out the importance of the ratio between the bond energy, directly related to the electrostatic forces, and the thermal energy, related to the Brownian forces. This ratio can be written with a non-dimensional number $F^e R/(k_b T)$, where F^e is the electrostatic force scale and R the radius of the particle, and is actually the inverse of the reduced temperature T^*. We have chosen in our model to preserve the value of $F^e R/(k_b T)$ of the Laponite. It is necessary first to compute the electrostatic force scale of a Laponite particle. Let us recall that we assume a total negative charge of $-700\ e$, and a positive charge of $70\ e$. Knowing the negative charges are normally situated between the basal planes, we assume a symmetric repartition of the charges between the surfaces. As a result, a Laponite particle could be modeled as a disk-shaped particle of aspect ratio $1:30$ with $-350\ e$ charges per face and $70\ e$ charges spread on the rim. Due to the strong charge anisotropy, there are two crucial types of $F^e R/(k_b T)$: the one in the repulsive face-face configuration (see Figure 3.6b), and the one in the attractive face-edge configuration (Figure 3.6a). In Figure 3.6, only a quarter of the domain is modeled owing to symmetries of the system. Using the PoBos code (Poisson-Boltzmann Solver) developed at Laboratoire de Génie Chimique (LGC) we have solved the three-dimensional non-linear Poisson-Boltzmann equations and, therefore, the electrostatic potential field ψ as shown in Figure 3.6 (a blue color stands for a negative potential and a red color for a positive). From the potential field, it is possible to compute the forces applied to the particles as a function of the distance between their centers of gravity. These forces are reported in Figure 3.7 as the blue points (discrete values). As expected, the forces are attractive in the T-shape configuration and repulsive for the face-face arrangement.

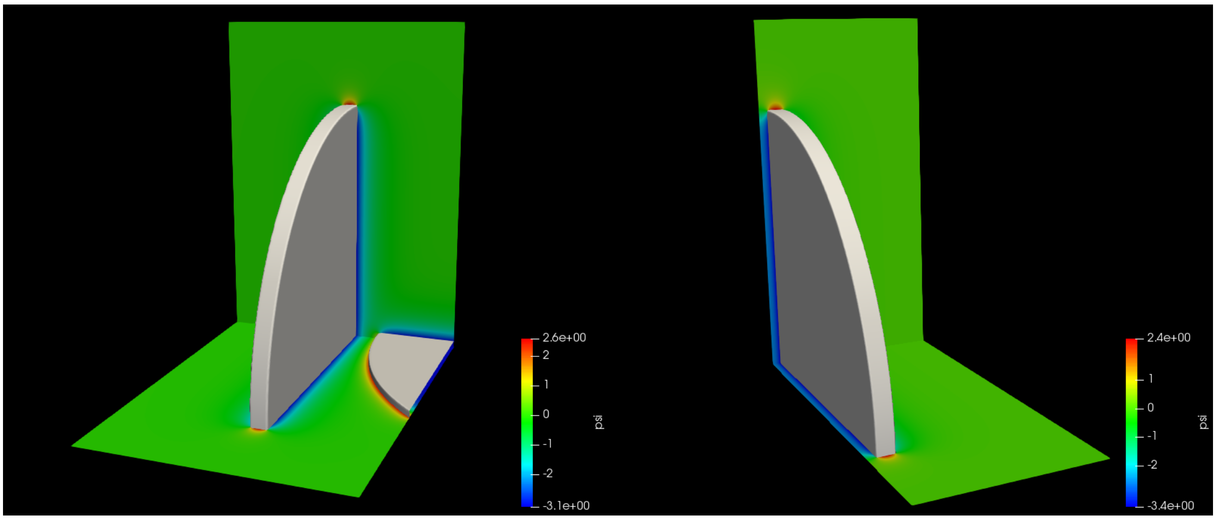

(a) Face-edge arrangement (T-shape)

(b) Face-face arrangement

Figure 3.6: The 3-dimensional electrostatic potential between two disk-shape particles computed by Poisson-Boltzmann Solver (PoBoS). The particles are arranged in (a) face-edge and (b) face-face configuration. The surface charges are set to $-350\ e$ per face and $70\ e$ spread on the rim. The Debye length is set to $\kappa^{-1} = 1\ \mathrm{nm}$.

Now that we have computed F^e of Laponite for different spatial configurations, we want to ensure the preservation of $F^e R/(k_b T)$ in our model. As the radius of an $AR7$ particle is approximately four times smaller than a Laponite particle, the electrostatic force scale applied to an $AR7$ particle must be multiplied by four to preserve $F^e R/(k_b T)$ of the Laponite. We recall that electrostatic interactions between $AR7$ particles are modeled by a Yukawa potential between charged sites, as described in section 2.4. Both short and long-range attractive and repulsive interactions are taken into account as in the model used by Jönsson and coworkers and later by Delhorme and coworkers. Consequently, the preservation of $F^e R/(k_b T)$ of the Laponite in our model will be ensured by the attribution of effective charges to the spheres making up an $AR7$ particle. To determine these effective charges, $AR7$ particles are positioned with the same spatial configuration as the disks. The charges attributed to the face and rim spheres are estimated to generate a force four times larger than the force computed with PoBoS for disk-shaped particles, thanks to an optimization solver. The fitted $AR7$ forces are reported in Figure 3.7 (full black line). Note the difference in the order of magnitude between the face-edge and the face-face configuration. The fits are in very good agreement with the real forces between Laponite particles, indicating that despite their small aspect ratio, $AR7$ particles capture both the short- and long-range electrostatic behavior of the latter. The procedure described above leads to the definition of "effective" charges to be used in the Yukawa *site model* of an $AR7$ particle. By design, these effective charges generate the same $F^e R/(k_b T)$ as computed with the non-linear PB theory for Laponite. It appears clearly that neither the total net charge nor the charge density of an $AR7$ particle will be the same as for a Laponite particle.

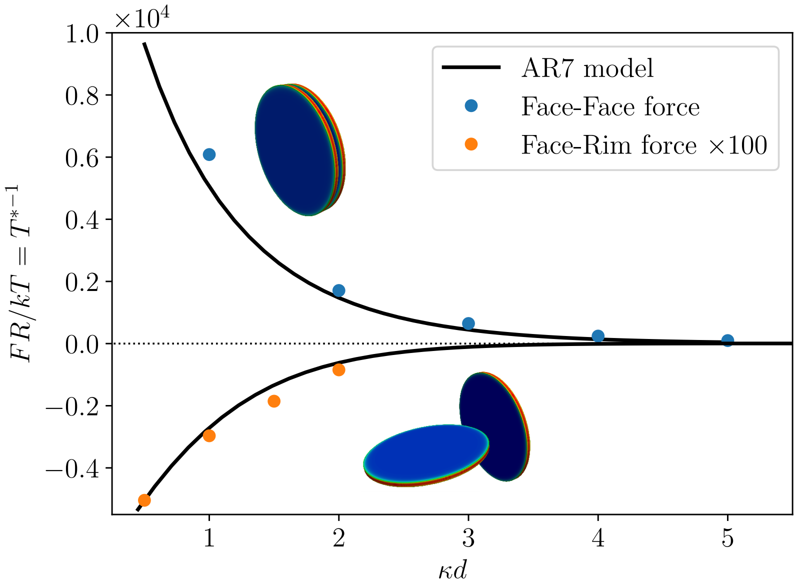

Figure 3.7: Electrostatic forces between two disk-shaped particles of aspect ratio 30 and two $AR7$ plate-like particles as a function of the distance. The blue and orange points stand for the forces computed by Poisson-Boltzmann Solver (PoBoS), the black curves are the forces computed using the linear theory and the Yukawa potential for optimized charges. The small d in the x-axis legend stands for the distance between surfaces, and r between the centers of gravity.

One should recall that the electrostatic forces depend on the screening length, and therefore the charges of a Laponite particle and the effective charges of an $AR7$ particle should be computed for each of the interaction ranges studied. In the current study, the charges were optimized only for the range of $\kappa D = 7.3$, equivalent to $\kappa^{-1} = 1$ nm. Although considering the same charges for other range of interactions is not strictly correct, we have used the following total charges for all simulations: $Z^t_{face} = -178.6\ e$ and $Z^t_{rim} = 108\ e$. Given that the face is composed of 19 sites, and the rim 18 sites, the charge per site is equal to $Z^s_{face} = -15.4\ e$ and $Z^s_{rim} = 6.0\ e$ (see Figure 2.5).

Now that the system used to simulate clay-like particles is fully described, we will present in the next section all the quantities used to characterize it quantitatively.

1.4 Computed quantities

Due to the anisotropy of particles, the local structure must be described with both positional and orientational correlation functions. As we are able to track at any time the position of the center of gravity of the particles, the radial distribution function can be computed. This function represents the probability of finding a plate-like particle at a position **r** from the center of gravity of any particle:

$$g(r) = \frac{1}{4\pi r^2 N_p \rho} \left\langle \sum_{i=1}^{N_p} \sum_{j\neq i}^{N_p} \delta(r - r_{ij}) \right\rangle \tag{3.2}$$

where the bracket $\langle . \rangle$ denotes an ensemble average, N_p the number of particles, ρ the mean density, r_{ij} the distance between the centers of gravity of particles i and j, and δ the Dirac delta function. A value below 1 corresponds to a depletion zone, whereas $g(r) > 1$ corresponds to an elevated probability of finding a particle.

In the Fourier space, the density-density correlation is defined as [15]:

$$S_L(\boldsymbol{q}) = \sum_{i=1}^{N_p} \sum_{j=1}^{N_p} \langle\ exp\left[-i\boldsymbol{q} \cdot \mathbf{r}_{ij}\right]\ \rangle \tag{3.3}$$

where $\boldsymbol{q}$ stands for the incident scattering vector, $\mathbf{r}_{ij} = \mathbf{r}_j - \mathbf{r}_i$, and the subscript L refers to the system size, *i.e.*, a three dimensional simulation box of length L and volume L^3. Due to the finite size of the system and its periodicity, the microscopic density is enforced to be a periodic function. Thus, the values of admissible $\boldsymbol{q}$ must be commensurate with the box length, corresponding to the periodicity of the system [39] and can be defined as:

$$\boldsymbol{q} = \frac{2\pi}{L}(n_x, n_y, n_z) \tag{3.4}$$

where n_x, n_y and n_z are any integers. It is important to stress that any vector $\|\boldsymbol{q}\|$ smaller than $2\pi/L$ is unphysical. The static structure factor will often be represented as a function of the modulus $q = \|\boldsymbol{q}\|$ to provide information concerning the arrangement of percolated structures and glassy states. The static structure factor allows knowing the position of the first neighbor and the limit of q going to 0 reflects the compressibility of the system: if $\lim\limits_{q\to 0} S_L(q) = \rho k_b T \chi_T$ where ρ is the number density and χ_T the isothermal compressibility [15]. One should be aware of the fact that due to the relatively small number of particles simulated and the small box size, the function $S_L(q)$ could sometimes appears to be sampled too coarsely at low scattering vector. The only way to improve this is to increase the size of the box. However, increasing the latter while keeping the volume fraction constant increases the number of particles and, consequently, the computing cost. Moreover, the far-field hydrodynamic interactions are computed by FFT on a grid with $64 \times 64 \times 64$ nodes, and these numbers must be powers of two, increasing the volume of the box by 20% requires doubling the mesh size, which is extremely computationally demanding. As mentioned in section 1.3, some calculations were carried out with twice as many particles while keeping the volume fraction constant to be sure that we are able to capture the correct behavior with 60 particles.

The incoherent (one particle) part of the intermediate scattering function $F(\boldsymbol{q}, t, t_w)$ is the time correlation function of the density in the Fourier space:

$$F_L(\boldsymbol{q}, t) = \sum_{i=1}^{N_p} \langle\, exp\,[-i\boldsymbol{q} \cdot (\mathbf{r}_i(t + t_w) - \mathbf{r}_i(t_w))\,]\,\rangle \tag{3.5}$$

where t and t_w are respectively the time and the waiting time. The latter corresponds to the aging time at which the intermediate scattering function starts to be computed. This function provides information concerning the dynamic behavior of the particles. When particles can move freely, the position of the particles will progressively lose correlation with their initial positions: $\lim\limits_{t\to\infty} F_L \to 0$, the system is considered as ergodic. From a statistical point of view, the system is ergodic if the time average correlation functions are equal to their ensemble-averaged values. The aging time needed experimentally for suspensions of Laponite to reach the ergodic regime varies from hours to months or even years, depending on the volume fraction and the ionic strength. Although we are working at higher concentrations compared to experiments, we do not expect to be able to reach an ergodic state and, therefore, to evaluate the ergodicity breaking time. Despite the fact our simulations are short compared to experiments, we are able to capture similar qualitative behaviors as the one obtained experimentally for both gels and glasses by Jabbari and coworkers [18, 20], Ruzicka et al. [33] and numerically using Brownian dynamics by Mossa and coworkers [29].

The orientational correlation function is represented by the average of the second Legendre polynomial of the azimuthal angle θ between the normals of two plate-like particles. Thus, $cos(\theta) = \mathbf{n}_i \cdot \mathbf{n}_j$, where $\mathbf{n}_i$ and $\mathbf{n}_j$ are the normal vectors of particles i and j. Then, the orientational distribution function is defined as:

$$P_2(r) = \left\langle \frac{1}{2}\left(3cos^2\,\theta(r) - 1\right) \right\rangle. \tag{3.6}$$

When $P_2(r) = -1/2$ the particles are perpendicular while $P_2(r) = 1$ refers to parallel particles. The combination of the radial distribution and orientation pair distribution functions provides a good insight into the microstructure of the system. Nevertheless, these functions do not furnish any information concerning the formation of a gel state, or any percolated structure.

We introduced a criterion of distance to determine when two particles are connected and form a cluster: if the gap between two spheres of distinct plate-like particles is less than $0.2\ a$, where a is the radius of one sphere, the particles are considered in contact. It is interesting to compute the mean azimuthal angle $< \theta >$ defined previously for the second Legendre polynomial function between touching particles. This allows investigating the possible correlation between this angle and the position of the contact relative to the center of gravity of the particles. The distance between the contact point in red in Figure 3.8 and the center of gravity of the particle will be referred to as the "touching distance". This combination of both the angle and the touching distance allows a complete insight into the spatial arrangement between particles in contact.

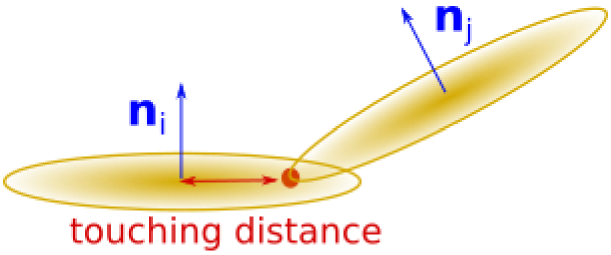

Figure 3.8: Definition of the touching distance between two disk-shaped particles. The red point corresponds to the contact point, and the touching distance is defined as the distance between the center of gravity of particle i and the contact point.

Other useful quantities are the size and number of aggregates, which are computed using the criterion of distance mentioned above. We present some snapshots of the obtained structure, where particles belonging to the same cluster will be represented using the same color (see Figure 3.9). A particle without any contact will be colored in white, as pointed out by the red circle in Figure 3.9.

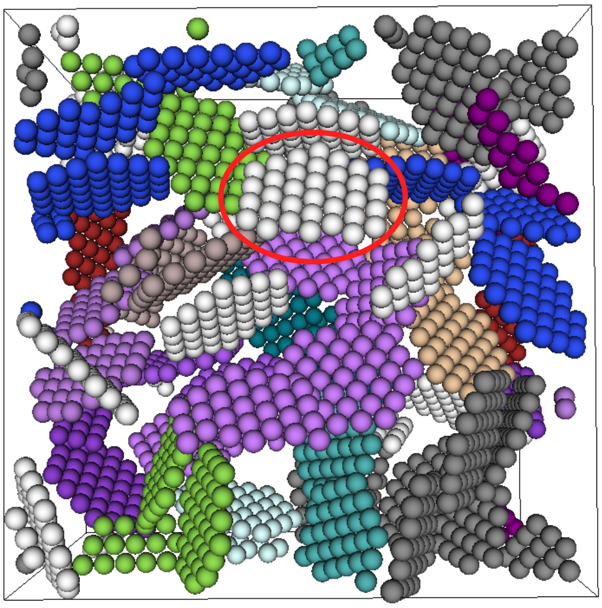

Figure 3.9: Example of a snapshot of the microstructure. Each color represents a cluster except for the white color which represents particles without contact (see the particle in the red circle).

The number of neighbors of a particle belonging to a cluster is also called the coordination number, and is simply equal to its number of contacts with distinct particles. Based on the criterion of distance previously mentioned, we can calculate the average number of neighbors for a platelet in a cluster $< N_{nei} >$, which varies in the present simulations from zero (no connection) to four. One should notice the similarity of our coordination number with the model used by Ruzicka and coworkers, where the valence number is equal to five. We can also compute the average number of platelets in a cluster $< N_p^{cl} >$ and the number of clusters N_{cl}. These parameters provide a good insight into the dynamics of the formation of the clusters. It is possible to measure $N(t)/N_0$ with N_0 the initial number of individual particles and $N(t)$ the number of distinct entities (a cluster of disks is defined as a unique entity) at time t:

$$\frac{N(t)}{N_0} = 1 + \frac{N_{cl}\left(1 - < N_p^{cl} >\right)}{N_0} \tag{3.7}$$

At $t = 0$, the value is equal to 1 and decreases to $1/N_0$ if all the particles are in the same cluster. With these pieces of information at hand, we will be able to quantify and compare the kinetics of aggregation as a function of the volume fraction and the range of electrostatic interactions. This is one of the topics of the last chapter.

Finally, to investigate the transition from an isotropic to a nematic state we track the evolution of the nematic order parameter S_{nem} defined as the largest eigenvalue of the second rank tensor $\boldsymbol{Q}_{\alpha\beta}$:

$$\boldsymbol{Q}_{\alpha\beta} = \frac{1}{N_p}\sum_{i=1}^{N_p}\frac{1}{2}\left(3n_\alpha^i n_\beta^i - \delta_{\alpha\beta}\right) \tag{3.8}$$

When the nematic order parameter is greater than 0.4, the suspension is considered to be in a nematic phase, while below 0.4 it is considered to be isotropic. The eigenvector corresponding to the largest eigenvalue of $\boldsymbol{Q}_{\alpha\beta}$ is the director $\hat{\mathbf{n}}$ and characterizes the dominant orientation of the particles. The nematic order parameter S_{nem} is also used as a convergence parameter: when it stops fluctuating, the suspension has reached an arrested state that can correspond to a thermodynamic equilibrium or not.

2 Equilibrium structure

We have seen in chapter 1 that the final microstructure of a suspension of particles with both shape and charge anisotropy depends on the range of electrostatic interactions (ionic strength) and the volume fraction. Ionic strength is often used as an axis in a phase diagram, but it is not so well adapted to compare different results as it sets the interaction range, which should be compared to any other length scale of the system. That is why instead of using the ionic strength, results will be presented as a function of the non-dimensional number κD involving the inverse of the Debye length κ and the diameter of a particle D. The values of κD studied are $\kappa D = [1.46;\ 7.3;\ 14.6;\ 29.2;\ 44;\ 73]$ and the volume fractions are $\phi = [0.05;\ 0.075;\ 0.10;\ 0.124]$. The statistical measured quantities used to compare the different structures are averaged over the last 25 time units of the simulation.

We stress once again that we simulate clay-like particles with a different aspect ratio than Laponite, so some discrepancy can be expected relative to experimental results. Nevertheless, as the ratio between the Brownian force and the electrostatic force is preserved, the clay-like particles simulated in the current study allow reproducing a phase diagram (see Figure 3.10) similar to those obtained in experiments. In Figure 3.10 one can observe four different phases: **A**-repulsive glass, **B**-phase separation, **C**-equilibrium gel, **D**-liquid-like structure. The full description of the phase diagram is developed and compared with the literature (see section 1.2) following the qualitative terms: long-range, intermediate-range, and short-range electrostatic interactions. These qualitative terms are based on the size of the Debye length relative to the mean distance between the surfaces of the particles. The latter is measured at the beginning of the simulation and varies from $0.14\ R$ at $\phi = 0.124$ to $0.28\ R$ at $\phi = 0.05$. When the double layers of the particles fully overlap and also include their center of gravity, the interaction is considered as long-ranged, and corresponds to the first line of the phase diagram, *i.e.*, $\kappa D = 1.46$. When the double layers overlap but do not include the center of gravity of the particles, interactions are considered as intermediate-ranged and are found in the second line, $\kappa D = 7.3$. Finally, when the double layers do not superimpose on average, such that displacement due to the Brownian motion is necessary to cause the overlapping of the double layers, the interaction is referred to as short-ranged. This corresponds to the cases $\kappa D = [14.6;\ 29.2;\ 44;\ 73]$.

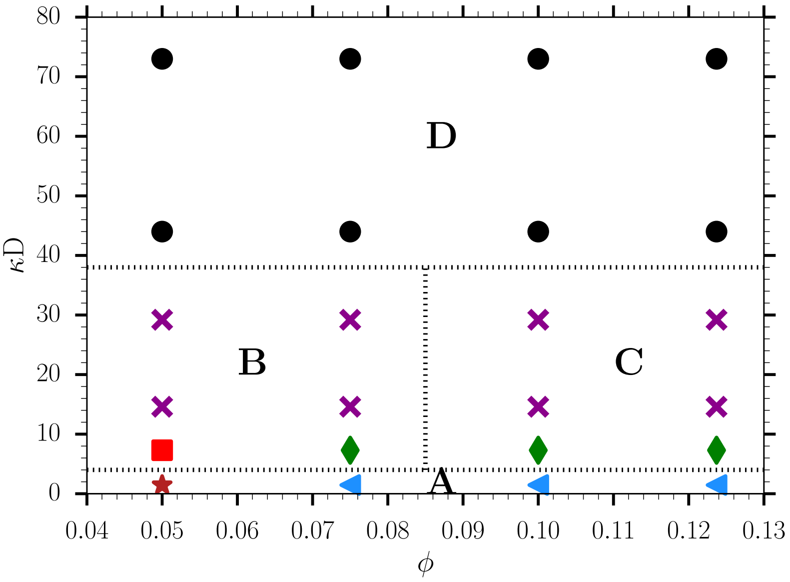

Figure 3.10: Phase diagram proposition: **A**-repulsive glass, **B**-phase separation, **C**-equilibrium gel, **D**-liquid-like structure. The brick-colored star (the lowest κD point at $\phi = 0.05$) represents a classic Wigner glass, the blue triangles a repulsive structure with particles in contact with overlapping coin configurations, the red square a structure with particles mainly in an overlapping coin configuration, the green diamonds for particles in both overlapping coin and house of card configuration, the purple crosses stand for HOC configuration, and finally the black filled circles a liquid-like phase.

2.1 Long-range electrostatic interactions

Long-range electrostatic interactions are obtained experimentally when no salt is added to colloidal suspensions. Then, the screening of the charges is only due to the counterions released by the colloids and therefore depends on the volume fraction. As Laponite is highly charged, the number of counterions released is important enough to prevent the electrostatic interaction range from being several times the radius of the particle unless the suspension is dialyzed. In such conditions, a solid-like structure is observed experimentally for different ranges of interaction, concentration, and aging. The dynamical route followed by the suspension to reach its final arrested state was widely studied by Jabbari and coworkers [18, 19, 20], Ruzicka et al. [33, 34] and Angelini and coworkers [4]. To increase the range of interactions in experiments, Levitz and coworkers [26] added ion exchange resins to their suspension of Laponite to reduce the ionic strength and therefore increase the interaction range, which also led to the appearance of a soft solid-like phase, the Wigner glass, at low volume fraction instead of a phase separation commonly observed at sufficiently low volume fraction ($< \phi = 0.4\%$). Our simulations are carried in the same interaction range as the experiments of Levitz, as the long-range electrostatic interaction ($\kappa D = 1.46$) corresponds to a screening length equivalent to 1.37 times the radius of the particle. Consequently, the double layers strongly overlap.

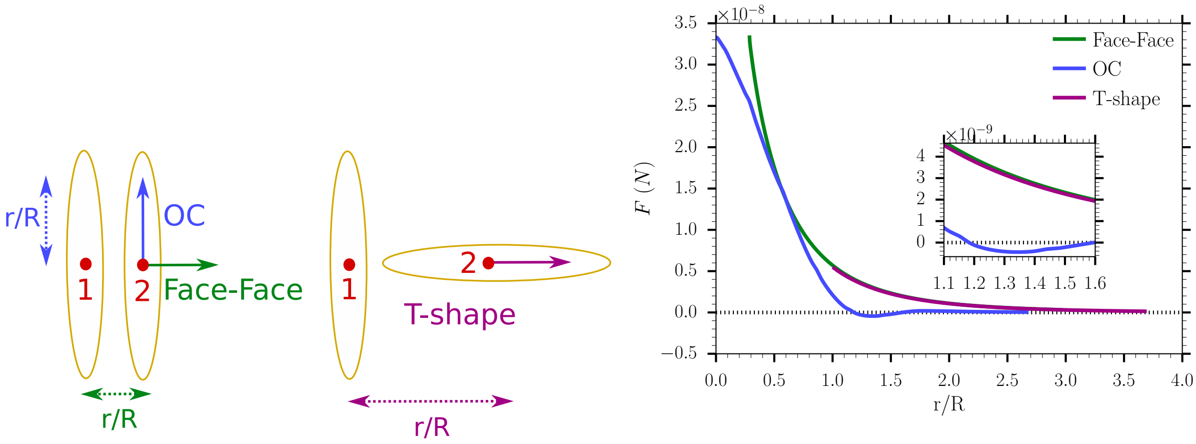

(a) Spatial configurations

(b) Electrostatic Force

Figure 3.11: Electrostatic forces on a plate-like particle as a function of the distance between the centers of gravity, at $\kappa D = 1.46$, for three different spatial configurations: T-shape (purple color), face-face (green color), and OC (blue color). The inset is simply a zoom to distances where some attractions occur.

To provide an idea of the forces between particles, let us consider two $AR7$ particles in a face-face configuration (see the left configuration in Figure 3.11a) and in a T-shape configuration (see the right configuration in Figure 3.11a). In Figure 3.11a, the red points correspond to the center of gravity of particles 1 and 2, and the arrows plotted with a full line correspond to the direction of the displacements considered. Starting from the initial face-face configuration, if the particle 2 moves toward the direction represented with the blue arrow, the configuration is referred to as OC configuration, while a displacement toward the green arrow is referred to as a face-face configuration. The center to center distances are referred to as r/R and therefore are different for each of the three spatial configurations studied. The normal forces to the particle 1 are reported in Figure 3.11b as a function of the distance r/R with the second particle. A positive value of the force stands for a repulsive behavior (pushing outward and increasing r if unrestrained) while a negative value means that particles are attracted one to the other. One can see that for both the T-shape and the face-face configuration the system of two $AR7$ particles is purely repulsive. Concerning the OC configuration, for $r/R < 1.2$ particles are repulsive, then become attractive for $1.2 < r/R < 1.55$ and repulsive at larger distances. The system of two interacting particle is mainly repulsive but a narrow attraction field exists for the OC configuration. To reach this attractive state, the system must overcome the small energy barrier corresponding to repulsive forces at distance larger than $r/R = 1.55$. Therefore we could expect this attractive configuration to be favored for dense systems where particles are crowded to a short distance from one another. Obviously these pair forces are just a first approach to be able to understand more complex systems.

As explained in paragraph 1.4, the nematic order parameter is used as a criterion of convergence: when this parameter reaches a plateau, the microstructure is assumed to be at equilibrium. The evolution of the nematic order parameter is reported in Figure 3.12. Note the tremendous difference of the nematic order parameter at the two extremes concentration: $S_{nem}(\phi = 0.05)$ and $S_{nem}(\phi = 0.124)$. At the lowest concentration, the system is nematic, $S_{nem}(\phi = 0.05) > 0.4$. After having reached a first plateau ranging from 3 to 10 units of non-dimensional time, the system slowly evolves toward a nematic state. This slow organization is undoubtedly due to the strong electrostatic interactions creating local cages, and therefore drastically slowing down the system. To be certain of the final state, we have extended the calculation for $\phi = 0.05$ up to 66 units of non-dimensional time. The value of the nematic order does not appear to evolve anymore and slightly oscillates around $S_{nem} = 0.5$. At intermediate concentrations, the nematic order parameters reach a plateau with similar values for $\phi = 0.075$ and $\phi = 0.10$ indicating the same degree of order. At the highest volume fraction, the system is isotropic and exhibits the lowest final value. Quite surprisingly, the nematic order parameter is not a monotonic function of the volume fraction and does not exhibit a sigmoid shape as it is commonly observed [11]. This sigmoid shape is normally due to crowding effects, and we can wonder if the face-rim attraction occurring at short distance and for OC configurations prevents the isotropic to nematic transition (see Figure 3.11b)

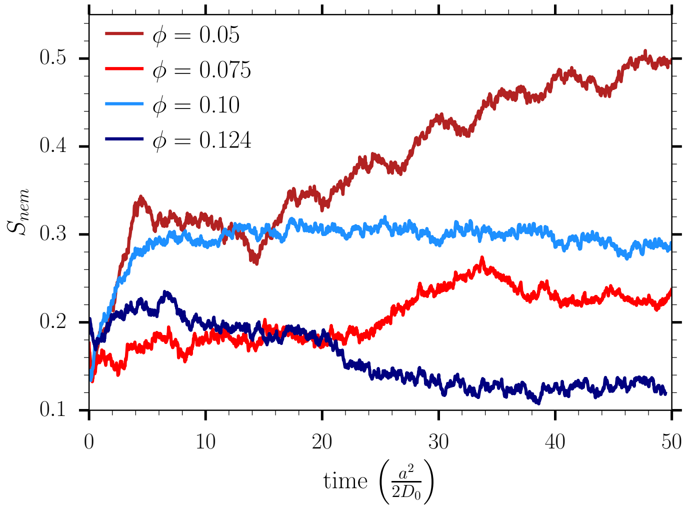

Figure 3.12: Evolution of the nematic order parameter as a function of the non-dimensional time for $\kappa D = 1.46$.

The evolution of the system towards an arrested state is particularly noticeable on the incoherent intermediate scattering function reported in Figure 3.13 for $\phi = 0.124$. We have chosen the smallest accessible scattering vector, *i.e.* $q = 2\pi/L$ with L the length of the cubic box, and $F(q, t, tw)$ was plotted for four different waiting time t_w. One should notice that the value of F never relaxes significantly on the available time window. Therefore, the ergodicity breaking time cannot be estimated even if it seems almost instantaneous in our conditions of simulation. However, it seems clear that the system has evolved towards a non-ergodic, arrested state. The same dynamical behavior is observed for lower volume fractions but the curves are not reported here.

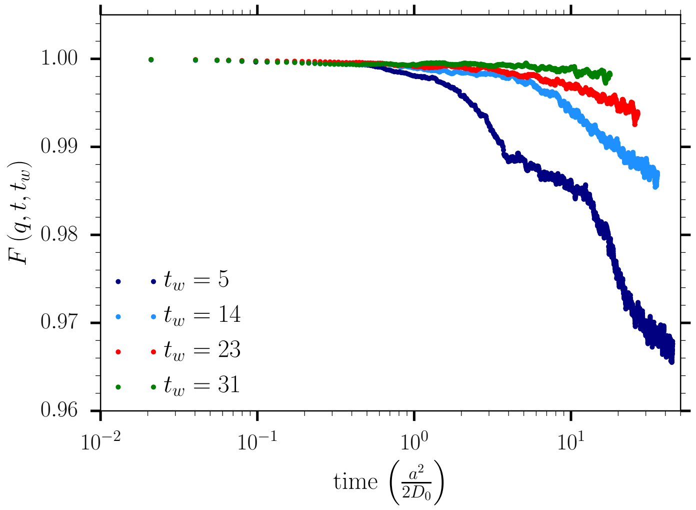

Figure 3.13: Incoherent (one particle) intermediate scattering function for $\phi = 0.124$ and $\kappa D = 1.46$. The term t_w stands for the waiting time in non-dimensional time units.

Several methods exist to determine if the system has evolved toward a glass or a gel. One can cite for instance the method which consists in fitting the intermediate scattering function with a sum of a fast decaying exponential and a stretched exponential [19, 20, 29]. When the ratio τ_2/τ_1 of the characteristic time τ_2 (stretched exponential) with the characteristic time τ_1 (fast decaying exponential) remains constant over at least half of the ergodicity breaking time, the system has evolved toward a glass. In contrast, an increase of the ratio means the system evolves toward a gel [20]. As we are not able to predict the ergodicity breaking time in the present work, this method is not adapted. We will instead study the evolution of the translational short-time diffusion coefficient as a function of the waiting time. Jabbari and coworkers [20] observed that the translational short-time diffusion coefficient D_s was remaining approximately constant and equals to its initial value $D_{s,0}$ ($0.7 < D_s/D_{s,0} < 1$). This behavior is referred to as the "rattling in the cage". Concerning the structures evolving toward a gel, Jabbari et al. observed a decrease of $D_s/D_{s,0}$ with the aging times. Values of $D_s/D_{s,0} < 0.6$ are observed close to the ergodicity breaking time. In this case, the reduction of the diffusion is induced by the development of a gel network.

Although both the translational perpendicular and parallel diffusion coefficients in infinitely dilute suspension have almost the same value, we have decided to study separately their evolutions with the waiting time. Indeed, due to the strong charge anisotropy, we could expect different behaviors concerning the displacements parallel and perpendicular to the normal of the particle (vector **n** in Figure 3.8). The parallel and perpendicular short-time translational diffusion coefficients in the absence of interparticle interactions are respectively equals to $D_{(\perp,0)}/D_0 \approx 1.72\ 10^{-1}$ and $D_{(\parallel,0)}/D_0 \approx 1.75\ 10^{-1}$ (see Table 2.2) where D_0 is the diffusion coefficient of non interacting sphere of radius $0.137\ R$. In the present study, we do not have access to the short-time self diffusion defined as $k_bT < \mathcal{M}_{11} >$ all along the simulations.

We have computed instead both the translational parallel and perpendicular mean square displacements[1] of the platelets over a certain time-window. Then, we have calculated the slope of these mean square displacements at short-time which will be referred to as the diffusion coefficients of the particles. These coefficients are reported in Figure 3.14 as a function of the waiting time. The coefficients at the beginning of the simulations, $t_w = 0$, are not reported, because the strong long-range electrostatic interactions were generating "diffusion" 20 times larger than the diffusion of the particle without interaction. One can observe parallel diffusion coefficients (filled symbols) almost constant with the waiting time. Concerning the perpendicular coefficients (empty symbols), they seem to slightly decrease with the waiting time for the two higher volume fractions. However, one can wonder if this decrease could not be due to the fact that at high volume fraction, the motions parallel to the direction vector could be inhibited by the electrostatic forces. In contrast, motions perpendicular to the direction vector are less constrained. Although a slight decrease is observed for the perpendicular diffusion coefficient at high volume fraction with the waiting time, the diffusion coefficients remain close to their infinitely dilute values. Following the criterion from Jabbari and coworkers [20], as $D/D_0 > 0.6$ for all volume fractions, the structures observed with long-range interactions are glasses.

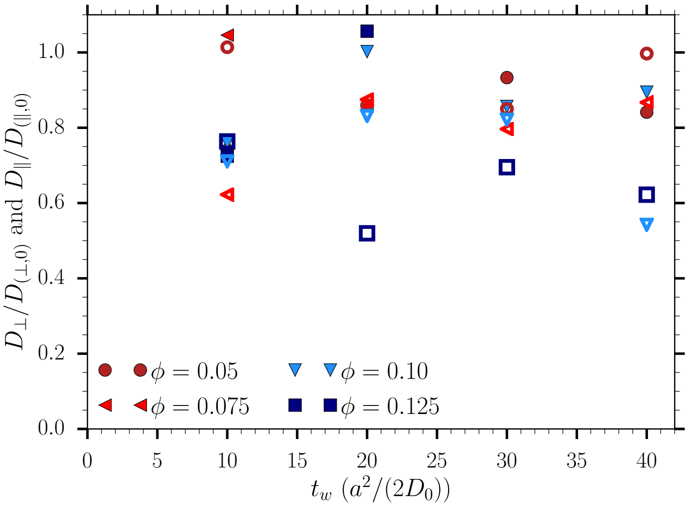

Figure 3.14: Evolution of the parallel (empty symbols) and perpendicular (filled symbols) diffusion coefficient normalized to its infinitely dilute value, ($D_{(\perp,0)}$ and $D_{(\parallel,0)}$), at $\kappa D = 1.46$.

Among these glass structures, two different final arrested states are observed: a disconnected structure corresponding to a classic Wigner glass at $\phi = 0.05$ and a system highly compressed with interconnected structure at higher concentration (see Figure 3.10). Then, the study is divided into two parts, each one leading to a distinct structure.

2.1.1 Classic Wigner glass

In Figure 3.15 is reported the snapshot at $\phi = 0.05$ at the end of the simulation. Considering this snapshot along with observation of the dynamics, one can clearly notice a classic Wigner glass: particles

---

[1] the displacements include the effects of hydrodynamics, electrostatics and thermal fluctuations.

are disconnected and seem trapped in electrostatic cages. Indeed, at low volume fraction, the free volume per particle particle is important enough to allow particles to remain far away from one to another, and no contact between particles was observed.

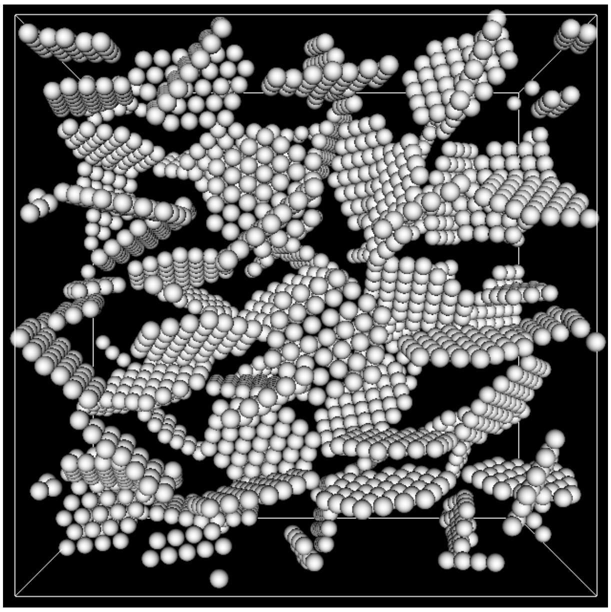

Figure 3.15: Snapshot of the microstructure at equilibrium for $\phi = 0.05$ at long-range of interactions.

Analyzing both the radial and angle distribution functions presented in Figure 3.16 provides a good insight into the microstructure. The maximal peak of the radial distribution function is reached between 2.27 R and 2.43 R. Over this range of distance, one can observe in Figure 3.16b that the orientational correlation function exhibits a kind of plateau at $P_2(r) = 0.43$ indicating that a proportion of the particles are nearly parallel to each other. Note also the peak of the orientational correlation at 1.9 R indicating again the preferential parallel orientation of the particles. Broadly speaking, the particles are disconnected and an important proportion of them are parallel one to another.

We hypothesize that the particles are jammed in a kind of electrostatic cage as classically observed for a Wigner glass. To verify this assumption, we have reported in Figure 3.17 the mean square displacement over the last five units of non-dimensional time. The dotted curve in Figure 3.17 corresponds to the diffusion of non-interacting particles, and was taken equal to $D/D_0 = \left(D_{(\|,0)} + D_{(\perp,0)}\right)/(2D_0)$. One can clearly notice that the diffusion of the particles at a short time is similar to D/D_0 and decreases at a longer time, indicating a caging effect. One should remark that the translational perpendicular diffusion seems less impacted by the caging effect than the parallel coefficient. Remember that at this volume fraction, the closest particles are mainly parallel, so motions parallel to the normal vector are expected to be inhibited by the electrostatic forces, while motions perpendicular to the direction vector are less constrained.

Finally, we have reported in Figure 3.18 the static structure factor for different time windows. Firstly, note that the static structure factor does not evolve with the increase of the "aging" time. This result is in agreement with the assumption of a non-ergodic arrested state within the available simulation time window. The low q behavior indicates that the system has a low compressibility. The first peak corresponds

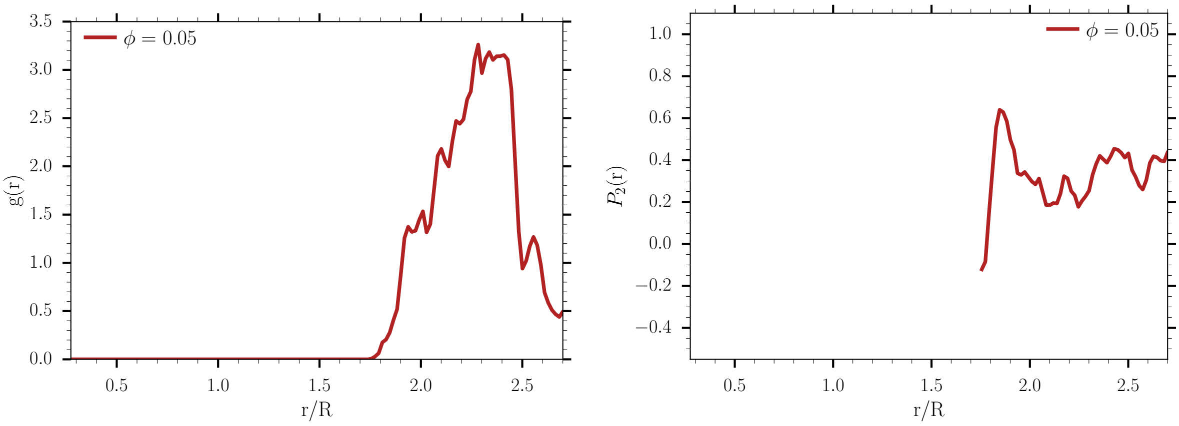

(a) Radial distribution function (b) Angular correlation function

Figure 3.16: Center of mass radial distribution (left) and second Legendre polynomial function (right) for $\phi = 0.05$ and $\kappa D = 1.46$.

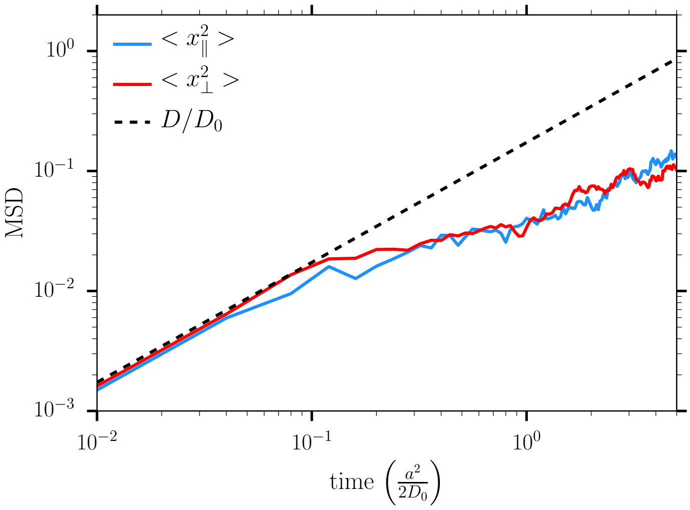

Figure 3.17: Mean square displacement of particles at $\phi = 0.05$, $< x_{\perp}^2 >$ and $< x_{\parallel}^2 >$ stand for respectively the perpendicular and parallel translational mean square displacement.

to the position of the nearest neighbor and reaches a value of $S_L \approx 2.6$, a value indicating the suspension is almost frozen according to the empirical Hansen-Verlet rule ($S_{L,max} \sim 3.2$ for a spherical suspension; see *e.g.* [16, 17] and references therein for a discussion of this criterion for Yukawa spheres).

Owing to all the pieces of information cited above, we can conclude that a classic Wigner glass forms at the lowest volume fraction and for long-range interaction, *i.e.*, for $\phi = 0.05$ and $\kappa D = 1.46$. This result is in line with experimental results, where a classic Wigner glass was observed at low volume fraction and very long-range interactions by Levitz et al. [26], or for volume fractions larger than $\phi = 0.008$ equivalent to $C_w = 2\%$ and smaller ionic strength by Ruzicka and coworkers [32] and Jabbari et al. [20].

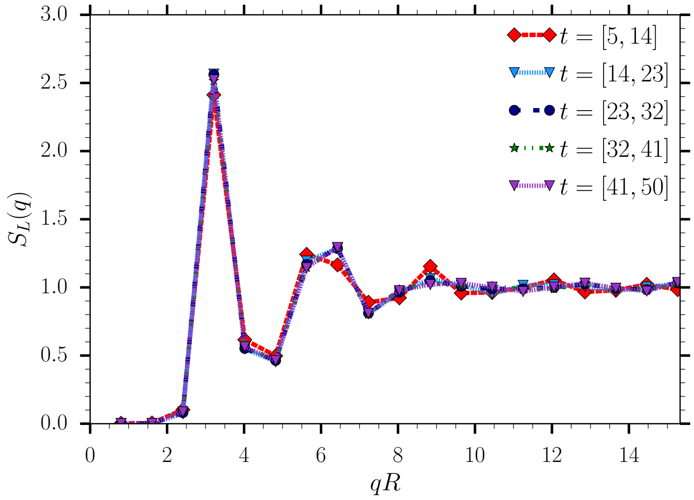

Figure 3.18: Static structure factor at $\phi = 0.05$ and $\kappa D = 1.46$, computed over different time windows.

2.1.2 Repulsive glass with particles in overlapping coin configuration

We have reported the final structures obtained at $\phi = 0.075$, 0.10 and 0.124 in Figure 3.19. One can notice that the compression of the Wigner glass obtained at $\phi = 0.05$ leads to a higher number of contacts between particles as the volume fraction increases. At $\phi = 0.075$, the particles seem to minimize the bulk energy by forming small clusters and frequently adopting OC configurations (see the two particles in olive color on the center in Figure 3.19a). At $\phi = 0.10$ and 0.124, most of the particles are interconnected, and at the highest volume fraction for instance, one can only observe three different clusters (light blue, purple, and green) and two isolated particles (in white in Figure 3.19c).

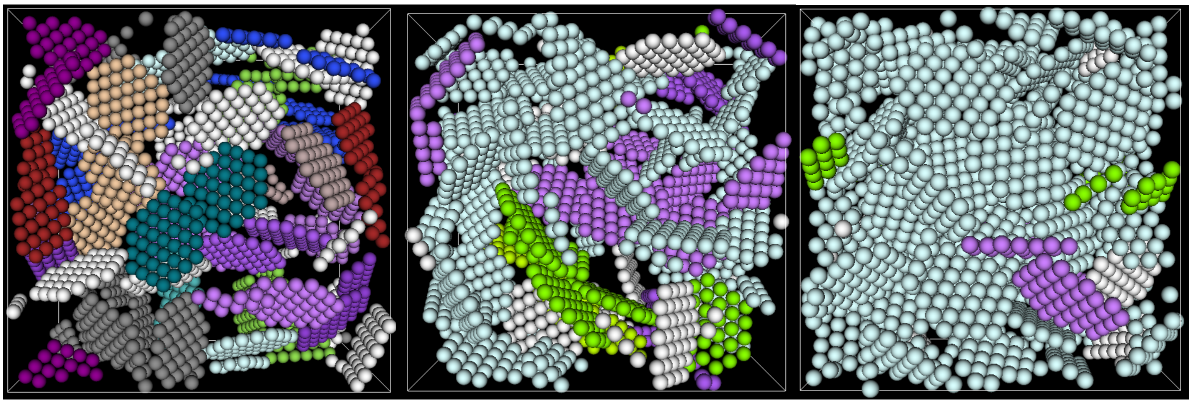
(a) $\phi = 0.075$ (b) $\phi = 0.10$ (c) $\phi = 0.124$

Figure 3.19: Snapshot of the microstructure at equilibrium for $\phi = 0.075$, 0.10 and 0.124 at $\kappa D = 1.46$.

The observation of contacts for long-range interactions is not surprising. Indeed, Ruzicka and coworkers [34] observed the development of long-range and long time attractions for a suspension of Laponite at fixed concentration of salt $C_s = 10^{-1}$ mM equivalent to $\kappa D = 3$, and a concentration of $C_w = 2.4\%$. These authors considered that despite the long-range attractions, particles were still disconnected. Such an assumption has led to the study by Angelini et al. [4], where the authors called the obtained structure Disconnected House of Card (DHOC, see section 1.2). However, we want to expose a different point of view based on our numerical results: we think that the aging phenomenon does not preserve the disconnected structure of the repulsive glass. Indeed, the structure factor obtained by Ruzicka and coworkers exhibits a peak at $q \approx 0.18\ \mathrm{nm}^{-1}$ corresponding to a distance of $1.40\ R$, with $R = 25$ nm, which could be due to particles in OC configuration, as shown later in this section. This assumption could explain the strengthening of the glass and the fact that no rejuvenation was observed.

Let us go back to the present simulations. Note the vanishing value of the static structure factor reported in Figure 3.20 for low scattering vectors. As for $\phi = 0.05$, the static structure factors do not evolve with time (not shown here). Such behaviors indicate that the systems evolved toward an arrested state with a vanishing compressibility. These observations are in line with the assumption of a glass structure as mentioned before. Therefore, we will call it a glass with contacts.

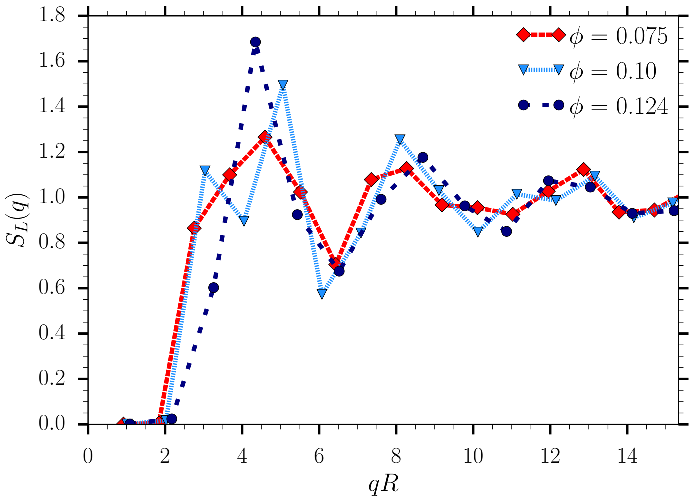

Figure 3.20: Static structure factor for $\phi = 0.075$, 0.10 and 0.124 and $\kappa D = 1.46$.

Let us now characterize the contacts observed for $\phi = 0.075$, 0.10 and 0.125. In Figure 3.21a, one can clearly notice that increasing the volume fraction above 0.05 shifts drastically the peak of the radial distribution to lower values. Most of the particles are at a distance equal to $r/R \approx 1.5$ to their neighbors. The intensity of the peak increases and is slightly shifted to lower values with the increase of volume fraction. This could presumably be attributed to an aggregation effect. If one considers the radial distribution functions of the particles in contact (see Figure 3.21b), they exhibit a peak at $1.5R$ with an intensity several times lower than the usual $g(r)$ (see Figure 3.21a) indicating that only a small fraction of the particles located at this distance are in contact. A brief discussion concerning the classic evolution of the peak as a function of the volume fraction is reported in Appendix 2.

The angular correlation functions are reported in Figure 3.22 for all the particles on the left-hand side figure, and only for particles in contact on the right-hand side figure. Concerning the larger peak intensity observed a distance $r = 1.5R$ in Figure 3.22a, note that it slightly decreases as the volume fraction increases indicating multiple configuration angles for isolated particles. In contrast, $P_2(r)$ seems

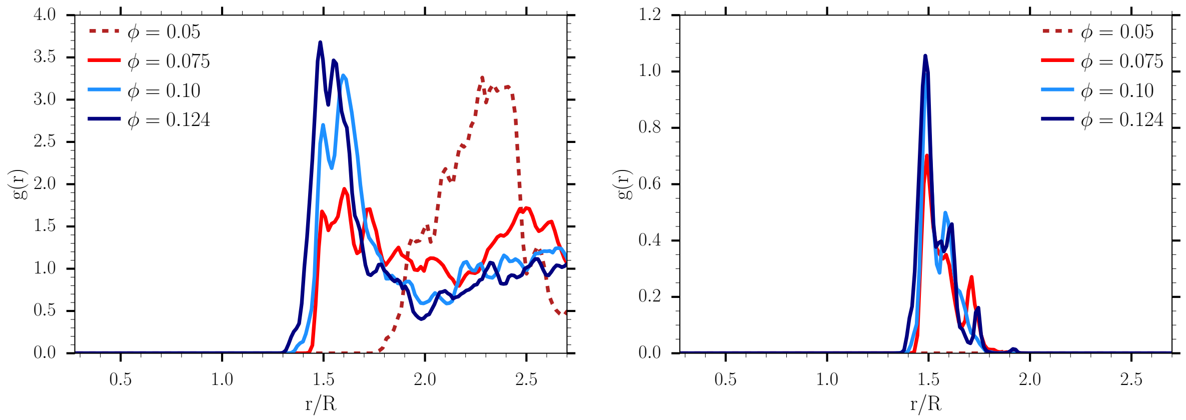

(a) Radial distribution function

(b) Radial distribution function of particles in contact

Figure 3.21: Center of mass radial distribution for the totality of the particles (left) and only for touching particles (right) for long-range electrostatic interactions: $\kappa D = 1.46$.

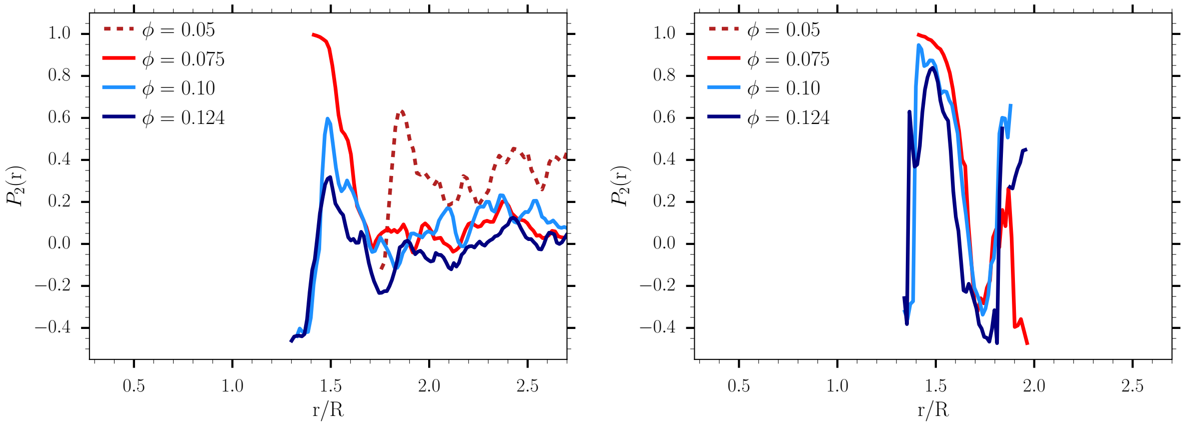

(a) Angular correlation function

(b) Angular correlation function of particles in contact

Figure 3.22: Second Legendre polynomial function for all the particles (left) and only for particles in contact (right) for long-range electrostatic interactions, $\kappa D = 1.46$.

independent of the volume fraction for particles in contact (see Figure 3.22b) which are in OC configuration, in line with the low energy state expected for OC configuration at this distance (see Figure 3.11b). Concerning the orientation of closest particles ($P_2(r_{min})$ in Figure 3.22a), they are parallel to one another for $\phi = 0.075$, while almost perpendicular for higher volume fraction. As these negative values of $P_2(r_{min})$ for touching particles disappear, we can assume that the small number of particles forming the T-shape are disconnected. Such a structure appears very similar to the structure described by Angelini and coworkers as Disconnected House Of Card (DHOC) [4].

The mean square displacements are reported in Figure 3.23 to provide an idea of the dynamics of the system. As already discussed in section 2.1, the perpendicular diffusion coefficient is similar to its value for an infinitely dilute particle. In contrast, the parallel coefficients are slightly lower than their infinitely dilute value. This is consistent with the OC structures observed whose displacements toward parallel directions to their normal vector are drastically slowed by the electrostatic attractions.

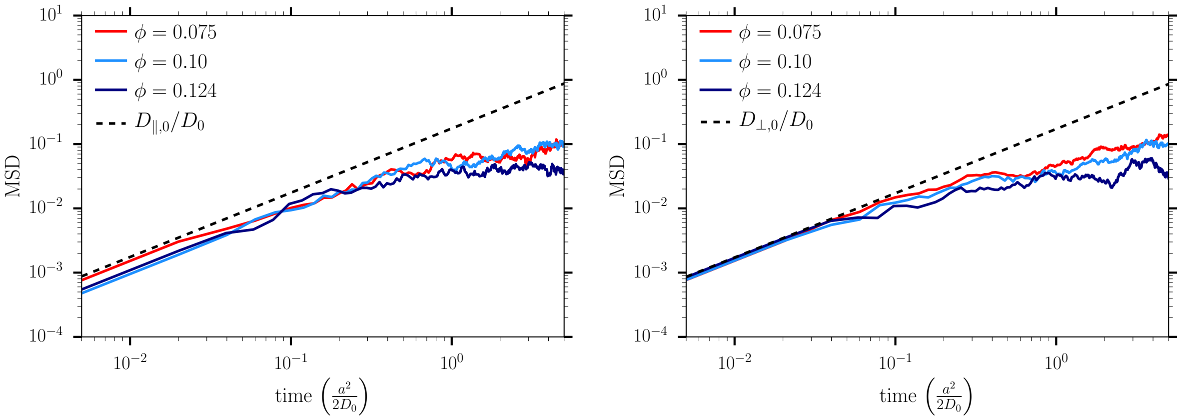

(a) MSD $< x_\perp^2 >$

(b) MSD $< x_\parallel^2 >$

Figure 3.23: Mean square displacement computed for particles with long-range interactions, $\kappa D = 1.46$.

2.1.3 Summary

For suspensions of clay-like particles with long-range electrostatic interactions, two different structures have been reported. The first one concerns the most dilute system simulated, *i.e.* $\phi = 0.05$, where a classic Wigner glass was observed: the particles are disconnected and trapped in a local energy minimums corresponding to an electrostatic cage (see Figure 3.24).

The second structure concerns volume fractions ranging from 0.075 to 0.124. At these concentrations, the free volume is not significant enough to allow the system to behave as a classic Wigner glass. Then, to minimize the total free energy of the system, particles form clusters through OC interactions. Delhorme and coworkers have observed in this range of volume fraction and for slightly shorter interaction range the formation of a smectic B phase for $AR15$ particles [10]. We could wonder if the systems simulated have reached their final spatial arrangement or if the OC configuration obtained here was the first step towards the formation of the smectic B phase. However, the incoherent structure factor seems to indicate that we already have reached an arrested state, and therefore we do not think that our system would be able to reach such a phase. As the translational perpendicular and parallel diffusion coefficients do not sharply decrease with the waiting time, the structures obtained can be considered as glasses with particles in OC configuration.

The organization of the present mainly repulsive disks into clusters highlights the importance of the charge anisotropy on the final microstructure. Indeed, Jabbari and coworkers [22] observed a plastic BCC crystal for purely repulsive particles at an equivalent density and low ionic strength. This phase cannot be reached by a suspension with strong charge anisotropy.

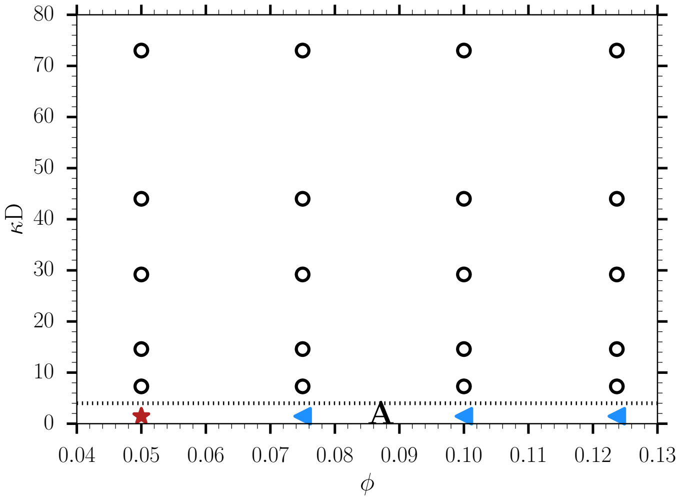

Figure 3.24: Construction of the phase diagram: the star represents a Wigner glass, the triangles a repulsive glass with overlapping coin configurations, and the circle the phases not studied yet.

2.2 Intermediate-range electrostatic interactions

We start this section by recalling that here "intermediate-range electrostatic interactions" stands for $\kappa D = 7.3$. This regime can be obtained in experiments by adding a small amount of salt to the suspension.

2.2.1 Qualitative observations of the structure

In Figure 3.25a can be seen the snapshot corresponding to the final structure at $\phi = 0.05$. Note that the majority of the particles are in an OC configuration. The particles are forming a kind of open structure with multiple layers. Once again, we could wonder if the final structure is reached or if the system could have evolved towards a smectic B phase as observed by Delhorme and coworkers [10]. These authors have considered salt concentrations corresponding to $13.93 < \kappa D < 14.65$. They found the smectic B structure at the same volume fraction, $\phi = 0.05$, the same Debye length, $\kappa^{-1} = 1$ nm but for particles with a higher aspect ratio ($AR15$). They have since studied the influence of the aspect ratio on the phases of the suspension and obtained the smectic B phase only for aspect ratios greater than 9 [11]. The particles studied here have a lower aspect ratio, but remember that we use a different surface charge distribution so the achieving of a smectic B phase at longer times cannot be completely ruled out. Increasing the volume fraction to 0.075 leads to the appearance of both the HOC and OC configurations, respectively encircled in yellow and in red in Figure 3.25b. Above $\phi = 0.075$, the structure is difficult to analyze with a simple snapshot as the latter totally spans the available space. Corresponding snapshots are therefore not reported here.

The previous qualitative observations are in line with the behavior of the electrostatic forces between two particles (see Figure 3.26). A strong attraction occurs for a pair of particles in OC configuration for distances ranging from 1.1 R to 1.6 R as shown in Figure 3.26. Over this range of distance, the T-shape

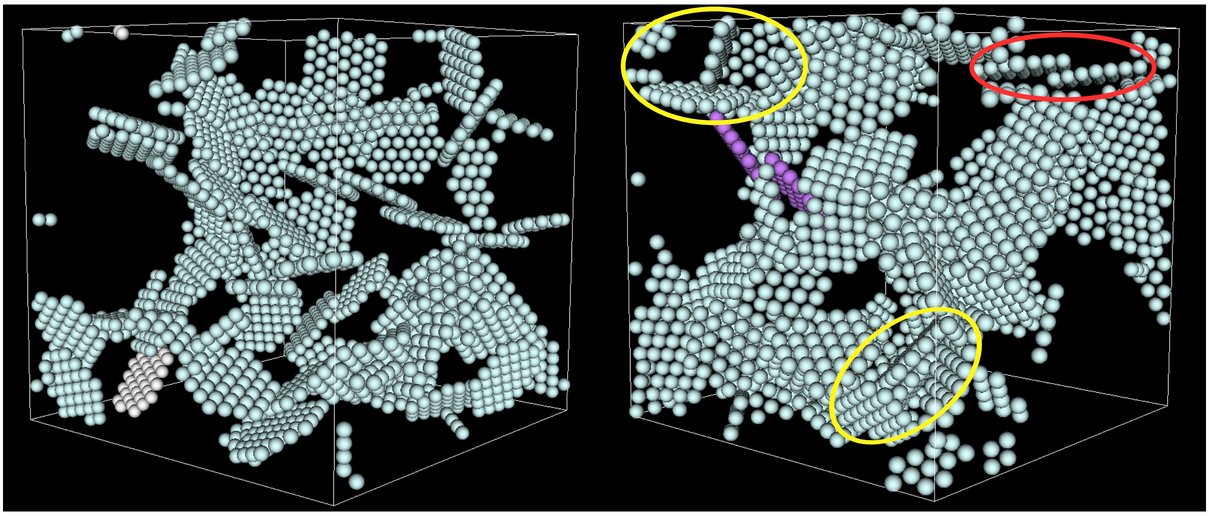

(a) $\phi = 0.05$ (b) $\phi = 0.075$

Figure 3.25: Snapshot of the microstructure at equilibrium for $\phi = 0.05$ and $\phi = 0.075$ at intermediate-range electrostatic interactions, $\kappa D = 7.46$. Example of particles in T-shape configuration encircled in yellow and particles in OC configuration encircled in red.

configuration is attractive but its intensity is 10 times smaller than for the OC configuration. Finally, the face-face configuration is always strongly repulsive, and therefore we do not expect to observe any stacking of particles in the present study. We recall that the definitions of the configurations are given in Figure 3.11a. We emphasize the fact that Figure 3.26 provides an overview of the favored structures in simulations, as only three very specific spatial configurations are studied.

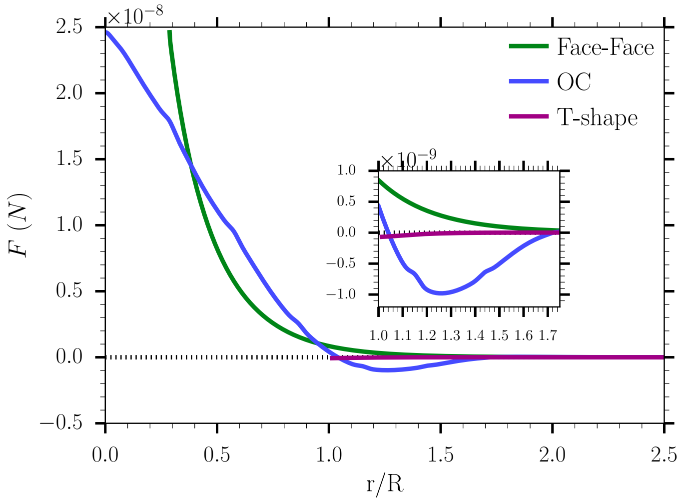

Figure 3.26: Electrostatic forces on a plate-like particle as a function of the distance between the centers of gravity, at $\kappa D = 7.3$, for three different spatial configurations: T-shape (purple color), face-face (green color), and OC (blue color) (see Figure 3.11a). The inset is simply a zoom to distances where attraction occurs.

As for the long-range case, the microstructure at the lowest volume fraction is slightly different from the one obtained for concentrated suspensions. However, in both cases, particles aggregate, and only the spatial configuration of the touching particles differs. Therefore, we have decided to describe the case of intermediate-range electrostatic interactions for all the volume fractions at once.

2.2.2 Study of the microstructure

The nematic order parameter is related to the dynamic of evolution of the microstructure: when it reaches a plateau, the microstructure has reached its final spatial arrangement. For the higher volume fractions, $\phi = 0.10$ and 0.124, S_{nem} behaves the same way, and quickly reaches a plateau which is also its final value, $S_{nem} \approx 0.15$ corresponding to an isotropic structure (see Figure 3.27). The reduction of the volume fraction to 0.075 leads to a slightly different behavior as we do not observed any plateau, but S_{nem} still converges toward ~ 0.15. Note for $S_{nem}(\phi = 0.05)$ that after having reached a plateau equal to 0.25 between 12 and 40 time units, S_{nem} seems to decrease toward the same final value as for higher volume fractions. This could be explained with the slowing down of the dynamics of the system with the reduction of the volume fraction. The nematic order parameter remains below the value of 0.4 at each volume fraction, meaning that the suspensions are quite isotropic.

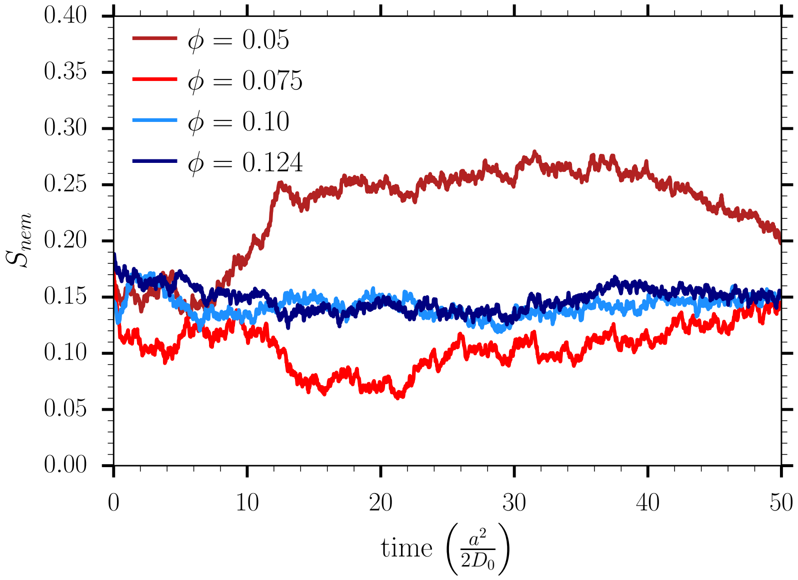

Figure 3.27: Evolution of the nematic order parameter with non-dimensional time at $\kappa D = 7.3$.

The difference in the microstructure between the suspension at $\phi = 0.05$ and suspensions at higher volume fractions is notable on the radial distribution function given in Figure 3.28a. If $g(r)$ exhibits a unique peak at a distance of $1.35R$ irrespective of the volume fraction, one should focus on the peak intensity. The increase of the volume fraction reduces the latter, pointing out a reduction of the strong radial correlation observed at low volume fraction. The spatial arrangement correlation is not particularly obvious when studying the angular correlation functions presented in Figure 3.28b. Indeed, the curves are quite similar: the closer plate-like particles are at a distance of $1.1R$ in a T-shape configuration as $P_2(r) = -0.5$, then at $1.35R$ the second Legendre polynomial increases to ≈ 0.5 except at $\phi = 0.05$ where the peak is slightly more intense indicating a preferential overlapping coin configuration. This difference in the peak intensity of the $P_2(r)$ must be interpreted as an increase of the observed orientational configurations. The particles interact through contact angles above 40 degrees, and structure in HOC configuration.

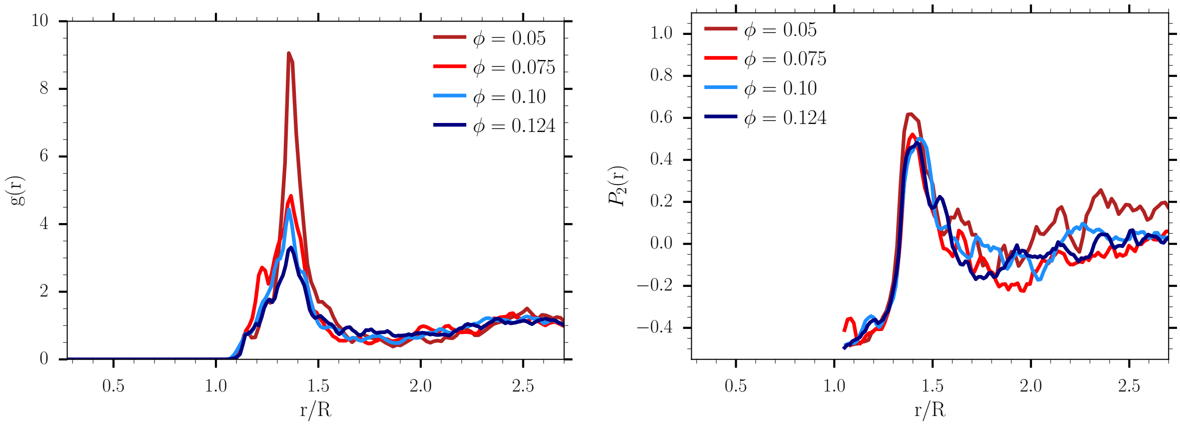

(a) Radial distribution function

(b) Angular correlation function

Figure 3.28: (a) Center of mass radial distribution and (b) second Legendre polynomial function for intermediate range of electrostatic interactions.

In Figure 3.29 is reported the probability that two touching particles take a certain angle at their contact point for $\phi = 0.05$ and $\phi = 0.075$. In this figure, the mean distance to contact (cf. section 1.4) is also reported and is referred to as $\langle r/R \rangle$. Note a similar θ dependence of this mean distance to contact for all volume fractions. One can observe a striking difference in the angular distribution function at low angles values.

At $\phi = 0.05$, P_θ exhibits a sharp peak for angles from $\theta = 5$ to 12 degrees corresponding to the OC configuration. Then, the probability of having a contact angle $\theta > 20$ degrees slightly decreases up to 45 degrees where two consecutive broad peaks centered at respectively 55 and 78 degrees can be observed. These peaks are only half the intensity of the peak observed at low contact angle, and one can wonder if they are related to the coarse-graining of the particles. The drop of $\langle r/R \rangle$ and P_θ at 90 degrees indicates that configurations close to a perfect right angle seem almost forbidden. It may be an unstable configuration.

At $\phi = 0.075$, P_θ does not exhibit a sharp peak at low θ values indicating that the OC configuration is not favored anymore. One can also notice the fairly equiprobability of the angle at contact. Consequently, contrary to what is observed at $\phi = 0.05$, increasing the volume fraction leads to a higher number of particles in a HOC than in an OC configuration. This can be explained as follows: consider three $AR7$ plate-like particles stacked with their normal vector pointing to the positive y-direction. When the system evolves, the platelets will move further apart, and given that OC configuration is the global minimum of energy (see Figure 3.26), the particles will slide and arrange in an OC configuration in a second time period. Now consider that the top and bottom platelets are submitted to a considerable pressure in the y-direction preventing them to move by more than a quarter of radius: once the platelets are as far apart as they can be, the top platelet will move for instance to the right direction and the bottom platelet to the opposite direction to reduce the repulsive electrostatic forces coming from the faces of the particles and, the one in the middle will simply reduce its free energy by creating a bond between the top and bottom particles forming a HOC structure.

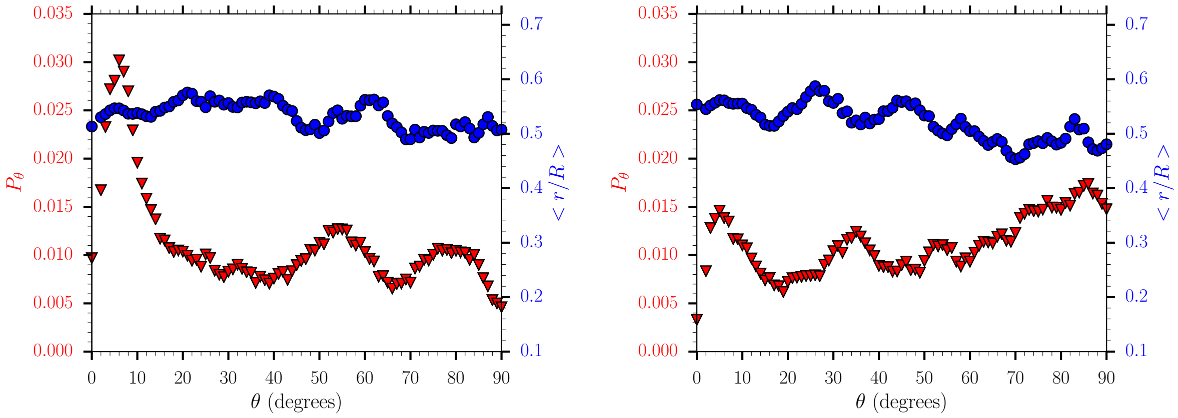

(a) $\phi = 0.05$ (b) $\phi = 0.075$

Figure 3.29: Angle probability P_θ and mean distance to contact $\langle r/R \rangle$ for $\kappa D = 7.3$.

The small differences in the first peak position noticeable on the static structure factors in Figure 3.30a and corresponding to the mean nearest neighbor must be considered with caution. Indeed, one should recall that increasing the volume fraction leads to a reduction of the size of the simulated box, and therefore to a lower discretization of the scattering vector $\boldsymbol{q}$ (see section 1.4). Considering the position of the first peak as the distance of the nearest neighbor is risky as the differences can only be due to the poor q discretization.

The behavior of the static structure factor at low q is striking. Increasing the volume fraction reduces the value of $S_L(0)$, indicating a direct correlation between the compressibility of the system and the volume fraction. At $\phi = 0.05$ and $\phi = 0.075$ the value of $S_L(0)$ is greater than one, which could be interpreted as a system evolving toward a phase separation. The structures at higher volume fraction are in a more compressed state ($S_L(0) < 1$) due to the net colloidal charges and to smaller inter-particle distances. Such structures could be considered as equilibrium gels.

To verify the assumption of the presence of a phase separation below $\phi = 0.08$ and a gel above, we have reported in Figure 3.30b the evolution of the static structure factor at the smallest scattering vector. Note that for $\phi = 0.05$ and $\phi = 0.075$, $S_L(0)$ keeps increasing with time, while a saturation is observed for higher volume fraction. Such a behavior was obtained in experiments by Ruzicka and coworkers who observed a phase separation and a static structure factor greater than one at low q for suspensions of Laponite at low volume fraction [34]. In a more concentrated system, these authors reported an equilibrium gel state [35] with $\lim\limits_{q \to 0} S_L(q) < 1$. These authors obtained the same behavior with the primitive model of patchy particles mentioned in section 1.2 in chapter 3.

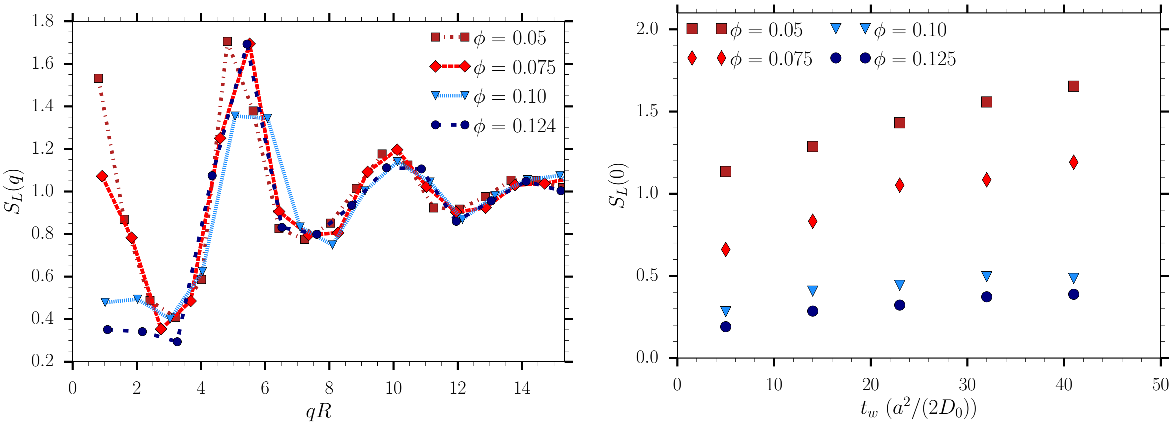

(a) $S_L(q)$

(b) $\lim\limits_{q\to 0} S_L(q)$ as a function of the waiting time

Figure 3.30: Static structure factor (left) and its vanishing scattering vector evolution (right), at $\kappa D = 7.3$. Recall that $\lim\limits_{q\to 0} q = 2\pi/L$.

2.2.3 Summary

With intermediate-range electrostatic interactions, a phase separation was observed at $\phi = 0.05$ and $\phi = 0.075$, and a compressed gel at higher volume fraction. At $\phi = 0.05$, the phase rich in colloids is composed of particles mostly interconnected in an overlapping coin configuration, whereas a mix between between OC and house of card configuration is observed at $\phi = 0.075$. The structure observed for the gels is a mix of OC configuration and HOC. This is in line with the results of Delhorme and coworkers [10] who also observed a transition from what the authors called a liquid phase with particles in OC configuration to a gel with particles in HOC configuration at $\phi = 0.08$ and $\kappa D = 15$ $(\kappa^{-1} = 1\, nm$ as the aspect ratio is equal to 15). Our results are qualitatively in line with those of Ruzicka and coworkers [35], as we also observed a phase separation at the lowest volume fractions and an equilibrium gel at higher concentration.

We want to stress that we are not able to determine if the structure is an equilibrium gel or an empty liquid [5] due to the low number of particles modeled in our simulations. Indeed, the fluctuation of the particle density cannot be conclusive as we only simulate 60 particles.

The different phases observed in this section are reported in Figure 3.31 on the second line starting from the bottom of the phase diagram as a red square for the phase separation with particles in OC configuration, and green diamonds for the mixes between OC and HOC configurations.

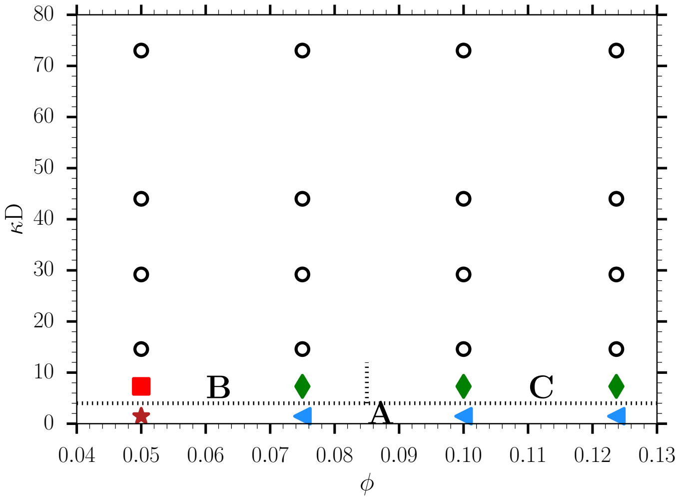

Figure 3.31: Construction of the phase diagram: the star represents a classic Wigner glass, the triangles a repulsive glass with overlapping coin configurations, the square a phase separation defined by $S_L(0) > 1$ with particles mainly in overlapping coin configuration, the diamonds an equilibrium gel above $\phi = 0.08$ ($S_L(0) < 1$) and a phase separation below, with particles in both overlapping coin and house of card configuration, and finally the circle the phases not studied yet.

2.3 Short-range electrostatic interactions

For short-range interactions, the double layers of the particles do not overlap on average at the beginning of the simulation and correspond here to $\kappa D = [14.6;\ 29.2;\ 44;\ 73]$. We have reported in Figure 3.32 the forces acting on a pair of particles for the two extremes ranges: $\kappa D = 14.6$ and 73. The oscillations of the curves in Figure 3.32b are due to the coarse-graining of the particles. One can see that only the very short-range interaction is sensitive to the coarse-graining. For both ranges, face-face interactions are always repulsive, and T-shape configuration is favored compared to OC configuration at short distances. Note that forces at $\kappa D = 73$ are one order of magnitude less intense than at $\kappa D = 14.6$.

The differences in the amplitude of forces play a crucial role in the dynamics of the system, and influence the final microstructure. We have reported in Figure 3.33 snapshots of the final structure as a function of the interaction range for $\phi = 0.05$. At $\kappa D = 14.6$ and irrespective of the volume fraction, the system is fully percolated, and the particles appear to be in a T-shape configuration, as expected from the study of the electrostatic forces between two particles. The reduction of the range to $\kappa D = 29.2$ leads to the appearance of isolated clusters and particles for $\phi = 0.05$ and 0.075, while higher volume fractions still generate a fully percolated spanning network. Interestingly, Delhorme and coworkers [10] have noticed the same phase transition from a liquid cluster phase to a gel phase despite the higher shape anisotropy used in their work. At $\kappa D = 43$, the bond energy is not important enough compared to the Brownian motion to create durable clusters, and for instance, not even a dimer is observed at the end of the simulation at $\phi = 0.05$ (see Figure 3.33c). Indeed, by watching the movie, we can see that transient clusters are formed, but the Brownian motion prevents particles from remaining in contact. Therefore, we can conclude that Brownian energy is several times higher than the bond energy for interactions shorter than $\kappa D = 43$. For such short-range interactions corresponding to high ionic strength, the vdW forces should certainly be taken into account to produce similar results to experiments as recommended by Jönsson and coworkers [23].

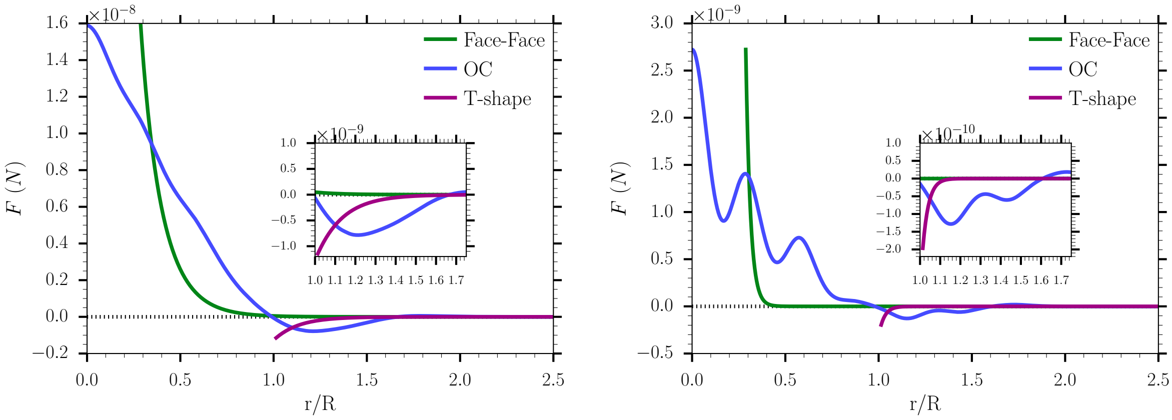

(a) $\kappa D = 14.6$ (b) $\kappa D = 73$

Figure 3.32: Electrostatic forces on a plate-like particle as a function of the distance between the centers of gravity, at $\kappa D = 14.6$ (left) and $\kappa D = 73$ (right), for three different spatial configurations: T-shape (purple color), face-face (green color), and OC (blue color) (see Figure 3.11a). The inset is simply a zoom to distances where attraction occurs.

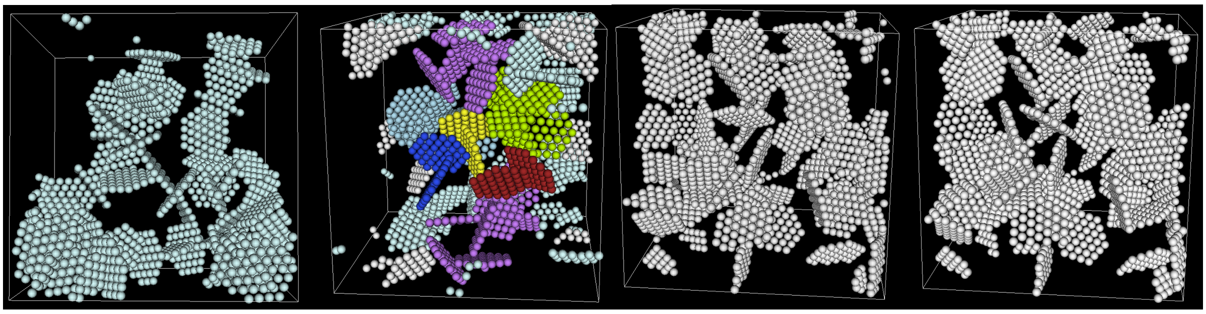

(a) $\kappa D = 14.6$ (b) $\kappa D = 29.2$ (c) $\kappa D = 44$ (d) $\kappa D = 73$

Figure 3.33: Snapshot of the final microstructure obtained for $\phi = 0.05$ and short-range electrostatic interactions: $\kappa D = [14.6;\ 29.2;\ 44;\ 73]$.

To summarize, in the short-range interaction regime, the two longest ranges of interaction generate aggregation whereas the two shortest ranges lead to a liquid-like phase. Then, the study of short-range electrostatic interactions cases is split into two parts, the first one corresponding to aggregated systems, and the second one to liquid-like states.

2.3.1 Aggregated system

In this section only $\kappa D = 14.6$ and 29.2 are investigated. Considering the evolution of the nematic order parameters, one can note that they seem to converge to approximately 0.07 at $\kappa D = 14.6$ (see Figure 3.34a), whereas they do not stabilize for $\kappa D = 29.2$ (see Figure 3.34b). However, one can assume the structures to be isotropic as the nematic order parameters remain well below 0.4.

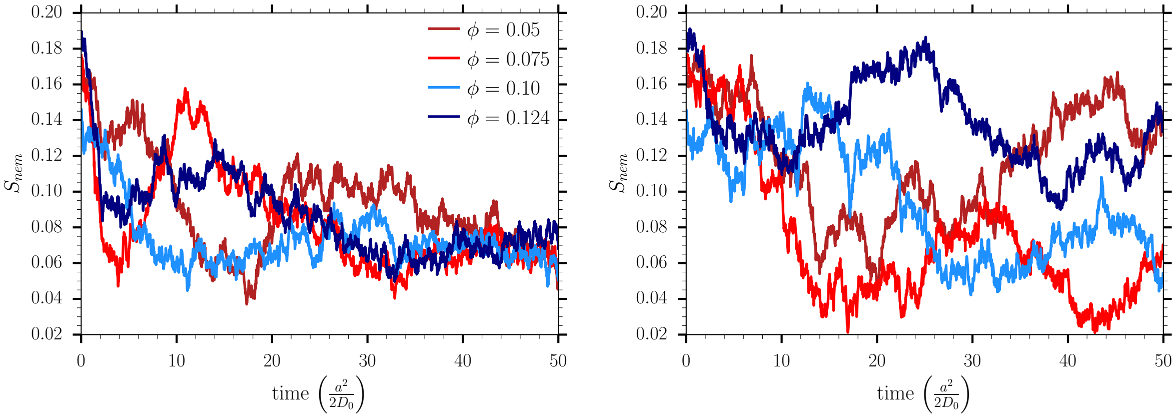

(a) $\kappa D = 14.6$

(b) $\kappa D = 29.2$

Figure 3.34: Nematic order parameter for $\kappa D = 14.6$ (left) and $\kappa D = 29.2$ (right).

The fact that S_{nem} never stabilizes at $\kappa D = 29.2$ during the entire simulations indicates that the suspensions is stil evolving, in contrast to simulations at $\kappa D = 14.6$. One can assume that the reduction of the convergence speed is due to a shorter interaction range. This assumption can be verified owing to the incoherent structure factors reported in Figure 3.35 for $\phi = 0.10$ (the same behavior is observed for other volume fractions). Note that the system has already evolved toward an arrested state at $\kappa D = 14.6$, whereas at $\kappa D = 29.2$, the curves perfectly superimpose, indicating that the dynamics of the system is larger than the simulated time window. Therefore, as expected, the shorter the interaction, the longer the simulation must be to capture the evolution of the system towards an arrested state. Nevertheless, as we have stopped the simulations at 50 units of non-dimensional time for all the simulations, we can compare the behavior of different suspensions qualitatively at this common final time. However, we expect some measures, such as the static structure factor, to be noisy, especially at low q and $\kappa D = 29.2$.

To determine if the arrested states observed at $\kappa D = 14.6$ were either a gel or a glass, we have studied the translational diffusion coefficients reported in Figure 3.36. Both the translational perpendicular and parallel diffusion coefficients decrease with time and stabilize below 0.7. If we compare the global behavior of the diffusion coefficients with the one reported for aggregated systems at low ionic strength ($\kappa D = 1.46$, see Figure 3.14), one can notice that the reduction of the interaction range has induced a decrease of the values of the coefficients. Following the study of Jabbari and coworkers on the diffusion coefficients [20], the lower coefficients are generated by the integration of particles into a gel network. Thus, the arrested structures observed at $\kappa D = 14.6$ are gels.

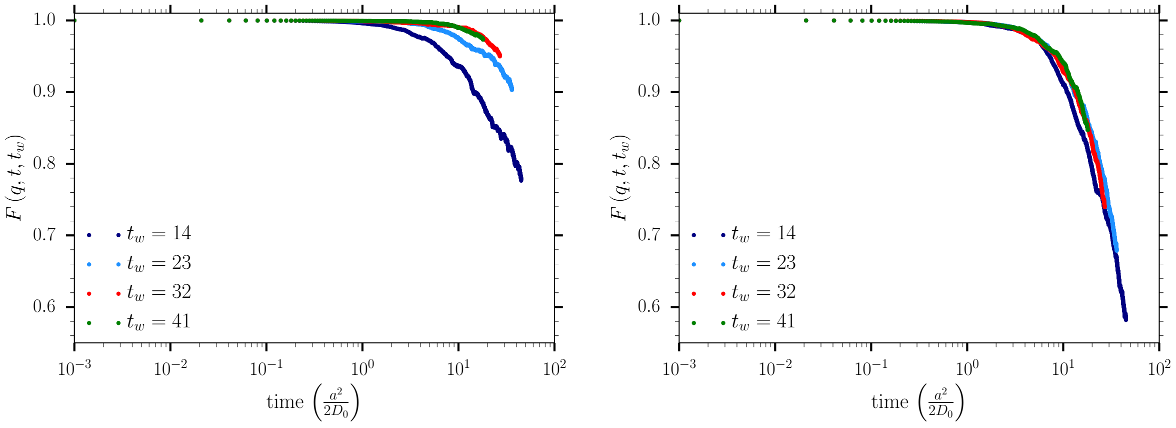

(a) $\kappa D = 14.6$

(b) $\kappa D = 29.2$

Figure 3.35: Incoherent (1 particle) structure factor for $\kappa D = 14.6$ (left) and $\kappa D = 29.2$ (right) at $\phi = 0.10$.

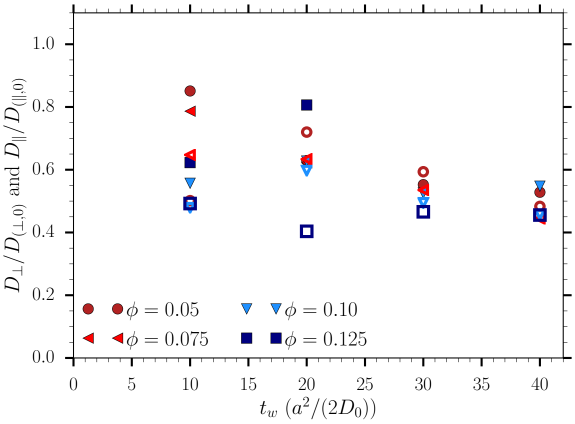

Figure 3.36: Translational diffusion coefficients for $\kappa D = 14.6$.

To characterize these gels, we have reported their static structure factors in Figure 3.37a. Firstly, note that the peaks at $qR \approx 7.4$ correspond to a dimer in a T-shaped configuration. The relatively low q dependence on the volume fraction is quite surprising considering that we would have expected to observe $S_L(0) > 1$ for low volume fractions, and $S_L(0) < 1$ for high volume fractions. If we now look at the evolution of the static structure at vanishing scattering vector (see Figure 3.37b), two different routes can be observed for concentrations either above or below $\phi = 0.08$. Below $\phi = 0.08$, $\lim_{q\to 0} S_L(q)$ keeps increasing with waiting time and reaches a final value greater than two. Then, we can assume that these systems are evolving toward a phase separation. Above $\phi = 0.08$, one can observe a kind of saturation of $\lim_{q\to 0} S_L(q)$, indicating that the systems are evolving toward an equilibrium gel. Such assumptions could allow being in line with Ruzicka and coworkers [35]. Indeed, they obtained numerically $S_L(0) > 1$ for an equilibrium gel at $\phi = 0.119$.

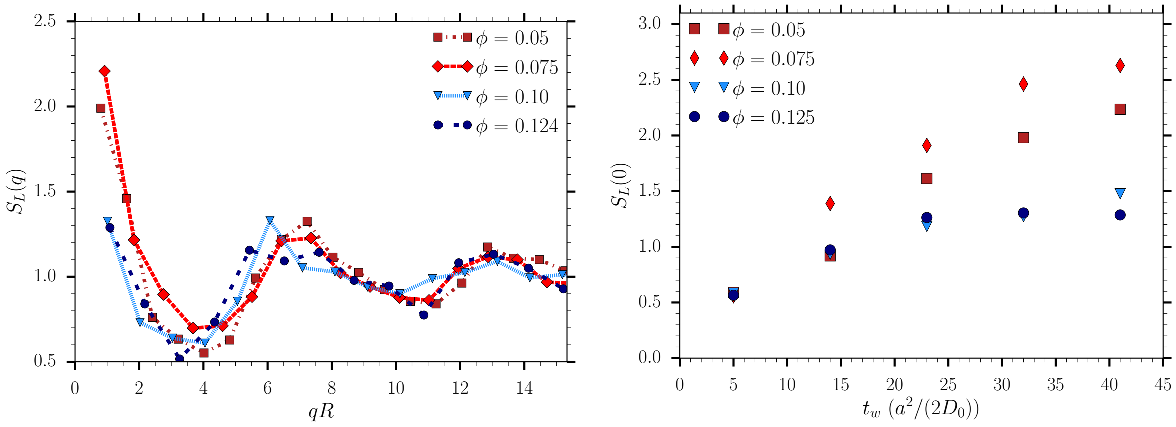

(a) $S_L(q)$ (b) $\lim_{q \to 0} S_L(q)$

Figure 3.37: Static structure factors for different volume fractions for $\kappa D = 14.6$ (left) and the evolution of its vanishing scattering vector value as a function of the waiting time (right).

Concerning the static structure factor at $\kappa D = 29.2$ (see Figure 3.38), one can observe peaks ranging from $qR = 1.9$ to $qR = 2.1$ corresponding to signatures of clusters. The observation of such peaks is the consequence of the slowing down of the dynamics of aggregation with the reduction of the Debye length. As mentioned earlier, the static structure factors at $\kappa D = 29.2$ and low q are really noisy and no conclusion can be drawn concerning the formation of a phase separation or an equilibrium gel (see Figure 3.38). Nonetheless, we made the assumption that the spanning networks observed at $\phi = 0.10$ and $\phi = 0.124$ will evolve toward equilibrium gels while the cluster phases observed at lower concentrations will evolve toward a phase separation.

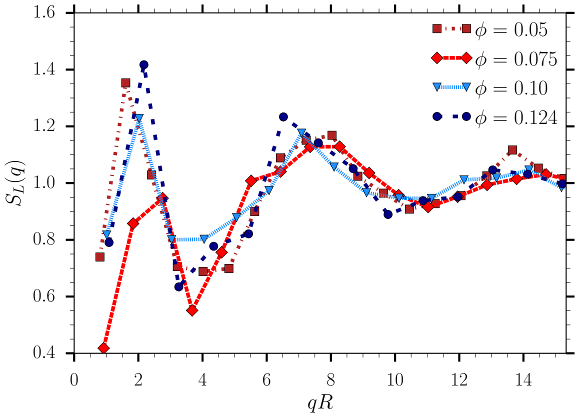

Figure 3.38: Static structure factor for different volume fractions and $\kappa D = 29.2$.

We will now quantitatively characterize the differences due to the interaction ranges on the microstructure. At $\phi = 0.05$, the latter is strongly impacted by the electrostatic interaction range as shown in the radial distribution functions reported in Figure 3.39a. At $\kappa D = 14.6$, the radial distribution function exhibits a sharp and very intense peak at exactly one radius of distance. At this distance, the corresponding value of the second Legendre polynomial reported in Figure 3.39b is -0.4, which indicates that particles are in a T-shape configuration. Note the absence of a peak at $r/R \approx 1.35$ of the radial distribution function, corresponding to the specific distance of the OC configuration observed earlier for longer interaction ranges. The radial distribution function exhibits a small second peak at $2R$ corresponding to the second neighbor in a chain of particles in a T-shape configuration (*e.g.*: –|–), which corroborates with the peak on $P_2(r)$ at that same distance. To conclude, at $\phi = 0.05$ and $\kappa D = 14.6$ particles are mostly in the T-shape configuration.

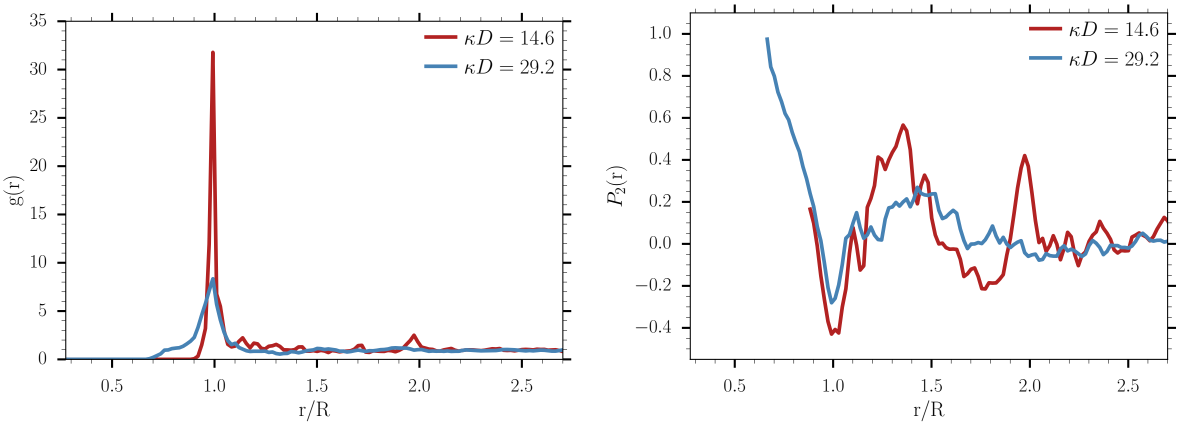

(a) Radial distribution function

(b) Angular correlation function

Figure 3.39: Radial distribution and angle correlation functions at $\phi = 0.05$ for two range of electrostatic interactions.

Reducing the range of electrostatic interaction to $\kappa D = 29.2$ decreases the intensity of the peak of $g(r)$ located at one radius of distance. The latter is also broadened at shorter distances, which is only possible for angles lower than 90 degrees. This change of configuration is linked to the double layer thickness. To illustrate this, consider two particles composed of spheres with specific double-layer ranges. In Figure 3.40 the ratio between the range of the double layers and the size of the spheres are respected compared to the systems simulated: $\kappa D = 14.6$ corresponds to $\kappa a = 1$ with a the radius of one sphere and $\kappa D = 29.2$ to $\kappa a = 2$. The red spheres are negatively charged, and the green ones positively charged. The dotted lines represent qualitatively the double layers. The configuration presented in Figure 3.40a is not favored as both the red and the green double layers overlap, which would induce strong repulsions. The top platelet must move to a vertical position closer to the center of the horizontal particle, as shown in Figure 3.40b to avoid any double layer interpenetration and, therefore, to minimize the repulsive electrostatic forces. Now, consider the same configuration as in Figure 3.40a but with a shorter interaction range, as shown in Figure 3.40c. In this case, the double layers do not interpenetrate as much as before, and therefore the configuration displayed is more acceptable than before. Then, decreasing the range of electrostatic interactions increases the number of possible configurations between platelets and, statistically, generates denser clusters.

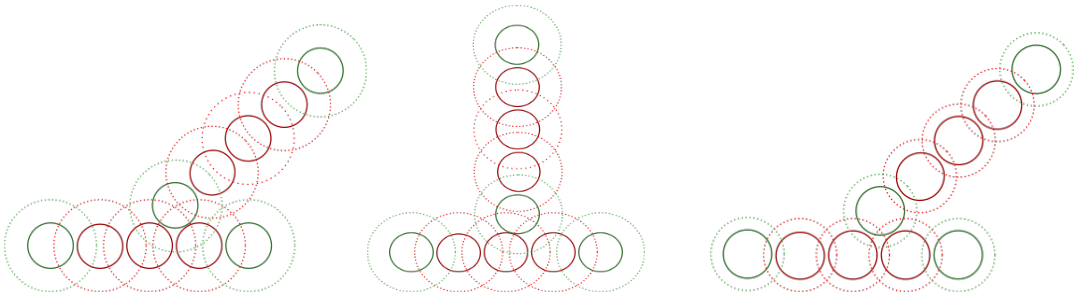

(a) $\kappa D = 14.6$ (b) $\kappa D = 14.6$ (c) $\kappa D = 29.2$

Figure 3.40: Examples of configurations of two particles with different ranges of interactions. The red color stands for negative spheres, the green for positive, and the double layers are represented with dotted lines. The ratio between the size of the sphere and the double layer are respected.

The increase of the number of possible configurations with the reduction of the electrostatic interaction range is confirmed by the study of the density of probability of the angle between particles in contact presented in Figure 3.41. For $\theta < 20$ degrees, P_θ remains almost equal to zero for both interaction ranges. It confirms that the overlapping coin configuration is not favored for these short-range interactions. At $\kappa D = 14.6$, the formation of T-shape configurations with angles closer to 90 degrees is greatly favored, whereas $\kappa D = 29.2$ exhibits an equiprobability for contact angles ranging from 55 to 90 degrees.

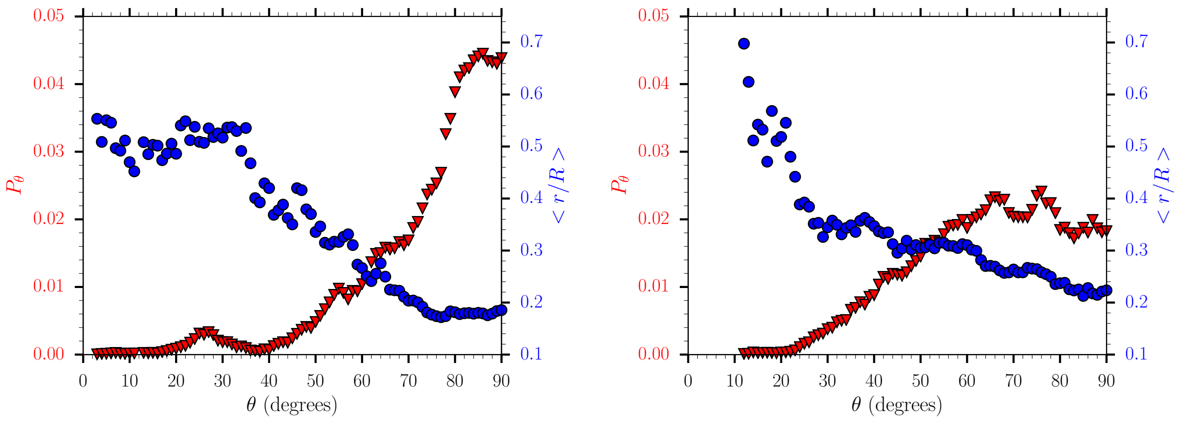

(a) $\kappa D = 14.6$ (b) $\kappa D = 29.2$

Figure 3.41: Angle probability P_θ and mean distance to contact $\langle r/R \rangle$ at $\phi = 0.05$ for $\kappa D = 14.6$ and $\kappa D = 29.2$.

Note that particles in a T-shape configuration are in contact closer to the center of gravity ($\langle r/R \rangle = 0.2$) compared to OC configurations described in Figure 3.29 ($\langle r/R \rangle = 0.5$). However, we want to stress the fact that these distances are certainly influenced by the coarse-graining of platelets in assemblies of spheres. With seven spheres along a diameter, there are only two preferred contact distances. They are represented in Figure 3.42 where we have drawn diagrams with two halves of

$AR7$ particles. One can notice that the positive double layers (green doted lines) slightly overlap in Figure 3.42b, and therefore this configuration will be less favored on average than the one represented in Figure 3.41a. If we consider that the first configuration corresponds to 75 percent of the T-shape configurations, we obtain an average distance of contact equal to $(0.75 * 1a + 0.25 * 3a) = 1.5a$ equivalent to $\langle r/R \rangle = 0.2$. For a particle with a smoother surface, obtained for example by using many small spheres to coarse-grain the platelet, many contact distances will be observed and the average contact distance $\langle r/R \rangle$ will not be 0.2 anymore. For a perfectly flat surface, it should be zero.

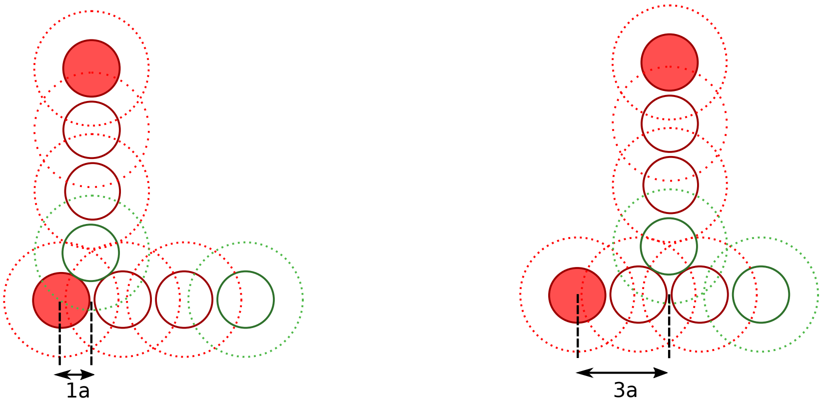

(a) 1^{st} T-shaped configuration (b) 2^{nd} T-shaped configuration

Figure 3.42: Diagram of the two possible T-shaped configurations for $AR7$ particles at $\kappa D = 14.6$. The red color stands for negative spheres, the green for positive, and the double layers are represented with dotted lines. The full red spheres represent the center of gravity of the particles.

Increasing the volume fraction from 0.05 to 0.075 does not change the microstructure significantly. However, the intensity of the peaks at one radius of distance in Figure 3.43a drops by approximately 50% when increasing the volume fraction from 0.05 to 0.075, certainly due to crowding effects which prevent the T-shape configuration from being reached. The value of $P_2(r)$ at R is slightly less negative corresponding to more possible angles configurations at this distance than for $\phi = 0.05$ (see Figure 3.41b).

At $\phi = 0.10$ and $\kappa D = 14.6$, the main peak of $g(r)$ is still located at a distance R, and the increase of the volume fraction reduces its intensity. The corresponding $P_2(R)$ indicates that particles are in average in a T-shaped configuration (see Figure 3.44b). The main difference with the structure observed at $\phi = 0.075$ lies in the presence of two secondary peaks situated at $1.15R$ and $1.3R$ (see Figure 3.44a). The first peak exhibits a value of the second Legendre polynomial equal to -0.2 indicating that particles are probably close to a T-shape configuration. At $1.3R$, orientations of the particles do not seem strongly correlated as $P_2(R) \approx 0.2$. The arrangement of the particles is verified by the angle probability density between particles in contact reported in Figure 3.45. This helps to explain the shape of the radial distribution function. As expected from the correlations functions, the highest probability of contact angle is found above 80 degrees and corresponds to T-shape configuration. Then, the secondary peak of the radial distribution function situated at $1.15R$ corroborates with the peak in Figure 3.45a for angles ranging from 50 to 70 degrees. Finally, the small peak at $\sim 1.3R$ in Figure 3.44a might correspond to contact angles ranging from 0 to 40 degrees. One should also note that $\langle r/R \rangle$ is more important for a low contact angle, and reaches its minimal value for a contact angle of 90 degrees.

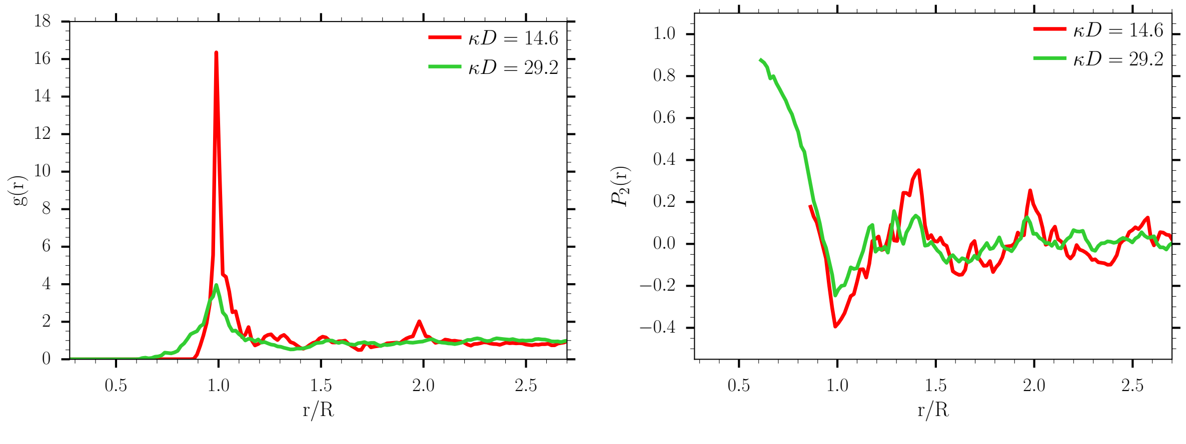

(a) Radial distribution function

(b) Angular correlation function

Figure 3.43: Radial distribution function at the angle correlation at $\phi = 0.075$ for two range of electrostatic interactions.

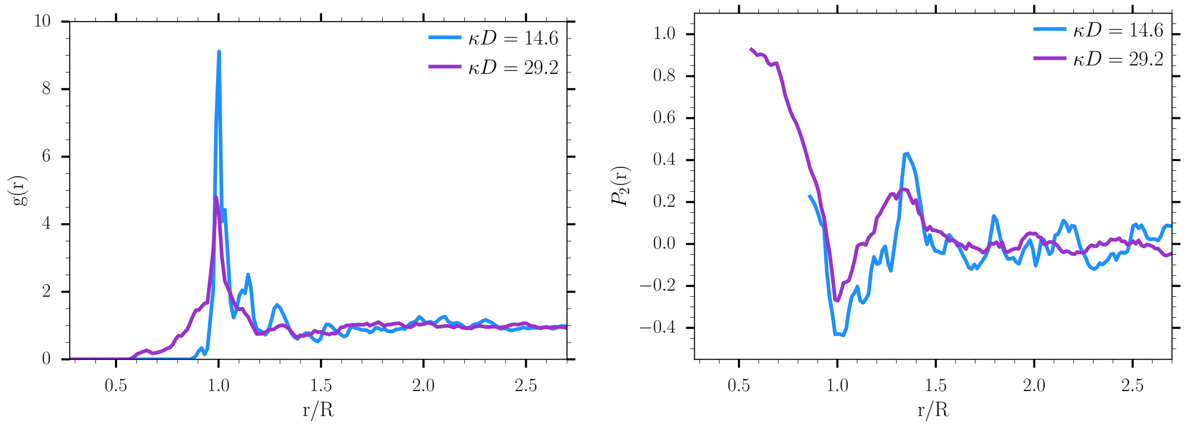

(a) Radial distribution function

(b) Angular correlation function

Figure 3.44: Radial distribution function at the angle correlation at $\phi = 0.10$ for two range of electrostatic interactions.

The structure at $\phi = 0.10$ and $\kappa D = 29.2$ is very similar to the one obtained for the same interaction range and lower volume fraction (see Figure 3.43a). Surprisingly the intensity of the peak at a distance R is the same as for $\phi = 0.075$, but still remains much lower than for $\kappa D = 14.6$ and $\phi = 0.10$. The small number of particles situated at a distance less than $0.8R$ are parallel as indicated by the angular correlation function in Figure 3.44b. We can expect some particles at distance R to be close to a T-shape configuration. Still, the low value of $P_2(r)$ does not allow a clear conclusion on the particle's average orientation. If we look at the angle probability in Figure 3.45b, we can observe a very low probability for contact angles $\theta < 20$ degrees. Then, the probability increases up to $\theta = 50$ degrees. Finally an equiprobability is observed for contact angles ranging from $50 < \theta < 90$ degrees. As for lower volume fractions, reducing the size of the double-layer shifts the probability distribution to lower angle values. The increase of the volume fraction from 0.075 to 0.10 has more impact on the structure at $\kappa D = 14.6$ than at $\kappa D = 29.2$.

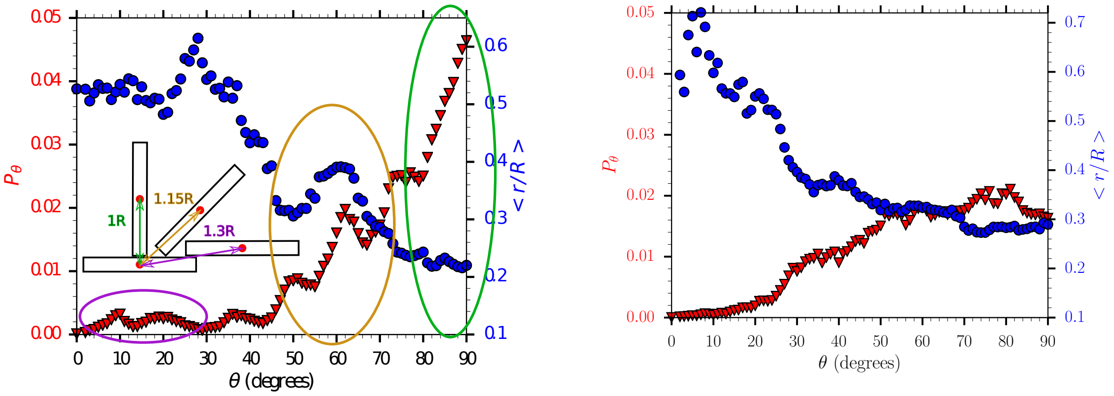

(a) $\kappa D = 14.6$

(b) $\kappa D = 29.2$

Figure 3.45: Angle probability P_θ and mean distance to contact $\langle r/R \rangle$ at $\phi = 0.10$ for $\kappa D = 14.6$ and $\kappa D = 29.2$. The three colored circles in (a) correspond to the peaks observed in the radial distribution function in Figure 3.44a: the purple circle corresponds to particles in OC configuration at distance $1.35R$, the yellow circle to particles in HOC configuration at distance $1.15R$ and the green circle to particle in a T-shape configuration at distance R.

The increase of the volume from $\phi = 0.10$ to 0.124 does not influence the intensity of the peak situated at a distance R on the radial distribution function (see Figure 3.46a) but slightly decreases the intensity of the secondary peak visible at $1.15R$. The angular correlation function in Figure 3.46b does not seem to be impacted by the increase of the volume fraction. As already observed at lower ϕ, reducing the interaction range favors denser clusters and the peak on the distribution function at R is broadened to smaller values.

To conclude this section concerning short-range electrostatic interactions generating aggregation, we emphasize the fact that at short but sufficiently extended interaction range, the T-shape configuration with an angle close to 90 degrees is preferred to configurations with smaller angles. Finite volume fraction effects prevents particles from forming local arrangements with the lowest free energy. Indeed, the 90 degree angle between two particles in contact is no longer accessible due to the higher spatial occupation, and therefore the angle density probability function is shifted to lower angle values, but never as low as OC configuration. It has been shown that the reduction of the range of interaction allows new denser configurations with smaller angles between two particles in contact (cf. Figure 3.40). Broadly speaking, the house of cards configuration has been observed at all volume fractions, with a phase separation below $\phi = 0.08$ and a system-spanning above. Due to the small size of the box and the low number of particles simulated we were not able to determine if the phase was empty liquid or an equilibrium gel. We have chosen to refer the phase as an equilibrium gel. These results are in line with Delhorme and coworkers [10] and Ruzicka et al. [35].

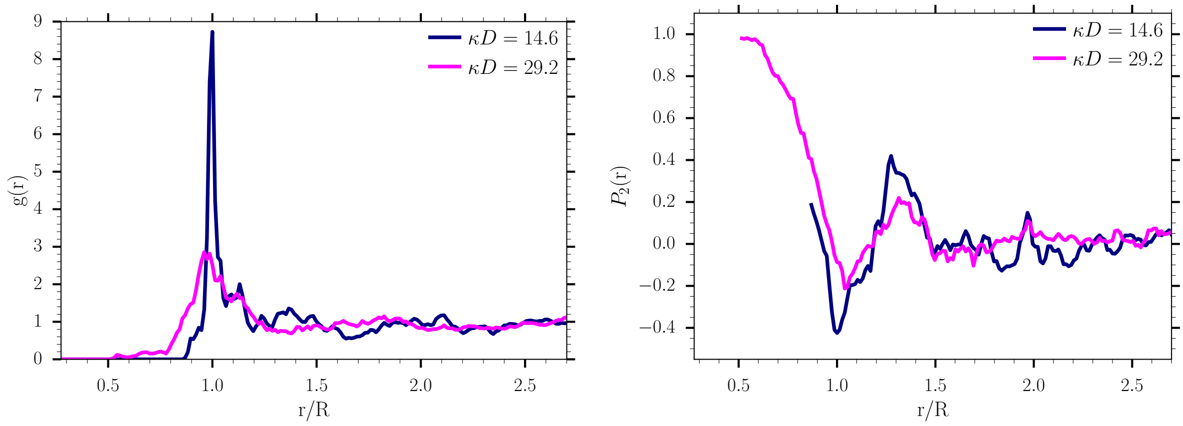

(a) Radial distribution function

(b) Angular correlation function

Figure 3.46: Radial distribution and the angle correlation functions at $\phi = 0.124$ for $\kappa D = 14.6$ and $\kappa D = 29.2$.

2.3.2 Liquid like system

When reducing even more the range of electrostatic interactions, *i.e.*, $\kappa D = 44$ and $\kappa D = 73$, the ratio between the attraction forces and the Brownian forces is not high enough to allow the formation of permanent clusters. Particles feel the attractions but never create a permanent bond. This state was described by Ruzicka and coworkers [35] and was placed above the percolation line, in the liquid phase. In such conditions, increasing ϕ increases the number of clusters created, but these are not permanent, and it is only a question of time before the particles in contact separate. However, as mentioned before, even if the bond energy is not sufficient to create permanent clusters, electrostatic interactions have an impact on the microstructure of the suspension has shown in Figure 3.47 where the radial distribution function is reported for $\phi = 0.05$. The results are compared with hard disks, *i.e.*, $\kappa D \to \infty$.

Overall, we see that interactions with such a short range do not influence the structure significantly. Note that in practice, and as emphasized by Jönsson and coworkers [23], van der Waals interactions will play an important role in such high salt conditions.

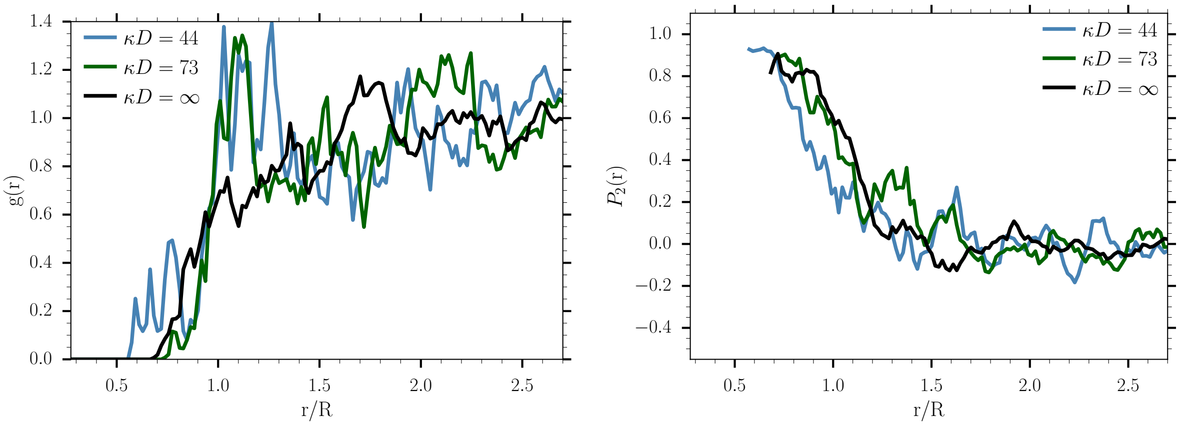

(a) Radial distribution function (b) Angular correlation function

Figure 3.47: Radial distribution and angular correlation functions at $\phi = 0.05$ for very short-range interactions . The black line stands for hard disks.

3 Conclusion

By application of the numerical method and coarse-grained model of platelets presented in chapter 2, we have been able to produce a rich "phase diagram" (with quotes because the simulation time does not always allow us to reach an equilibrium state) for a suspension of particles with both shape and charge anisotropy. We paid attention to the parameters emphasized in the literature as important, such as the number of charged sites per particle [11, 23, 24] and the ratio between attractive interactions and Brownian energy [35]. We have also chosen particular ranges of electrostatic interactions to obtain a phase diagram in line with several published studies: a purely repulsive system [4, 22], a phase separation with particles in overlapping coin configuration [10], an equilibrium gel with particles in house of card configuration [10, 35] or even a liquid-like phase. These different phases were studied as a function of the qualitative terms: long, intermediate, and short-range of interactions.

For long-range electrostatic interactions, a Wigner glass was observed at low volume fraction as already noticed experimentally by Levitz and coworkers [26] for deionized suspensions. Increasing the volume fraction leads to the appearance of a glass, following the definition of Jabbari et al. [20], with interconnected particles in an overlapping coin configuration with a vanishing compressibility. Although such a phase was never observed numerically in the previous works, we suggest that this could explain the static structure factor shape obtained experimentally by Angelini and coworkers [4].

For electrostatic interactions in the intermediate range and low volume fraction, a phase separation with a spatial arrangement of the clusters dominated by particles in overlapping coin configuration was observed. Increasing the volume fraction leads to the appearance of more diverse spatial configurations and a mix between the house of card and overlapping coin configurations. These observations are in agreement with the work from Delhorme and coworkers [10]. Moreover, we observed a phase separation at low volume fraction and an equilibrium gel at higher volume fraction, in line with the work from

Ruzicka et al. [35].

For short-ranged electrostatic interactions, the house of cards configuration is observed for all volume fractions studied, which is once again in agreement with the works from Delhorme et al. and many historical experiments on Laponite. At large enough interaction range and low volume fraction, particles are in a T-shape configuration and form an angle close to 90 degrees at contact. Increasing the volume fraction shifts the mean contact angle to lower values due to crowding, thus compressing the system ($S(0) < 1$). Reducing the electrostatic range of interactions allows lower angles between particles in contact. Thus, a lower interaction range leads to denser aggregate structures. Finally, at very short range, electrostatic interactions slightly impact the orientation of the particles but do not allow the creation of permanent bonds between particles, corresponding to a liquid-like structure.

We have been able to reproduce the majority of the phases observed in simulations performed with Monte-Carlo for suspensions of clay-like particles (cf. Figure 3.48). Nonetheless, it is important to stress that the ASD method used here is far from being the best method to study equilibrium phases. Indeed, due to its high computational cost, only a small number of particles can be simulated and for a limited physical time, and therefore the simulations may have not reached their equilibrium, and the statistical correlations are often noisy. However, the advantage of using such a costly method is it capacity to compute accurate dynamical quantities depending in particular on the complex many body hydrodynamic interactions, such as aggregation rates, viscosity and normal stresses. This is the topic of the next chapter.

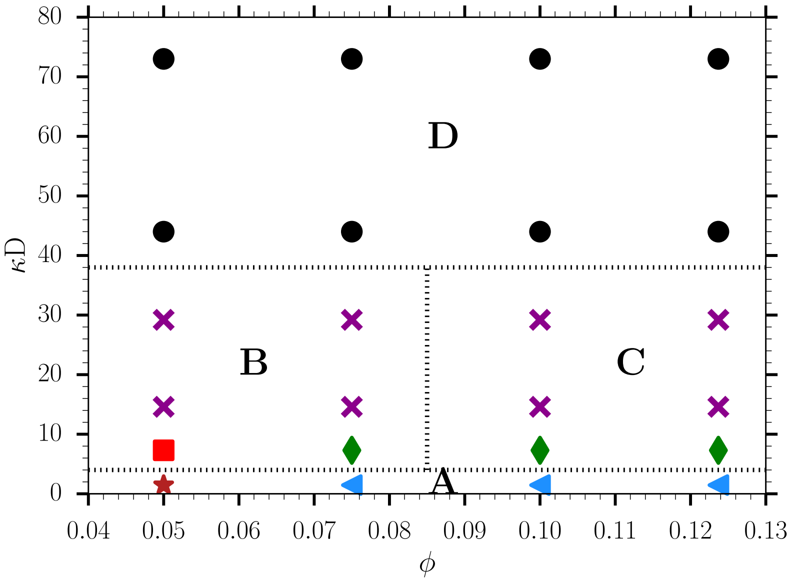

Figure 3.48: Phase diagram proposition: **A**-repulsive glass, **B**-phase separation, **C**-equilibrium gel, **D**-liquid-like structure. The star (the lowest κD point at $\phi = 0.05$) represents a classic Wigner glass, the triangles a repulsive structure with particles in contact with OC configurations, the square a structure with particles mainly in an OC configuration, the diamonds for particles in both OC and HOC configuration, the purple crosses a structure with mainly HOC configuration, and finally the filled circles a liquid-like phase.

References

[1] Bérengère Abou, Daniel Bonn, and J. Meunier. Nonlinear rheology of Laponite suspensions under an external drive. *Journal of Rheology*, 47(4):979–988, July 2003.

[2] R. Agra, E. Trizac, and L. Bocquet. The interplay between screening properties and colloid anisotropy: Towards a reliable pair potential for disc-like charged particles. *The European Physical Journal E*, 15(4):345–357, December 2004.

[3] Samim Ali and Ranjini Bandyopadhyay. Effect of electrolytes on the microstructure and yielding of aqueous dispersions of colloidal clay. *Soft Matter*, 12(2):414–421, 2016.

[4] Roberta Angelini, Emanuela Zaccarelli, Flavio Augusto de Melo Marques, Michael Sztucki, Andrei Fluerasu, Giancarlo Ruocco, and Barbara Ruzicka. Glass–glass transition during aging of a colloidal clay. *Nature Communications*, 5(1), September 2014.

[5] Emanuela Bianchi, Julio Largo, Piero Tartaglia, Emanuela Zaccarelli, and Francesco Sciortino. Phase Diagram of Patchy Colloids: Towards Empty Liquids. *Physical Review Letters*, 97(16), October 2006.

[6] Laurent Bippus, Maguy Jaber, and Bénédicte Lebeau. Laponite and hybrid surfactant/laponite particles processed as spheres by spray-drying. *New Journal of Chemistry*, 33(5):1116, 2009.

[7] Barthélémy Brunier, Nida Sheibat-Othman, Mehdi Chniguir, Yves Chevalier, and Elodie Bourgeat-Lami. Investigation of Four Different Laponite Clays as Stabilizers in Pickering Emulsion Polymerization. *Langmuir*, 32(24):6046–6057, June 2016.

[8] Instruments BYK. Technical information B-RI 21, 2014.

[9] Joost de Graaf, Wilson C. K. Poon, Magnus J. Haughey, and Michiel Hermes. Hydrodynamics strongly affect the dynamics of colloidal gelation but not gel structure. *Soft Matter*, 15(1):10–16, 2019.

[10] Maxime Delhorme, Bo Jönsson, and Christophe Labbez. Monte Carlo simulations of a clay inspired model suspension: the role of rim charge. *Soft Matter*, 8(37):9691, 2012.

[11] Maxime Delhorme, Bo Jönsson, and Christophe Labbez. Gel, glass and nematic states of plate-like particle suspensions: charge anisotropy and size effects. *RSC Adv.*, 4(66):34793–34800, 2014.

[12] Maxime Delhorme, Christophe Labbez, and Bo Jönsson. Liquid Crystal Phases in Suspensions of Charged Plate-Like Particles. *The Journal of Physical Chemistry Letters*, 3(10):1315–1320, May 2012.

[13] Marjolein Dijkstra, Jean-Pierre Hansen, and Paul A. Madden. Statistical model for the structure and gelation of smectite clay suspensions. *Phys. Rev. E*, 55(3):3044–3053, March 1997.

[14] R. Eppenga and D. Frenkel. Monte Carlo study of the isotropic and nematic phases of infinitely thin hard platelets. *Molecular Physics*, 52(6):1303–1334, August 1984.

[15] Jean-Pierre Hansen and Ian R. McDonald. *Theory of simple liquids*. Elsevier / Academic Press, Amsterdam ; Boston, 3rd ed edition, 2007. OCLC: ocm62290613.

[16] Marco Heinen, Peter Holmqvist, Adolfo J. Banchio, and Gerhard Nägele. Erratum: "Pair structure of the hard-sphere Yukawa fluid: An improved analytic method versus simulations, Rogers-Young scheme, and experiment" [J. Chem. Phys. 134, 044532 (2011)]. *J. Chem. Phys.*, 134(12):129901, March 2011. Publisher: American Institute of Physics.

[17] Marco Heinen, Peter Holmqvist, Adolfo J. Banchio, and Gerhard Nägele. Pair structure of the hard-sphere Yukawa fluid: An improved analytic method versus simulations, Rogers-Young scheme, and experiment. *The Journal of Chemical Physics*, 134(4):044532, January 2011.

[18] S. Jabbari-Farouji, Hajime Tanaka, G. H. Wegdam, and Daniel Bonn. Multiple nonergodic disordered states in Laponite suspensions: A phase diagram. *Physical Review E*, 78(6), December 2008.

[19] S. Jabbari-Farouji, R. Zargar, G. H. Wegdam, and Daniel Bonn. Dynamical heterogeneity in aging colloidal glasses of Laponite. *Soft Matter*, 8(20):5507, 2012.

[20] Sara Jabbari-Farouji, Gerard H. Wegdam, and Daniel Bonn. Gels and Glasses in a Single System: Evidence for an Intricate Free-Energy Landscape of Glassy Materials. *Physical Review Letters*, 99(6), August 2007.

[21] Sara Jabbari-Farouji, Jean-Jacques Weis, Patrick Davidson, Pierre Levitz, and Emmanuel Trizac. On phase behavior and dynamical signatures of charged colloidal platelets. *Scientific Reports*, 3(1), December 2013.

[22] Sara Jabbari-Farouji, Jean-Jacques Weis, Patrick Davidson, Pierre Levitz, and Emmanuel Trizac. Interplay of anisotropy in shape and interactions in charged platelet suspensions. *The Journal of Chemical Physics*, 141(22):224510, December 2014.

[23] Bo Jönsson, C. Labbez, and B. Cabane. Interaction of Nanometric Clay Platelets. *Langmuir*, 24(20):11406–11413, October 2008.

[24] S. Kutter, J.-P. Hansen, M. Sprik, and E. Boek. Structure and phase behavior of a model clay dispersion: A molecular-dynamics investigation. *The Journal of Chemical Physics*, 112(1):311–322, January 2000.

[25] R. J. F. Leote de Carvalho and N. T. Skipper. Atomistic computer simulation of the clay–fluid interface in colloidal laponite. *The Journal of Chemical Physics*, 114(8):3727–3733, February 2001.

[26] P Levitz, E Lecolier, A Mourchid, A Delville, and S Lyonnard. Liquid-solid transition of Laponite suspensions at very low ionic strength: Long-range electrostatic stabilisation of anisotropic colloids. *Europhysics Letters (EPL)*, 49(5):672–677, March 2000.

[27] Philippe Mongondry. *Structure et comportement rhéologique des suspensions aqueuses de Laponite en présence de plusieurs additifs*. PhD thesis, Université du Maine, Le Mans, 2003.

[28] Philippe Mongondry, Taco Nicolai, and Jean-François Tassin. Influence of pyrophosphate or polyethylene oxide on the aggregation and gelation of aqueous laponite dispersions. *Journal of Colloid and Interface Science*, 275(1):191–196, July 2004.

[29] S. Mossa, C. De Michele, and F. Sciortino. Aging in a Laponite colloidal suspension: A Brownian dynamics simulation study. *The Journal of Chemical Physics*, 126(1):014905, January 2007.

[30] A. Mourchid and P. Levitz. Long-term gelation of laponite aqueous dispersions. *Phys. Rev. E*, 57(5):R4887–R4890, May 1998.

[31] G. Odriozola, M. Romero-Bastida, and F. de J. Guevara-Rodríguez. Brownian dynamics simulations of Laponite colloid suspensions. *Physical Review E*, 70(2), August 2004.

[32] B. Ruzicka, L. Zulian, R. Angelini, M. Sztucki, A. Moussaïd, and G. Ruocco. Arrested state of clay-water suspensions: Gel or glass? *Phys. Rev. E*, 77(2):020402, February 2008.

[33] B. Ruzicka, L. Zulian, and G. Ruocco. More on the Phase Diagram of Laponite. *Langmuir*, 22(3):1106–1111, January 2006.

[34] B. Ruzicka, L. Zulian, E. Zaccarelli, R. Angelini, M. Sztucki, A. Moussaïd, and G. Ruocco. Competing Interactions in Arrested States of Colloidal Clays. *Physical Review Letters*, 104(8), February 2010.

[35] Barbara Ruzicka, Emanuela Zaccarelli, Laura Zulian, Roberta Angelini, Michael Sztucki, Abdellatif Moussaïd, Theyencheri Narayanan, and Francesco Sciortino. Observation of empty liquids and equilibrium gels in a colloidal clay. *Nature Materials*, 10(1):56–60, January 2011.

[36] Andrey Shalkevich, Anna Stradner, Suresh Kumar Bhat, François Muller, and Peter Schurtenberger. Cluster, Glass, and Gel Formation and Viscoelastic Phase Separation in Aqueous Clay Suspensions. *Langmuir*, 23(7):3570–3580, March 2007.

[37] Santosh L. Tawari, Donald L. Koch, and Claude Cohen. Electrical Double-Layer Effects on the Brownian Diffusivity and Aggregation Rate of Laponite Clay Particles. *Journal of Colloid and Interface Science*, 240(1):54–66, August 2001.

[38] Dudley W Thompson and James T Butterworth. The nature of laponite and its aqueous dispersions. *Journal of Colloid and Interface Science*, 151(1):236–243, June 1992.

[39] Dario Villamaina and Emmanuel Trizac. Thinking outside the box: fluctuations and finite size effects. *Eur. J. Phys.*, 35(3):035011, May 2014. arXiv: 1401.2683.

Rheology and dynamics of a suspension of clay-like particles

In the previous chapter, we have been able, using the ASD method to reproduce the majority of the phases observed in simulations performed with Monte-Carlo for suspensions of clay-like particles. The characterization of a suspension at rest represents only a small part of its complete description, but it is crucial to understand its rheological behavior. The latter is related to the dynamics of the system and, therefore, to complex many-body hydrodynamic interactions. One can cite, for example, the ability of a clay suspension to form a gel at rest, as observed in the previous chapter, and then, when sheared, to exhibit yield stress and to shear-thin in a time-dependent fashion. The microscopic interactions between particles drive all of these macroscopic behaviors. Therefore, relating some macroscopic quantities, such as the viscosity, to microscopic observations may provide some information to predict the rheological properties of suspensions of clay-like particles.

In this chapter, we focus on the dynamics of a suspension of clay-like particles. As a first step, the aggregation rate with and without flow is studied. This study allows us to emphasize the physical phenomenon involved in the different aggregation processes. Then, the origin of the thixotropic behavior classically observed for suspensions of clays is investigated numerically using the ASD method. The dependence of the rheological properties observed during start-up shear on both the initial microstructure and the ratio between the hydrodynamics and the electrostatics is studied. Finally, the shear-ordering observed at long-range interaction is analyzed.

1 Kinetics of aggregation of clay-like particles

Aggregation can be seen as a chemical reaction between two species, which may have different sizes and different number densities. A species can be a single particle, a dimer, or a cluster composed of more than two particles. The aggregation process occurs when two species encounter one another through transport phenomena and remain in contact owing to particle-particle interactions. Therefore, aggregation depends on the collision rate between species and on the collision efficiency, which corresponds to the probability of two species to remain in contact after a collision. Three common aggregation processes exist: perikinetic aggregation driven by the diffusion of the particles, orthokinetic aggregation induced by shear flow, and differential settling due to sedimentation. Since gravity is not considered in this work, differential settling is not presented. For perikinetic and orthokinetic aggregation, one can prove that the number of species can be written at a very short time:

$$N_T(t) = \frac{N_0}{1 + \frac{t}{\tau}} \tag{4.1}$$

where N_T is the total number of objects irrespective of their size, N_0 the initial number of objects, t the time and $\tau = 2/(N_0\ k^{mech})$ a characteristic aggregation time scale depending on the transport mechanism leading to the aggregation through the rate constant k^{mech}. For spherical particles, models exist to estimate the rate constant k^{mech}. For perikinetic aggregation $k^{peri} \simeq 8k_bT/(3\eta W)$, with η the fluid viscosity and W the stability ratio, where $1/W$ represents the proportion of contacts leading to the formation of a permanent bond. For orthokinetic aggregation $k^{ortho} \simeq (32/(3W))\ \dot{\gamma}a^3$, with $\dot{\gamma}$ the shear rate and a the radius of a particle. This theory is valid at a very short time, *i.e.*, during the formation of dimer and trimer. Note that W involves hydrodynamic interactions, the Brownian energy and the potential of interaction between particles. Given the fact that the potential of electrostatic interactions in Laponite suspension depends on the ionic strength, W also varies with the salt concentration. Huang and Berg [9] estimate this ratio experimentally for a Laponite suspension with different concentration of $BaCl_2$. These authors defined W as the ratio between k^{peri} of a classical perikinetic law for spherical particles, and the initial growth rate of the mean hydrodynamic radius of aggregates. To this end, they used a concentration of 10^{11} particles of Laponite per milliliter in deionized water at pH 10 and reported the evolution of the mean hydrodynamic radius with time. Huang & Berg have found that the stability ratio was first reduced from 40 to 1 with the increase of the concentration of $BaCl_2$ from 10^{-3}M to 10^{-1}M, then W exhibits a plateau up to 2 10^{-1}M and increases at higher salt concentration. In the present study, we directly compute τ and we do not now the formula of k^{mech} of particles with both shape and charge anisotropy. Therefore the only way to compute a sort of stability ratio would be to consider the rate constant k^{mech} of spheres of an arbitrarily radius. Note that we did not try to compute the stability ratio from our simulations.

No theory exists concerning the estimation of a characteristic time scale for suspensions of particles with both charge and shape anisotropy. Using the ASD method, we have been able to study the kinetics of aggregation of a suspension of clay-like particles with and without background flow and to compare the characteristic aggregation time scale of clay-like particles with the one classically used for spherical particles. We were also able to determine a minimal system able to capture the characteristic aggregation time scale of clay-like particles.

1.1 Without background flow

When no background flow is applied to the suspension, the competition between attraction and repulsion forces can either slow down or speed up aggregation. The kinetics of aggregation depend mostly on the range of electrostatic interactions κ^{-1} and on the volume fraction.

1.1.1 Short-range interactions

At a small interaction range compared to the average distance of the closest approach $\langle d \rangle$, the particles must diffuse one another before electrostatics collapse them together. This regime could not be captured with the ASD method. Indeed, as mentioned earlier, the limited maximum simulation time requires using fairly concentrated suspensions to observe a significant structuring in a short period of time. Thus, the average distance of the closest approach is often of the same order of magnitude as the screening length, and therefore the condition of a large interparticle distance compared to κ^{-1} is never fulfilled.

For very dilute suspensions, the distance to travel before electrostatics collapses particles together is $d' = \langle d \rangle - 2/\kappa$ which must be read as the average initial distance between the surfaces of the particles minus twice the Debye length. This distance d' is covered on a time scale $\tau = d'^2/(2\mathcal{D})$ where $\mathcal{D}$ is the diffusion coefficient of a plate-like particle. The expected time scale could be written as:

$$\tau = \frac{\langle d \rangle^2 (1 - 2/(\kappa \langle d \rangle))^2}{2\mathcal{D}}. \tag{4.2}$$

1.1.2 Long-range interactions

Large interaction ranges correspond to salt-free cases. The double layers of the particles overlap, and the motion is therefore driven by electrostatics. Particles move towards each other with a velocity scale $\mathcal{M} F_T^e$ where $\mathcal{M} = 1/6\pi\eta R$ is the mobility scale of the particles, R the radius of a particle, and F_T^e the sum of all the electrostatic forces acting on the particle. Then, we can write the associated aggregation time scale as:

$$\tau = \frac{\langle d \rangle}{\mathcal{M} F_T^e}. \tag{4.3}$$

The calculation of the estimated time scale is straightforward for spherical particles bearing opposite charges and interacting through a Yukawa potential. To simplify the system, we first consider plate-like particles with a vanishing net total charge. Thus, particles do not feel any long-range repulsion, so favoring aggregation whatever the interaction range. Moreover, as the number of sites situated on the rim (18) is almost equal to the number of sites on the face (19), the sites are bearing similar charges. Then, for plate-like particles with vanishing total net charge, competition occurs between attractive face-rim and repulsive face-face and rim-rim forces. The total attractive force F_T^e depends on the number of charged sites interacting, and, therefore, the larger the screening length, the stronger the competition between attraction and repulsion. The electrostatic force between two spheres i and j of radius a, and carrying respectively a charge Z_i and Z_j is equal to:

$$F^e = \frac{k_b T Z_i Z_j l_B}{(1+\kappa a)^2} e^{-\kappa \langle d \rangle} \frac{1 + \kappa \langle d \rangle + 2\kappa a}{(\langle d \rangle + 2a)^2}. \tag{4.4}$$

Assuming each pair of interacting sphere generates an attraction, equation (4.3) can be written

$$\tau = \frac{6\pi\eta R \langle d \rangle}{n_i^2} \frac{(1+\kappa a)^2}{k_b T Z_i Z_j l_B} e^{\kappa \langle d \rangle} \frac{(\langle d \rangle + 2a)^2}{1 + \kappa \langle d \rangle + 2\kappa a} \tag{4.5}$$

for interacting plate-like particles, where n_i stands for the number of interacting spheres per platelet and is considered as a free parameter in this model.

To verify this scaling model, we carried out simulations of suspensions of plate-like particles bearing a vanishing net charge. We considered three different volume fractions, $\phi = 0.035$, 0.055, and 0.07 and different interaction ranges. The initial spatial configurations were set to minimize the interparticle surface distance distribution, while maximizing this distance at the same time as shown in Figure 4.1.

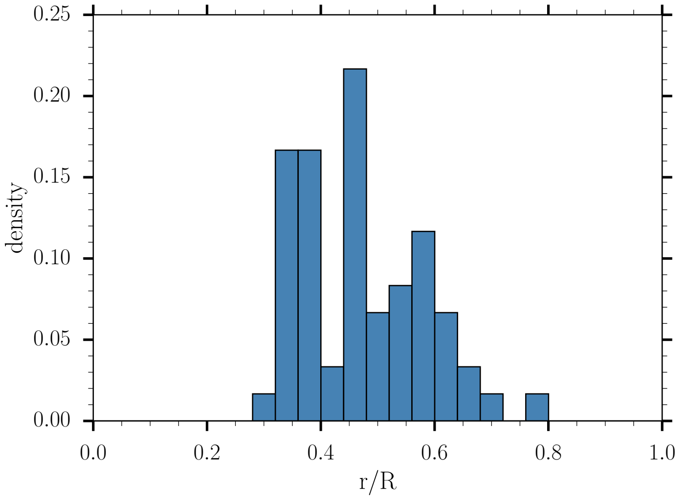

Figure 4.1: Initial distribution of the nearest neighbor distances r/R with R the radius of a particle and for $\phi = 0.055$.

For each simulation, the aggregation time scale was estimated and compared with the one obtained using equation (4.5). The characteristic time scales obtained from the simulations were estimated by fitting the variation of $N(t)/N_0$ versus time with the function $f = 1/(1 + t/\tau)$ as shown in Figure 4.2. One should recall that this function is usually valid for perikinetic and orthokinetic aggregation at short times. We have therefore chosen to fit $N(t)/N_0$ with f over the time window ranging from $t = 0$ to the time corresponding to $N(t)/N_0 = 0.6$. For example, in Figure 4.2b the time window considered goes from $t = 0$ to 1 unit of time.

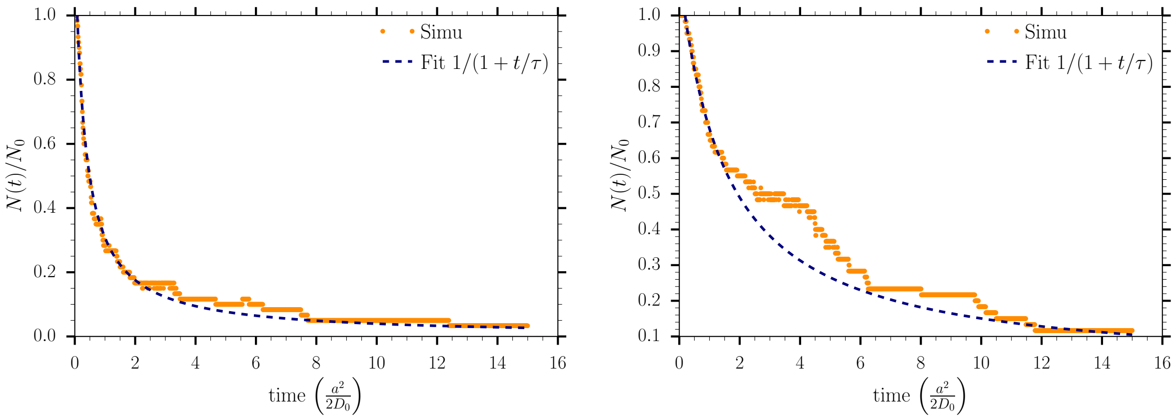

(a) $\kappa D = 7.3$

(b) $\kappa D = 14.6$

Figure 4.2: Evolution of $N(t)/N_0$ as a function of the time for $\phi = 0.05$ and for $\kappa D = 7.3$ and 14.6. The orange points are numerical results, and the dark blue curve is a fit with the function $f = 1/(1 + t/\tau)$ where τ is the optimized parameter.

The characteristic time scales obtained numerically for the different interaction ranges, and volume fraction are reported in Figure 4.3. Note that the horizontal axis is presented in scaled form as the inverse of the screening length multiplied by the mean distance $\kappa\langle d\rangle$. This non-dimensionalization allows a reasonable collapsing of the curves. The grey curve in Figure 4.1 corresponds to the model given by equation (4.5) computed for $\phi = 0.055$. The parameters used for this model are the mean distance $\langle d\rangle(\phi = 0.055) = 3.22a$ and the number of interacting spheres n_i taken equal to 1.3. One can notice that the model is slightly off at a large interaction range ($\kappa\langle d\rangle \sim 0$), probably due to the expected strong competition between attractive and repulsive forces. However, the model clearly captures the aggregation behavior, so the characteristic time scaling proposed in equation 4.5 is validated. Note that although the diffusive regime could not be simulated as stated before, the curves in Figure 4.3 tend to asymptote reasonably well towards these values.

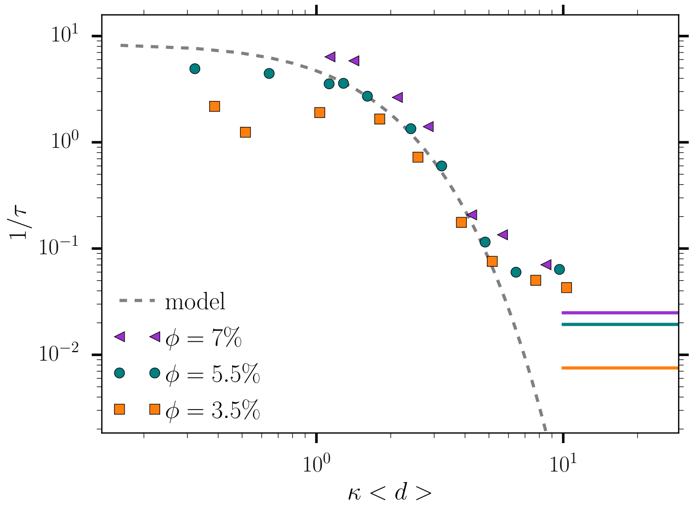

Figure 4.3: Characteristic aggregation time scale as a function of the interaction range for plate-like particles with vanishing total charge. The symbols correspond to simulations data and the grey dashed curve to the model given in equation (4.5). The horizontal lines correspond to the very short range interaction regime given by equation (4.2) and expected to be obtained at value of $\kappa\langle d\rangle$ larger than those investigated in simulations.

Let us now focus on the aggregation kinetics of the clay-like $AR7$ particles studied in the previous chapter (see section 2), and presenting a significant negative net charge, $Z_{net} = -185e$. We have seen that this net charge prevents aggregation from occurring at $\kappa D = 1.46$. Then, only the interaction ranges leading to aggregation are studied, here $\kappa D = 7.3$, 14.6 and 29.2. The corresponding characteristic aggregation time scales are reported in Figure 4.4. The black dotted curve in Figure 4.4 corresponds to the model given by equation (4.5) with $\langle d\rangle(\phi = 0.05) = 1.66a$ and $n_i = 0.5$. This model must be compared with the "model $Z_{net} = 0$" used for particles with vanishing net charge defined for $\langle d\rangle(\phi = 0.055) = 3.22a$ and $n_i = 1.3$. One should recall that the positions of the particles used to model the suspensions of clay-like particles in the third chapter were initialized randomly without any optimization concerning the minimal particle distance, leading to an initial mean distance $\langle d\rangle(AR7, \phi = 0.05)$ equals to half the mean distance used in the vanishing net charge model $\langle d\rangle(Z_{net} = 0, \phi = 0.055)$. Note that the number of interacting particles is one-third of the "model $Z_{net} = 0$". The low value of n_i can certainly be attributed to the strong and complex competitions between attractive and repulsive interactions.

The "model $AR7$" fairly well captures the reduction of the inverse of the characteristic aggregation time scales for $\kappa\langle d\rangle > 2$. Note that the expected asymptotic behavior at a very short interaction range (see horizontal lines in Figure 4.4) seems slightly overestimated. One should recall that the asymptotic behavior corresponds to perikinetic aggregation, where collision efficiency is assumed equal to one. For suspensions of particles with a significant negative net charge this assumption is obviously incorrect and the real aggregation time scale is much larger than that given by equation (4.2) due to inefficient collisions. This is consistent with the low value of $1/\tau$ at high $\kappa\langle d\rangle$ observed in Figure 4.4.

For larger interaction ranges, $1/\tau$ reaches a plateau. Values of the characteristic aggregation time scales for $\kappa\langle d\rangle < 2$ are dispersed and do not collapse as well as for higher $\kappa\langle d\rangle$ on the curve of "model $AR7$". This is not surprising as the increase of the interaction ranges leads to numerous competitions between attractive and repulsive interactions not captured by the model.

If we compare these results with the characteristic aggregation time scales obtained for particles with vanishing net charge, it is obvious that the presence of a net charge drastically slows down the aggregation process, irrespective of the volume fraction and the interaction range.

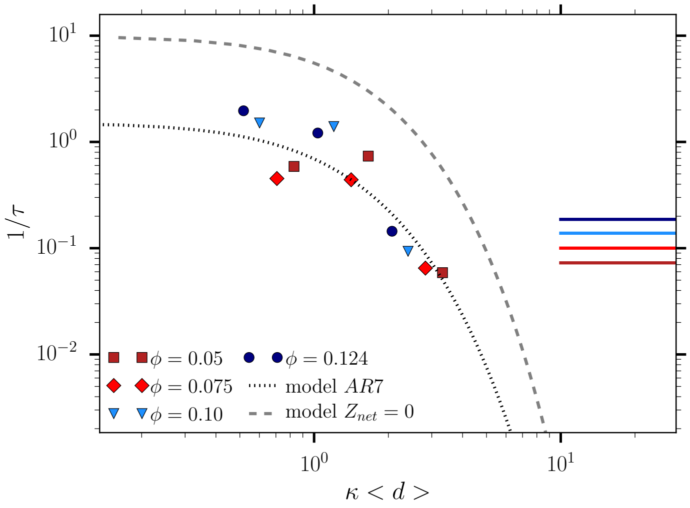

Figure 4.4: Characteristic aggregation time scale as a function of the interaction range for $AR7$ clay-like particles. The horizontal lines correspond to the very short range interaction regime given by equation (4.2).

1.1.3 Summary

We have proposed a scaling model of the characteristic aggregation time for particles with a charge anisotropy. This model is based on the idea that two different transport phenomena can be involved in the aggregation process when no flow is applied to the suspension: Brownian diffusion and migration to reduce electrostatic energy.

At short interaction range compared to the initial average distance of the closest approach, the aggregation is expected to be driven by diffusion and might follow perikinetic aggregation. This assumption could not be verified using simulations as too short-range electrostatic interactions lead to a transient liquid-like phase that does not evolve significantly during the limited simulation time. However, the simulations involving the shortest interaction ranges values tested seem to converge relatively well towards this model.

For longer screening lengths, we were able to predict the scaling of the characteristic aggregation time for plate-like particles with a vanishing net charge, using a simple model. However, this model did not allow us to capture the long-range aggregation kinetics of clay-like particles studied in the third chapter. The long-range repulsion slows down the aggregation and plays a role in the scaling of the characteristic aggregation time. The surface charge anisotropy can thus lead to counter-intuitive results on both the equilibrium structure and the system dynamics depending on the interaction range.

1.2 Shear induced aggregation

To investigate the influence of shear flow on the aggregation kinetics of $AR7$ particles, it is crucial to define the main forces correctly, *i.e.* the viscous, the Brownian and the electrostatic forces. One should recall that the ratio between the viscous and the Brownian forces is the Péclet number, which is defined in this work as $Pe = 3\pi\eta R^3\dot{\gamma}/(k_bT)$. We choose to associate the variation of Pe to the shear rate $\dot{\gamma}$, and therefore, to set the temperature to $T = 293.15\ K$ and the dynamic viscosity of the fluid (water) to $\eta = 1.00\ 10^{-3}$ $\mathrm{Pa\,s}$. Note that due to the very small value of R (3.65 nm), even $Pe = 1$ leads to orders of magnitude for the shear rates that are not achievable in experiments: $\dot{\gamma} = 1.1\ 10^6\ \mathrm{s}^{-1}$. Therefore, one should keep in mind that this study is realized from an academic point of view and should not be directly transposed to experimental systems.

To represent the ratio between the viscous forces and the magnetic forces, the Mason number Ma is classically defined. In this study, the electrostatic forces replace magnetic forces and so we will use a Mason number based on the electrostatic force scale F^e computed in the third chapter (see section 1.3.2). We arbitrarily select the electrostatic force computed between two $AR7$ particles in a face-face configuration (see Figure 3.6), with a distance between the centers of gravity equal to $0.82\ R$ and an interaction range of $\kappa D = 7.3$ as the electrostatic force of reference. For a Péclet number[1] of 389 the Mason number is equal to:

$$Ma(Pe = 389) \sim \frac{F_p^h}{F_p^B}\frac{k_bT}{F^eR} \sim \frac{F_p^h}{F^e} \sim \frac{389}{379} = 1.026. \tag{4.6}$$

If the Mason number is well defined, $Ma << 1$ means that electrostatic interactions prevail over hydrodynamic interactions.

Then, we have chosen an electrostatic interaction range leading to aggregation of particles, $\kappa D = 14.6$, and we have studied the following Péclet numbers: $Pe = 3.89\ 10^{-3}$, 38.9, 117, 195, 389, 778, 1556, and 3890. The charges on the particles were adapted to preserve the Mason number constant and equal to one for $Pe > 1$ and to preserve $F^eR/(k_bT)$ for $Pe < 1$. The volume fraction was set

---

[1] Note that $Pe = 389$ corresponds to $Pe^s = 1$, where Pe^s is the Péclet number of a sphere of radius a

to $\phi = 0.03$ and the positions of the particles were initialized to obtain a mean distance of the closest approach centered at $5a$ and with low dispersion (see Figure 4.5).

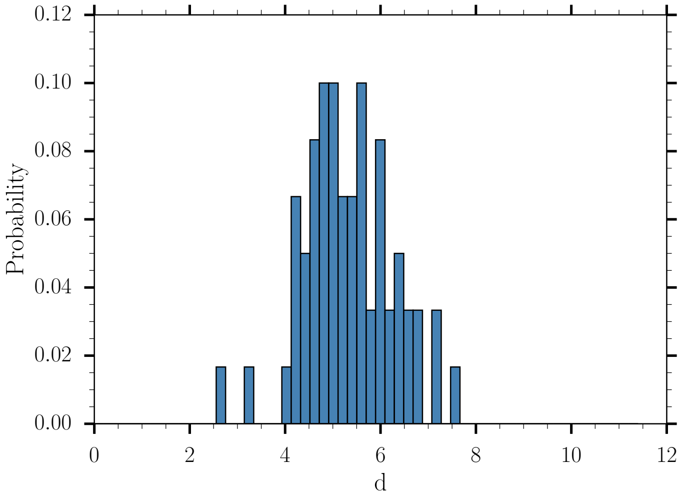

Figure 4.5: Initial particles distribution as a function of the distance d for $\phi = 0.03$.

As in the previous section, the characteristic aggregation time scales were estimated by fitting $N(t)/N_0$ with a function $f = 1/(1 + t/\tau)$ (see Figure 4.6a). The aggregation scaling for $Pe = 38.9$, 117 and 195 seems to be linear with a slope decreasing with the reduction of the Péclet number (see Figure 4.6b). We were not able to explain this change of behavior over this specific range of Péclet number. These curves were also fitted with the function f (quite poorly), but one should keep in mind that these results must be considered with caution. The aggregation time for $Pe = 38.9$, 117 and 195 are represented with open symbols in Figure 4.7 while the time extracted from Figure 4.6a is represented with full symbols. The orthokinetic scaling with $\tau = \pi/(4\phi\dot{\gamma})$ for two different ϕ are reported as dotted lines in Figure 4.7 for comparison. These two volume fractions correspond to the cases where the volume fraction of the spheres constituting the particles $\phi_{spheres} = 0.03$ and the volume fraction of the platelets including the spheres plus the double layer $\phi_{Platelets+\kappa^{-1}} = 0.165$. For $Pe < 100$, τ remains constant, which could be interpreted as the fact that the aggregation process is driven by the electrostatic forces and, therefore, the interaction range and not by a collision frequency depending on $\dot{\gamma}$. For $Pe > 100$, the dependence of the characteristic time scale on the Péclet number is well described by the orthokinetic model using $\phi_{Platelets+\kappa^{-1}}$. It is interesting to see that despite the shape and the charge anisotropy of clay-like particles, the orthokinetic scaling used for spherical particles still works when using an effective volume fraction based on the volume fraction of the platelets including the spheres plus the double layers.

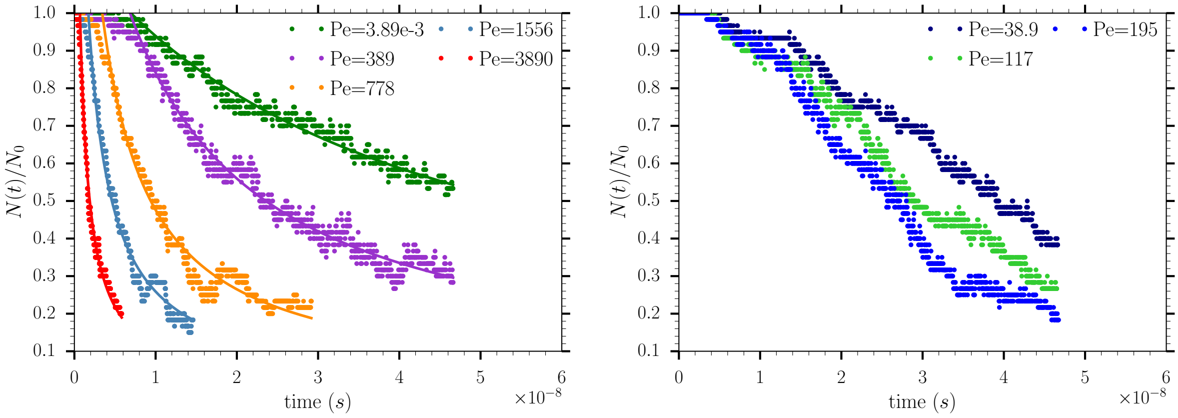

(a) $N(t)/N_0$ (b) $N(t)/N_0$ linear scaling

Figure 4.6: $N(t)/N_0$ for different Péclet numbers as a function of time. In the left figure, numerical data are fitted with $f = 1/(1 + t/\tau)$ (full lines) while in the right figure the scaling seems to be linear.

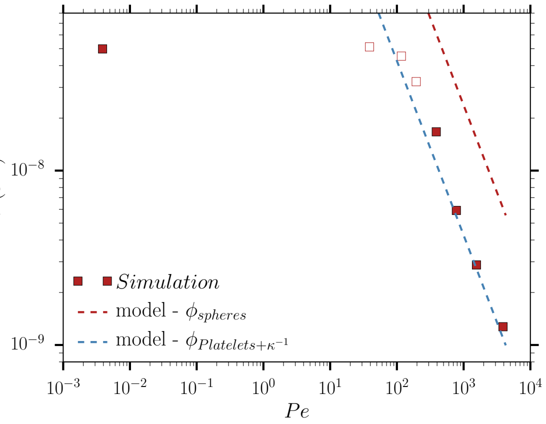

Figure 4.7: Characteristic times scale of aggregation. The dotted lines represent the orthokinetic scaling for the volume fraction of the spheres constituting the particles, and the volume fraction of the platelets including the spheres plus the double layer.

1.3 Summary

In this section we reported simulation data concerning the aggregation process first without shear flow and by varying the range and strength of electrostatic interactions, and then with increasing shear rates for a constant Mason number.

When no shear flow was involved, we varied the electrostatic range of interactions and the net charge of the particles. We have proposed a scaling model based on the idea that electrostatic migration was the dominant effect driving the aggregation process. This model requires interaction ranges leading to aggregation and was found satisfactorily accurate for particles with vanishing net charge irrespective of the interaction range. For particles with a net negative charge, the long-range repulsion slows down the aggregation and severely influences the scaling of the characteristic aggregation time. Due to the long-range repulsion between the particles, the model was only able to capture the aggregation dynamics at intermediate interaction ranges reasonably well but could not capture the long-range interaction aggregation regime.

Kinetics of aggregation of particles with both shape and charge anisotropy is very complex to foresee due to the numerous experimental parameters influencing the aggregation process. One can cite the volume fraction of the suspension, the net charge of the particles, the ionic strength of the suspension, or even the charge distribution. Indeed, for very similar charge densities, Paineau and coworkers [19] have observed that tetrahedrally charged clays were undergoing stronger electrostatic repulsions than clays with octahedrally charged sites. It could be interesting to simulate $AR7$ particles with the total negative charge spread over half of the center particles and to verify if the scaling model developed for vanishing net charge particle would be unchanged. When particles need to be oriented to aggregate, the mobility of the particles becomes an evident parameter of the aggregation's kinetics. Note that this mobility will be influenced by the size and shape of the particle, the hydrodynamic interactions, and the electrostatic stresses arising from the nearest neighbors. We also emphasize that the lower the ionic strength, the stronger the influence of the net charge. At very short-range interactions, the aggregation is driven by the Brownian diffusion, and the net charge might only influence the stability ratio but not the scaling of the kinetics of aggregation. For intermediate and long-range interactions, a net charge will slow down the aggregation process and can even prevent any aggregation from occurring. For all these reasons, no theory perfectly describes the kinetics of aggregations of particles with both shape and charge anisotropy. The observation of a scaling behavior is already interesting to estimate roughly the dynamics of aggregation of a complex system.

When the shear flow is significant ($Pe > 100$), the aggregation is described by orthokinetic arguments with an effective volume fraction based on the volume fraction of the platelets plus the double layers. This is not a trivial result as the orthokinetic law is originally designed for spheres. However, anisotropic particles such as platelets follow the Jeffery's orbits under shear, and therefore the sweeping volume can be assimilated to a spherical volume. We have shown that the effective volume used to describe the orthokinetic regime of platelets with charge anisotropy was the volume fraction of the platelets increased by the double layers. In general, the application of a shear flow to a suspension of clay-like particles speeds up the first aggregation events, although it can inhibit the formation of large aggregates, as will be discussed later in this chapter.

2 Thixotropy

As presented in the first chapter, the thixotropy of a suspension is characterized by its structuring ability during a period of rest (healing process) and by its shear-thinning behavior in a time-dependent fashion when shear is applied. Such behavior is interesting in many industrial processes, and thixotropic suspensions are used in biomedical products, printing inks, personal-care products, or in the food industry [16].

Laponite suspensions exhibit a thixotropic behavior above a certain volume fraction and for ionic strengths leading to aggregation [1, 13, 23, 24, 30]. The thixotropic behavior observed in Laponite suspensions is due to their ability to form a gel structure at rest which can be disrupted or even destroyed when shear is applied. The conclusion of the study from Pignon et al. was that the thixotropic behavior of Laponite was a reversible aggregation process involving structures of different length scales, ranging from $\sim 35\ \mathrm{nm}$ for the sub-units to microdomains $\sim 1\ \mu\mathrm{m}$ whose assembly forms super-aggregates [24]. Martin and coworkers have shown that thixotropy can be tuned by varying the charge anisotropy of the particles [13]. These authors compared both the rheological and structural behaviors of suspensions of Laponite with and without peptizers. The peptizers were used to decrease the edge to face attraction by reducing the rim charge or even by making it negative. Martin and coworkers observed that the addition of peptizers weakened the structure network producing the solid-like aspect of Laponite. The presence of peptizers also impacts the transient response to a small shear rate after a period of rest: the suspension with peptizers undergoes a viscoelastic behavior while the suspension without peptizers follows a stress curve characteristic of the thixotropic fluid, which consists of an overshoot stress and a relaxation toward a steady regime. This study points out the importance of the face-rim interactions in the rheological response of Laponite suspension to an external drive.

To verify that using the $AR7$ model particles in the ASD code allows us to reproduce the thixotropic behavior of clay-like suspension, we applied intermittent shear flows to suspensions of $AR7$. Due to the number of particles simulated, we will not be able to observe the behavior at the micron scale. However, we should be able to capture the destruction of the subunits of the fractal structure composing the gels of clay particles due to the shear and the healing process of the suspension during rest periods.

2.1 System simulated

For this study, we set the volume fraction to $\phi = 0.05$, and the electrostatic interaction range to $\kappa D = 14.6$. As shown in the third chapter (see section 2.3.1), at this specific interaction range and volume fraction, $AR7$ particles aggregate with particles mainly in T-shape configuration.

We applied to the suspensions of clay-like particles intermittent flows composed of several periods of shear and rest. The shear flow is given by $\mathbf{u} = (\dot{\gamma}y, 0, 0)$, and therefore the x-y plane is the plane of the shear and the y-z plane is perpendicular to the mean flow. The shear disrupts or even destroys the structure (shear breakdown), while during the rest period, we should observe the rejuvenation of the structure. One can wonder if the history of the suspension could influence either the structure at equilibrium or the steady viscosity during shear.

To answer this question, two different regimes of shear were considered and applied to two distinct suspensions. The first one, referred to as the low Mason regime, has $Pe = 389$ and $Ma = 1$. The second one, the high Mason regime, $Pe = 3.89\ 10^6$ and $Ma = 1\ 10^4$. Both regimes can be considered as non-Brownian. Given the Mason number's definition, the electrostatic forces in the low Mason number regime are of the same order of magnitude as the viscous forces. Therefore, one could expect to observe a disruption of the aggregate, but with particles remaining in contact and forming several aggregates. In contrast, the second regime will probably tear every particle assembly apart, as the viscous forces are four orders of magnitude higher than the electrostatic attractions.

At the end of the period of shear, the flow is stopped, and we let the suspensions evolve without background flow. During these periods of rest, the Péclet number was set to $Pe = 3.89\ 10^{-3}$ while keeping $F^{elec}R/(k_bT)$ constant (see section 1.3.2). Consequently, the suspension is expected to aggregate with particles mainly in T-shape configuration.

We used the same random initialization of the particles for the high and the low Mason regime. Then, we applied successively periods of shear and rest (intermittent flow), as presented in Figure 4.8. Each simulation is composed of four periods of shear and three periods of rest. The periods of shear last for $30/\dot{\gamma}$ and the periods of rest for $25\ a^2/(2D_0)$. Concerning the shearing time, we were confident to reach a stationary state, as the time to obtain it scales as $1/\dot{\gamma}$ [1]. The resting time is chosen to allow the suspensions to reach a fully aggregated structure.

The use of the cycles should allow us to answer the following questions: i) is the microstructure of the suspension at rest sensitive to the history of the suspension? ii) does a suspension of $AR7$ exhibit a thixotropic behavior irrespective of the shear regime?

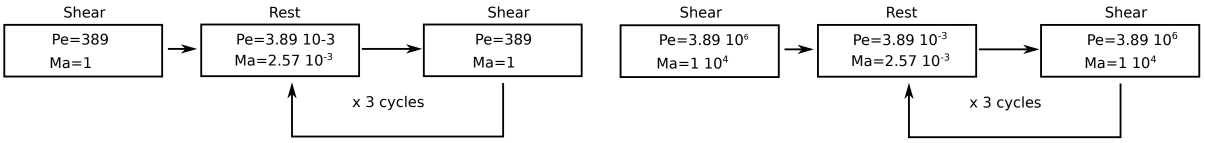

(a) Low Mason number (b) High Mason number

Figure 4.8: Flow chart of the simulations used for the study of the Thixotropy.

2.2 Analyze of the cycles

When one looks at the snapshots of the structures at the end of a period of shear, the difference between the low and the high Mason number regimes is striking (see Figure 4.9). In the low Mason number regime, one can observe five different colors corresponding to five independent clusters. The particles seem to be interconnected through the house of card configuration. The particles at the high Mason number regime are not interconnected due to the strong viscous forces. However, one can notice the presence of two tactoids circled in red in Figure 4.9b. Note that in the pure hydrodynamic regime Meng & Higdon found a similar formation of tactoids [14]. Many particles seem to be aligned in the velocity-vorticity plan.

The snapshots at the end of the first period of rest are very similar, as shown by Figure 4.10. For both simulations, particles are in a T-shape configuration, and all the particles, except one in Figure 4.10b, are forming a single aggregate. In a short time, the suspensions were able to reach a similar microstructure. Although they were started with a visibly different initial state, the suspensions evolved toward the same arrested state as the one observed in section 2.3.1 which confirms the validity of the results obtained in the third chapter.

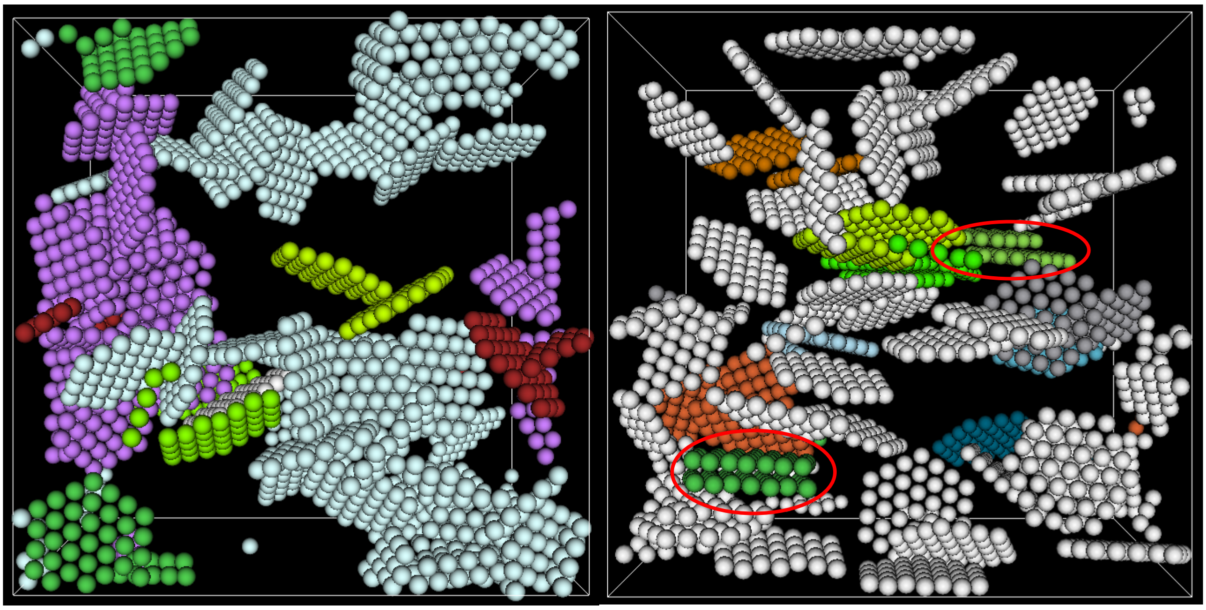

(a) Low Mason number

(b) High Mason number

Figure 4.9: Snapshots at the end of the first shear period for the low Mason number regime (left) and the high Mason number regime (right). Two tactoids are circled in red in the right figure.

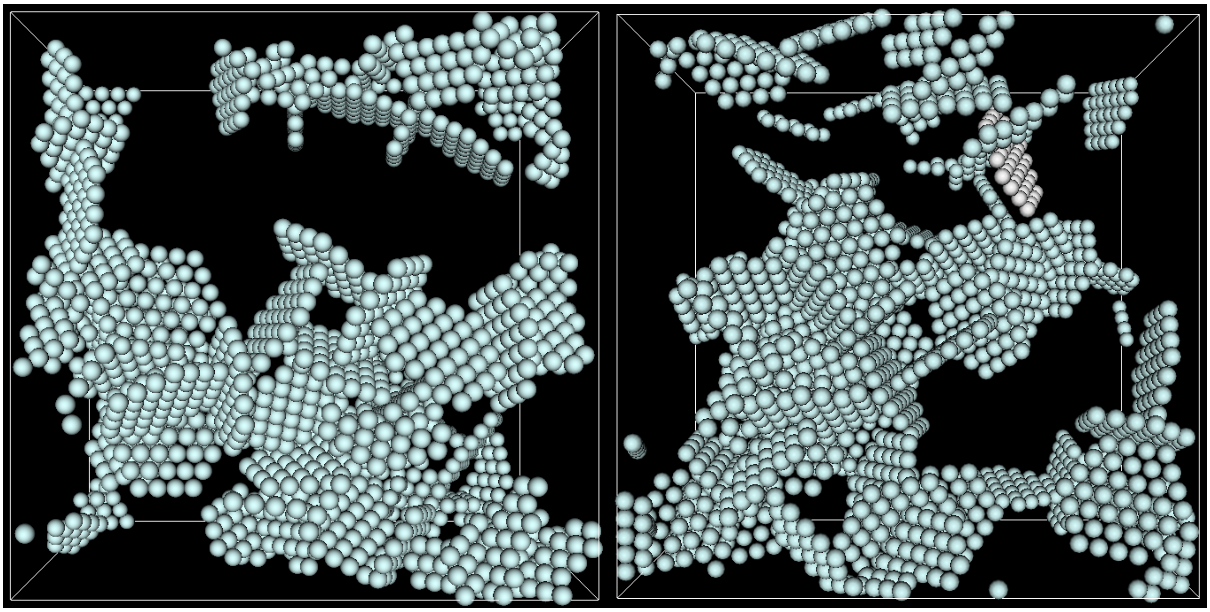

(a) Low Mason number

(b) High Mason number

Figure 4.10: Snapshots at the end of the first rest period for the low Mason number regime (left) and the high Mason number regime (right).

These observations based on the snapshots of the suspensions are verified with the evolution of the average number of neighbors reported in Figure 4.11. At $Ma = 1$ and for the first start-up shear, one can observe a building up of aggregates corresponding to an increase of $\langle N_{nei} \rangle$ up to 2. At rest, the suspension structure itself, and the average number of neighbors increases to 2.7 which seems to be a plateau value common to each period of rest. At the very beginning of the start-up shear after a resting period, the number of $\langle N_{nei} \rangle$ drops down from 2.7 to 2, indicating a kind of erosion of the structure, where the particles with the weakest bonds have been separated from the main aggregate.

Concerning the high Mason number regime, $\langle N_{nei} \rangle$ is on average equal to 0.5 which is considerably lower than the value observed at $Ma = 1$. As expected, the strong hydrodynamic interactions prevents particles aggregation. This value of $\langle N_{nei} \rangle = 0.5$ reached during the first shear must be analyzed with caution. If it can be related to the presence of tactoids, one should recall that $\langle N_{nei} \rangle$ is based on a criterion of distance. Owing to the volume fraction considered, particles cannot rotate freely without encountering another particle. During any rotation of a particle, if the distance between the surfaces of two particles is less than this criterion, particles will be considered as having a neighbor even if the contact is brief. Therefore, the average number of neighbors during the periods of shear at $Ma = 10^4$ is related to tactoids and brief contacts between particles due to crowding effects. During the cessation flows, $\langle N_{nei} \rangle$ sharply increases up to 2.1. Note that the final structure does not seem to be reached in $25\ a^2/(2D_0)$ as the average number of neighbors keeps increasing, which could explain why it is slightly lower than at $Ma = 1$. At the very first moments of the start-up flow after a period of rest, $\langle N_{nei} \rangle$ drops down to 0.6, indicating a total breakdown of the structure.

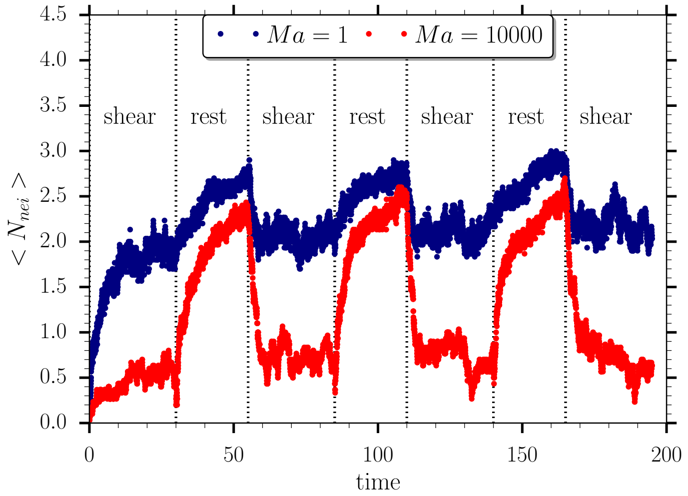

Figure 4.11: Evolution of the average number of neighbors $\langle N_{nei} \rangle$ for the low and high Mason number regime. The time has been made non-dimensional by $1/\dot{\gamma}$ for the periods of shear and by $Pe/\dot{\gamma}$ for the periods of rest.

If we now look at the nematic order parameter and the deviation of the mean direction vector of the $AR7$ particles reported respectively in Figure 4.12a and 4.12b, one can note the repetition of the same pattern throughout with the cycles for the two Mason number regimes. For the low Mason number regime, the nematic order parameter fluctuates around 0.2 during the shearing periods and drops down to ~ 0.1 at rest (see Figure 4.12a). The oscillations during the shear are correlated with the alignment of the particles with the flow direction (see u^1_y in Figure 4.12b). This correlation is particularly noticeable for the high Mason number regime. During these periods of shear, the y component of the deviation vector sharply increases to values above 0.5, meaning that such direction is highly favored. Each fluctuation of the direction vector corresponds to a variation of the nematic order parameter. Broadly speaking, at the end of the periods of rest, both the nematic order parameter and the deviation of the direction vector behave in the same manner, irrespective of the shear history: the deviation of the mean direction vector almost vanishes indicating a relatively isotropic structure (see Figure 4.12b), confirmed by the low value of S_{nem} (see Figure 4.12a). During the periods of shear, particles align their direction vector with the gradient velocity vector (y-axis in this study). This alignment is strong for the high Mason number regime leading to a highly nematic suspension. In the low Mason number regime, the structure remains fairly isotropic even though the y-axis alignment seems slightly favored.

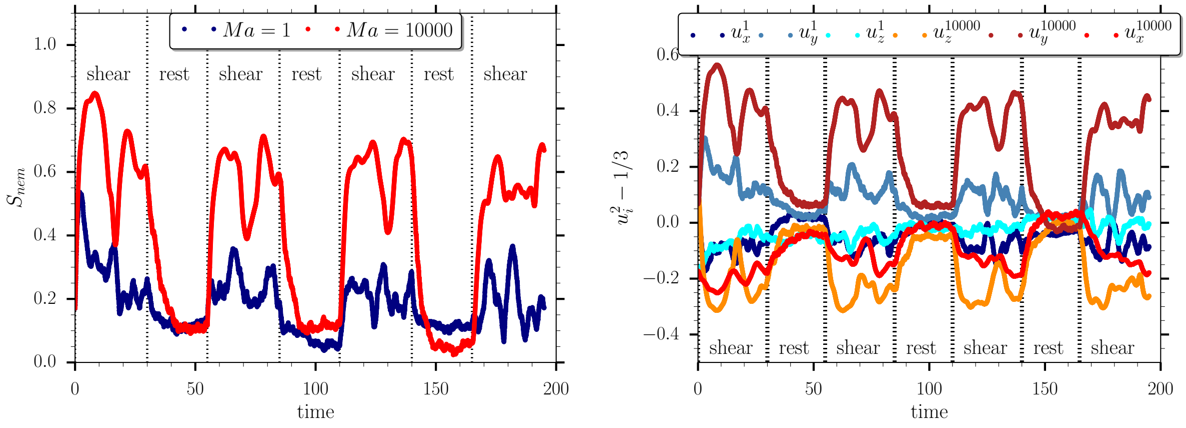

(a) Nematic order parameter

(b) Deviation of the mean direction vector

Figure 4.12: Nematic order parameter (left) and deviation of the mean direction vector (right) during the intermittent flows. The superscript 1 and 10000 on the right figure correspond to the Mason number. The time has been made non-dimensional by $1/\dot{\gamma}$ for the periods of shear and by $Pe/\dot{\gamma}$ for the periods of rest.

The frequency of the peaks of S_{nem} during the periods of shear can be related to Jeffery's orbit of an isolated $AR7$ particle. We have reported in Figure 4.13a the evolution of the angle ϕ (see section 3.1.1) of an $AR7$ particle in a shear flow with an infinite Péclet number ($Pe = 10^4$). The particle was initialized with its direction vector pointing to the flow direction (x-axis) corresponding to $\theta = 0$ and $\phi = 0$. As θ remains equal to zero throughout the simulation, it is not reported hereafter. The particle rotates in 28.6 units of strain, however owing to the symmetry of its shape, only a half rotation allows bringing back the particle to its initial state in 14.3 units of strain. One can notice that this strain corresponds to the separation of the peaks of S_{nem} in Figure 4.12a. Note that the particle spends on average more time aligned with the flow, corresponding to angles where the viscosity is lower than when particles are perpendicular to the flow approximately equal to $\sim \pi/2$ ($\pm \sim \pi$).

The evolution of the viscosity as a function of the strain for the high Mason number regime is reported in Figure 4.14b. One can relate, once again, the oscillations of the viscosity to the mean orientation of the particles. Particles aligned with the flow show an important deviation of the mean direction vector in the y direction (see Figure 4.12b). In this case the suspension becomes highly nematic (see Figure 4.12a), and the viscosity is the lowest (see Figure 4.14b). This behavior does not exist in the low Mason number regime as the suspension remains fairly isotropic throughout the simulation due to the ordering caused by electrostatic interactions.

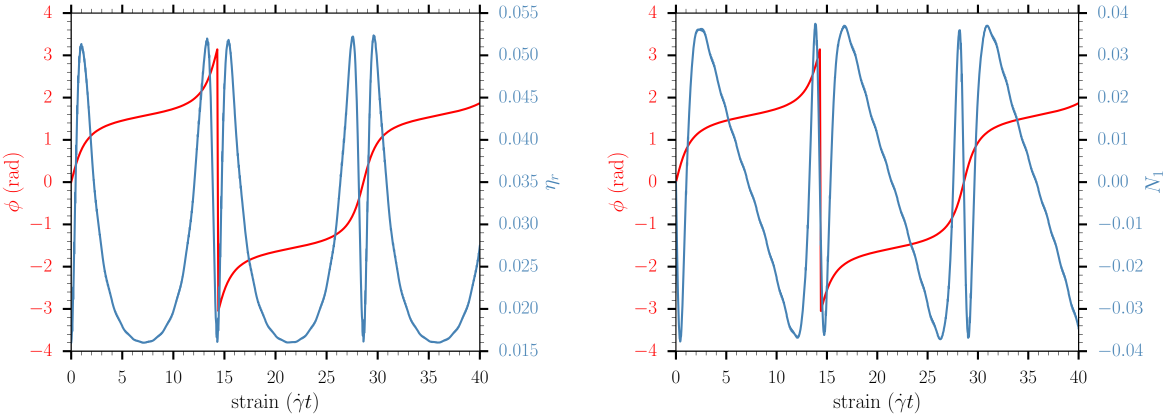

(a) Relative viscosity

(b) N_1

Figure 4.13: Viscosity (left) and normal stress difference (right) and angle ϕ evolution for one $AR7$ particle as a function of the strain.

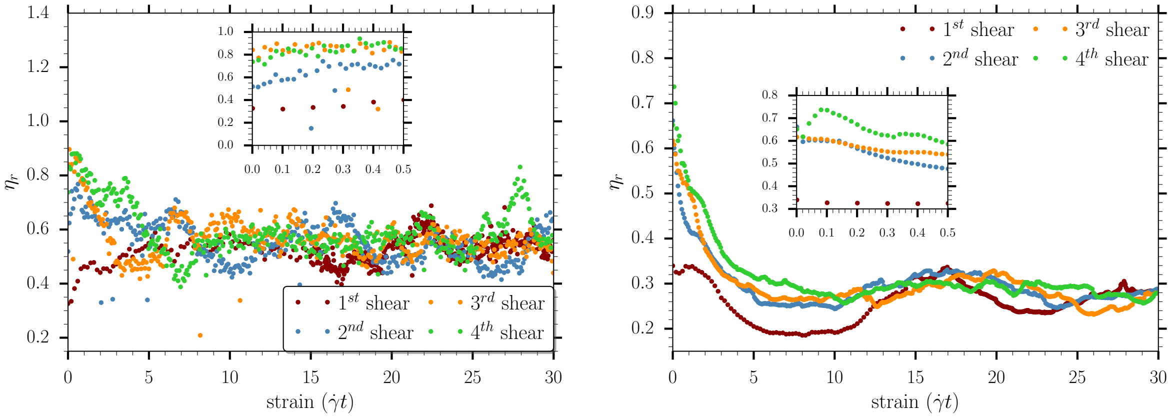

(a) Low Mason number regime

(b) High Mason number regime

Figure 4.14: Evolution of the viscosity as a function of the strain for the low Mason number regime (left) and the high Mason number regime (right) over the four periods of shear. The insets are a zoom over the first 0.5 strain units.

Let us now focus on the evolution of the viscosity over the different periods of shear. Concerning the low Mason number regime, the viscosity of the second, third and fourth shear periods behave the same way (see Figure 4.14a). All these periods of shear have a similar initial viscosity value, indicating that the microstructure at the end of the periods of rest must be also similar (see the inset in Figure

4.14a). Then, one can observe a shear-thinning of the suspension in a time dependent fashion over the first five units of strain, characteristic of thixotropic suspensions. Finally, the viscosity converges around $\eta_r = 0.65 \ \pm 0.15$. The first shear period does not exhibit shear-thinning because the particles were initialized randomly. On the contrary, one can observe a slight shear-thickening due to the building up of aggregates. Concerning the high Mason number regime, the shear-thinning behavior is more important than at low Mason number, and the final viscosity is equal to $\eta_r = 0.3 \pm 0.05$ for each of the periods of shear. The increase of the Mason number reduces both the value and the dispersion of the viscosity.

Note that the initial viscosities at the beginning of the shear periods are the same for both the low and the high Mason number regime, indicating a similar microstructure at the end of the rest periods. Moreover, if one relates the viscosity of the high Mason number regimes to the deviation of the mean vector (see Figure 4.12b), it appears that each average spatial orientation corresponds to a viscosity. This observation is in line with the works from Bihannic and coworkers [5] and Philippe et al. [22]. These authors were able to reproduce the experimental shear-thinning behavior of purely repulsive clays (ionic strength 10^{-5}M) using the following ad hoc modeling. They assumed the viscosity could be written with Quemada's model $(1 - \phi_{eff}/\phi^{*})^{-2}$ [25] where $\phi_{eff} = \alpha\phi$, and α would be some shear dependent factor accounting for the preferred orientation of the platelets. They built some model that will not be detailed here to associate their SAXS patterns to some average orientation vector (u_x, u_y, u_z) and Philippe et al. [22] observed experimentally some correlation between alpha and the anisotropy factor $(u_x/u_y)^2$, leading to the model:

$$\eta_s = \eta_f \left(1 - \frac{(u_x/u_y)^2 \phi_{sphere}}{\phi^{*}}\right)^{-2} \tag{4.7}$$

where η_s is the suspension viscosity, η_f the fluid viscosity, $\phi_{sphere} = 4/3R\phi/t$ with R the radius of the particle and t its thickness, and ϕ^{*} stands for the packing volume fraction. In their study, the authors considered $\phi^{*} = 1$. Using this model, Philippe et al. could describe the shear-thinning behavior of beidellite for a volume fraction ranging from $\phi = 0.0038$ to 0.0145 [22]. Note that the model was validated over the totality of the volume fraction range studied and for high enough shear stress, indicating that it was able to take into account complex hydrodynamic interactions such as lubrication. The fact that the model was valid only above a minimal shear stress increasing with the volume fraction indicates that it is not valid when electrostatic interactions drive the suspension's behavior. Therefore, one can conclude that this model is only valid when the hydrodynamic interactions prevail over any other forces (Brownian or electrostatic), which corresponds to the high Mason number in the present study. Note also that due to the low ionic strength used by Philippe et al. [22], the model was only validated for non-aggregated initial structures. We emphasize that the main result of the study from Bihannic et. al [5] and Philippe et al. [22] is that the viscosity is strongly related to the anisotropic factor (u_x/u_y).

Although the initial state before the start-up shear is an aggregated structure, we first tried to apply similar reasoning to compute the viscosity of the suspensions at $Ma = 10^4$. The evolution of the viscosity is only presented for the second and third shear periods as we have seen that the suspensions were exhibiting similar shear-thinning behavior. We have reported in Figure 4.15 model (4.7) referred to as "model 1", using the average orientation vector measured in simulation. If this model is able to capture the shear-thinning and the correlation between viscosity and average orientation qualitatively, one can see that it overestimates the dependence of the viscosity on the orientation of the particles and underestimate the average viscosity.

In order to adapt this model to the present system, we replaced the ϕ_{sphere} from equation (4.7) by the volume fraction of the platelets including the spheres $\phi_{platelet}$ and we left the exponent on the anisotropy factor and the value of ϕ^* as free parameters. The model called "model 2" in Figure 4.15 corresponds to the following equation:

$$\eta_r = -1 + \left(1.0 - \frac{(u_x/u_y)^{\alpha}\phi_{platelet}}{\phi^*}\right)^{-2}, \tag{4.8}$$

where u_x and u_y are the coordinate of the average direction vector of the particles measured in the simulation, and with $\phi^* = 0.65$, $\alpha = 0.4$ and $\phi_{platelet} = 0.108$. This model, based on the evolution of the average direction vector, captures quite well the shear-thinning behavior and the dependence of the relative viscosity on the particles' spatial orientation. One can wonder if the values of α and ϕ^* used for a suspension of $AR7$ at $\phi = 0.05$ depend on the volume fraction or to the small aspect ratio of the present $AR7$ compared to natural clays. Further investigations for different volume fractions and aspect ratios would be necessary to conclude on the final form of the scaling.

We stress once again that the "model 1" and "model 2" only relate the viscosity to the anisotropy factor u_x/u_y. Note that the fit of the viscosity in Figure 4.15 could have been realized with the following simpler model:

$$\eta_r = A + B\,\frac{u_x}{u_y}, \tag{4.9}$$

where A corresponds to a constant value sligthly lower than the minimal viscosity observed during the simulation, and B a free parameter. This model is reffered to as "model 3" in Figure 4.15, and $A = 0.17$ ($\eta_{min} = 0.23$) and $B = 0.3$. We emphasize that this "model 3" does not have any power scaling but the value of A must be changed according to to the system studied. One can notice that the "model 3" captures fairly well both the shear-thinning and the correlation between viscosity and average orientation. To prove that "model 2" and "model 3" can also capture the shear-thinning of non aggregated system, we have reported in Figure 4.16 the case $\kappa D = 1.46$ to reproduce similar conditions to the study of Philippe et al. [22]. As in the experiments of these authors, when no flow is applied to the suspension, it structures in a Wigner glass. Moreover, the Mason number is important enough to consider electrostatics insignificant. Note that $A = 1.14$ for the "model 2", the rest of the parameters remains unchanged for both models. One can conclude that in this $Ma \gg 1$ and $Pe \gg 1$ regime the hydrodynamic viscosity of a suspension of anisotropic particles can be described using only the average direction vector parallel to the flow and to its gradient, in line with the literature [5, 20, 22].

In this section, we have seen that at low Mason number and for the totality of the applied cycles, the suspension was quite isotropic, in contrast to the high Mason number regime, for which the suspension was nematic during the periods of shear. We have seen that during a start-up shear, the suspension was undergoing a shear-thinning behavior for both regimes, which is characteristic of thixotropy. Finally, we could relate the shear-thinning and the oscillations of the viscosity to the average orientation direction vector for the high Mason regime. This is in line with the studies from Bihannic et al. [5] and Philippe and coworkers [22] although we used simpler viscosity expressions depending only on the orientation vector. The study of the microstructure will bring us information concerning the origin of the thixotropy

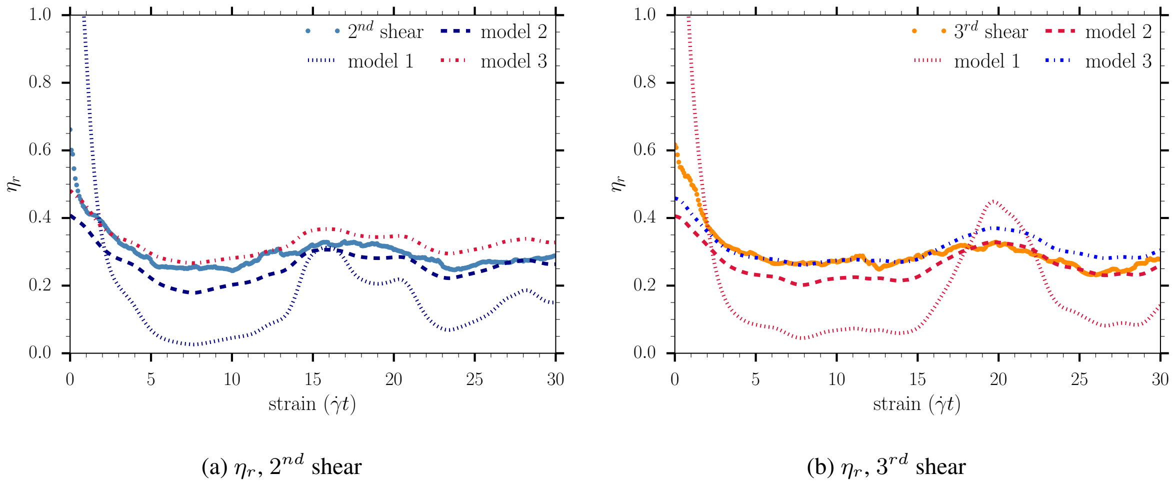

(a) η_r, 2^{nd} shear

(b) η_r, 3^{rd} shear

Figure 4.15: Fit of the relative viscosity obtained during the second shear, with the model proposed by Bihannic et al. [5] and Philippe and coworkers [22] referred to as η_r Phil. (dotted curve) and a fit of this model using different parameters (dashed curve).

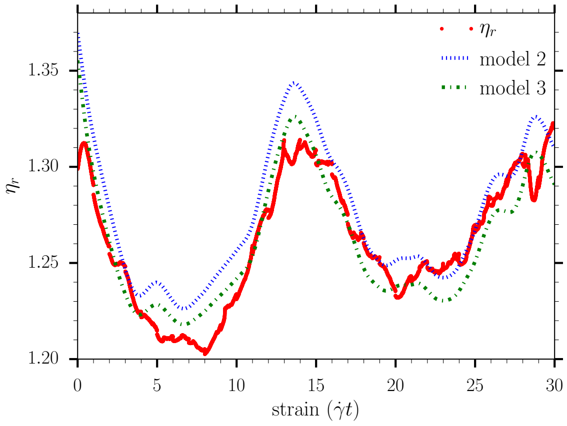

Figure 4.16: Relative viscosity for $\kappa D = 1.46$ using "model 2" (equation (4.8)) and "model 3" (equation (4.9)) at $Ma = 100$.

observed for these suspensions of $AR7$ particles.

2.3 Microstructure of the suspension at rest

In the previous section, we have seen that the microstructure at rest was always very similar irrespective of the Mason number regime studied during the periods of shear.

The radial and orientational distribution functions during the rest periods are reported in Figure 4.17. We have also reported in Figure 4.17 the functions of the equilibrium structure studied in section 2.3.1, for $\phi = 0.05$ and $\kappa D = 14.6$. These functions are referred to as "Random" in Figure 4.17. The first number in the brackets of the legends used in these figures corresponds to the Mason number applied during the periods of shear, and the second to the current period of rest. Then, $(10^4, 3^{rd})$ corresponds to the third period of rest, for $Ma = 10^4$. At first sight, the radial distribution function reported in Figure 4.17a is independent of the Mason number applied during the periods of shear and of the current resting period studied. One can observe a sharp peak at a distance R characteristic of T-shaped configurations. This is confirmed by the angular correlation function, which has a value of -0.5 (see Figure 4.17b). However, one can note the variation of peaks of the radial distribution functions (see the inset in Figure 4.17a). As no clear relation between the Mason regime and the intensity of the peak appears, one could wonder if this difference comes from a poor statistical convergence.

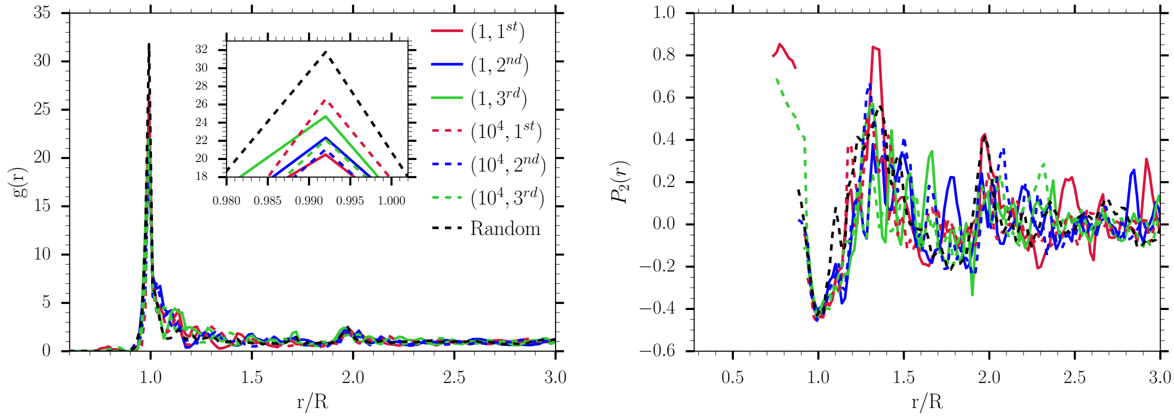

(a) Radial distribution function

(b) Angular correlation function

Figure 4.17: Radial distribution function (left) and second Legendre polynomial (right) for the two Mason regimes studied. The legend must be read as follow : (Mason number applied during the periods of shear, Number of the rest period currently studied). Then $(1, 2^{nd})$ correspond to the second period of rest of $Ma = 1$. The term "Random" designs the suspension studied in chapter three, where the equilibrium structure was studied after a random initialization of the particles. The same legend is used in both figures and the inset in the left figure corresponds to a zoom on the peaks of $g(r)$.

If one focuses on the structure of particles in contact, one can observe that the contact angle's probability function does not depend on the Mason number or the resting period studied (see Figure 4.18a). The probability of the contact angle remains very low for $\theta < 50$ degrees, then increases and reaches its maximum value at $\theta = 90$ degrees. Note that some simulations exhibit a small peak at $\theta = 10$ degrees, corresponding to OC configuration, and others at $\theta = 70$ degrees. We have already seen such behavior during the study of the microstructure without background flow, but these peaks disappear with a larger simulation time (see "Random" in Figure 4.18a).

The static structure factor is reported in Figure 4.18b. Note that only the value of $\lim_{q\to 0} S_L(q)$ varies with the simulation considered. However, these values do not seem to depend on the Mason number regime: for $Ma = 1$, one can observe $S_L(0) = 3.6$ at the first rest, 1.9 at the second and 4 at the third. Longer simulations should be carried out to really determine if the periods of shear play a role in the compressibility of the suspension. Nonetheless, we can conclude that the suspensions are evolving toward a phase separation, as observed in the third chapter and represented in Figure 4.18b as the

"Random" simulation.

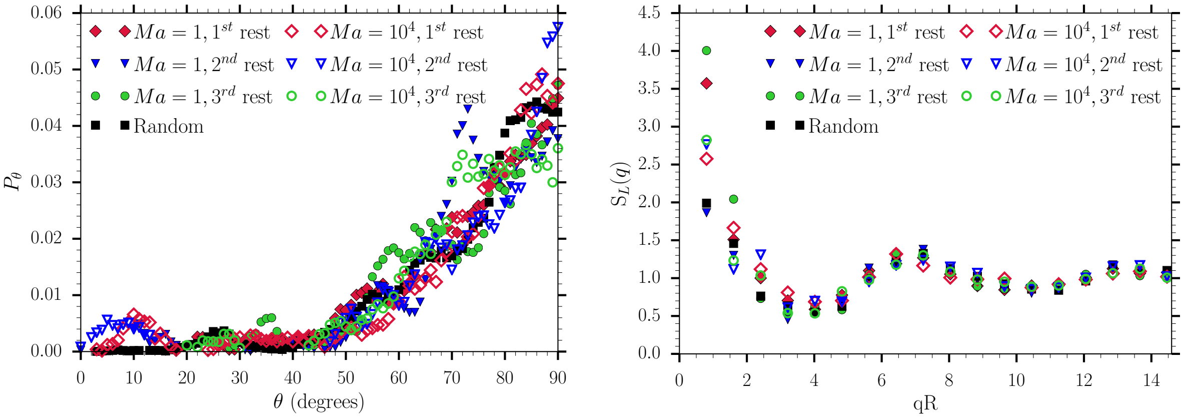

(a) Probability of the contact angle (b) Static structure factor

Figure 4.18: Probability of the contact angle (left) and the static structure factor (right) for the suspensions at rest.

To conclude, the microstructure of the suspensions leading to an aggregated structure at rest seems to depend neither on the number of cycles nor on the Mason number regime during the periods of shear, *i.e.*, the microstructure of the suspension of $AR7$ particles do not depend in a major way on the history of the suspension. We will see later in this manuscript (see section 4) that suspensions of particles with long-range repulsions have a strong dependence on their history. We have seen that even if we carry out intermittent flows over a short period of time, the suspensions structure quickly. The suspensions undergo a shear-thinning behavior in a time-dependent fashion, and given the fact that the suspensions structure at rest, we can conclude that suspensions of $AR7$ particles are thixotropic.

2.4 Microstructure of the suspension under shear

As the suspensions behave differently depending on the Mason number regime studied, we have decided to study the microstructure of the suspensions at low and high Mason number separately.

2.4.1 High Mason number

In this regime, hydrodynamic interactions are strong enough to prevent the aggregation of the particles through electrostatic interactions. In section 2.2, we have seen that during the four different periods of shear composing the entire cycle simulated, the suspension was highly nematic, with particles having their normal vector pointing to the direction of the gradient of the flow. The snapshots at the end of the shear periods are reported in Figure 4.19. All of these structures seem similar and it seems impossible to distinguish them as a function of the number of shear cycles applied. Then, instead of studying the microstructure at each shear period separately, we have chosen to average the data to increase the sampling for the statistics of the measured quantities.

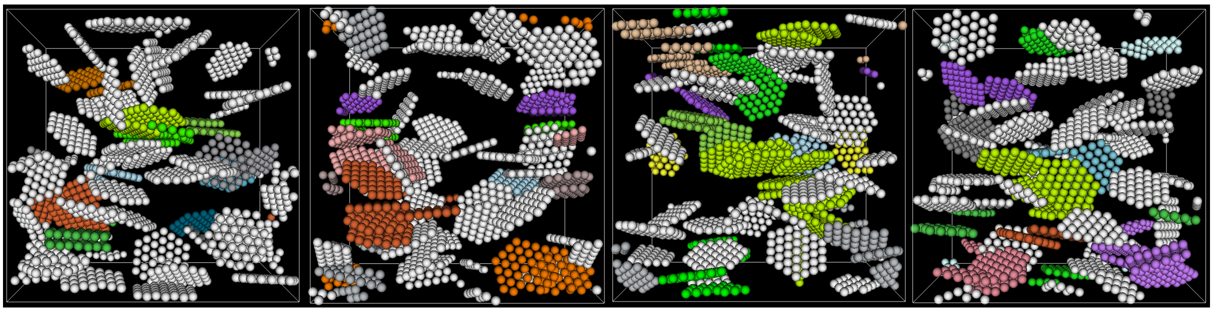

(a) First shear (b) Second shear (c) Third shear (d) Fourth shear

Figure 4.19: Snapshot of the final microstructure obtained after the application of a shear flow with $\phi = 0.05$, $\kappa D = 14.6$ and $Ma = 10^4$.

As the suspension of particles is no more isotropic, we define a pair distribution function $g(\mathbf{r})$ in the x-y plane (flow-gradient plane) and a second pair distribution in the y-z plane (gradient-vorticity plane). The details of the mathematical definition can be found in Appendix 3. To describe the orientation of the particles, we define an angular distribution function $P_2(\mathbf{r})$ on a grid, where the value of this function on each bin is equal to the average of the second Legendre polynomial of the particles belonging to this bin (see Appendix 3 for the description of the grid). Note that only extreme values, above 0.8 and below -0.4, are significant as a value of zero can be obtained either for totally uncorrelated particles, or with the sum of a pair of particles in a T-shape configuration, for which $P_2(\mathbf{r}) = -0.5$, and a pair of nearly parallel particles, for which $P_2(\mathbf{r}) = 0.5$. As for the pair distribution function, the angular distribution function was defined in both the x-y and y-z plane.

In Figure 4.20 are reported the radial and the orientational distribution functions. One can clearly observe in Figure 4.20a a layering of the particles in the shear direction for $|y| > R$, indicating that the suspension is dilute enough to allow particles to move on average in parallel planes and, owing to the high value of the orientational function (see Figure 4.20b), particles are parallel to one another. Note also the high probability of particles forming a kind of "eye" with closed trajectories (see Figure 4.20a for $|x| < R$ and $|y| < R$). These particles remain parallel to one another as indicated by $P_2(\mathbf{r}) > 0.9$ which is a characteristic of tactoids.

We want to emphasize that even if the number of tactoids is small, the long time needed by a tactoid to be torn apart induces very large statistical weights. Indeed, just by studying the distribution functions in the x-y plane, we could have thought that particles were mainly in a tactoid configuration. In contrast, the radial distribution functions in the y-z plane reported in Figure 4.21a shows that particles are uniformly spread inside the simulation box. However, one can observe some hot spots at $z = 0$ and $|y| < 0.27R$ corresponding to particles parallel to one another (see Figure 4.21b): the tactoids. Note also that most of these points are at a distance greater than to half of the particles' thickness, indicating that strong lubrication occurs between the particles preventing them from stacking and slowing down the sliding due to the coarse-graining of the $AR7$ particles.

To summarize, at high Mason number the aggregates formed during the resting periods of the suspension are totally destroyed. This destruction of the structure is often called shear rejuvenation in the literature [16] and is in line with the expected behavior of clay particles. During the periods of shear, the particles are on average aligned with the flow, which is well explained by the fact that particles tend to minimize their surface tractions by following Jeffery's orbits resulting in a highly nematic state previously observed. Note that some tactoids are formed in this regime, which tends to leave more free volume and lowers overall viscous dissipation, in line with the work from Meng & Higdon [15].

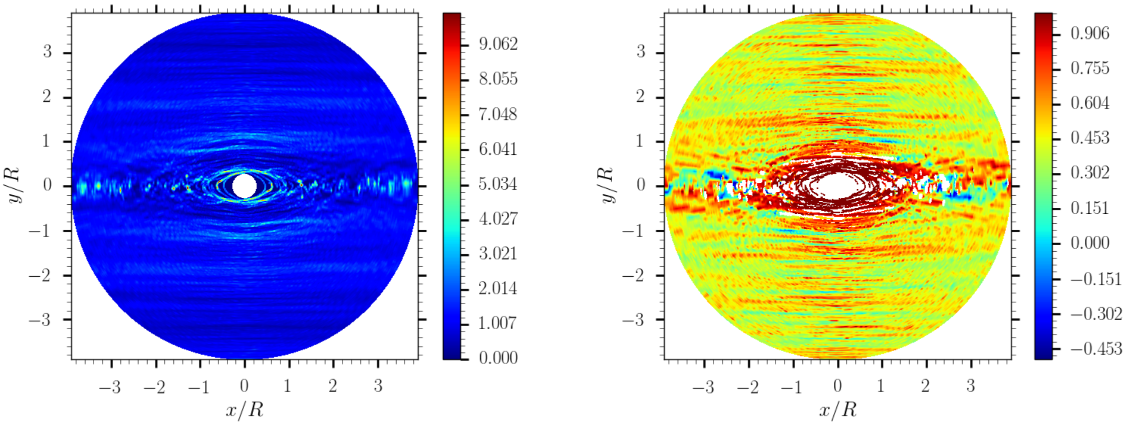

(a) Radial distribution function in the x-y plane (b) Orientational distribution function in the x-y plane

Figure 4.20: Radial (left) and orientational (right) distribution function in the x-y plane averaged over the periods of shear at $Ma = 10^4$.

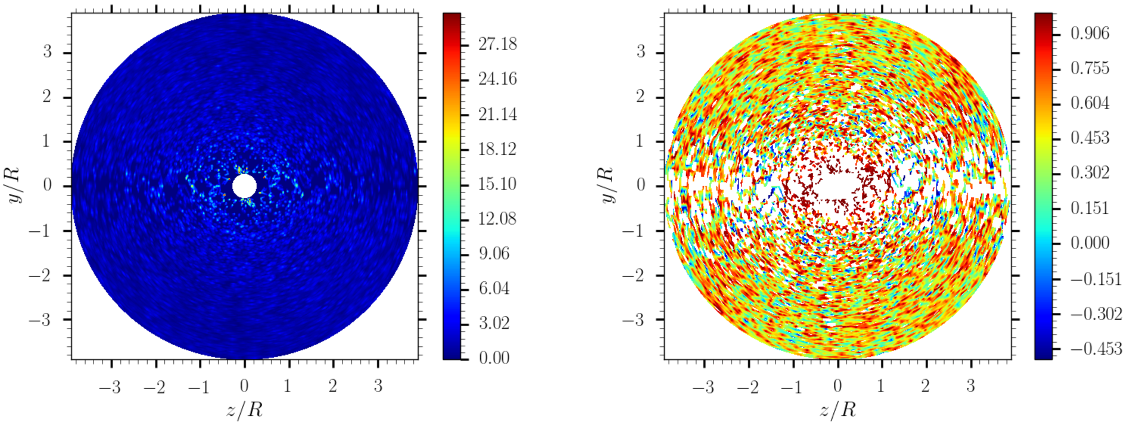

(a) Radial distribution function in the y-z plane (b) Orientational distribution function in the y-z plane

Figure 4.21: Radial (left) and orientational (right) distribution function in the y-z plane averaged over the periods of shear at $Ma = 10^4$.

2.4.2 At low Mason number

At low Mason number, the shear flow does not generate hydrodynamic forces strong enough to fully disaggregate the plate particles. Shear tears the particles with the lowest bond energy apart. This event seems to be situated in the region with the lowest density. This will have as a consequence the formation of several aggregates with different sizes. The small number of particles simulated does not allow us to obtain meaningful statistics on the size distribution of these smaller aggregates. In Figure 4.22 are reported the snapshots of the microstructure obtained at the end of the shear periods. Note that the structures do not seem influenced by the history of the suspension.

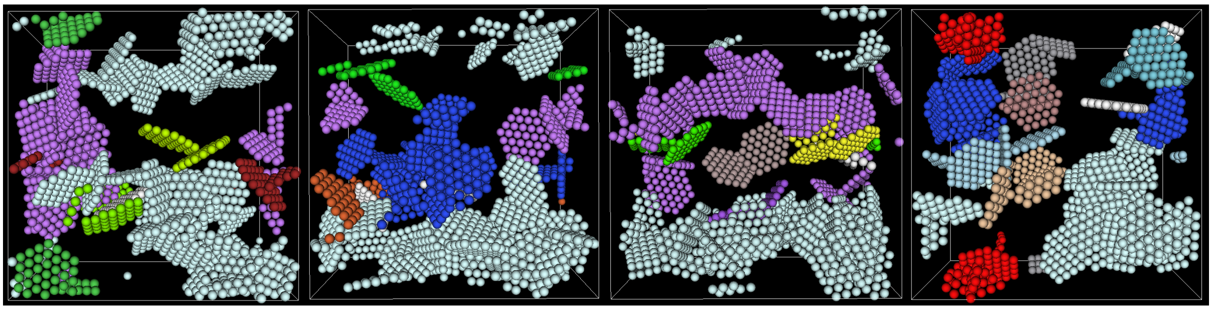

(a) First shear (b) Second shear (c) Third shear (d) Fourth shear

Figure 4.22: Snapshot of the final microstructure obtained after the application of a shear flow with $\phi = 0.05$, $\kappa D = 14.6$ and $Ma = 1$.

Let us now describe the microstructure during these periods of shear quantitatively. One should recall that the suspension remains fairly isotropic throughout the periods of shear when $Ma = 1$ (see Figure 4.12a). Therefore it is consistent to study first the one dimensional radial and orientational distribution functions reported in Figure 4.23. Note that the radial distribution functions have a sharp peak at a distance R, as the one observed at rest. These particles are on average in a T-shape configuration as indicated by the value of the second Legendre polynomial $P_2(R) = -0.4$, and as observed during healing periods. However, the intensity of the peaks of $g(r)$ ranges from 6.4 to 11.4 while it was ranging from 19 to 26 during rest. This drop in the intensity indicates that the T-shape configuration is less favored during shear than during rest. Indeed, if we compute the average probability of having a contact angle above 85 degrees, we obtain approximately 0.24 at rest and 0.17 when the shear flow is applied (see Figure 53a in the Appendix).

Broadly speaking, the application of shear flow at $Ma = 1$ slightly disturbs the microstructure generated during the healing periods by increasing the number of spatial configurations represented in the simulations. As most of the particles remain in contact, we cannot talk about shear rejuvenation, which requires stronger hydrodynamic forces. We also observed that the application of successive periods of shear and rest do not influence the microstructure as the measured quantities are not correlated with the suspension's history. Then for the rest of this section, we will compute quantities as an average over the four different periods of shear.

We have reported in Figure 4.24 the two dimensional distribution functions in the x-y plane. The function exhibits a depletion area for distances less than R as already observed in the one dimensional $g(r)$. Beyond this depletion appears a high density crown corresponding to the peak in Figure 4.23a. As expected, particles belonging to this high density area are perpendicular to the central particle (see the orientational distribution in Figure 4.24b). Note also that the probability density is higher in the flow direction ($y = 0$) than in the gradient direction ($y = R$). We propose the following explanation. Consider a dimer of particles in a T-shape configuration with the particle on the left perpendicular to the flow and referred to as particle 1, and the particle 2 on the right aligned with the flow, *i.e.*, "⊢". At this instant, the center of gravity of this dimer is situated on the y-z plane defined by the normal of the particle 2. Following Jeffery's orbits' dynamics, the rotation of this dimer is driven by particle 1. This particle starts to rotate, but its double layers quickly encounter the double layers of opposite charges from particle two. When the electrostatic pressure is high enough to prevent the reduction of the angle between the two particles, the dimer will rotate. Note that such a configuration could have led to the creation of a tactoid at high enough Mason number.

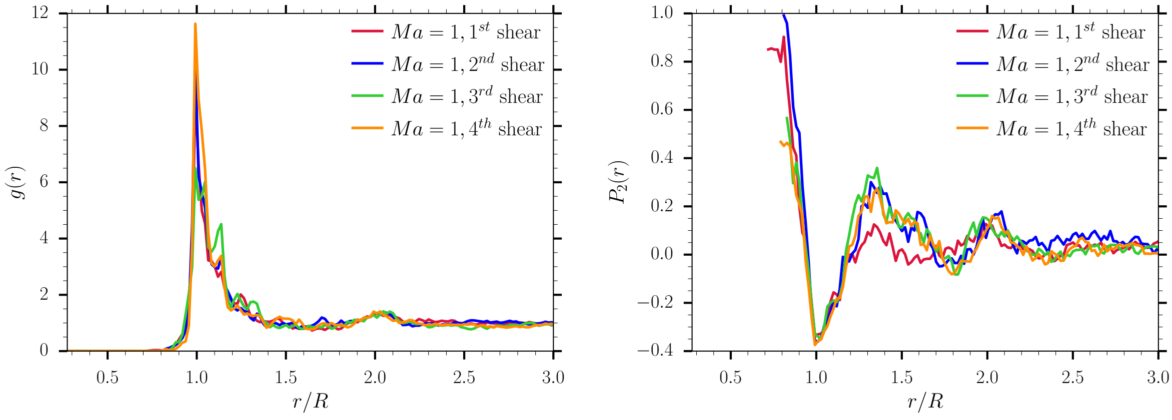

(a) Radial distribution function

(b) Angular distribution function

Figure 4.23: Radial (left) and angular (right) distribution function at $Ma = 1$, $\kappa D = 14.6$ and $\phi = 0.05$.

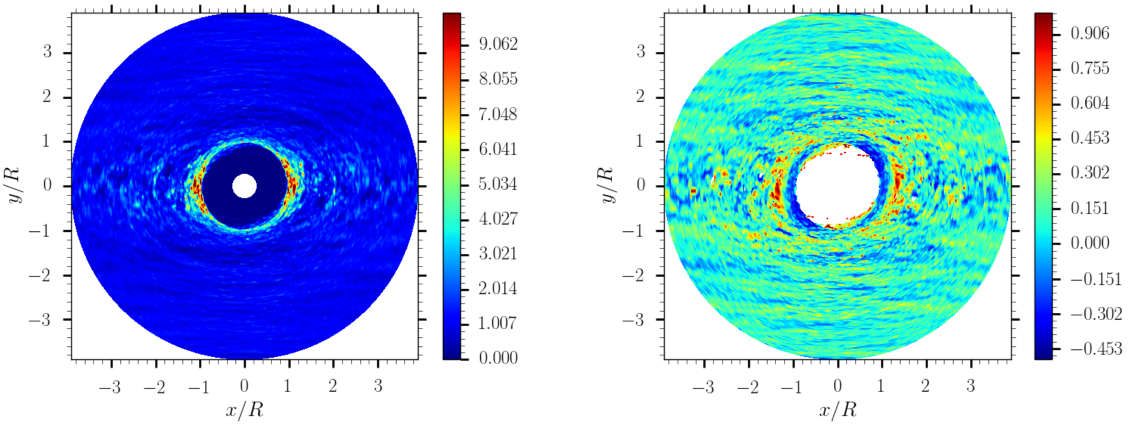

(a) Radial distribution function in the x-y plane

(b) Orientational distribution function in the x-y plane

Figure 4.24: Radial (left) and orientational (right) distribution function in the x-y plane averaged over the shear periods and with $Ma = 1$.

Let us now focus on the structure in the y-z plane, normal to the flow direction, represented in Figure 4.25. Once again, one can observe a depletion area around the particles, indicating that tactoids are forbidden. Note that the probability of presence is higher in the vorticity plane ($y = 0$). This is suggestive of the roller structures described by Pignon and coworkers [23] for a Laponite suspension below the critical shear rate tearing apart even the micrometer-sized aggregate. This could also be due to planes of aligned particles sliding one over another.

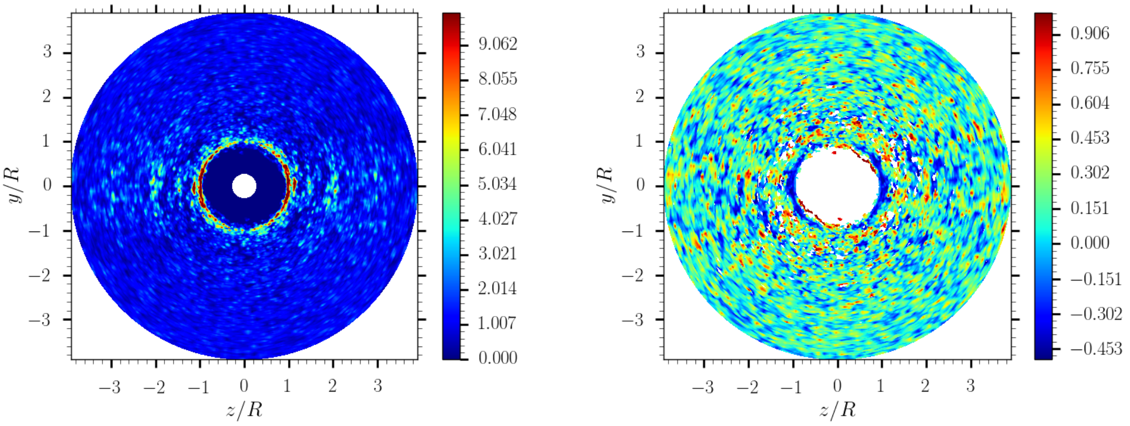

(a) Radial distribution function in the y-z plane

(b) Orientational distribution function in the y-z plane

Figure 4.25: Radial (left) and orientational (right) distribution function in the y-z plane averaged over the periods of shear at $Ma = 1$.

From the observations of the microstructure, one can conclude that suspensions do not rejuvenate during the shear at the lower Mason number reported here, i.e., $Ma = 1$.

2.5 Summary

In this section, we have studied the thixotropic behavior of two suspensions of $AR7$ particles with $\phi = 0.05$ and $\kappa D = 14.6$. Intermittent flows were applied to both suspensions, with four periods of shear and three periods of rest. The shear flows applied were at $Ma = 1$ in one case and $Ma = 10^4$ in the other for the entire protocol for each suspension.

Concerning the high Mason number regime, the application of shear led to a highly nematic phase, with particles having their normal vector aligned on average with the flow gradient. We observed the presence of some tactoids, as expected for hard platelets following the work from Meng & Higdon [14]. Note that larger aggregates (*i.e.* not tactoids) did not survive in the flow, and therefore the flow can be considered as shear rejuvenation. In contrast, the low Mason number regime allowed the formation of clusters with particles in T-shape configuration. Note that the history of the suspensions, *i.e.*, the number of previous periods of shear or rest, did not affect their microstructure.

At rest, the suspensions were once again not influenced by their histories. Particles structured in the same fashion as the one described in section 2.3.1, *i.e.*, in T-shape configuration and evolving towards phase separation.

Following the work from Martin and coworkers [13], the healing process is the key in the thixotropic behavior of suspensions of $AR7$ particles. During this period, the formation of aggregates increases the viscosity of the suspension (expected but not observed in this study), and the sudden application of shear breaks the most fragile bonds leading to a drop of the viscosity in a time-dependent fashion. This behavior is expected to occur for thixotropic suspensions. In the high Mason number regime, as no aggregate survives, the viscosity is lower than at $Ma = 1$. The viscosity could also be related using different simple models based on the average spatial orientation of the particles, in line with the studies from Bihannic and coworkers [5] and Philippe et al. [22].

3 Rheological dependence on the electrostatic range of interactions

We have shown that the $AR7$ model used with the ASD code was able to capture the thixotropic behavior of clay particles. Among the hallmarks of clay suspensions, one can cite, for instance, the elastic behavior at low strain and the shear-thinning at large strain, and the propensity of the suspensions to exhibit overshoot stress during start-up shear. Both the elastic behavior and the overshoot stress are expected to be influenced by the initial microstructure of the suspension [16] and by the interactions between particles. It is therefore interesting to realize a systematic study of the response of different initial spatial configurations to start-up shear at different Mason numbers.

3.1 System simulated

To study the rheological response of suspensions to start-up shear, the microstructures obtained at $\phi = 0.05$ in section 2 are sheared while varying the Mason number. Note that for the startup shear study we used initial microstructures obtained after an equilibration time of 25 $a^2/(2D_0)$ at zero shear. It represents half the total time used in the third chapter. One should recall the microstructures as a function of the electrostatic range of interactions:

- $\kappa D = 1.46$: Wigner glass with disconnected particles,
- $\kappa D = 7.3$: percolated structure with particles mainly in OC configuration,
- $\kappa D = 14.6$: percolated structure with particles mainly in HOC configuration and a contact angle close to 90 degrees,
- $\kappa D = 29.2$: flocculated but not fully percolated structure with particles in HOC configuration,
- $\kappa D = 73$: liquid-like structure,

These structures are sheared considering a Péclet number equal to 3.89 10^6 and the following Mason numbers: $Ma = 0.25$, 1, 4, 100, and ∞, the final corresponding to hard platelets. The high Péclet number allows to avoid any significant Brownian fluctuation, and therefore to focus on the influence of the hydrodynamic and electrostatic interactions. Here variations of the Mason number are considered as variations of the particle charge since we consider fixed particle size, fixed temperature and fixed Péclet number, so a fixed shear rate. Thus, considering $Ma = 1$ as the reference, $Ma = 0.25$ corresponds to charges multiplied by two (the electrostatic force scales as the square of the charge), and ∞ to charges set to zero.

The simulations carried out are split into two regimes: a high Mason number regime, $Ma = \infty$ and 100, where the electrostatic forces are insignificant compared to the hydrodynamic forces, and a low Mason number regime, $Ma = 0.25$ and 1 and 4, where competition between hydrodynamic and electrostatic forces occurs. The rheological behavior will, therefore, strongly depend on the range of interaction in the low Mason number regime. In contrast, a constant behavior should be observed for $Ma \geq 100$. This rheological behavior is described at low strain by the shear modulus G^* which is equal to the sum of the elastic modulus G' and the viscous modulus G''. The shear modulus relates the stress to the strain for a suspension undergoing an oscillatory flow [16]. The application of oscillatory flows to suspensions of $AR7$ particles is part of the perspectives offered at the end of this manuscript. The estimation of the storage modulus G' is instead calculated as the initial slope of the stress when plotted as a function of the strain in a startup shear test. To illustrate this we have reported in Figure 4.26 the evolution of the relative viscosity defined as $\eta_r \equiv \sigma_{12}/(\eta_0\dot{\gamma})$ where σ_{12} is the shear stress, using the convention that 1 and 2 are, respectively, the flow and the gradient directions, η_0 is the viscosity of the fluid, for $Ma = 1$. Note that the initial linear increases of η_r corresponds to $G'/(\eta_0\dot{\gamma})$. This elastic behavior is represented with the dashed lines of equation $\eta_r = G'/(\eta_0\dot{\gamma})\ \dot{\gamma}t$ in Figure 4.26b and is only observed for $\dot{\gamma}t < 0.1$, in qualitative agreement with Paineau and coworkers [20] who demonstrated the limitation of the elastic regime below 0.1 $\dot{\gamma}t$ irrespective of $\dot{\gamma}$ for suspensions of natural clays. Then, one can observe in Figure 4.26b an overshoot stress, particularly visible for long-range interactions, *i.e.*, $\kappa D = 1.46$.

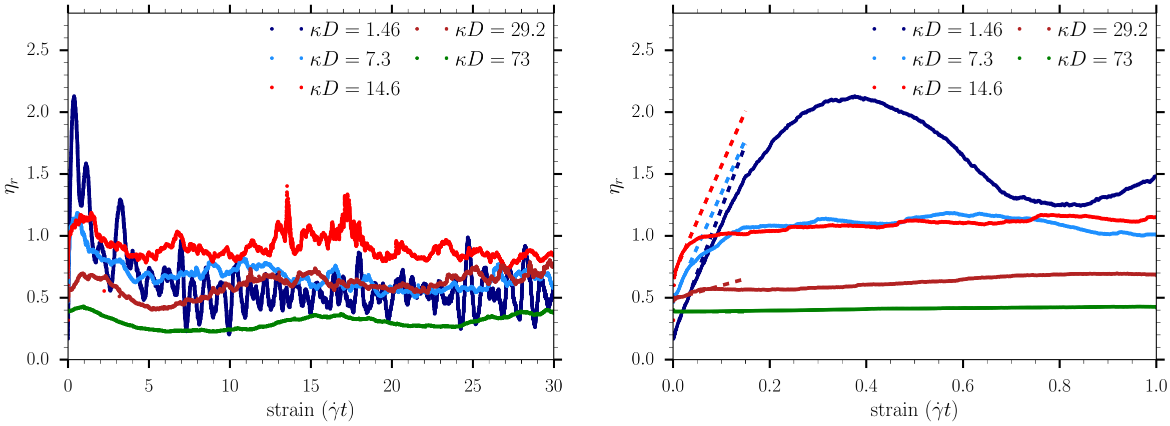

(a) Stress

(b) Stress, zoom over the first instants

Figure 4.26: Stress over the entire simulation (left) and over the first instants (right) for $Ma = 1$. The initial stresses in the right figure are fitted with dashed lines which represent $G'/(\eta_0\dot{\gamma})\ \dot{\gamma}t$.

We have gathered in Figure 4.27 the information concerning both the relative viscosity and the elastic modulus for all the interaction ranges studied, $\kappa D = 1.46$, 7.3, 14.6, 29.2, 73, and for the different Mason numbers $Ma = 0.25, 1, 4, 100, \infty$. Note that the red triangles in Figure 4.27 were extracted from

Figure 4.26.

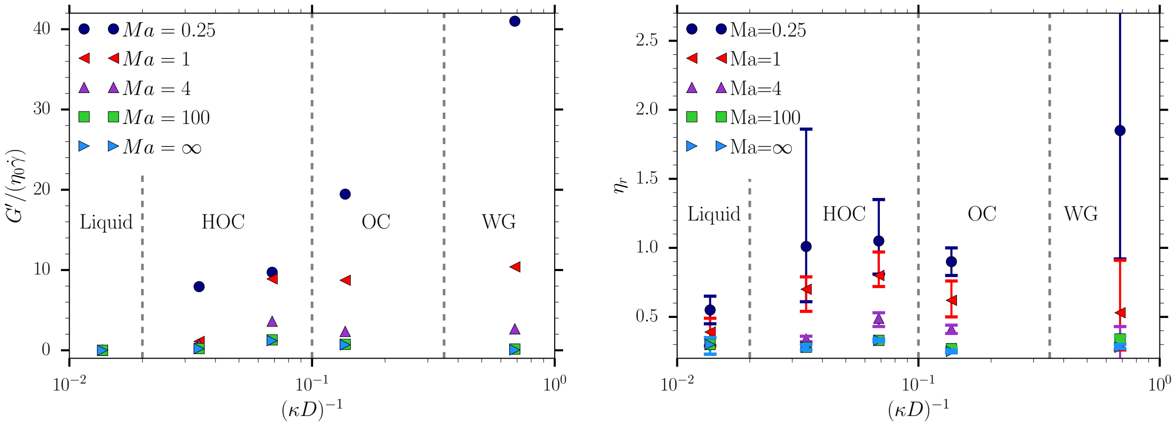

(a) Elastic modulus G'

(b) Relative viscosity η_r

Figure 4.27: Elastic modulus G' (left) and the relative viscosity η_r with its error bars (right) as a function of the non-dimensional Debye length $(\kappa D)^{-1}$.

The elastic modulus is reported in Figure 4.27a as a function of the non-dimensional Debye length $(\kappa D)^{-1}$. We stress the fact that the origin of the elasticity is different for the aggregated structures and the Wigner glass. Indeed, for the aggregated structures, elasticity comes from the separation of particles previously in contact due to the shear flow while for the Wigner glass, the elasticity is related to the deformation of the electrostatic cages. Consequently, the dependence of G' on the range of interactions can be interpreted only when the same physical mechanism is involved.

Then, for a purely repulsive system in a glassy state, the stronger the repulsions, the more the system is elastic. Note that for such a case, G' increases roughly linearly with the Mason number, *i.e.*, G' is multiplied by four between $Ma = 4$ and $Ma = 1$ and between $Ma = 1$ and $Ma = 0.25$.

The behavior of the elastic modulus for the aggregated structures deserves attention. At $Ma = 0.25$, electrostatic stresses strongly prevail over the hydrodynamic stresses and control the elasticity of the system. The increase of the range of interactions also increases the attractive interactions and consequently the elasticity of the system as shown in Figure 4.27a. Note that this remark is also valid for $\kappa D = 29.2$ corresponding to $(\kappa D)^{-1} = 3.4\ 10^{-2}$ despite the fact that the initial configuration is not percolated (we recall that we observed isolated clusters with particles in HOC configuration). One possibility is that the observed elasticity comes from the electrostatic interactions between clusters. For $4 \geq Ma \geq 1$, hydrodynamic forces are strong enough to tear the particles with the most fragile bonds apart and to break the percolated structure. Note that as the structure is not percolated at $(\kappa D)^{-1} = 3.4\ 10^{-2}$, $G' \approx 0$ due to the fact that isolated clusters are free to rotate We propose to relate the elastic modulus of larger interaction ranges to the resistance of the bonds to the breakage. The stiffness of the bonds are related to the attractive electrostatic forces of the particles with their neighbors. Given that attractive forces of particles in T-shape configuration at $(\kappa D)^{-1} = 6.8\ 10^{-2}$ and in OC configuration at $(\kappa D)^{-1} = 1.4\ 10^{-1}$ are of the same order of magnitude (see section 2.3.1), the elastic modulus is also of the same order of magnitude.

Finally, for $Ma >> 4$, the structures are instantaneously destroyed by the strong hydrodynamic forces and none of the suspensions at these conditions exhibit an elastic behavior.

Concerning the evolution of the relative viscosity reported in Figure 4.27b, one can observe that η_r is fairly constant in the high Mason number regime and increases with the reduction of the Mason number. This increase is due to both the modification of the microstructure generated by the electrostatic interactions and by the increase of the electrostatic stress. For example, the sharp increase between $(\kappa D)^{-1} = 1.4\ 10^{-2}$ and $(\kappa D)^{-1} = 3.4\ 10^{-2}$ is due to the formation of clusters and therefore to the increase of the hydrodynamic stress. Note also the reduction of η_r during the transition from HOC to OC configuration. The details and the origin of these observations are studied in the next sections.

Let us now consider the relative viscosity as a function of the Mason number reported in Figure 4.28a. At $\kappa D = 1.46$, we observe that the viscosity scales as $\dot{\gamma}^{-0.9}$. For smaller interaction ranges, η_r scales as $\dot{\gamma}^{-1/4}$. Understanding this will require further investigations. Note also that this exponent my be dependent on the volume fraction. Suspensions undergo a shear-thinning behavior, and do not exhibit any shear-thickening at a high shear rate most probably because ϕ is too low.

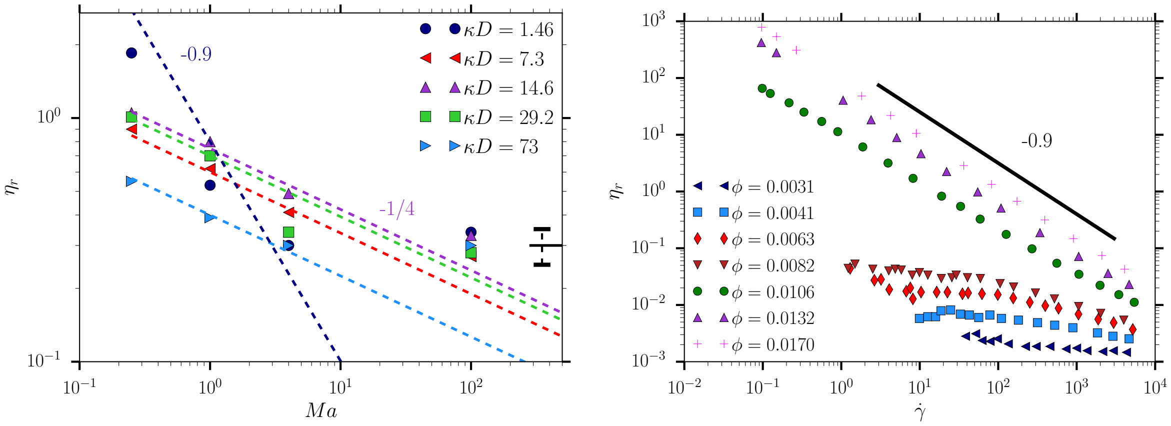

(a) η_r from our study

(b) η_r from [20]

Figure 4.28: Relative viscosity as a function of the Mason number from the simulations of $AR7$ suspensions at $\phi = 0.05$ (left) and relative viscosity of a suspension of montmorillonites at 10^{-5} M as a function of the rate of strain (right), reproduced from the Figure 5 B in ref. [20]. The black line in the left figure stands for the infinite Mason number limit.

To verify that the scaling observed was not unphysical, we compared our results with the ones from Abou et al. [1]. These authors studied Laponite suspensions and observed a shear-thinning following a scaling behavior $\eta_r \propto \dot{\gamma}^{-\alpha}$ where $\alpha = 0.5\pm0.1$. Abou and coworkers studied the rheological behavior of two suspensions, one with $\phi = 0.015$ and 10^{-4} M added salt and the second with $\phi = 0.006$ at $7\ 10^{-3}$ M added salt. Note that at the highest volume fraction, the Laponite suspension is nematic [17], while the suspensions at the lowest volume fraction are in a gel state [26]. It is possible that the discrepancy of the scaling observed by Abou and coworkers with the scaling obtained in this study for $AR7$ suspensions (for example at $\kappa D = 14.6$), is due to the volume fraction considered or to the different aspect ratio of the $AR7$ particles compared to Laponite. Due to a lack of time, we could not study the volume fraction dependence of the exponent α during this work, but it should definitely be done to complete this study.

Then, we compared our results with the study from Paineau and coworkers [19, 20] who analyzed the rheological behavior of natural clays: one type of beidellite and three different montmorillonites. We have reproduced in Figure 4.28b the evolution of the viscosity of a suspension of montmorillonites with an average aspect ratio of 188, and ionic strength of 10^{-5} M. Note that particles are highly repulsive at such a low ionic strength, and therefore the solidification of the suspension observed at high concentration is due to its evolution toward a Wigner glass state. One can observe that for the three higher concentrations of montmorillonites, the suspensions exhibit yield stress, and the viscosities follow the same power-law as the one observed for $AR7$ suspensions with long-range interactions, *i.e.*, $\eta_r \propto \dot{\gamma}^{-0.9}$. The natural clay suspensions do not exhibit any yield stress for lower concentrations, which indicates that particles are not trapped in electrostatic cages. Consequently the exponent of the power slightly decreases with the reduction of the volume fraction, ranging from $\dot{\gamma}^{-0.25}$ at $\phi = 0.0082$ to $\dot{\gamma}^{-0.15}$ at $\phi = 0.0031$. These cases can be compared to the behavior of $AR7$ suspension at $\kappa D = 73$, as it is the only condition where particles do not strongly interact on average with their neighbors. In our simulations, we observed a scaling behavior of $\dot{\gamma}^{-0.25}$, which seems to be in fair agreement with the results from Paineau and coworkers.

Our model seems to capture the rheological behavior of suspensions of clay-like particles fairly well and is in surprisingly good agreement with Paineau and coworkers [19, 20] considering the difference of aspect ratio. This might be attributed to the fact that suspensions of particles with larger aspect ratio get similar behavior to suspensions of particles with smaller aspect ratio at higher volume fraction. Moreover, the low ionic strength and long-range interactions could make the real platelets act as thicker ones. In the next sections, we will study in detail the influence of the Mason number on the rheology of suspensions of $AR7$ particles.

3.2 High Mason numbers

The high Mason number regime cases studied in this work are $Ma = \infty$ and 100. In such a regime, electrostatic interactions are insignificant compared to hydrodynamic interactions. The stress due to interactions between particles only arises from lubrication and long-range hydrodynamics. Note that this regime is similar to the one used in the previous section concerning thixotropic behavior.

In Figure 4.29a we report the evolution of the relative viscosity η_r as a function of the strain at $Ma = \infty$. The same behavior is observed at $Ma = 100$ which confirms that for both $Ma = \infty$ and 100 the hydrodynamic forces strongly prevail over the electrostatic forces. As expected for thixotropic suspensions, the suspensions undergo a shear-thinning behavior for aggregated structures corresponding to $\kappa D = 7.3$, 14.6 and 29.2. The liquid-like structure also exhibits a shear-thinning due to the alignment of the particles toward the flow-vorticity plane. One can notice that η_r of a suspension with an initial Wigner glass configuration ($\kappa D = 1.46$) slightly decreases with time. The relative viscosities of the suspensions, for both $Ma = \infty$ and $Ma = 100$, converge toward $\sim \eta_r = 0.3$ irrespective of the initial microstructure and range of interactions.

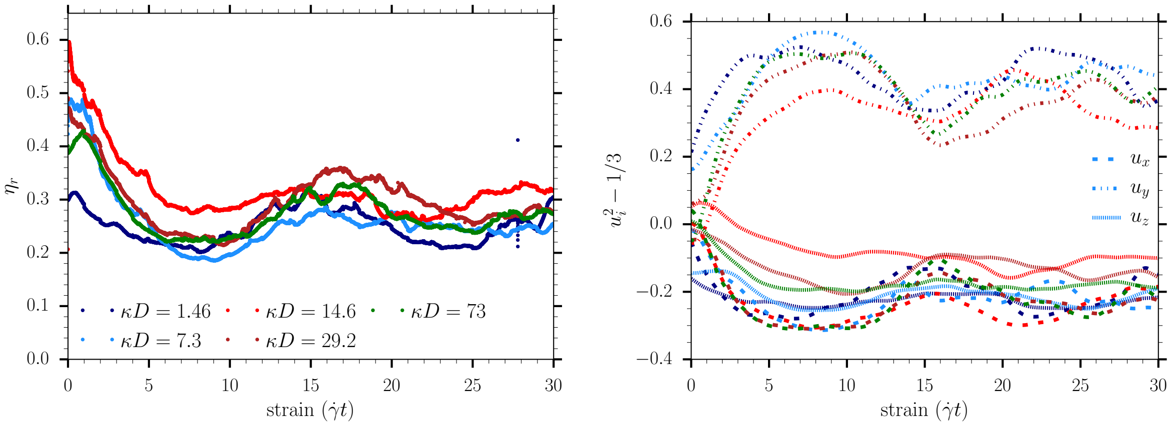

(a) Relative viscosity

(b) Deviation of the average direction vector

Figure 4.29: Relative viscosity (left) and deviation of the average normal vector (right) as a function of the strain at $Ma = \infty$. The colors used in on both figures relate to the same κD.

The initial spatial configuration seems to determine the initial viscosity and to play a role only over the initial strain, up to 12 strain. Concerning the initial value, one can note that at $\kappa D = 1.46$ and $\kappa D = 7.3$ the particles are initially more aligned with the flow direction (respectively $u_y^2 - 1/3 = 0.22$ and $u_y^2 - 1/3 = 0.165$) whereas for others interaction ranges, the microstructures are fairly isotropic ($u_y^2 - 1/3 \approx 0$). The more the particles are aligned with the flow, the lower is the stress, and therefore, the lower will be the shear-thinning of the suspension. Let us now focus on the shear-thinning behavior. The shear-thinning is related to the tilting of the director towards the direction of the gradient of the flow, as shown in Figure 4.29b. The rotation velocity of the normal vector seems independent of the initial microstructure except for $\kappa D = 7.3$ which exhibits a slower dynamics (see the initial slope of u_y in light blue color in Figure 4.29b). One possible explanation for the intensity of the shear-thinning may be related to the easiness for the particles to rotate toward the flow direction. Investigating the rotation dynamics of a pair of particles in T-shape and OC configuration could be interesting.

To conclude, one can assume that two phenomena influence the intensity of the shear-thinning: i) an aggregated structure exhibits a stronger shear-thinning behavior than a non-percolated structure, ii) an isotropic structure exhibits a stronger shear-thinning behavior than an ordered one. Then, the microstructure only influences the initial viscosity value and the shear-thinning intensity and not the steady viscosity.

Note that the shear-thinning seems to exhibit a similar relaxation time irrespective of the initial microstructure. The relaxation time τ is obtained from a fit of the relative viscosity with

$$\eta_r = (\eta_r^0 - \eta_r^\infty)exp(-t/\tau) + \eta_r^\infty \tag{4.10}$$

where η_r^0 stands for the viscosity once η_r begins decaying, and η_r^∞ the viscosity at the end of the first decay. In these simulations, $\eta_r^0 = \eta_r(\dot{\gamma}t = 1)$ and $\eta_r^\infty = \eta_r(\dot{\gamma}t = 8)$. The values of η_r^0, η_r^∞ and τ are reported in Table 4.1 as a function of the initial microstructure depending on the value of the interaction ranges κD at $Ma = \infty$ and $Ma = 100$. Note that τ has been made non-dimensional by $\dot{\gamma}$. Surprisingly the relaxation time is fairly independent of the initial microstructure even for the case at $\kappa D = 1.46$ where the shear-thinning was the less intense. It indicates that the same physical phenomenon is probably involved irrespective of the initial microstructure: the tilting of the director towards the gradient direction. One can observe some small differences between $Ma = 100$ and $Ma = \infty$ for the longest interaction ranges. However, these differences are not significant and validate the assumption that the suspensions at these two Mason numbers behave similarly.

	$Ma = 100$			$Ma = \infty$		
κD	η_r^0	η_r^∞	τ	η_r^0	η_r^∞	τ
1.46	0.31	0.21	3.33	0.29	0.20	2.71
7.3	0.49	0.20	2.18	0.49	0.19	2.33
14.6	0.59	0.27	2.69	0.51	0.28	2.70
29.2	0.44	0.23	2.67	0.44	0.23	2.67
73	0.43	0.22	2.16	0.43	0.22	2.17

Table 4.1: Relative viscosity once η_r begins to decay (η_r^0) and at the end of the first decay (η_r^∞), and the related relaxation time τ for different initial microstructures depicted by the interaction ranges κD at $Ma = \infty$ and 100. Note that τ has been made non-dimensional by $\dot{\gamma}$.

The first normal stress difference at $Ma = \infty$ is reported in Figure 4.30a. N_1 sharply increases and reaches a peak at $\dot{\gamma}t \approx 3$. Then, it decreases and reaches vanishing or negative values at $\dot{\gamma}t = 13$. The same dynamics were observed in Figure 4.13b for an isolated platelet in unbounded shear flow following Jeffery's orbits. However, N_1 in Figure 4.30a does not exhibit successive peaks related to Jeffery's period, probably due to the fact that this first peak reflects an instantaneous collective behavior of the particles aligning with the flow direction. Such behavior is not observed later in the simulation because the dynamics of the particles is not driven by a collective motion anymore. Moreover, particles spend most of their time aligned with the flow (see Figure 4.30a), *i.e.*, for angles ranging from $-\pi/4 \leq \phi_{angle} \leq 3\pi/4$, and the average of N_1 over these configurations vanishes. This could explain why the normal stresses also tend to zero with time (see Figure 4.30a). Concerning the second normal stress difference, one can observe a sort of overshoot at very short time, then N_2 decreases and vanishes at long time within statistical uncertainty (see Figure 4.30b).

To conclude, at high Péclet and Mason numbers, the microstructure at the beginning of the start-up shear influences the initial values of the viscosity but does not influence the viscosity and the normal stress differences at long times. Note that the normal stress differences go to zero at long time. As expected for clay-like suspensions, aggregated suspensions exhibit a higher initial viscosity. Note that at low Péclet number and for aggregated systems, a yield stress is often observed for clay suspensions. The initial configuration does not have any effect on the shear-thinning behavior, as it exhibits the same relaxation time irrespective of the microstructure. The shear-thinning was found once again related to the tilting of the normal vector towards the gradient of the flow, in line with most of the literature studies concerning Laponite suspensions [5, 21, 22, 23] and natural clays such as montmorillonites and beidellite [20].

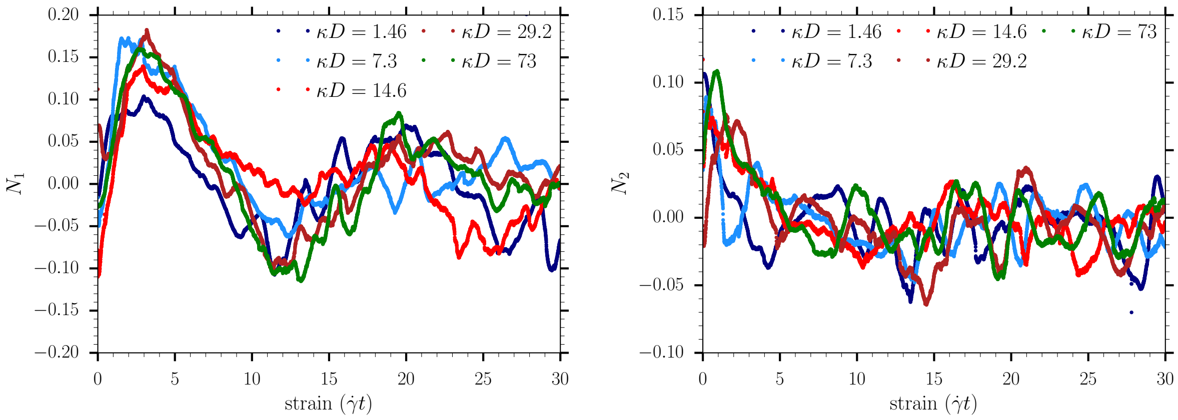

(a) N_1 (b) N_2

Figure 4.30: Normal stress differences at $Ma = \infty$ for different initial microstructures related to the interaction ranges κD.

3.3 Low Mason numbers

The reduction of the Mason number leads to more complex systems because of the increasing competition between the hydrodynamic and electrostatic interactions. The modifications of the structures formed during the healing periods is expected to be strongly related to the Mason number.

3.3.1 $Ma = 4$

At $Ma = 4$, the electrostatic forces are important enough to influence the microstructure of the suspensions, as shown in Figure 4.31. At $\kappa D = 73$, particles behave the same at $Ma = 4$ as at $Ma > 100$, *i.e.* they rotate freely, form some tactoids, and are on average aligned with the flow. For $\kappa D = 7.3$, 14.6, and 29.2 one can observe several aggregates indicating that the application of the shear broke the percolated structure observed at rest. Note that at $\kappa D = 1.46$ we observed a shear-ordering of the suspension. The particles are forming lines in the flow direction and a slightly tilted hexagonal structure in the gradient-vorticity plane (not shown here), as commonly observed in shear-ordering suspensions of spheres [11]. However, although particles seem trapped in their cages, we could notice that some of them were free to rotate due to the shear. Such behavior is reminiscent of the study of Liu and coworkers [12] who observed a multitude of crystalline structures for long-range electrostatic repulsive rods. In this study, the particles were trapped in a cage but could rotate (plastic crystal), which was associated with a modification of the spatial arrangement of the nearest neighbors. We will not extend the discussion concerning the shear-ordering as we have dedicated a section to this phenomenon later in this chapter (see section 4).

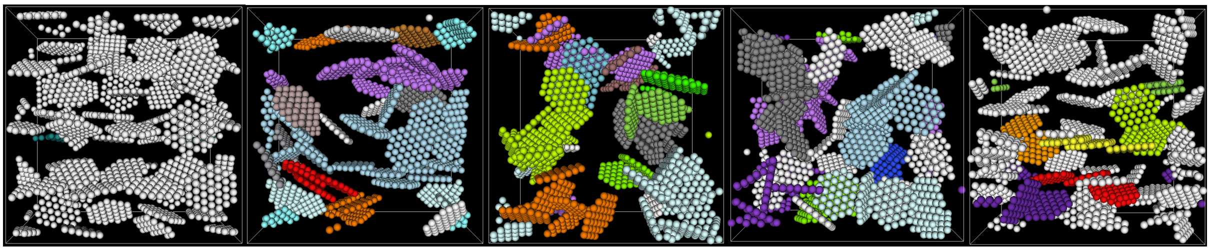

(a) $\kappa D = 1.46$ (b) $\kappa D = 7.3$ (c) $\kappa D = 14.6$ (d) $\kappa D = 29.2$ (e) $\kappa D = 73$

Figure 4.31: Snapshot of the final microstructures after a start-up shear at $Ma = 4$ in the flow-gradient plane.

As expected, at $Ma = 4$, the relative hydrodynamic viscosity η_r^h prevails over the interparticle viscosity η_r^f arising from the interparticle electrostatic interactions (see Figure 4.32). Note that we observe a slight shear-thinning of η_r^h, which can be interpreted as the reduction of the hydrodynamic radius of the largest aggregates. Indeed, one should recall that hydrodynamic viscosity is due to long-range interactions, lubrication, and the drag resistance of the particles and aggregates to the flow. Surprisingly, both the long and very short-range interaction cases, $\kappa D = 1.46$ and $\kappa D = 73$ respectively, exhibit a final hydrodynamic viscosity equal to the one observed in the high Mason regime, *i.e.*, $\eta_r^h = 0.3$. One explanation could be that particles do not aggregate in under these conditions for the ϕ studied. Then, one can observe that the final hydrodynamic viscosity follows the order $\eta_r^h(\kappa D = 14.6) > \eta_r^h(\kappa D = 7.3) \approx \eta_r^h(\kappa D = 29.2)$. This difference must be related to the microstructure of the suspension when sheared. Indeed, shearing an aggregated structure breaks it in many smaller aggregates, decreasing the hydrodynamic radius of the initial aggregate and, therefore, the net many-body stresslet. Consequently, it is crucial to study the number of aggregates and their spatial arrangement to understand the origin of the difference of η_r^h.

The number of clusters is equal to ~ 11 irrespective of the interaction range, but the average number of particles per cluster varies with κD. It is approximately equal to five at $\kappa D = 7.3$ and 14.6 and to three at $\kappa D = 29.2$. Then, if the number of particles per cluster was the only parameter driving the hydrodynamic viscosity, we would observe $\eta_r^h(\kappa D = 14.6) \approx \eta_r^h(\kappa D = 7.3) > \eta_r^h(\kappa D = 29.2)$. That is why one should also characterize the structure of these aggregates. At $\kappa D = 7.3$, the OC configuration is highly favored compared to HOC configuration, in contrast to cases $\kappa D = 14.6$ and $\kappa D = 29.2$ whose particles are in HOC configuration (see Figure 53b). For the same number of particle per cluster, an aggregate with particles in HOC configuration will have a larger hydrodynamic radius than if the particles were in OC configuration, and therefore a higher viscosity. Then, although $\kappa D = 7.3$ generates larger clusters than $\kappa D = 29.2$, they probably exhibit a similar hydrodynamic radius, which could explain why they have the same final hydrodynamic viscosity. To conclude, this qualitative discussion shows that the viscosity cannot be linked easily to only one parameter such as the number of clusters or the average number of particle per cluster. We observe that a more complete description of the microstructure of the suspensions is required, in particular at the level of the internal structure of the clusters that survive the shear flow. One solution could have been to use the same reasoning as Seto and coworkers [27]. These authors studied the restructuring of colloidal aggregates composed of attractive spheres in shear flow using Stokesian Dynamics. In their model, authors take into account neither the lubrication forces nor the Brownian motion, which are very demanding computationally. To characterize a cluster they used two parameters, the first one being its radius of gyration, and the second one being its effective volume fraction (see Appendix A in ref. [27]) used to represent its compaction. The application of this reasoning for clay-like particles requires larger simulation boxes to allow clusters to rotate, and an increase of the number of particles to increase the sampling for the statistics of the measured quantities. However, given the number of particles require and the computational cost of hydrodynamic interactions, such a study is not doable with the current ASD version.

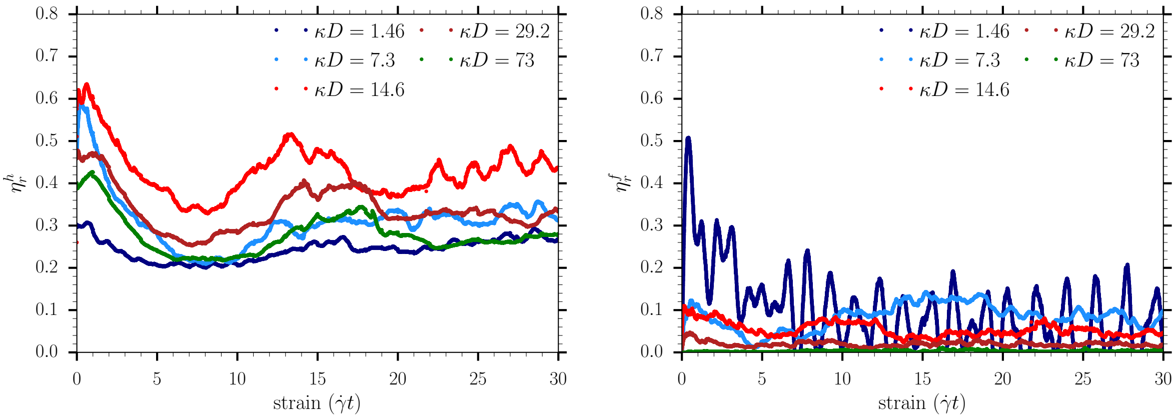

(a) η_r^h (b) η_r^f

Figure 4.32: Relative hydrodynamic (left) and interparticle viscosity (right) at $Ma = 4$ for different initial microstructures related to the interaction ranges κD.

Let us now focus on the interparticle viscosity η_r^f reported in Figure 4.32b and arising from the xF stress, *i.e.*, the electrostatic stress. This stress is a monotonic function of the interaction range except for $\kappa D = 1.46$ which exhibits strong oscillations with a period of approximately 1 strain unit. To understand the origin of these oscillations, one should recall that the suspension is ordered, with particles forming lines in the flow direction and hexagonal structure in the gradient-vorticity plane. Note that particles are separated roughly by one diameter in both the extensional and gradient to the flow direction. The double layer of a particle belonging to one of these lines overlaps with the double layer of particles belonging to another line. Consider only two particles in a shear flow moving on a straight line, parallel to one another, and in a simulation box with periodic boundaries of length equal to exactly one particle's diameter. It is obvious that the electrostatic stress is higher when the distance between the centers of gravity is minimized, and lower when the distance between the centers is maximized which will generate oscillations with period commensurate to the size of the box. In the simulations, this corresponds to the average separation between particles. One can conclude that the oscillations observed in Figure 4.32b are related to the successive encounters of the double layers of particles in separate lines in this ordered structure.

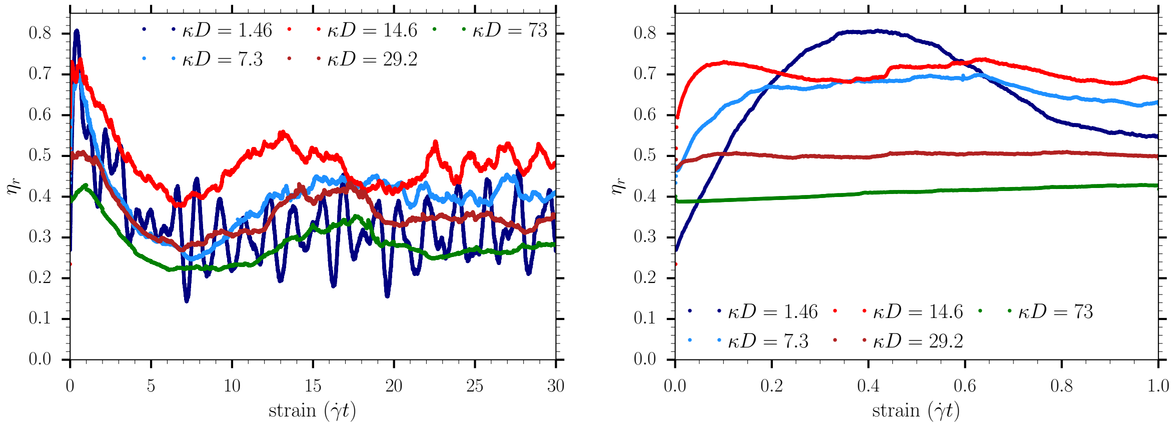

(a) $\eta_r = \eta_r^h + \eta_r^f$

(b) Zoom η_r

Figure 4.33: Relative viscosity over the entire simulation (left) and the first strain unit (right) at $Ma = 4$ for different initial microstructures related to the interaction ranges κD.

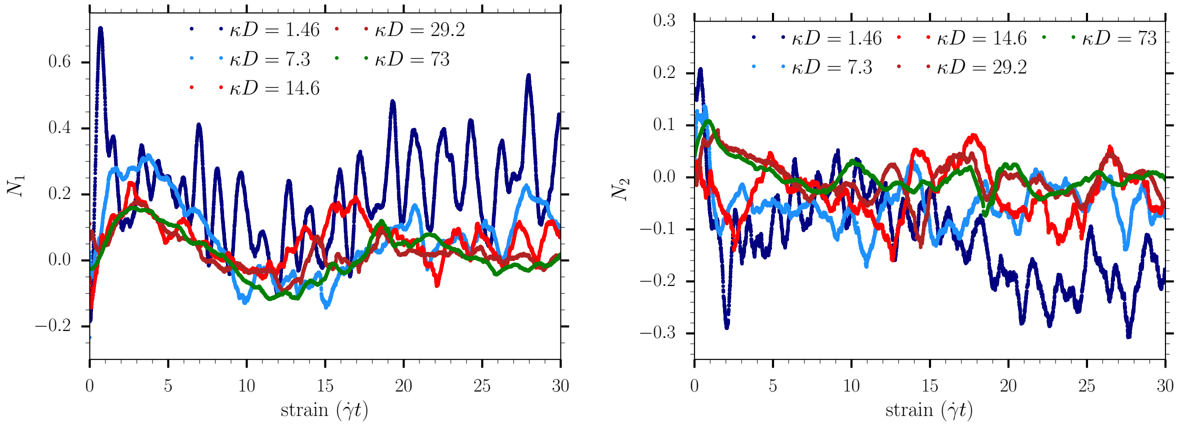

(a) $N1$

(b) $N2$

Figure 4.34: First (left) and second (right) normal stress differences at $Ma = 4$.

As the suspensions are considered as non-Brownian, the total relative viscosity reported in Figure 4.33 is obtained by summing η_r^h and η_r^f. Focusing attention on the first strain unit (see Figure 4.33b) allows the observation of a well-defined elastic regime preceding the overshoot stress, particularly visible at low ionic strength. One can conclude that the origin of the overshoot stress is a combination of the collective tilting of the particles toward the direction of the flow and the break-up of bonds or electrostatic cages. The overshoot stress is therefore expected to increase with the reduction of the Mason number. Concerning the elastic regime, note that G' is independent of the initial structure even though its origin is totally different. Indeed, one can easily imagine that the elastic component at $\kappa D = 1.46$ corresponds to the energy needed to deform the electrostatic cages of the nearest neighbors since the initial equilibrium structure is a repulsive glass. In contrast, for larger κD, G' is associated to the energy needed to break the most fragile bonds in the initially percolated network.

These assumptions are confirmed by the normal stress differences at $\kappa D = 1.46$. N_1 exhibits a positive peak at the strain corresponding to the overshoot stress, indicating that the cages are initially compressed in the direction of the gradient to the flow when the shear reorganizes them and that repulsive electrostatic forces try to prevent this deformation. Then, N_1 relaxes to a lower value after cage breakup and oscillates around 0.3. N_2 seems to slightly decrease with the strain and longer simulations are necessary to conclude about these normal stresses. For shorter interactions ranges N_1 relax to zero after 12 units of strain, indicating a fairly isotropic stress.

3.3.2 $Ma = 1$

At $Ma = 1$, the hydrodynamic and the electrostatic forces are comparable. The bonds between the particles in contact are strengthened, and the energy brought by the flow is not sufficient to break as many bonds as at $Ma = 4$ (see Figure 4.35).

At $\kappa D = 1.46$ the shear-ordered structure is more ordered due to the increase of the electrostatic interactions, and the particles are not able to rotate around the vorticity axis. Note also that shear brings a sufficient amount of energy to overpass the repulsive barrier allowing particles to aggregate in OC configuration. We emphasize that this configuration was not observed at $\kappa D = 1.46$ without flow in the third chapter.

At $\kappa D = 7.3$ and 14.6, the system, which was percolated before the start-up shear, is composed of approximately three different clusters at the end of the simulation. This increase in the number of clusters is due to the break-up of some attractive bonds caused by the flow. Note that a kind of layer at the bottom of the simulation box in Figure 4.35b appeared at $\kappa D = 7.3$, preventing particles belonging to it to rotate. At $\kappa D = 29.2$, the shear allowed the creation of larger aggregates, probably due to the speed-up of aggregation kinetics (see section 1.2 of the current chapter). At $\kappa D = 73$, the tactoids disappeared, and one can observe the formation of some OC configuration.

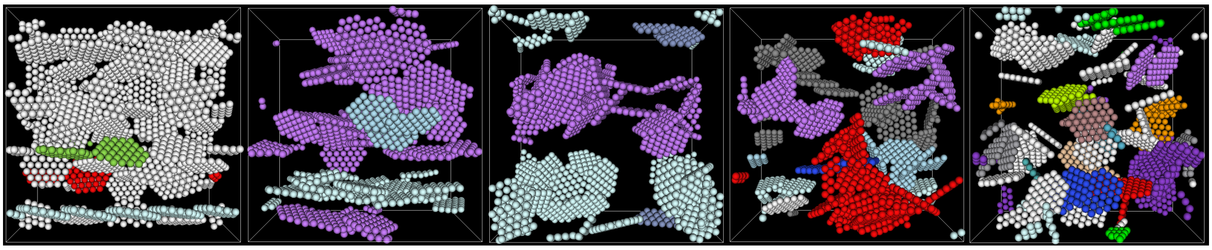

(a) $\kappa D = 1.46$ (b) $\kappa D = 7.3$ (c) $\kappa D = 14.6$ (d) $\kappa D = 29.2$ (e) $\kappa D = 73$

Figure 4.35: Snapshot of the final microstructures in the flow-gradient plane after a start-up shear at $Ma = 1$.

Let us now focus on the influence of these structures on the viscosity. Firstly, one should note that η_r^h does not increase in a monotonic fashion with the interaction ranges. If we compare the hydrodynamic viscosities obtained for $\kappa D = 1.46$ and $\kappa D = 73$ at $Ma = 1$ with the ones observed at $Ma = 4$ (compare Figure 4.32a and 4.36a), it only increases from $\eta_r^h = 0.3$ to 0.35. However, the increase with the reduction of the Mason number is more striking at $\kappa D = 29.2$, where η_r^h increases from 0.35 to 0.6. This increase can be related to the formation of larger clusters due to the stronger electrostatic interactions and therefore to the increase of the average hydrodynamic radius of the aggregates. Although the hydrodynamic viscosity is relatively noisy, we observed that interaction ranges leading to complete aggregation which correspond to $\kappa D = 7.3$, 14.6 and 29.2 exhibit a similar final hydrodynamic relative viscosity ≈ 0.6, while the other ranges exhibit a smaller hydrodynamic viscosity.

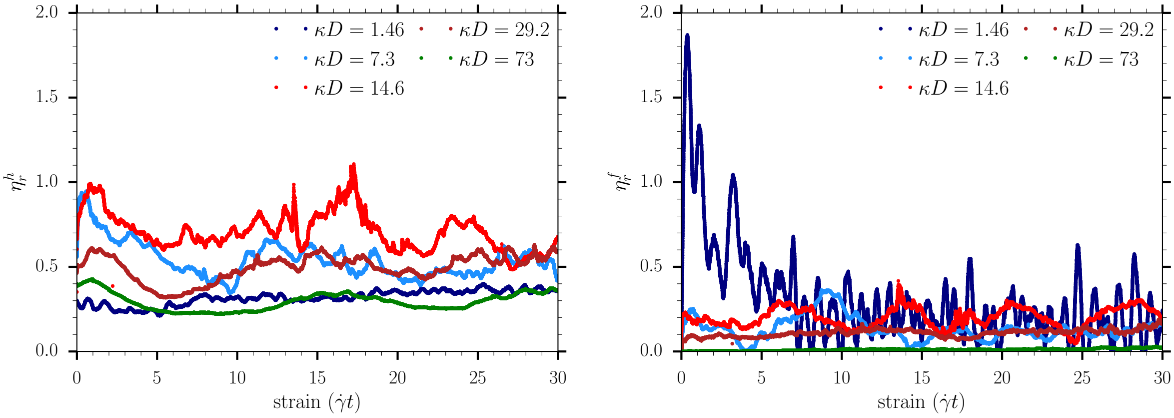

(a) η_r^h

(b) η_r^f

Figure 4.36: Relative hydrodynamic (left) and interparticle viscosity (right) at $Ma = 1$ for different initial microstructures related to the interaction ranges κD.

As expected, the electrostatic stress is more impacted by the reduction of the Mason number (see Figure 4.36b). The η_r^f of the suspension with long-range interactions exhibits a sharp and very intense peak at the same strain than at $Ma = 4$ indicating a higher G' than at higher Mason number. Then, η_r^f decreases toward ≈ 0.2 and oscillates around this value as observed for $Ma = 4$. Note that the interparticle viscosity is, on average, the same for all the interaction ranges except at $\kappa D = 7.3$. Such a result was not obvious a priori, as we would have expected to observe a higher interparticle viscosity for longer interaction ranges, as it is commonly observed for a repulsive system of spherical particles (see the study from Nazockdast & Morris [18]). Here, contrary to these repulsive systems, interactions are essentially attractive for most interaction ranges. It is possible that under strong shear flow the important parameter is the strength of interactions at contact, which controls the erosion of aggregates and their final size. It could explain why the viscosity does not depend that much on the range of interactions. The only purely repulsive system we considered is $\kappa D = 1.46$ and it has the peculiarity to shear-order so its viscosity cannot be compared directly to that of the other systems.

To summarize, the total viscosity increases with the reduction of the Mason number but is still dominated by the hydrodynamic viscosity. However, we have seen that η_r^h also depends strongly on the Mason number and, therefore, on the electrostatic interactions.

Let us now focus on the normal stress differences reported in Figure 4.37. The first normal stress difference (see Figure 4.37a) is on average equal to zero for suspensions having $\kappa D > 14.6$. The increase of the interaction range leads to a small positive value of N_1 with strong oscillations. One should be aware that the electrostatic first normal stress difference is negative while the hydrodynamic contribution is positive. The oscillations arise only from the electrostatic contributions. The second normal stress differences is, on average, equal to zero for $\kappa D \geq 14.6$. For $\kappa D = 7.3$ it was equal to zero until the last five strain units, where it seems to decrease. Once again, longer simulations are required to conclude on its behavior. At $\kappa D = 1.46$, N_2 shows a comparable intensity to N_1 but its precise value depends on the tilt of the cristal relative to the simulation box and will thus not be commented further. To resume, both N_1 and N_2 are, on average, equal to zero for $\kappa D \geq 14.6$ indicating that the stresses of these systems are fairly isotropic.

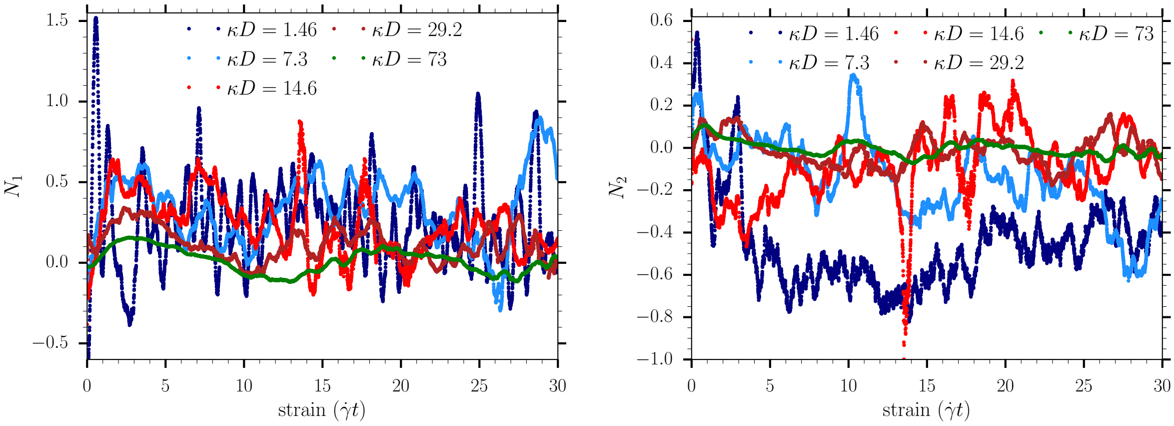

(a) $N1$

(b) $N2$

Figure 4.37: First (left) and second (right) normal stress differences at $Ma = 1$.

3.3.3 $Ma = 0.25$

At $Ma = 0.25$, the electrostatic forces strongly prevail over hydrodynamic forces. The Mason number reduction does not strongly influence the microstructure at $\kappa D = 1.46$, as the long-range repulsions already determined it at $Ma = 1$. However, one can note that the energy brought by the flow is not important enough anymore to overpass the energy barrier allowing particles to aggregate with an OC configuration. Note that we do not observe the same spatial configuration of the particle belonging to the bottom string in Figure 4.38a compared to Figure 4.35a due to the fact that this string is composed of four particles at $Ma = 0.25$ and five particles at $Ma = 1$. For the ranges $\kappa D = 7.3$ and 14.6 one can observe two distinct aggregates, one above the other. Note that particles percolate in the flow direction for the top clusters and both the extensional and vorticity direction for the bottom cluster. One could wonder if the clusters do not aggregate due to the strong repulsions. Such behavior was already observed for a system of spherical particles with long-range interactions and short-range attractions by Varga & Swan [28] and it also resembles the smectic B phase observed by Delhorme and coworkers [6, 7]. At $\kappa D = 29.2$, one can observe a unique aggregate, while at the shortest interaction range, particles form a multitude of small-sized clusters.

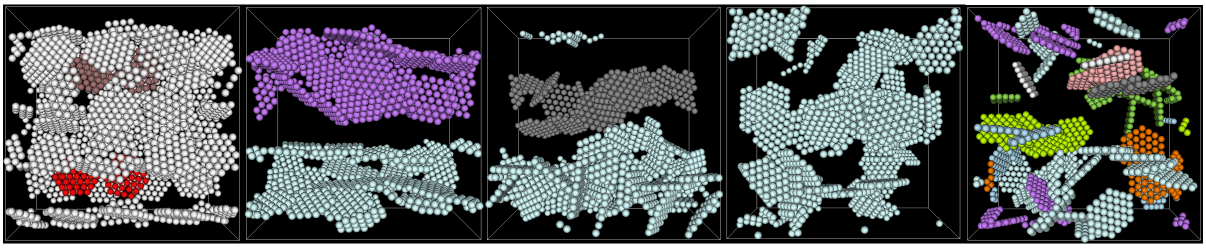

(a) $\kappa D = 1.46$ (b) $\kappa D = 7.3$ (c) $\kappa D = 14.6$ (d) $\kappa D = 29.2$ (e) $\kappa D = 73$

Figure 4.38: Snapshot of the final microstructures after a start-up shear at $Ma = 0.25$ in the flow-gradient plane.

Concerning the viscosities (see Figure 4.39), note that the hydrodynamic viscosity is higher at $\kappa D = 7.3$ than for shorter interaction ranges leading also to aggregated structures, and at the same time the electrostatic viscosity is smaller than that observed for any other interaction ranges. It can seem quite surprising at first sight. This system has a very special structure with aggregated planes sliding one over the other, so we could understand these viscosities by imagining solid-like planes with hydrodynamic forces tearing particles apart but with a structure stabilized by the electrostatic interactions. The viscous dissipation is therefore concentrated in the shear flow between the planes. This kind of structure is quite reminiscent of the shear-banding phenomenon that can be observed in dense hard sphere suspensions. One can also wonder if the hydrodynamic viscosity could be related to the microstructure observed. At $\kappa D = 29.2$, we observed the successive formation and destruction of a percolated structure, and the number of clusters was varying from three to one, while the average number of neighbors was remaining approximately constant and equal to 2.7. At $\kappa D = 14.6$ and $\kappa D = 7.3$, the suspensions are composed of two distinct clusters, one with 44 (34) particles and the other 16 (26) particles at $\kappa D = 14.6$ (7.3). Surprisingly, the suspension with the biggest cluster has a lower hydrodynamic viscosity which highlights the point made above that the hydrodynamic viscosity does not only depend on the radius of the largest cluster. We also observed that $\langle N_{nei} \rangle$ was equal to 2.9 for $\kappa D = 14.6$ and 3.3 for $\kappa D = 7.3$. Therefore, we observe a correlation between the hydrodynamic viscosity and the average number of neighbors, as a higher viscosity seems related to denser clusters.

The interparticle viscosity behaves very similar at $Ma = 0.25$ and at $Ma = 1$ for the interaction ranges shorter than $\kappa D = 1.46$ (see Figure 4.39b). In contrast, η_r^f at $\kappa D = 1.46$ is four times higher at $Ma = 0.25$ than at $Ma = 1$. This is not a surprising result, given that η_r^f arises mainly from repulsive interactions. Then increasing the electrostatic force by four also increases the xF stress by four. Note that the overshoot stress is observed once again after 0.48 strain units, as for $Ma = 1$ and 4. Consequently, as the viscosity at $\kappa D = 1.46$ is driven by the electrostatic forces, the elasticity of the suspension, which corresponds to the deformation of the electrostatic cages, also increases by a factor four. For repulsive systems, the elasticity is directly related to the Mason number.

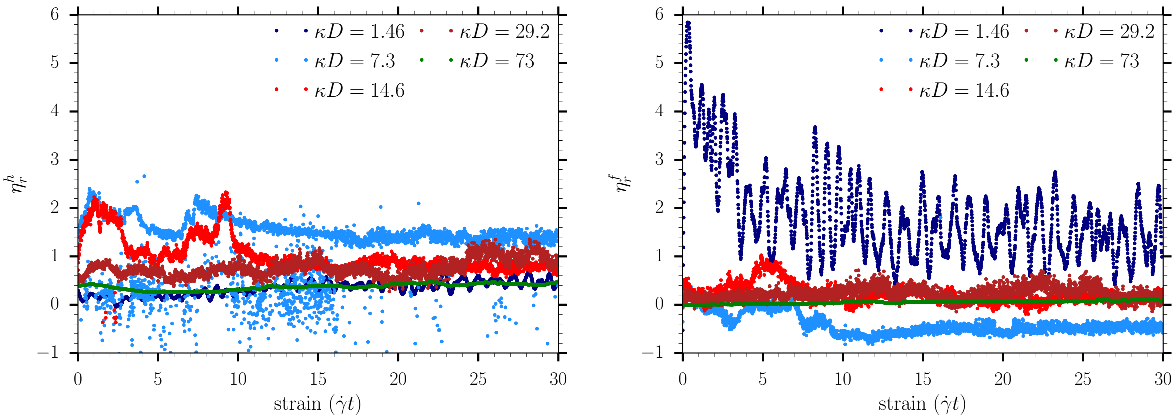

(a) η_r^h (b) η_r^f

Figure 4.39: Relative hydrodynamic (left) and interparticle viscosity (right) at $Ma = 0.25$ for different initial microstructures related to the interaction ranges κD.

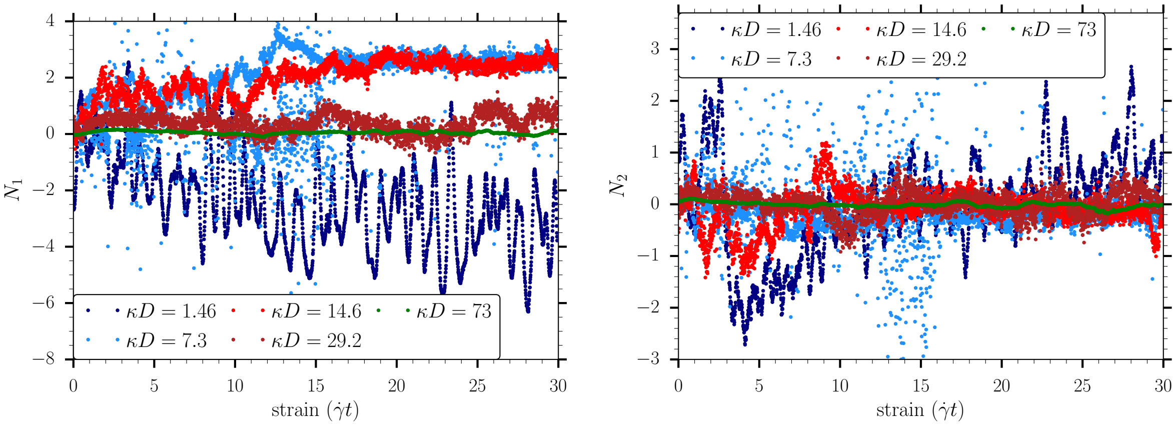

(a) $N1$ (b) $N2$

Figure 4.40: First (left) and second (right) normal stress differences at $Ma = 0.25$.

The normal stress differences are reported in Figure 4.40. N_1 is equal to zero for the shorter interaction ranges indicating fairly isotropic stresses in the flow and gradient direction, and exhibits positive values for $\kappa D = 14.6$, 7.3 and a strong negative value for $\kappa D = 1.46$. Note that N_1 at $\kappa D = 14.6$ and $\kappa D = 7.3$ exhibit similar value of ~ 2.65. One could wonder if the first normal stress differences observed at such ranges arises from the flow-induced stretching exerted on the two separate aggregates which are percolated in the flow direction (see Figure 4.38b and 4.38c) and sliding one over the other. The origin of the strong negative value of N_1 at $\kappa D = 1.46$ comes from the shear-ordering of the system. It will be discussed latter in section 4.2.1 that the hydrodynamic component of N_1 is positive, while the electrostatic interactions highly compress the system in the flow direction and generate a negative N_1^f. Previously, at $Ma = 1$, N_1 was positive because hydrodynamic interactions slightly prevailed over electrostatic interactions which is not the case at $Ma = 0.25$. That is why we can observe a change of the sign of N_1 while decreasing the Mason number. The second normal stress vanishes for all the ranges of interactions except for $\kappa D = 1.46$ where it seems to keep evolving. Simulations in larger domains, with different initial configurations should be undertaken in order to analyze normal stress differences properly.

3.4 Summary

In this section we have studied the rheological response of suspensions of $AR7$ clay-like platelets with different initial microstructures to start-up shear while varying the Mason number, *i.e.*, the strength of electrostatic interactions relative to the shear flow as well as the interaction range.

When the electrostatic forces are insignificant compared to hydrodynamics, the initial microstructure only influences the initial viscosity value. However, it is not involved in the shear-thinning dynamics because the flow is strong enough to break all the interparticle bonds instantaneously. The shear-thinning was related to the tilting of the particles toward the direction of the flow with the same relaxation time irrespective of the initial microstructure.

When the Mason number is reduced, electrostatic forces strongly influence both the microstructure and the stresses of the suspensions. We observe a shear-ordering of the suspension for long-range interactions corresponding to a repulsive system, which will be studied in the next section. We found that the corresponding viscosity was following a power law $\eta_r \propto \dot{\gamma}^{-0.9}$, in line with the results from Paineau and coworkers on suspensions of beidellite at low ionic strength [20]. For smaller interaction ranges, we observed a scaling in $\eta_r \propto \dot{\gamma}^{-0.25}$ in fair agreement with the results from Paineau and coworkers [20] for very dilute suspension but underestimated compared to the scaling observed by Abou et al. [1] on Laponite suspensions (one nematic and the other percolated). Further investigations are necessary to study the likely dependence of the power-law coefficient on the volume fraction studied and to clarify the effect of the aspect ratio of the colloids.

The elastic behavior of a suspension could be related to the Mason number for a repulsive system (long-range interactions). For low Mason numbers, the first normal stress was found positive at $4 > Ma \geq 1$ and negative below. The electrostatic first normal stress difference is always negative while the hydrodynamic normal stress difference is always positive. Thus, the sign of the first normal stress difference depends strongly on the ratio between electrostatic and hydrodynamic forces. Therefore it is not surprising to observe a sign inversion of N_1 close to $Ma = 1$. In contrast, the second normal stress seem to vanishes and further investigations are require to study it properly.

Using the ASD method, the origin of the stresses could be studied, and the main conclusion is that it is very difficult, maybe impossible, to determine a unique parameter which could allow to foresee the viscosity of a system with both a charge and a shape anisotropy. Indeed the variation of either the interaction range or the Mason number strongly influences the microstructure of the suspensions and even changes the physical mechanisms involved in the systems response. For example, the reduction of κD could melt the glassy state observed at very long-range interactions, leading to a percolated structure, or even a liquid-like structure when particles behave as hard sticky platelets. The stresses involved in these suspensions would be dominated either by the electrostatic interactions or by the hydrodynamic interactions. Moreover, even for a system dominated by hydrodynamic forces, we have shown that the stresses related to the latter are not only dependent on the state of the suspensions (percolated or not), but also on the size of the clusters and on their own spatial arrangement.

To summarize, one important result of this study is the important complexity introduced by anisotropic interactions. In more classical systems such as repulsive spheres, there is hope to relate variations of the mechanical response of the system to some physico-chemical parameter because the system hardly changes its out of equilibrium structure, or "phase". Although a phase change can happen in some circumstances, there are large domains in the parameter space in which the microstructure is only deformed, and therefore one might be able to relate a mechanical response to a variation of a physico-chemical parameter. In the present system, the anisotropy of interactions and the fact that they change from repulsive to attractive with salt concentration makes the system prone to frequent and drastic microstructure changes, or say, "phase changes". Consequently, understanding and modeling the mechanical response of such systems should be done using small parameter variations, taking care to avoid unexpected major microstructure changes. In the next section, we will focus on one peculiar phase that could be obtained only by shearing the suspension initially in a Wigner glass state.

4 Shear-induced ordering

In this section, we study the formation and the relaxation of a shear-ordered structure from an initial Wigner glass state. This ordering is only observed for orientable objects experiencing long-range interactions, which corresponds to a suspension of $AR7$ clay-like particles at $\kappa D = 1.46$. The shearing of the Wigner glass structure leads to the formation of strings in the flow direction and a hexagonal structure in the gradient-vorticity plane with angular correlations between particles. To our knowledge, such a shear-ordering of clay-like particles into a two-dimensional crystal of strings was observed neither using simulations nor experimentally. Indeed, most of the simulations of particles with both shape and charge anisotropy leading to ordered systems were carried out without flow using MC simulations. One can cite for example the study from Delhorme et al. [8] on clay-like particles in which the suspensions exhibit crystalline structures for volume fraction above 0.2, or the work from Jabbari et al. [10] where a columnar hexagonal crystal is observed at high density and high ionic strength for purely repulsive and infinitely thin platelets accounting for anisotropy of the repulsions.

From a more general point of view, the study of colloidal crystals goes back to the early eighties with, for example, the work from Ackerson and Clark [4]. These authors experimentally observed that highly repulsive spheres ordered into body-centered cubic crystal at rest (BCC crystal) formed a two-dimensional hexagonal close-packed crystal at high shear rate with strings along the flow direction, due to the competition of the viscous and the electrostatic forces. If the applied shear is too strong, the structure can melt (this obviously depends on the volume fraction considered). The observation of the evolution of an ordered structure toward another ordered structure under shear is quite "intuitive". More surprisingly, several authors reported the oscillatory-shear-induced ordering of suspensions originally in a liquid-like state. Ackerson and Pusey [3] observed for a suspension of hard-spheres (PMMA) the formation of face-centered cubic structure (fcc) owing to oscillatory-shear flow. Such a crystalline structure was also observed for repulsive silica spheres by Yan and coworkers [31] at lower volume fraction. The formation of ordered structure is, therefore, typically associated with particles that are either forced to interact due to flow or having strong repulsive interactions corresponding to an important effective volume fraction. The complexity of experimental studies of shear-induced structures lies in the fact that it is challenging to relate the observed colloidal structure to the balance between the Brownian, hydrodynamic, and interparticle interactions [29].

Using the ASD method, we are able to understand how the hydrodynamic and electrostatic interactions influence the structure of clay-like particles, without and with background shear flow. The forces involved during the transition from a Wigner glass to the ordered structure can be analyzed, and the interesting question of the history dependence of ordered suspensions after the cessation of the flow can be answered.

4.1 Microstructure under flow

To provide an insight of the shear-ordered structure obtained $\kappa D = 1.46$, we first study its microstructure. Simulation is carry out over 30 strain units at $Ma = 1$ and $Pe \gg 1$ to only focus on the influence of the shear flow. The structure obtained will be compared to the cases $\kappa D = 7.3$ and $\kappa D = 14.6$ leading to aggregated structures, with particles in OC configuration and with particles mainly in HOC configuration respectively. In contrast to the classical structure deformation observed for other interaction ranges, when shear is applied to the glassy system, strong ordering is observed, as shown in Figure 4.50d. For a specific size simulation box studied, the structure is composed of 13 strings of four particles each, one string of three particles, and one string of five particles. The string composed of five particles is the only string with the totality of its particles in contact (see the bottom line in light blue color with particles in OC configuration in Figure 4.41b). This non-identical number of particles per line can be seen as a crystalline defect. Defaults are also present at $Ma = 4$ (12 lines with four particles and four lines with three particles) but disappear at $Ma = 0.25$, where 15 lines of exactly four particles each are observed. Note that the modification of the Mason number also influences the orientation of the particles. For example, at $Ma = 4$ one can observe the rotation of some particles around the vorticity axis, while for lower Mason number, rotations are forbidden by the strong electrostatic stresses. A complete description of the ordered structure at $Ma = 1$ is presented in the following paragraphs.

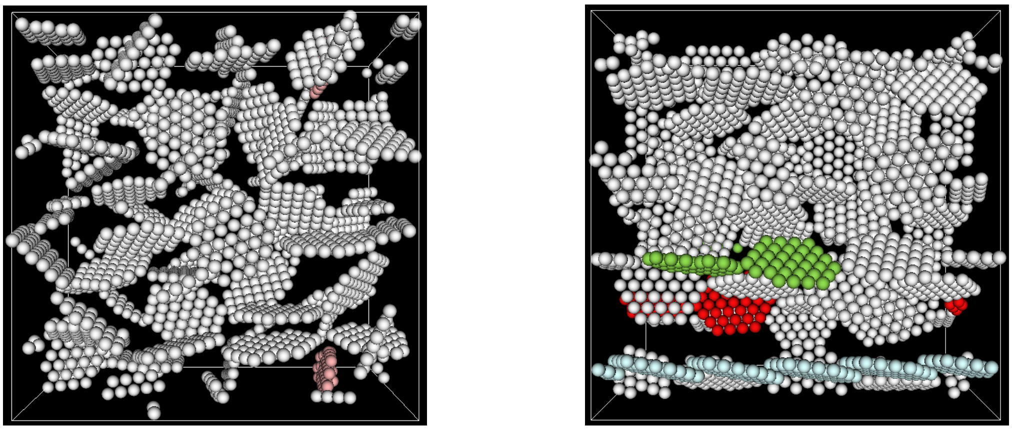

(a) Rest, x-y plane (b) Shear, y-z plane

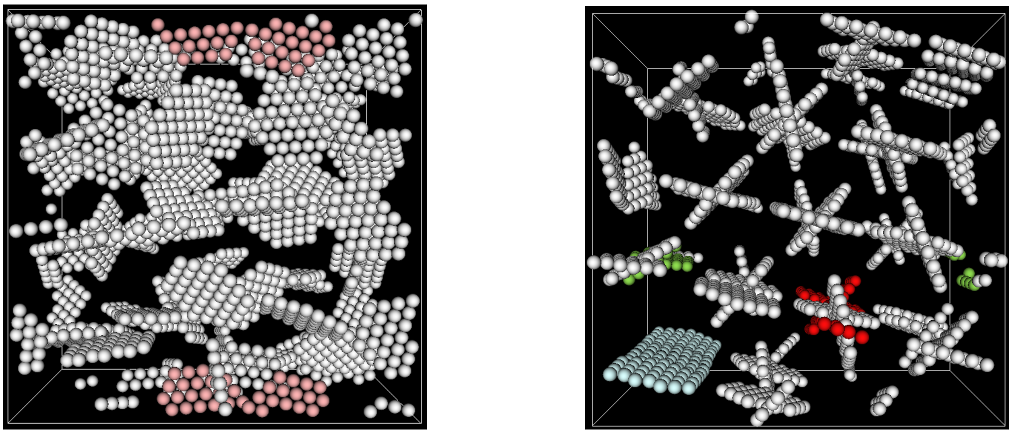

(c) Rest, x-y plane (d) Shear, y-z plane

Figure 4.41: Snapshot at rest just before the start-up shear (a,c) and average of the last five strain units (b,d) for $\kappa D = 1.46$.

4.1.1 Pair distribution function

The pair distribution function was computed in both the x-y and y-z planes. The mathematical description of the two-dimensional pair distribution function used here can be found in Appendix 3. The pair distribution of the suspension at rest is averaged over a time $5\ a^2/(2D_0)$ and over $25 < \dot{\gamma}t < 30$ under flow.

In Figure 4.42 we report the pair distribution functions in the x-y plane at rest (first column) and under flow (second column) for $\kappa D = 1.46$, 7.3, 14.6.

Concerning the structure at rest, one can observe that the increase of κD reduces the depletion zone around the central particle. One should recall from the third chapter that suspensions at $\kappa D = 7.3$ and $\kappa D = 14.6$ are isotropic which is consistent with Figures 4.42c and 4.42e. The suspension at $\kappa D = 1.46$ is nematic, and its radial distribution function exhibits a broad, intense peak between $2.2R$ and $2.5R$. We would have expected the positional isotropy of this Wigner glass structure. However, note that the spots centered around $(1, 2)$ and the symmetry values at $(-1, -2)$. These spots seem to break the expected isotropy. While one could argue that this may be due to weak shear flow, in the rest period, the flow is $Pe = 3.86\ 10^{-3}$ and is too small to displace the particles sufficiently to yield this structure. Instead, one should recall that such suspensions have an almost instantaneous ergodicity breaking time and are consequently very sensitive to the initialization of the particles. Therefore we assume that the spots mentioned before came from the lack of sampling events. Numerous simulations with random initialization are certainly required to observe an isotropic structure in a particular plane.

When these structures are sheared, the competition between electrostatic forces and hydrodynamic forces leads to new structures which involve different physical mechanisms as a function of the interaction ranges. The glassy system evolves toward a shear-ordered state and forms strings in the flow direction visible in the pair distribution function (see Figure 4.42b). Only one string is observed due to the fact that the crystalline structure in the gradient-vorticity direction is slightly tilted relative to planes of fixed y. Note that due to the crystalline structure, the pair distribution function exhibits unusually large values under shear. We stress that for such a structure, the pair distribution function must be analyzed while taking into account the structure observed in the snapshots. Indeed, as we only consider a limited volume for the bins, long-range correlation can sometimes not be captured by the pair distribution function. For example, the spots 1 and 4 of coordinates $(1.57, 0)$ and $(3.14, 0)$ correspond to the OC string line observed in the bottom line of Figure 4.41b. This string is not perfectly aligned with the shear, that is why the spot 4 is less intense and the pair distribution function is not able to capture the high probability of presence. Spot 3 is located with center in $(2.6, 0)$, which can easily be related to the structure observed in the box. Indeed, the length of the box is $7.82\ R$, and we have seen that one of the strings had only three particles on its line. Hence $7.82/3.0 \approx 2.6$ which is consistent with the position of the spot and also to the fact that this point has the lowest statistics. Finally, spots 2 and 5 of coordinates $(1.97, 0)$ and $(3.94, 0)$ correspond to the 14 strings composed of four platelets. Note that the distance between two particles is less than twice the radius, which can be surprising at first sight. However, one should recall that particles are not perfectly spherical and are, in reality, closer to ellipsoidal. We have chosen to use the largest radius as a reference, and the semi-axis of the ellipsoid are $(R,\ 0.88\ R)$. That is why particles can be at a distance of $1.97\ R$ on average without being in contact. Note that the possibility of having particles in OC configuration is not considered owing to the snapshots of the suspension (see Figure 4.41b and 4.41c). As already mentioned, reducing the Mason number prevents structural defects in the crystal from occurring and therefore spots 1, 3, and 4 disappear at $Ma = 0.25$ (not shown here). To summarize, each position of the spots observed in Figure 4.42b and their intensity can be related to the structure observed in the snapshots.

In comparison, the percolated structures (see Figure 4.42d and 4.42f) appear fairly uniform in the y direction and have a higher probability of presence in the extensional direction. Note that the depletion areas visible at rest for $\kappa D = 7.3$ and 14.6 are still visible, due to the strong electrostatic interactions. These interactions are able to prevent particles from approaching too close to one another and to preserve some aggregated structures corresponding to the circles of high probability with a radius of R for $\kappa D = 14.6$ and $1.35\ R$ for $\kappa D = 7.3$.

Let us now focus on the pair distribution functions in the gradient-vorticity, or y-z, plane. In general, the percolated structures at rest are quite similar to the ones observed in the x-y plane, which is consistent with the fact that these suspensions are isotropic. The structure in the y-z plane at $\kappa D = 1.46$ is slightly different from that observed in the x-y plane, but as explained earlier, this difference is certainly due to the fact that the final structure of suspension with such long-range repulsions is strongly related to the initial configuration of the particles and might disappear if the pair distribution functions were averaged over a large number of simulations.

When sheared, the Wigner glass state evolves toward a hexagonal structure with spots separated by a distance of $2.1\ R$ which is roughly of the same order of magnitude as the separation of the spots 2 and 5 in the x-y plane in Figure 4.42b. In contrast to what was observed in the flow-gradient plane, the structure does not possess any defect, and we observe a perfect hexagonal lattice. Each spot of high intensity corresponds to a string of particles observed in Figure 4.42b. Only three spots are numbered as the others are enforced by the symmetry of the pair distribution function.

At $\kappa D = 7.3$, a higher probability area is located in the vorticity direction at $1.35\ R$, indicating the formation of some layers with particles in OC configuration reminiscent of Smectic B phase. This observation is consistent with the presence of layers at large y distances. In contrast, at $\kappa D = 14.6$, the suspension appears fairly uniform at a large distance, and with particles in HOC configuration at shorter distances represented by the high density crown located at $r = R$. Note that some particles are in OC configuration, as shown by the probability area colored in light blue in the vorticity direction.

We could observe that shearing a Wigner glass leads to a more ordered structure, with particles forming strings in the flow direction and hexagonal structure in the plane perpendicular to the flow. This behavior is not observed for aggregated suspensions, which allows us to conclude that the shear-ordering transition occurs between $\kappa D = 1.46$ and $\kappa D = 7.3$.

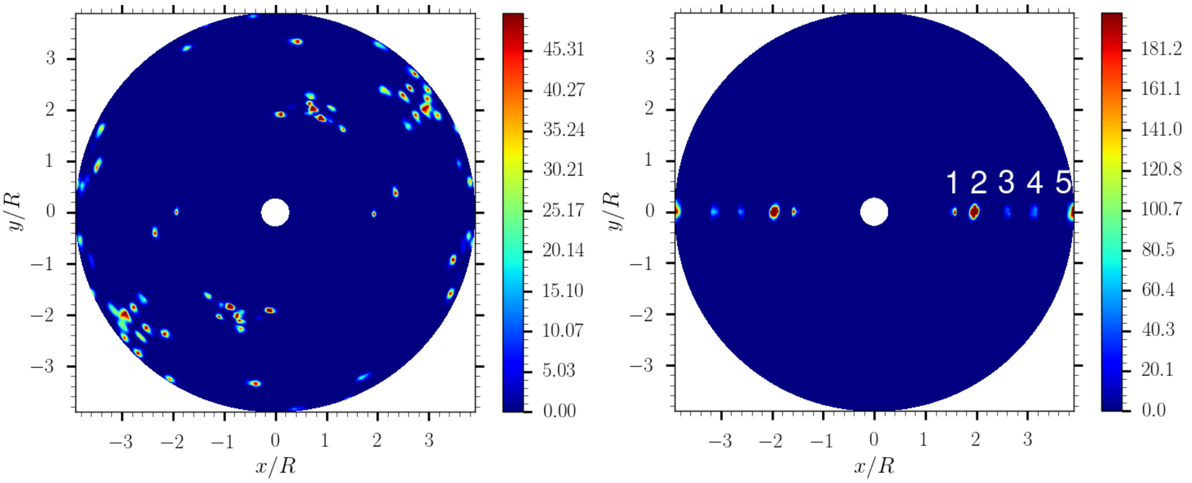

(a) Rest, $\kappa D = 1.46$

(b) Shear, $\kappa D = 1.46$

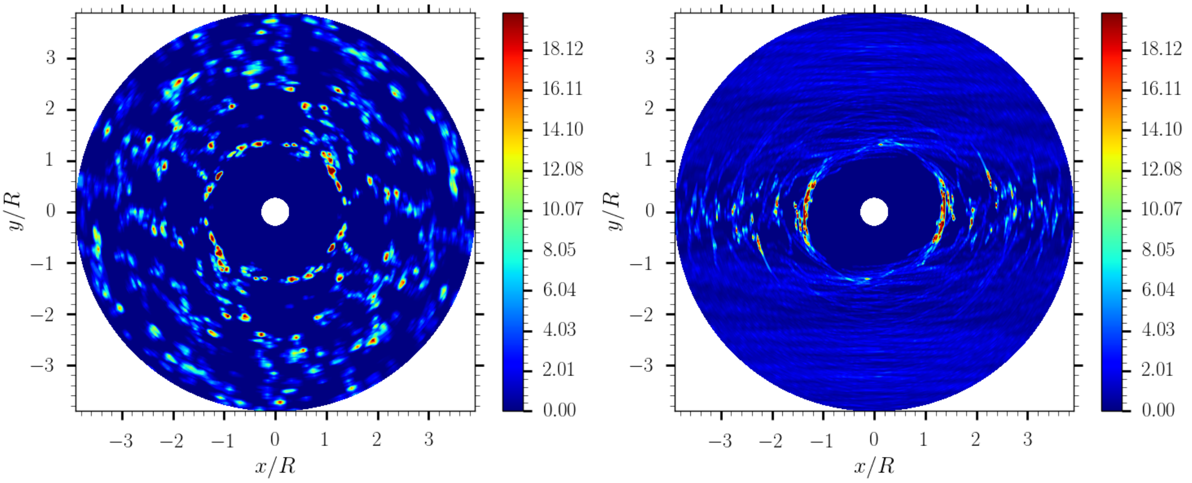

(c) Rest, $\kappa D = 7.3$

(d) Shear, $\kappa D = 7.3$

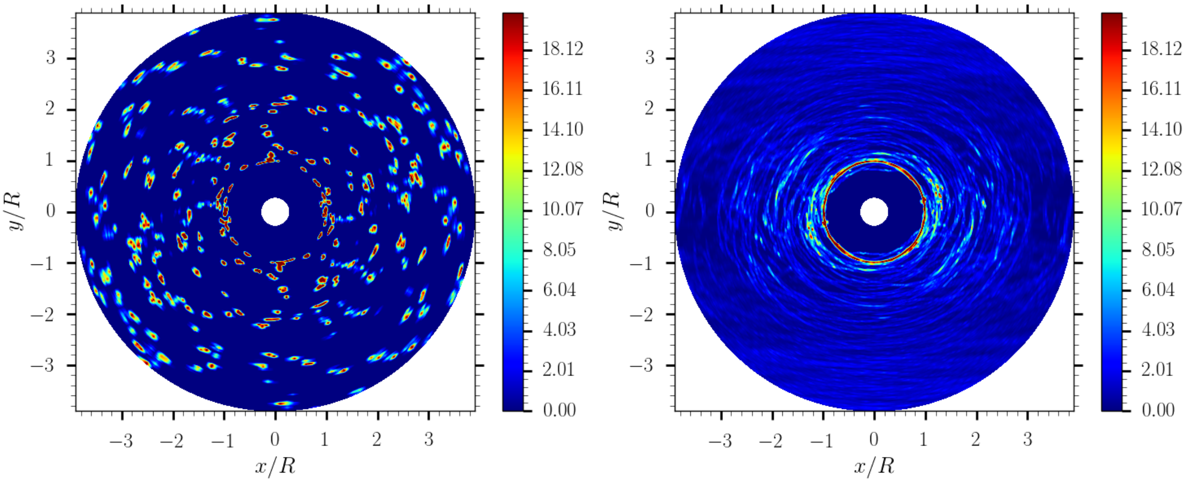

(e) Rest, $\kappa D = 14.6$

(f) Shear, $\kappa D = 14.6$

Figure 4.42: Microstructure at rest before the start-up shear (first column) and averaged of the last five strain units (second column) for different interaction ranges in the x-y plane corresponding to the flow direction and its gradient.

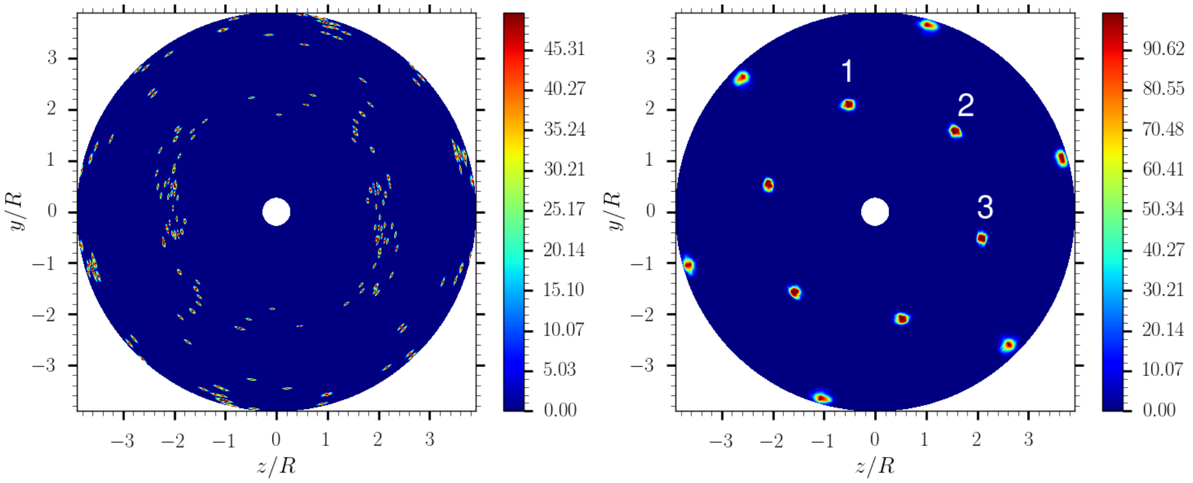

(a) Rest, $\kappa D = 1.46$

(b) Shear, $\kappa D = 1.46$

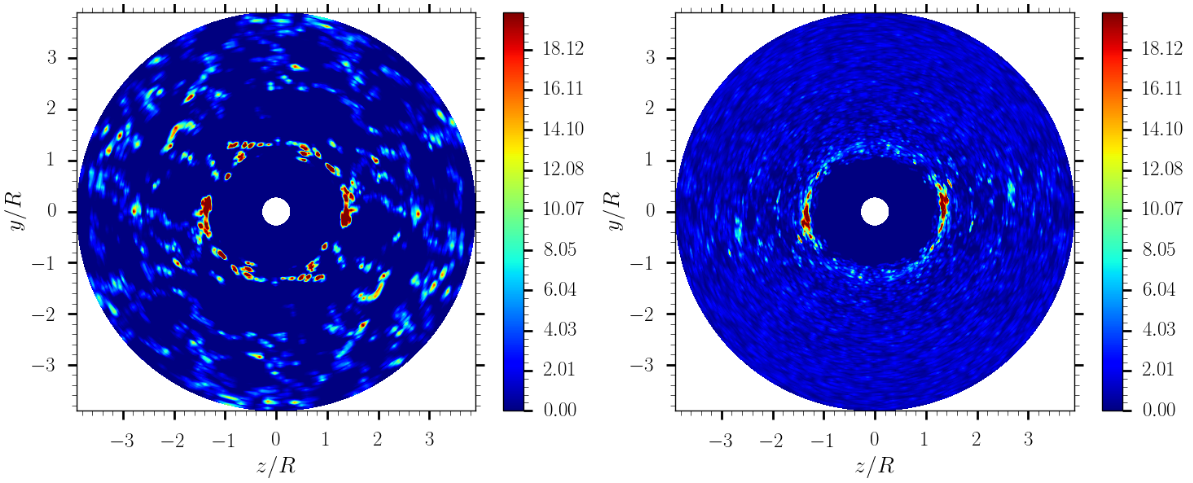

(c) Rest, $\kappa D = 7.3$

(d) Shear, $\kappa D = 7.3$

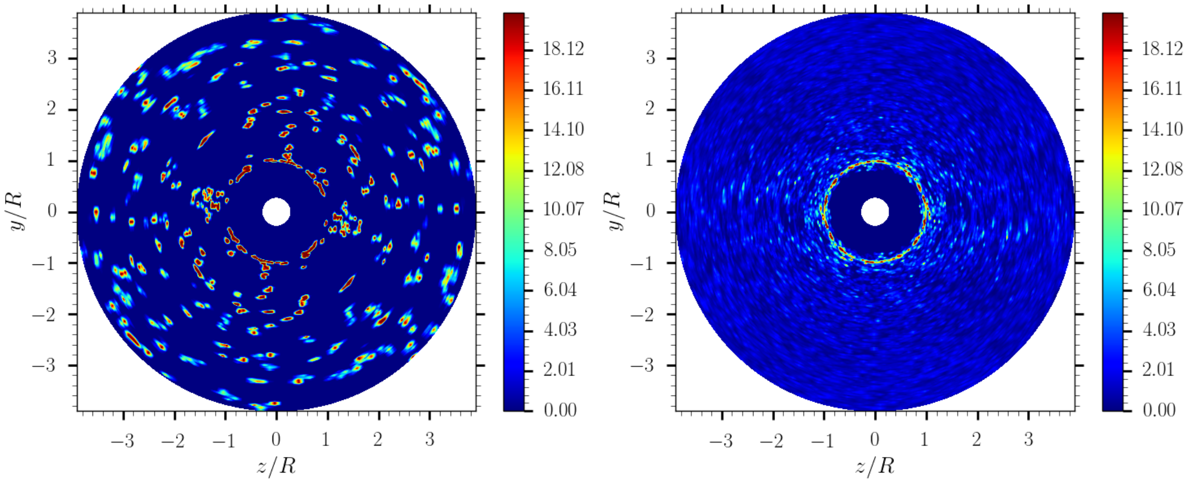

(e) Rest, $\kappa D = 14.6$

(f) Shear, $\kappa D = 14.6$

Figure 4.43: Microstructure at rest just before the start-up shear (first column) and average of the last five strain units (second column) for different interaction ranges in the y-z plane corresponding to the gradient-vorticity plane.

4.1.2 Static structure factor

We consider the microstructure of sheared suspensions using the static structure factor in both the x-y and y-z planes. Such data are related to the form which might be extracted from scattering experiments, and thus are included for completeness, although the information is present in the pair distribution, as g and S_L are related by Fourier transformation (see section 1.4 chapter 3). The scattering vector in the gradient direction is characterized by $\mathbf{q} = (0, q_y, 0)$ and in the vorticity direction by $\mathbf{q} = (0, 0, q_z)$. All the data are not plotted on the same graphic due to the huge difference in the peak intensities as a function of the interaction ranges.

The projected structure factors for $\kappa D = 1.46$ are reported in Figure 4.44 with a logarithmic y-scale while insets are the same curves but with a standard linear y-scale. The values of $\lim_{q \to 0} S(q)$ are well below one for q_y and q_z indicating that the system has low compressibility in both directions. Concerning the projection on the gradient direction, one can observe two strong peaks located at $q_y R = 12.1$ and $q_y R = 24.2$, respectively (see Figure 4.44a), indicating a crystalline structure. Note that similar peaks are observed for $S_L(q_z)$ but with an intensity approximately 20% lower (see Figure 4.44b), and the presence of two shoulders around the main peak and the secondary peak, these defaults can be attributed to the tilting of the structure in the y-z plane.

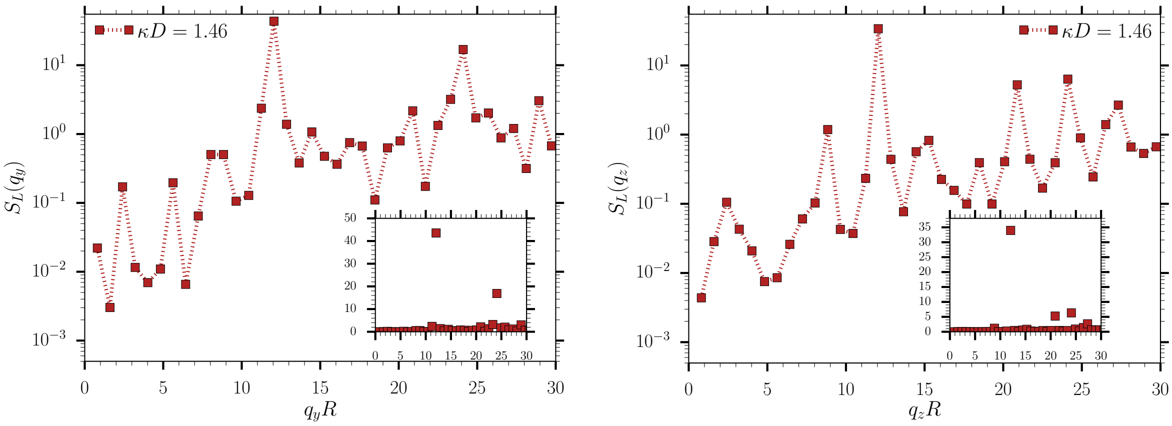

(a) $S_L(q_y)$

(b) $S_L(q_z)$

Figure 4.44: Projections of the static structure factor for $\kappa D = 1.46$, averaged over $25 \leq \dot{\gamma} t \leq 30$ on (left) velocity gradient axis and (right) the vorticity axis. The insets reproduce the curves with a linear y-scale. The dashed lines are added for eyes guidance.

The static structure factors in the gradient direction exhibit for the aggregated structures sharp peaks at $1.75\ q_y R$ and $2.62\ q_y R$ for $\kappa D = 14.6$ and 7.3 respectively indicating the presence of a structure along the x-y plane. Note that only $S_L(q_y)$ at $\kappa D = 7.3$ exhibits a peak at low q_z value.

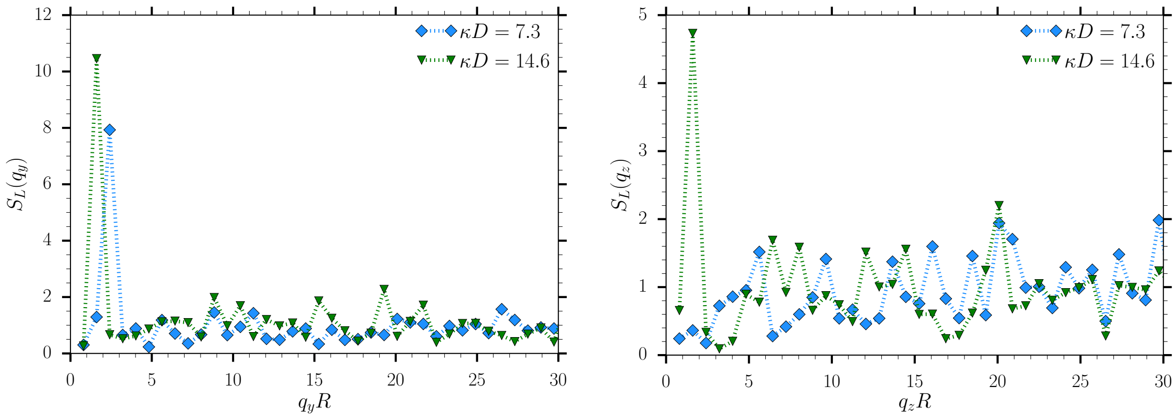

(a) $S_L(q_y)$ (b) $S_L(q_z)$

Figure 4.45: Projections of the static structure factor for $\kappa D = 7.3$ and 14.6 averaged over $25 \leq \dot{\gamma}t \leq 30$ on (left) velocity gradient axis and (right) the vorticity axis.

4.1.3 Orientational correlations

Let us now focus on the orientational correlations for the shear-ordered case, *i.e.*, $\kappa D = 1.46$. The probability of the relative angle between a pair of particles is computed between the particle centered at $(0, 0)$ in the pair distribution function (see Figure 4.42b and 4.43b), and the particles belonging to the five numbered spots in the x-y plane and the three numbered spots in the y-z plane. As expected from the analysis of the pair distribution function in the x-y plane particles belonging to spots 1 and 4 are in OC configuration as shown in Figure 4.46a. We recall that particles belonging to spot 3 are part of the string comprising only three particles. One can see in Figure 4.46a that these particles do not have a strong orientational correlation. Concerning the particles located in spots 2 and 5 which are the more characteristic of the ordered phase, we observe that angles below 10 degrees or around 60 degrees are greatly favored. It appears that denser strings (*i.e.* strings with particles packed more closely in the x direction) exhibit stronger orientational ordering.

The orientational correlation in the y-z plane is striking irrespective of the spot examined. Particles are either close to the parallel, ≈ 8 degrees, or with an angle of 60 degrees. One can assume that such a structure allows the suspension to minimize the electrostatic interactions between particles belonging to the same string and between the different strings of the hexagonal structure.

4.1.4 Summary

In this section, we have reported on a study of the microstructure a shear-ordered suspension. The transition from an aggregated state under flow to a shear-ordered state occurs between $\kappa D = 7.3$ and 1.46. At $\kappa D = 1.46$, particles arrange and form strings in the flow direction and a hexagonal structure in the plane perpendicular to the flow. Note that for $Ma \geq 1$, the number of particles per string is not constant. This can be considered as a crystalline defect. At $Ma = 0.25$, all these defects disappear, and each string is composed of four particles. We could observe that the presence of defects at $Ma = 1$ influences

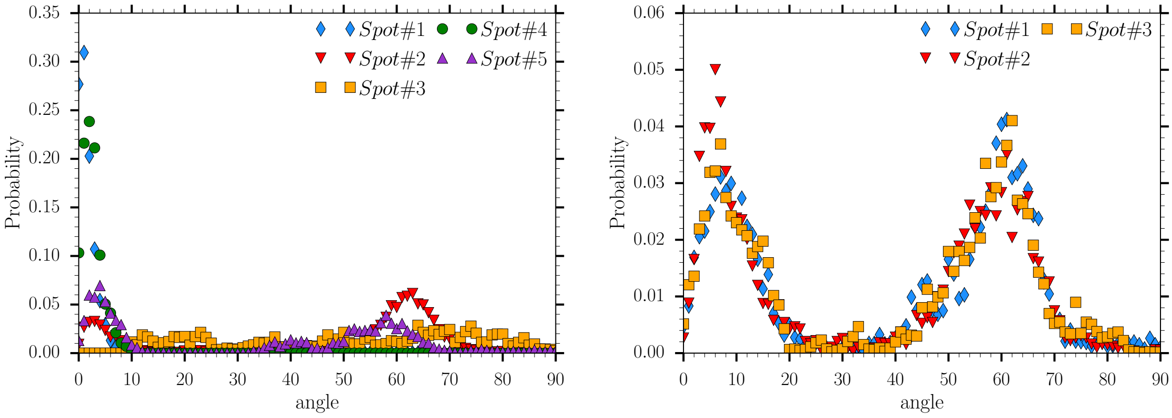

(a) x-y plane (b) y-z plane

Figure 4.46: Orientational correlations for $\kappa D = 1.46$ averaged over $25 \leq \dot{\gamma}t \leq 30$ on (left) flow-gradient plane and (right) the gradient-vorticity plane.

the orientational correlations between the particles as no correlation is observed when the number of particles per string is lower than four. In this case the structure is a plastic crystal. In contrast, strings with four particles exhibit two favored angles, 8 degrees, and 60 degrees, and the unique string with five particles has its particles in OC configuration and therefore with a strong orientational correlation. In these conditions, the structure is closer to a true crystal with defects.

4.2 Rheological behavior

Now, let us focus on the rheological behavior the suspension exhibiting shear-ordering. Without background flow, the suspension arranges into a Wigner glass state which is a condition to observe a shear-ordered structure in our conditions of interest, $\phi = 0.05$, $Ma = 1$ and $Pe \gg 1$. From a structural point of view, when such a suspension is sheared, the flow can bring additional energy to break some cages, which can help to reach a lower energy state.

4.2.1 Evolution toward the ordered state

To relate the structural transition to the stresses observed in the suspension, the viscosity, and the normal stress differences are reported in Figure 4.47 as a function of time in a startup-shear experiment. One can observe that η_r^h slightly increases from 0.27 at zero strain to 0.35 at the end of the simulation (see Figure 4.47a) which can probably related to the formation of the strings in the flow direction. Indeed, some particles are very close to another, and we can easily imagine that a small motion induced by long-range electrostatic interactions can generate lubrication and, therefore, slightly increases the η_r^h. Note that after eight strain units, the relative hydrodynamic viscosity is, on average, higher than the interparticle relative viscosity arising from the xF electrostatic stress between the particles.

For the viscosity component arising from electrostatic interactions η_r^f at low strain, one can notice an elastic regime and overshoot stress almost equal to ten times η_r^h at the same strain. Over this period, the stress of the suspension mainly originates from the strong long-range electrostatic interactions and corresponds to the transition from a Wigner glass state to the crystalline structure described in section 4.1. Then, once the structure is formed, the electrostatic stresses relax and η_r^f oscillates between 0 and 0.41. One should recall that these oscillations are related to the structure of the suspension. Indeed, the distance between particles belonging to the same string and two distinct strings is roughly equal 2 R, which is consistent with the period of oscillation of one strain observed on η_r^f.

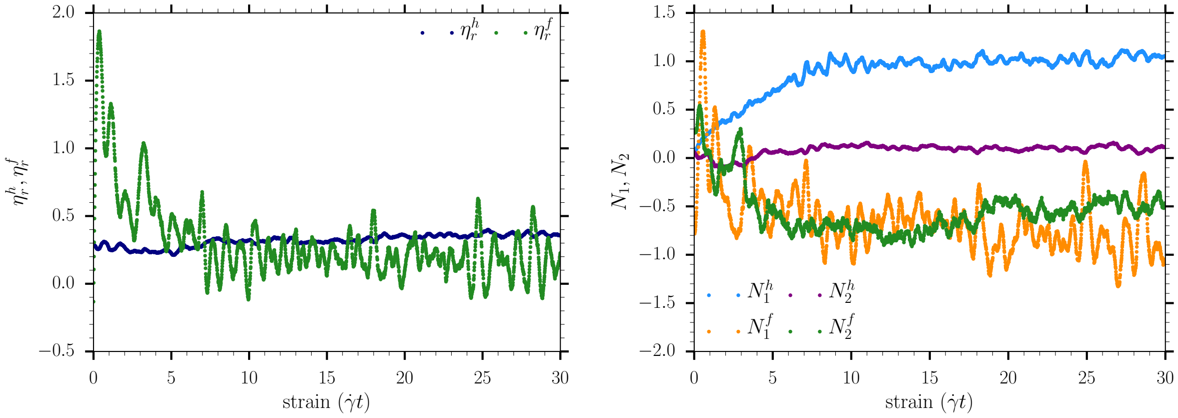

(a) Relative viscosity (b) Normal stress differences

Figure 4.47: Relative viscosity (left) and the normal stresses differences (right) for $\kappa D = 1.46$ and $Ma = 1$.

The evolution from a Wigner glass toward the ordered state is also noticeable on both normal stress differences N_1 and N_2. For example, N_2^h exhibits a lower value during this period compared to the rest of the simulation, while N_1^h linearly increases and reaches a positive plateau at the end of this period, *i.e.*, after eight strain units. The behavior of the first normal stress difference can be explained as follows: particles arrange in strings in the flow direction and, one can imagine that hydrodynamic interactions tend to tear these particles apart. Consequently, the hydrodynamic forces tend to generate a higher tension in the flow direction than in the gradient direction, thus explaining the negative sign of N_1^f.

Concerning the normal stress differences due to colloidal forces, one can relate the overshoot stress observed in Figure 4.47a to the positive peak of N_1^f in Figure 4.47b. When the suspension is sheared, the strong deformation of the double layers generate a significant force on the gradient direction, pushing the plates of the rheometer apart and allowing particles to arrange in a crystal structure. Over these first strain units the system is "dilatant". Then N_1^f relaxes and reaches a negative plateau while oscillating with the same period of one strain unit mentioned earlier for the relative viscosity. The absolute value of the plateau is slightly lower than the one observed for N_1^h. Therefore N_1^h and N_1^f almost compensate and the total first normal stress difference appears slightly positive, as observed in the previous section (see Figure 4.37a). Relating the final negative value of N_1^f to the microstructure is not obvious a priori. Indeed, the center of gravities of particles belonging to a string have a similar separation than between two strings (1.95 R in the string and 2.1 R between two strings). However, the distance between two charged sites of distinct particles is way shorter on average inside a string than between two strings. Then, electrostatic repulsions generate a stronger compression along the flow direction than the gradient direction.

The same kind of behavior is observed for N_2^f: it first exhibits a small positive overshoot at roughly the same time as N_1^f, then it decreases and reaches a first plateau at approximately -0.7, and finally decreases toward a second plateau at -0.46. As already mentioned, we assume that N_2^f is related to the tilt of the hexagonal structure which could explain why we observe that N_1^f and N_2^f are strongly dependent: when the average of one of the normal stress difference increases, the other decreases by the same amount. To summarize, once the system is structured, N_1^h is positive and N_1^f is negative: the hydrodynamic forces generate a tension in the flow direction which is almost compensated by the compression arising from the electrostatic repulsions. N_1^f is approximately equal to zero and N_2^f is negative. We assume that N_2^f depends on the tilting of the hexagonal structure. As this tilt is strongly related to the conditions of simulation (size of the box, number of particles) its value should not be generalized to ordered system.

4.2.2 Rest and recovery

After 30 units of shear, we stopped the flow and simulated the evolution of the structure over a time period of 25 $a^2/(2D_0)$. During this period of recovery, particles are not subjected to shear forces anymore and are able to arrange again spatially. Hereafter we will see that contrary to what could be observed for shorter interaction ranges (see section 2 concerning the thixotropic behavior), the suspension is not able to recover the initial spatial arrangement obtained from the first equilibration simulation at zero shear.

To provide an overview of the structural evolution from the initial state at zero shear to the end of the period of recovery we have reported the corresponding snapshots in Figure 4.48. Note that the initial state at zero shear is referred to as the "period of rest", while the period of recovery after the period of shear is referred to as "recovery". At first sight, particles have conserved their positional order during the period of recovery and exhibit a new orientational correlation as most of them are now aligned.

To analyze the evolution of the structure during the period of recovery quantitatively, the pair distribution functions in the x-y plane are reported in Figures 4.49 (a,b), and in the y-z plane in Figures 4.49 (c,d). Concerning the positional order in the x-y plane, one can observe that spots 1 and 4 are slightly less intense at the end of the period of recovery than during the shear. Recall that these spots are related to the particles remaining in OC configuration. After the cessation of the flow, these particles slightly lose their long-range alignment with the x-axis (see the bottom left corner in Figures 4.43b and 4.48f). Given that we used a bin of $0.27\ R$, a small displacement can indeed lead to a decrease in statistics, especially when only five particles built them. The spots 2 and 5 appear of the same intensity as at the end of the shear, indicating that particles have, on average, conserved their stings structure, which is consistent with the observation of the snapshot in Figure 4.48c. Note the presence of new spots located in $(2.96, 1.93)$, $(-2.92, 1.95)$ and their symmetries which indicates that the period of recovery allowed a few particles to align slightly better in the flow-gradient plane (recall that particles must belong to a specific bin to be accounted for in the pair distribution function). Such spots might be artifacts of the limited statistics.

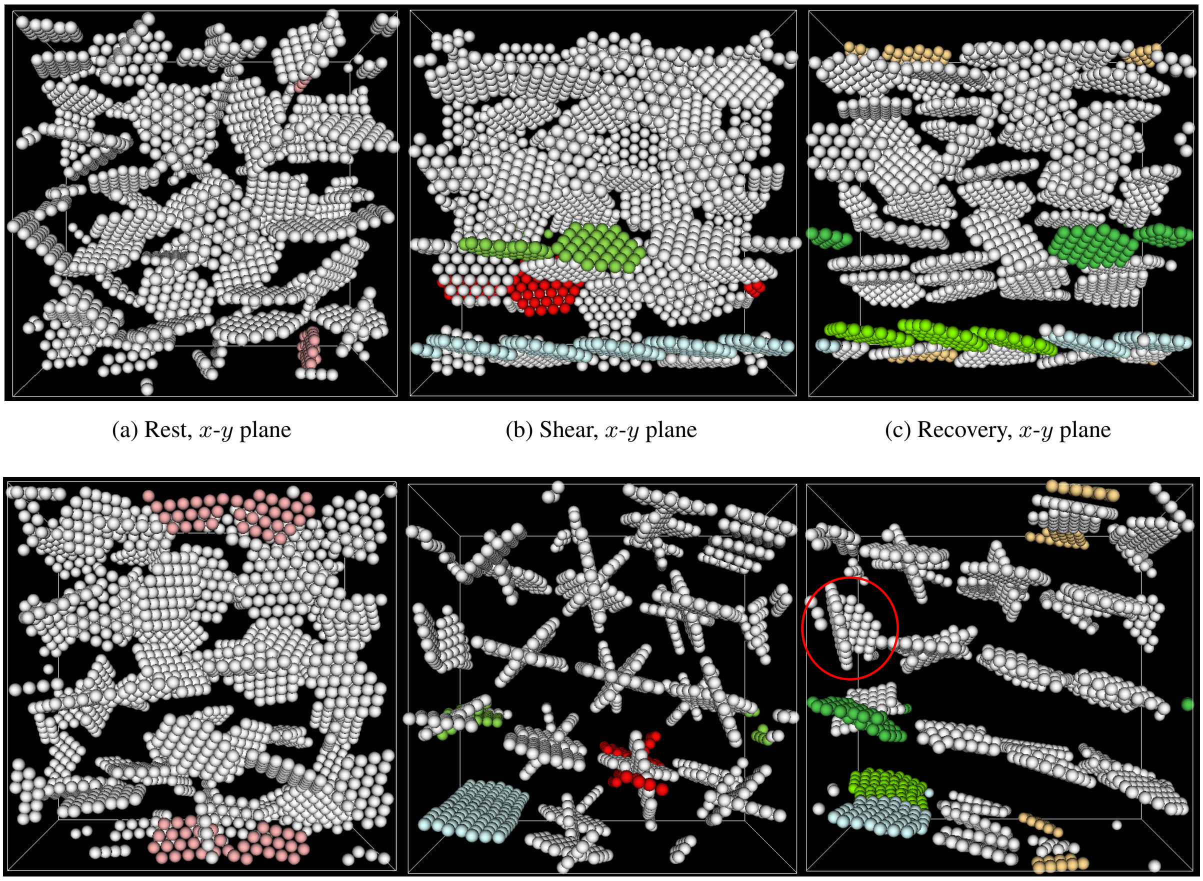
(a) Rest, x-y plane (b) Shear, x-y plane (c) Recovery, x-y plane

(d) Rest, y-z plane (e) Shear, y-z plane (f) Recovery, y-z plane

Figure 4.48: Microstructure at rest just before the start-up shear (a,d), averaged of the last five strain units (c,e) and at the end of a period of recovery (c,f) for $\kappa D = 1.46$.

Note that the hexagonal order in the y-z plane is conserved. However, one can observe that spots 1 and 2 are now less intense than the spot 3. The latter corresponds to the fact that particles are still forming a tilted plane even at the end of the period of recovery (see Figure 4.48e and 4.48f). The loss of statistics for spots 1 and 2 is related to the perturbation of the structure due to the string circled in red in Figure 4.48f and composed of three particles. This defect weakens the structure and generates small displacements of particles belonging to the neighbors' strings. Note that the perturbation of the order does not seem to be propagated at a long-range (see the spots in $(1.1, 3.68)$ and $(3.67, 0.95)$).

To summarize, the positional order in both the x-y and y-z plane acquired during the shearing period is fairly well conserved during the period of recovery. As expected in crystalline structures, the presence of defects weakens the structure and slightly disturbs the order of the particles closest to the defect.

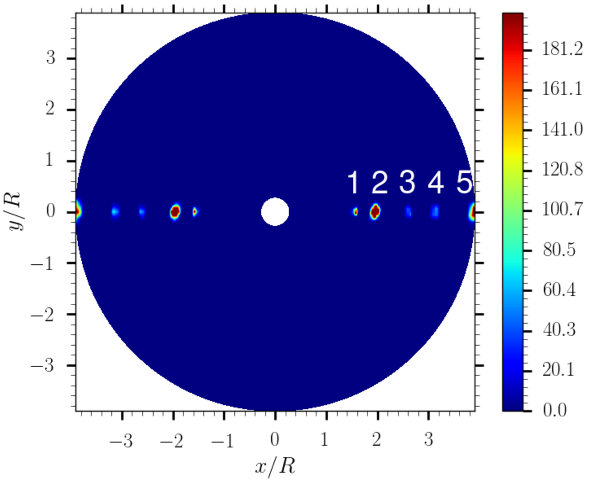

(a) Shear, x-y plane

(b) Recovery, x-y plane

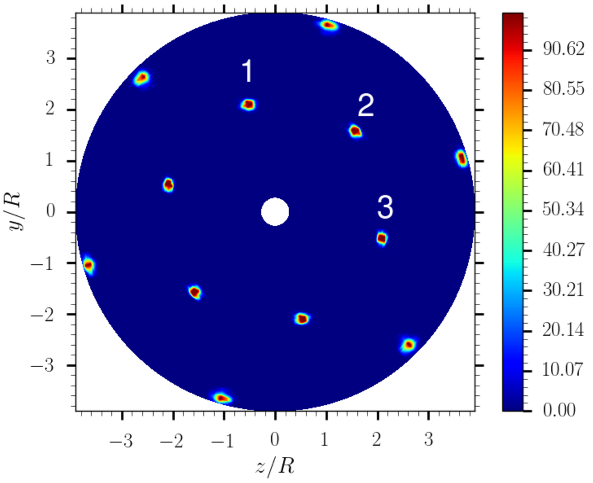

(c) Shear, y-z plane

(d) Recovery, y-z plane

Figure 4.49: Evolution of the pair distribution function for a suspension of highly repulsive particles from (a) and (b) the end of the period of shear and (c) and (d) the end of the period of recovery.

Let us focus on the angle distribution for particles belonging to the different spots previously mentioned. Concerning the spots in the x-y plane (see Figure 4.50), note that particles belonging to spots 2 and 4 are now mostly aligned with one another which is consistent with the qualitative observation of the snapshots. As particles belonging to spot 3 are only three in the string, they are more free to rotate due to lower electrostatic stresses compared to denser strings, which explains why we do not observe any angular correlation. In general, the angular correlations have changed compared to the end of the shear period, and we can observe that angles of 60 degrees are now way less favored compared to angles below 10 degrees (see Figure 4.50). Indeed, most of the particles are aligned at the end of the period of recovery except the particles of the top left corner in Figure 4.48f, which are influenced by the presence of the crystalline defect. This alignment of the particles generates a higher nematic order ($S_{nem} = 0.81$) than the one observed after 50 $a^2/(2D_0)$ of the first rest period ($S_{nem} = 0.50$). These observations point out first that the suspension cannot recover the same glassy state observed during the first period of rest, for the conditions and the simulation time investigated, and second that the shear-induced structure continues to age during the recovery period. So the shear-induced structure is clearly not optimal in terms of energy, but it is a starting point that allows a better energy minimization during a subsequent equilibration period.

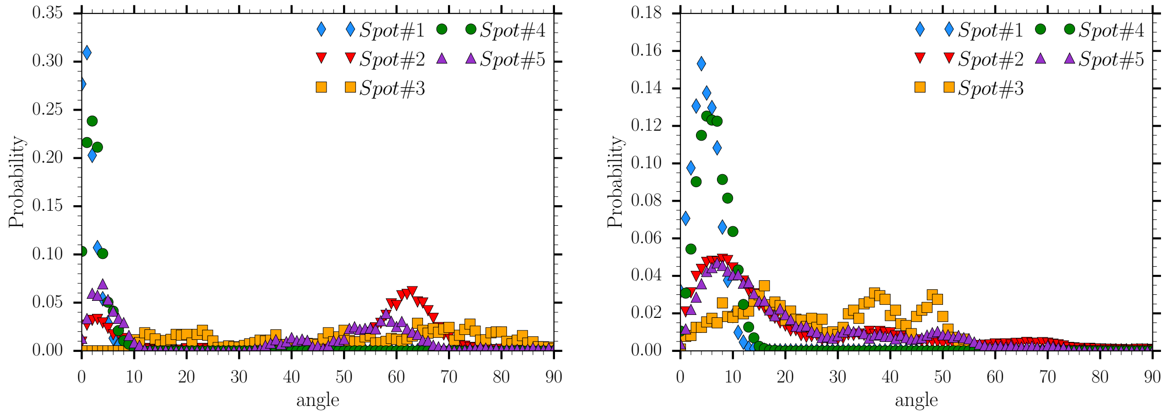

(a) Shear, x-y plane

(b) Recovery, x-y plane

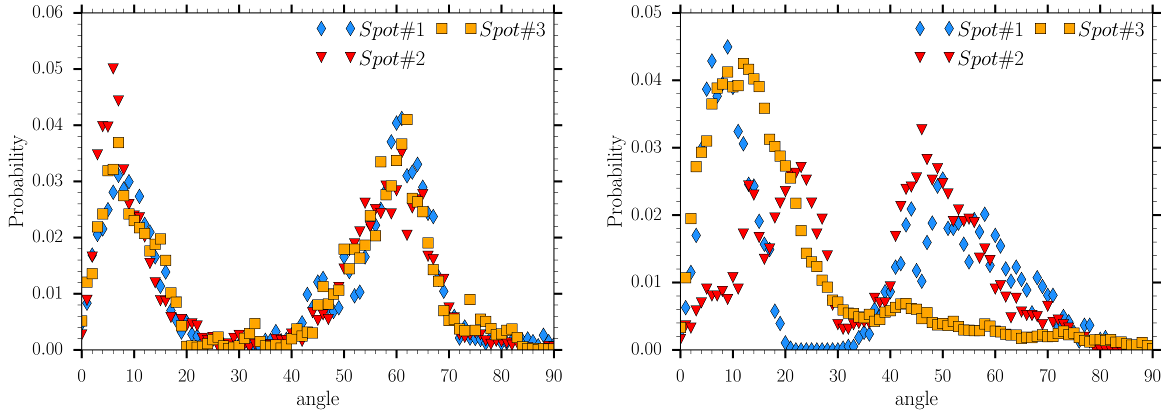

(c) Shear, y-z plane

(d) Recovery, y-z plane

Figure 4.50: Angle distribution for the spots in the x-y plane (a,b) and y-z plane (c,d).

Indeed, the state reached owing to the shear possesses a lower isotropic electrostatic pressure, as shown in Figure 4.51a than the Wigner glass (first period of rest). Note that during the Wigner glass state exhibits a fairly isotropic pressure ($P(i,i) \approx 1$), while the crystal obtained owing to the period of shear has a moderately anisotropic pressure along $(1,1)$ and $(2,2)$ corresponding to the flow and the gradient directions during the period of shear. Therefore, we can conclude that the electrostatic pressure of the system was reduced by the ordering of the suspension. One could wonder if the system might reach lower energy state after several cycles of shear and rest.

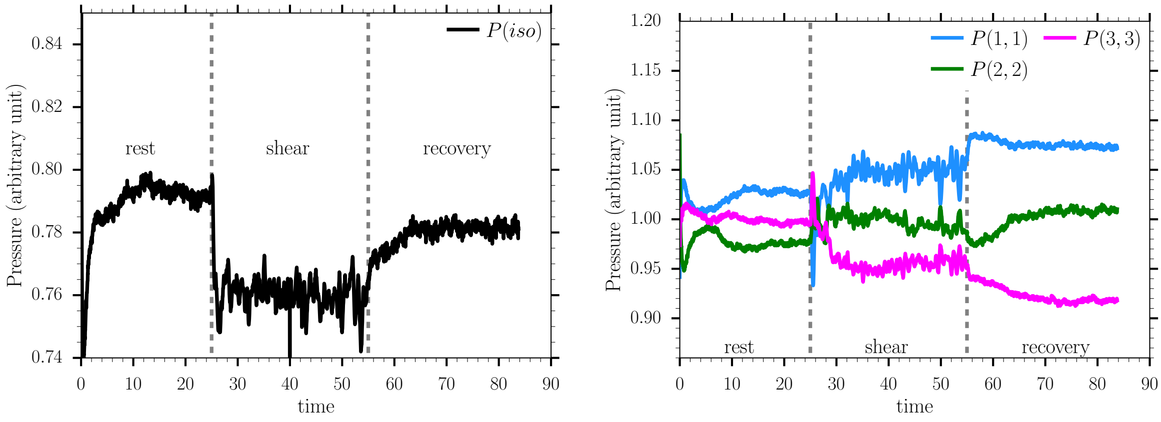

(a) Isotropic pressure

(b) Normalized pressure

Figure 4.51: Isotropic pressure (left) and the normalized normal stresses arising from electrostatic interactions of a suspension at $\kappa D = 1.46$ over one cycle of transient flow composed of two periods of rest and one period of shear.

To summarize, the positional order is conserved during the period of recovery, or at least evolves too slowly to be observed during the simulation time. In contrast, the orientational order changes more quickly, and particles align with one another to form parallel planes but not a smectic B phase that is quite close in terms of structure. The final spatial configuration reached after the period of recovery is really different from the one observed at the end of the first simulation at zero shear. Therefore, such a system shows strong memory effects, and is not thixotropic contrary to what was observed for lower interaction ranges (see section 2 on thixotropy). If the suspension were sheared again, it should not exhibit the strong overshoot stress observed in Figure 4.47a and we can also assume that the suspension should exhibit lower yield stress than during the first shear. Unfortunately, this simulation could not be carried out and analyzed by the time the writing of this manuscript was finished.

4.3 Summary

In this section we described in detail the shear-induced ordering observed for a system of highly repulsive orientable particles at $Ma = 1$. Such an ordering only occurs if the initial state of the suspension is a Wigner glass formed by long-range electrostatic interactions.

The shear-ordering could be related to a drop of the electrostatic pressure and an overshoot of the first normal stress difference was observed during the start-up shear indicating the "dilatant" behavior of the suspension. Then, particles arrange in strings along the flow direction and a hexagonal structure in the plane perpendicular to the flow. Moreover, we could observe an angular correlation between particles belonging to different strings. This structure resembles a crystal with the presence of two defects in its structure (note that the same system with a lower Mason number does not exhibit any defect). It was shown that the hydrodynamic and electrostatic first normal stress differences are similar but with opposite signs. Indeed, the hydrodynamic forces compress the system in the gradient direction while the electrostatic forces generate a compression in the flow direction, the sum resulting to a very small positive N_1.

The cessation of the flow did not disrupt the positional ordering, and particles were not able to recover the initial Wigner glass structure. We observed that orientational correlations were impacted by the flow cessation and particles aligned to form parallel planes, which could remind a Smectic B phase but without any contact.

The main point of this study is that this repulsive system of orientable particles has a very strong memory effects. When such a suspension exhibits an arrested Wigner glass state, the suspension shear-orders. The ordered suspension for the conditions studied here is composed of strings and a hexagonal structure, but we could also wonder what the observed structure would be if the suspension were sheared from an already ordered structure. After the cessation of the flow, the suspension cannot heal and preserves its ordered structure over at least a very long time, definitely not reachable using the ASD method. Such a system is, therefore, not thixotropic, contrary to what was observed for shorter interaction ranges. Moreover, the final state after a period of shear is even more ordered than what can be obtained without shear or during shear since the system continues to age towards a state with both positional and orientational order.

5 Conclusion

Using the numerical method developed in the second chapter, we have been able to study the dynamics of suspensions of clay-like particles with and without external shear flow.

When no shear flow is involved, we could relate the characteristic aggregation time of a suspension of clay-like particles to both the electrostatic forces and the initial average distance between particles using a scaling model. This model was based on the idea that electrostatic migration was the dominant effect driving the aggregation process. It was found accurate for vanishing net charge particles at intermediate- and long-range interactions, and only at intermediate-range interactions for particles with a net charge, as the slowing down of the aggregation due to long-range repulsion was not considered in the model. Concerning the very short-range interactions regime, it cannot be captured using the ASD method, as it requires either vanishing time-step or very large system, both leading to tremendous computational times. All these observations made us conclude that the aggregation kinetics are strongly related to the mobility of the particles and that the lower the ionic strength, the stronger the influence of the net charge.

With a significant shear flow, and for a Mason number equal to one, we were able to describe the scaling of the characteristic aggregation time with an orthokinetic law originally designed for suspension of spheres. We have shown that the adapted volume fraction was one of the platelets plus the double layer and not the sweeping volume fraction of the platelet as commonly used to describe the hydrodynamic volume of platelets [19]. Although it can inhibit the formation of large aggregates, the application of shear flow on suspensions of clay-like particles speeds up the aggregation by moving particles closer to one another.

When the shear flow is too strong compared to the attractive bonds between particles, it destroys the aggregated structure and generates a nematic structure with particles that are mainly aligned with the flow-vorticity plane. This process of destruction can be assimilated to the rejuvenation of the suspension and is commonly observed for thixotropic materials. After cessation of the flow, thixotropic materials are able to structure again and to exhibit, after a certain period of rest, always the same structure as the one observed at the end of any period of rest. Such a behavior was observed experimentally for Laponite suspensions by numerous authors [2, 13, 23, 24] and was successfully reproduced with our numerical method. It was shown that in the peculiar conditions leading to aggregated structure, suspensions of clay-like particles were influenced by their histories neither during the period of flow nor the period of rest. We observed that such suspensions shear-thin with the increase of the Péclet number. Note that we could also observe a shear-thinning during start-up shear as classically observed for thixotropic material.

Then, we studied the rheological behavior of clay-like suspensions during start-up shear. We investigated the responses to shear of the different microstructures obtained in the previous chapter while varying the balance between the electrostatic and hydrodynamic forces, *i.e.*, the Mason number. At very high Mason number, the flow instantaneously destroys the structures, aggregated or not, and therefore no elastic regime is observed. The shear-thinning of these suspensions could be related to the average spatial orientation of the particles using a very simple model. As the system is driven by the hydrodynamic forces, a single relaxation time was observed irrespective of the initial microstructure. The final viscosity also converges toward the same value.

When hydrodynamic and electrostatic forces are of the same order of magnitude, electrostatic forces strongly influence the microstructure of the suspension and, therefore, its rheological behavior. We have shown that the study of clay-like suspensions requires the separation of the initially suspensions states into three different cases: the repulsive ($\kappa D = 1.46$), the aggregated ($\kappa D = 7.3$, 14.6 and 29.2) and the liquid-like system ($\kappa = 73$). The liquid-like system exhibits similar behavior to the high Mason number regime for $Ma \geq 1$ while it starts to aggregate at $Ma = 0.25$ and therefore increases its viscosity. The initial aggregated structures exhibit an elastic regime and overshoot stress at very low strain related to the breakage of the most fragile interparticle bonds. It was shown that the viscosities of these suspensions were strongly influenced by the size of the clusters and by their own microstructure.

Finally, for a suspension initially in a Wigner glass state, we observed a shear-ordering of the suspension into a two-dimensional hexagonal crystal of strings in the flow direction. The application of a shear flow generates a very intense overshoot of the σ_{12} stress also noticeable on the electrostatic first normal stress difference indicating the strong compression of the electrostatic cages in the direction of the gradient of the flow. The elasticity of such suspensions was found inversely proportional to the Mason number, and it was shown that the relative final viscosity was following a power law $\eta_r \propto \dot{\gamma}^{-0.9}$ in line with the results from Paineau and coworkers [20]. We observed a change in the sign of the first normal stress difference between $Ma \geq 1$ and $Ma = 0.25$. In repulsive systems, we observed that the hydrodynamic component of the first normal stress difference was always positive, while the electrostatic component was always negative. Once again, the modification of the balance between the forces leads to a very distinct behavior of the suspension, which is found more compressed in the gradient direction than in the flow direction for $Ma \geq 1$ and the opposite below. Concerning the crystalline structure, we could observe that the positional correlations survived to the cessation of the flow, while the orientational correlations were impacted by their shear-induced alignment of the particles to form parallel planes. This final ordered structure is more ordered than the initial Wigner glass or the structure observed during shear. Moreover, its osmotic pressure is also found to be lower than that of the Wigner glass, but it is more anisotropic. The final significant result concerning the repulsive suspension of clay-like particles is that they show very strong memory effects and are not able to heal at rest or rejuvenate under shear, and therefore, they have lost their thixotropic behavior contrary to what is observed for aggregated suspensions.

To summarize, the rheological study of clay-like particles exhibits an important complexity introduced by anisotropic interactions. A simple change in the interaction range or the balance between the different forces involved in the system can lead to new structures governed by different physical mechanisms. However, using simulation allowed us to fix some parameters and better understand the role of the forces on the rheological properties of a clay-like suspension.

References

[1] Bérengère Abou, Daniel Bonn, and J. Meunier. Nonlinear rheology of Laponite suspensions under an external drive. *Journal of Rheology*, 47(4):979–988, July 2003.

[2] Bérengère Abou, Daniel Bonn, and J. Meunier. Nonlinear rheology of Laponite suspensions under an external drive. *Journal of Rheology*, 47(4):979–988, July 2003.

[3] B J Ackerson. Shear induced order of hard sphere suspensions. *Journal of Physics: Condensed Matter*, 2(S):SA389–SA392, December 1990.

[4] B. J. Ackerson and N. A. Clark. Shear-induced partial translational ordering of a colloidal solid. *Physical Review A*, 30(2):906–918, August 1984.

[5] Isabelle Bihannic, Christophe Baravian, Jérôme F. L. Duval, Erwan Paineau, Florian Meneau, Pierre Levitz, Johann Patrick de Silva, Patrick Davidson, and Laurent J. Michot. Orientational Order of Colloidal Disk-Shaped Particles under Shear-Flow Conditions: a Rheological-Small-Angle X-ray Scattering Study. *J. Phys. Chem. B*, 114(49):16347–16355, December 2010.

[6] Maxime Delhorme, Bo Jönsson, and Christophe Labbez. Monte Carlo simulations of a clay inspired model suspension: the role of rim charge. *Soft Matter*, 8(37):9691, 2012.

[7] Maxime Delhorme, Bo Jönsson, and Christophe Labbez. Gel, glass and nematic states of plate-like particle suspensions: charge anisotropy and size effects. *RSC Adv.*, 4(66):34793–34800, 2014.

[8] Maxime Delhorme, Christophe Labbez, and Bo Jönsson. Liquid Crystal Phases in Suspensions of Charged Plate-Like Particles. *The Journal of Physical Chemistry Letters*, 3(10):1315–1320, May 2012.

[9] Alvin Y. Huang and John C. Berg. High-salt stabilization of Laponite clay particles. *Journal of Colloid and Interface Science*, 296(1):159–164, April 2006.

[10] Sara Jabbari-Farouji, Jean-Jacques Weis, Patrick Davidson, Pierre Levitz, and Emmanuel Trizac. Interplay of anisotropy in shape and interactions in charged platelet suspensions. *The Journal of Chemical Physics*, 141(22):224510, December 2014.

[11] Sandeep D. Kulkarni and Jeffrey F. Morris. Ordering transition and structural evolution under shear in Brownian suspensions. *Journal of Rheology*, 53(2):417–439, March 2009.

[12] Bing Liu, Thijs H. Besseling, Alfons van Blaaderen, and Arnout Imhof. Confinement Induced Plastic Crystal-to-Crystal Transitions in Rodlike Particles with Long-Ranged Repulsion. *Physical Review Letters*, 115(7), August 2015.

[13] Céline Martin, Frédéric Pignon, Jean-Michel Piau, Albert Magnin, Peter Lindner, and Bernard Cabane. Dissociation of thixotropic clay gels. *Phys. Rev. E*, 66(2):021401, August 2002.

[14] Qingjun Meng and Jonathan J. L. Higdon. Large scale dynamic simulation of plate-like particle suspensions. Part I: Non-Brownian simulation. *Journal of Rheology*, 52(1):1–36, January 2008.

[15] Qingjun Meng and Jonathan J. L. Higdon. Large scale dynamic simulation of plate-like particle suspensions. Part II: Brownian simulation. *Journal of Rheology*, 52(1):37–65, January 2008.

[16] Jan Mewis and Norman J. Wagner. *Colloidal Suspension Rheology*. Cambridge Series in Chemical Engineering. Cambridge University Press, Cambridge, 2011.

[17] A. Mourchid, A. Delville, J. Lambard, E. LeColier, and P. Levitz. Phase Diagram of Colloidal Dispersions of Anisotropic Charged Particles: Equilibrium Properties, Structure, and Rheology of Laponite Suspensions. *Langmuir*, 11(6):1942–1950, June 1995.

[18] Ehssan Nazockdast and Jeffrey F. Morris. Effect of repulsive interactions on structure and rheology of sheared colloidal dispersions. *Soft Matter*, 8(15):4223, 2012.

[19] Erwan Paineau, Isabelle Bihannic, Christophe Baravian, Adrian-Marie Philippe, Patrick Davidson, Pierre Levitz, Sérgio S. Funari, Cyrille Rochas, and Laurent J. Michot. Aqueous Suspensions of Natural Swelling Clay Minerals. 1. Structure and Electrostatic Interactions. *Langmuir*, 27(9):5562–5573, May 2011.

[20] Erwan Paineau, Laurent J. Michot, Isabelle Bihannic, and Christophe Baravian. Aqueous Suspensions of Natural Swelling Clay Minerals. 2. Rheological Characterization. *Langmuir*, 27(12):7806–7819, June 2011.

[21] A. M. Philippe, C. Baravian, V. Bezuglyy, J. R. Angilella, F. Meneau, I. Bihannic, and L. J. Michot. Rheological Study of Two-Dimensional Very Anisometric Colloidal Particle Suspensions: From Shear-Induced Orientation to Viscous Dissipation. *Langmuir*, 29(17):5315–5324, April 2013.

[22] A M Philippe, C Baravian, M Imperor-Clerc, J De Silva, E Paineau, I Bihannic, P Davidson, F Meneau, P Levitz, and L J Michot. Rheo-SAXS investigation of shear-thinning behaviour of very anisometric repulsive disc-like clay suspensions. *Journal of Physics: Condensed Matter*, 23(19):194112, May 2011.

[23] Frédéric Pignon, Albert Magnin, and Jean-Michel Piau. Thixotropic behavior of clay dispersions: Combinations of scattering and rheometric techniques. *Journal of Rheology*, 42(6):1349–1373, November 1998.

[24] Frédéric Pignon, Albert Magnin, Jean-Michel Piau, Bernard Cabane, Peter Lindner, and Olivier Diat. Yield stress thixotropic clay suspension: Investigations of structure by light, neutron, and x-ray scattering. *Phys. Rev. E*, 56(3):3281–3289, September 1997.

[25] D. Quemada. *Modélisation rhéologique structurelle*. Lavoisier, editios tec edition, 2006.

[26] Barbara Ruzicka and Emanuela Zaccarelli. A fresh look at the Laponite phase diagram. *Soft Matter*, 7(4):1268, 2011.

[27] Ryohei Seto, Robert Botet, Günter K. Auernhammer, and Heiko Briesen. Restructuring of colloidal aggregates in shear flow: Coupling interparticle contact models with Stokesian dynamics. *The European Physical Journal E*, 35(12), December 2012.

[28] Zsigmond Varga and James Swan. Hydrodynamic interactions enhance gelation in dispersions of colloids with short-ranged attraction and long-ranged repulsion. *Soft Matter*, 12(36):7670–7681, 2016.

[29] J Vermant and M J Solomon. Flow-induced structure in colloidal suspensions. *Journal of Physics: Condensed Matter*, 17(4):R187–R216, February 2005.

[30] Norbert Willenbacher. Unusual Thixotropic Properties of Aqueous Dispersions of Laponite RD. *Journal of Colloid and Interface Science*, 182(2):501–510, September 1996.

[31] Y.D. Yan, J.K.G. Dhont, C. Smits, and H.N.W. Lekkerkerker. Oscillatory-shear-induced order in nonaqueous dispersions of charged colloidal spheres. *Physica A: Statistical Mechanics and its Applications*, 202(1-2):68–80, January 1994.

General conclusion and Perspectives

6 Conclusion

Colloidal suspensions are widely used in the industry and everyday life due to their ability to provide specific properties to other systems. If the presence of colloids can be beneficial, it can also be detrimental as they can for example, clog membranes and drastically reduce the performance of water filtration processes. Understanding the interactions between colloidal particles and between them and their surrounding media is crucial to optimize their use. Despite years of research, numerous uncertainties remain concerning the behavior of colloidal suspensions. The complexity of their study lies in the fact that colloids are so small that it is difficult to observe them with an optical microscope, and the particle interactions are very sensitive to their physico-chemical environment. A small change of the salinity of a suspension of Laponite, a synthetic clay, can for example cause either its aggregation and flocculation, or lead to a glassy state. Therefore, these changes can have a huge influence on the structure of the suspensions and on their response to an external flow, which can be problematic in industrial processes. These macroscopic changes are fairly easy to observe but cannot be predicted without a correct understanding of the microscopic interactions. That is why it can be interesting to carry out simulations to fix parameters such as the polydispersity of the particles or the salinity of the suspensions to precisely investigate the influence of the remaining parameters. In this thesis, we have numerically studied the rheology of particles with both shape and charge anisotropy. As these particles are quite similar to clays, they were referred to as "clay-like" particles in the manuscript. Moreover, the similarity with clay allowed us to compare our results with Laponite.

The first step was to find a method to model particles featuring both charge and shape anisotropy. The first option could have been to try to match the modeled particle as close as possible to a real anisotropic particle, but such a method is often very computationally expensive. An alternative way to compute the dynamics of anisotropic particles is to coarse-grain the system into elementary objects for which the theory is known and relatively "easy" to compute. The anisotropic particles were therefore modeled using spheres bound together to form platelet.

To compute the rheological behavior of the anisotropic particles, we used a method first introduced in the early 1980s by Bossis and Brady [2]: Stokesian Dynamics (SD). Since its first development, this method was improved and accelerated, allowing the simulation of hundreds of particles. It is now referred to as Accelerated Stokesian Dynamics (ASD). However, as this method was originally designed for spheres, we developed two different methods to enforce the motion of an assembly of spheres as a rigid object. The first method proposed relies on the coupling of spheres using springs, which can be represented as forces and torques applied to the centers of the spheres composing a particle. This method was found fairly accurate at high Péclet number but led to an erroneous diffusion of the particle at low Péclet number, probably due to a viscous dissipation arising from the wobbling of the spheres in the particle. The second method mathematically constrains the motion of spheres belonging to the same cluster to enforce rigid body motion. This method was able to reproduce known results for the motion of anisotropic particles. Its rheological behavior was validated by comparing the viscosity obtained for a suspension of plate-like particles with numerical and theoretical results from the literature. Due to the CPU cost required to compute accurately hydrodynamic interactions, the aspect ratio of a clay-like particle was taken four times smaller than the one of Laponite particles (7 vs. 30). Still, the typical number of spheres simulated was about 2200, which is quite high for the ASD method.

The charge anisotropy was then introduced. For comparability of the clay-like particles with Laponite, the rim of the coarse-grained particles was positively charged, and the faces, corresponding to the spheres in the center, negatively charged. Electrostatic interactions were computed in a pairwise additive fashion, considering point charges distributed on the surfaces of particles and interacting through a Yukawa potential. Although this method is widely used to compute interactions between anisotropic particles, one should keep in mind that it is originally valid for infinitely dilute spherical objects. Consequently, results obtained for interacting anisotropic particles can be quite far from reality, especially at a short distance. We discuss the limitations of such pairwise additive methods and, using a Poisson-Boltzmann Solver (PoBoS) developed at Laboratoire de Génie Chimique (LGC), we solved the full three-dimensional electric field around a pair of Laponite particles in both face-face and T-shape configurations. The point charges distributed on the coarse-grained clay-like particles were then determined such that the balance between electrostatic and Brownian forces (the reduced temperature) was the same as the one of true Laponite particles. This is crucial to study the structure of a suspension without background flow.

In the first application of the method to many-body systems, the structure of suspensions of clay-like particles without any background flow was studied. Such a study is commonly carried out with Monte Carlo (MC) or Brownian Dynamics (BD) simulations. These numerical methods do not take into account hydrodynamic interactions and are consequently less computationally expensive, so they can model clay-like particles with the aspect ratio of Laponite. The point of this study was not to discover new phases but rather to validate the approach developed here. Indeed, the high CPU cost associated to the computation of many-body hydrodynamic interactions only allowed us to simulate a small number of particles with an aspect ratio lower than that of Laponite. Therefore, we had to confirm that a phase diagram similar to the ones obtained with MC simulations could be recovered despite these limitations. A brief review of the literature concerning numerical simulations of Laponite suspensions allowed us to determine a range of volume fractions and interaction ranges to study. By varying these parameters, we observed numerous phases as: a Wigner glass at low ionic strength and low volume fraction, a repulsive glass with particles in overlapping coin configuration at high volume fractions and low ionic strength, two kinds of aggregated structures at intermediate- and short-range electrostatic interactions, one with particles mainly in house of cards configuration and the other with particles in overlapping coin configuration, and a liquid-like structure at very short-range interactions. We observed that the general macroscopic behavior of the suspension was driven by the range of electrostatic interactions, while the microstructure was strongly related to the volume fraction considered. For example, we could observe that suspensions below a critical volume fraction were evolving toward a phase separation while above this volume fraction, the suspensions could be considered as equilibrium gels. It was shown that the internal structure of the aggregated or percolated system was dependent on both the volume fraction and the ionic strength. This result is very important because it can explain why two suspensions with the same apparent phase, such as a gel, can exhibit a different rheological behavior during start-up shear.

Once the "equilibrium" (*i.e.*, quiescent) results were validated, we studied several aspects of the out-of-equilibrium dynamics of anisotropic plate-like suspensions. These dynamics could be computed quantitatively using the accurate computation of hydrodynamic interactions in the ASD method. We focused first of the aggregation dynamics of percolating systems without background flow while varying the range of electrostatic interactions and the net charge of the particles. A scaling model based on the idea that electrostatic migration was the dominant effect driving the aggregation process was proposed. This model was found to be reasonably accurate for anisotropic particles with a vanishing net charge and for both long- and intermediate-range of interactions; the very short-interaction range were not captured well by the ASD code. For clay-like particles, *i.e.*, particles with a net negative charge, the long-range repulsions strongly influence the scaling of the characteristic aggregation time by slowing down the aggregation process. Consequently, the model was only able to capture the scaling at intermediate-range of interactions. This study highlighted that the lower the ionic strength, the stronger the influence of the net charge on the aggregation process. The aggregation dynamics of anisotropic particles under significant shear flow was studied in a second time. We observed that the aggregation dynamics were well described by an orthokinetic law with an effective volume fraction based on the volume fraction of the platelets plus the double layers. In general, the application of a shear flow to a suspension of clay-like particles speeds up the initial aggregation process, but also inhibits the formation of a percolated structure.

Finally, we investigated the mechanical response of clay-like suspensions to a shear flow for different physico-chemical conditions. A start-up shear was applied to suspensions obtained without background flow at the lowest volume fraction investigated, and the resulting rheological properties were analyzed. To reduce the number of forces involved, we effectively turned off the thermal fluctuations of the particles by increasing the Péclet number to an "infinite" value ($Pe = 3.89\ 10^6$), and focused on the stress response as a function of the Mason number, the non-dimensional ratio between the hydrodynamic forces and the electrostatic forces. It was shown that this balance of forces strongly influences the microstructure of suspensions under flow and, therefore, the stresses obtained.

When the viscous forces strongly prevail over the electrostatic forces ($Ma \gg 1$), the shear flow destroys the aggregates and disrupts the Wigner glass. In such a case, hydrodynamic forces drive the global behavior of the suspension. Irrespective of the initial microstructure, shear tends to orient particles into the flow-vorticity direction. This tilt of the average normal vector from the planar face of the particles toward the gradient direction was found to be responsible for the shear-thinning observed. We related the evolution of the viscosity to the average spatial orientation of the particles with a simple model. In the conditions of investigated, the initial microstructure only influences the initial value of the viscosity (which depends on the average orientation). In contrast, neither the relaxation time of the suspension nor its final viscosity value are influenced by the initial microstructure.

The reduction of the Mason number increases the influence of electrostatic forces and drastically influences the rheology of clay-like suspensions. For a Mason number close to one, the microstructures are strongly related to the electrostatic ranges considered and consequently to the structure observed at zero shear. The liquid-like system behaves similarly to the high Mason number regime, except at very low Mason number ($Ma = 0.25$) where despite the short-range electrostatic interactions, particles start to aggregate, which results in an increase of the viscosity of the suspension. The application of a start-up shear to a percolated structure generates an elastic regime and overshoot stress, both related to the breakage of the most fragile bonds between particles. It was shown that the final viscosity was strongly influenced by the size of the remaining clusters and by their own structure (average number of neighbors per particle, angle of contact between particles). Finally, we observed the shear-ordering of a suspension initially in a Wigner glass state. When sheared, particles arranged in a two-dimensional hexagonal crystal of strings aligned in the flow direction. To our knowledge, such a structure has been observed neither experimentally nor using simulations. This ordering originates from the strong long-range repulsions between particles, and the structure exhibits both spatial and angular correlations. The start-up shear generates a very intense overshoot of the shear stress. It was shown that the intensity of the overshoot and the value of the elastic modulus was inversely proportional to the Mason number. These observations are related to the electrostatic first normal stress difference, indicating that the electrostatic cages were strongly compressed in the direction of the gradient of the flow during the initial restructuring period. The hydrodynamic first normal stress difference was always found positive at long times while, once the suspension ordered, the electrostatic first normal stress difference became negative, indicating a strong compression due to electrostatic effects along the strings of particles. We also observed that the final relative viscosity was following a power law $\eta_r \propto \dot{\gamma}^{-0.9}$ in line with results from the literature.

The observation of this new and unexpected shear-ordered structure leads us to the fundamental question of the history dependence of clay-like suspensions. Three different systems were considered, two leading to a percolated structure without flow and one being the Wigner glass state. Concerning the former, a shear flow at very high Mason and Péclet number was applied to one suspension ($Ma = 10^4$ and $Pe = 3.89\ 10^6$). This results in the complete destruction of the aggregated structures, of the shear-thinning of the suspension which rejuvenates, *i.e.*, erases its memory. After the cessation of the flow, we observed that particles arrange as before the shear, indicating the very limited history dependence of the suspension considered. The same cycles of periods of rest and shear were applied to another percolated suspension, but this time with a Mason number equal to one and a lower Peclet number ($Ma = 1$ and $Pe = 389$). In such conditions, the percolated structure is disturbed by the flow, but clusters of particles survive the flow. Once again, this suspension did not exhibit memory effects. Thus, it was shown that under the specific conditions leading to percolated systems, clay-like suspensions exhibit a thixotropic behavior. A completely different story happens for the Wigner glass. As mentioned previously, shearing the Wigner glass leads to the formation of a two-dimensional hexagonal crystal of strings aligned in the flow direction. In addition to the positional ordering of the particles, we observed a relative angular correlation between the particles of the same string and between two strings. Particles were either aligned or with an angle of 60 degrees. After the cessation of the flow, the positional ordering remained, and more surprisingly, particles increased their orientational correlation by forming parallel planes. Consequently, the structure became more ordered than both the initial Wigner glass and the crystalline structure observed under shear. The osmotic stresses of the shear-ordered structure were lower than those of the initial Wigner glass, but they were less isotropic. In contrast to percolated suspensions, the repulsive clay-like suspensions show very strong memory effects and are not thixotropic.

To summarize, we proposed in this manuscript a numerical method able to capture the rheology of particles with both charge and shape anisotropy. We observed that these anisotropies make the system drastically more complex because small changes of the conditions can lead to new structures governed by completely different mechanisms. However, we were able to provide some insight into the structure and rheology of suspensions of anisotropic particles. This allowed us to understand better the role of the balance between the hydrodynamic and electrostatic forces involved. This work leaves, as often, many open questions, so some perspectives are proposed in the following section.

7 Perspectives

All along this manuscript, the CPU cost of the ASD simulations of anisotropic particles has been an issue. Because many spheres are needed to represent one anisotropic colloid, simulations involve thousands of spheres even for a few tenth anisotropic particles. The associated high CPU cost limited the size of the systems studied and the maximum simulated strain, as well as the colloid aspect ratio. It would be highly desirable to reduce the CPU cost of the method first to improve the statistics presented here and second to reach aspects ratios closer to those of real systems. Therefore the first perspective of this work would be to find ways to reduce this CPU cost. A first solution would be to downgrade the physics simulated, especially hydrodynamic interactions. For similar reasons, some authors decided to account only for pairwise lubrication interactions [4] or long range hydrodynamic interactions via the Rotne-Prager-Yamakawa tensor (RPY). The latter is for example used by Varga et al. [5, 6] to study the microstructure anisotropy in sheared gel composed of attractive spheres. Here we do not think it would be a good idea because a system of anisotropic particle is on average very dilute, but can also be dense locally, especially when aggregation occurs. Then, both short- and far-field interactions must be considered. We could observed for example that without the far-field interactions, aggregation dynamics were approximately 10 times faster. Another solution is to accelerated again the Accelerated Stokesian Dynamics. It can be done by modifying the method, for example by using the Spectral Ewald Acceleration of Stokesian Dynamics (SEASD) developed by Wang & Brady in 2016 [7] which allow a speedup of 80% of the wave-space calculation for several thousands of spheres. This lead seems promising and would require the implemention of the rigid body method. It can also be done by parallelizing the code more efficiently. In 2016, Alexis Praga, a postgraduate from the LGC, studied the ASD method performance for about 500 spheres, a number classical for simulations of isotropic suspensions. He did not find any major area for optimization except the far-field computation. The latter requires the calculation of FFT on a grid of point forces. A certain number of point forces are required to capture the physics correctly. Therefore the size of the grid depends on the system, and more specifically, of the length of the simulation box. Alexis Praga parallelized the computation of the FFT using OpenMP, but as for 500 spheres on a $32 \times 32 \times 32$ grid the CPU time required for the computation of the far-field interactions is fairly comparable to the other parts of the code, only a small speedup of the total CPU time was observed. He has shown that the code might be used with four threads to optimize its performance. If these observations are valid for the usual number of spheres considered, it is no more the case for anisotropic particles. Indeed, the typical number of anisotropic particles considered in this work is 60 for a total number of spheres of approximately 2200, corresponding to point forces distributed into a $64 \times 64 \times 64$ grid. We notice that this increase in both the number of particles and the size of the grid drastically increases the CPU cost of the ASD method which was mainly due to the computation of the far-field contribution. One solution to reduce the CPU cost would be to parallelize the far-field contribution using MPI and parallel FFT libraries such as P3DFFT.

The anisotropic particles simulated in this work have an aspect ratio of seven, which is four times less than the one of Laponite. One could wonder if the results observed, such as the phase diagram or the scaling of the viscosity, strongly depend on the aspect ratio of the particle considered. Indeed, we have found some good agreement with several experimental results on Laponites suspensions despite the reduced aspect ratio. This surprising observation could be linked to the presence of electrostatic interactions that "thicken" the effective volume of colloids, thus reducing the effective aspect ratio difference between the simulated and real colloids. One could simulate particles with an aspect ratio of nine and 11 and observed their influence on both the microstructure and the rheological responses of the systems to shear. The same kind of study could also be realized for different charge anisotropies. Instead of distributing the charges of a clay-like particles on the totality of the available sites, one can imagine to reduce the number of charged site and to observe the influence of this new anisotropy as a function of the range of interaction.

The third perspective presented here is the extension of the work on the shear-ordering presented in the last chapter. It could be interesting to repeat one or two cycles of the transient flow to observe both the structure and the rheological response of the suspension to these consecutive cycles. One can expect to observe less intense overshoot stresses during the next start-up shear periods due to both the orientational and positional order acquired during the previous periods. The structure could also conserve its new orientational order, and in such a case we could observe planes of particles sliding one above the other. In contrast, if particles orient again to form relative angles either below 10 degrees or 60 degrees, as previously observed during the first period of shear, that would indicate that the hydrodynamic forces are responsible for this structure. Concerning the preferred angle of 60 degrees under shear, one could wonder if it its due to the charge anisotropy as it is not classically observed for instance in liquid crystals. To answer this question, we would consider the same particles but without any charged sites except at the center of the particle. This charged site should bear the totality of the net charge of a clay-like particle. Then the interaction ranges should be tuned to obtain a similar effective volume fraction as for charged clay-like particles. As the system is purely repulsive, we should observe a hexagonal structure with particles aligned in the flow direction, as reported by Ackerson & Clark [1] for a system of highly repulsive spheres. If particles exhibit the same orientational behavior, we could conclude on the fact that the anisotropy do not play an important role in such a system. This simulation would provide an insight into the importance of the charge anisotropy on a purely repulsive system.

Finally, the last perspective is the investigation of the rheological behavior of clay-like suspensions under oscillatory shear flow. This should allow us to capture with an increased precision the elastic regime of the suspensions. It would also allow to analyze the transition from a Wigner glass to the crystalline structure to those observed experimentally for spherical particles with or without electrostatic interactions under oscillatory shear. The oscillatory shear flow was already implemented in the ASD code by Marenne et al. [3] and should not require any supplementary developments.

References

[1] B. J. Ackerson and N. A. Clark. Shear-induced partial translational ordering of a colloidal solid. *Physical Review A*, 30(2):906–918, August 1984.

[2] G. Bossis and John F. Brady. Dynamic simulation of sheared suspensions. I. General method. *The Journal of Chemical Physics*, 80(10):5141–5154, May 1984.

[3] Stéphanie Marenne and Jeffrey F. Morris. Nonlinear rheology of colloidal suspensions probed by oscillatory shear. *Journal of Rheology*, 61(4):797–815, July 2017.

[4] Ryohei Seto, Romain Mari, Jeffrey F. Morris, and Morton M. Denn. Discontinuous Shear Thickening of Frictional Hard-Sphere Suspensions. *Physical Review Letters*, 111(21), November 2013.

[5] Zsigmond Varga and James Swan. Hydrodynamic interactions enhance gelation in dispersions of colloids with short-ranged attraction and long-ranged repulsion. *Soft Matter*, 12(36):7670–7681, 2016.

[6] Zsigmond Varga and James W. Swan. Large scale anisotropies in sheared colloidal gels. *Journal of Rheology*, 62(2):405–418, March 2018.

[7] Mu Wang and John F. Brady. Spectral Ewald Acceleration of Stokesian Dynamics for polydisperse suspensions. *Journal of Computational Physics*, 306:443–477, February 2016.

Appendix

1 The ASD method flowchart

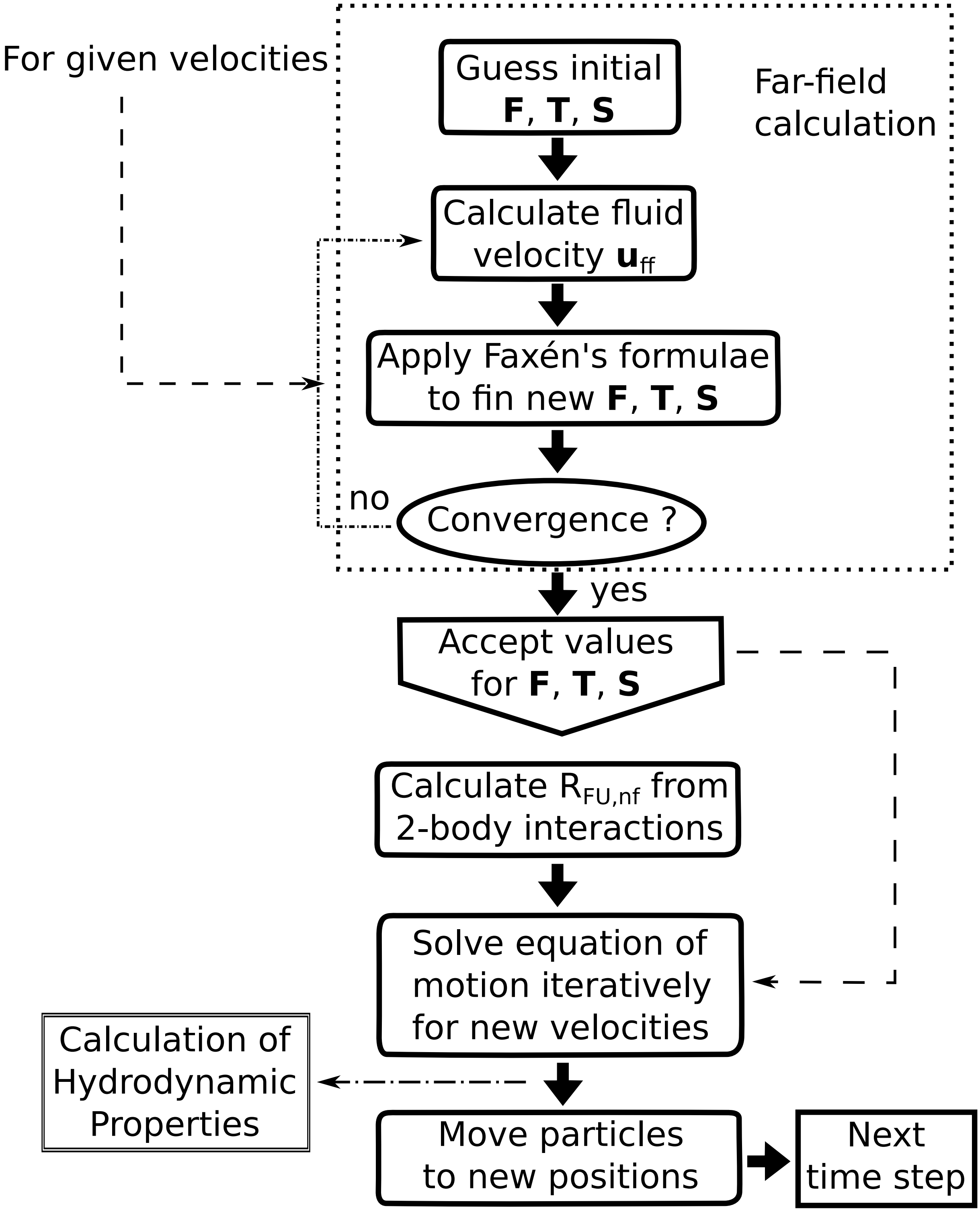

Figure 52: Flow chart reproduced from [2].

2 Discussion concerning the position of the peak for $\phi > 0.05$

One should have expected the shift of the peak on the radial distribution function to be a function of the volume fraction, as usually observed in experiments for repulsive systems of disks. In such a case, the nearest-neighbor distance $< r_{nn} >$ is expected to scale as $\phi^{-1/3}$ at low density and as ϕ^{-1} at high density. Jabbari and coworkers [1] have observed, for purely repulsive thin disks at low-density, the scaling of $< r_{nn} >$ as $\phi^{-1/3}$, the increase of the density has led to unexpected scaling behaviors. For concentrated systems, these authors obtained a scaling varying with the interaction range, ranging from -0.24 at long interaction range to -0.62 at the shortest interaction range. They have attributed this difference to the fact that in experiments, system are trapped in arrested states which prevent them from reaching the scaling mentioned above. In previous calculations (not shown here), we observed a scaling of $< r_{nn} >$ as $\phi^{-0.44}$ for plate-like particles with a higher net charge (twice higher). Such a result is in qualitative agreement with the scaling observed by Jabbari and coworkers. As this behavior disappears while reducing the net charge of the particles, one can conclude that $< r_{nn} >$ not only scales as a function of the volume but also depends on both the charge anisotropy and the total net charge of the particles.

3 Definition of the two dimensional pair distribution function

The pair distribution function $g(\mathbf{r})$ is defined on a grid where $\mathbf{r} = (r, \theta, \mathbf{z})$ is the vector between the centers of gravity and r its norm, $0 \leq \theta \leq 2\pi$ the polar angle measured on a counterclockwise fashion from the x-axis, and $\mathbf{z}$ the projection of $\mathbf{r}$ in the y-z plane. Then, taking into account the histograms of occurrence $\mathcal{H}(r, \theta, \mathbf{z}, \Omega)$ where Ω is the number of sampling events equal to four in the present study (four periods of shear), the pair distribution function can be written as

$$g(r, \theta, \mathbf{z}) = \frac{\mathcal{H}(r, \theta, \mathbf{z}, \Omega)}{\rho \Omega \Delta V}, \tag{11}$$

where ρ is the mean number density and $\Delta V = r^2 \Delta r \Delta z \Delta \theta$ is the volume of one bin. Note that the number of events considered in this study does not allow to obtain results independent of the number of samples. We have chosen the following values for the discretization mesh: $\Delta r = 0.039R$, $\Delta\theta = 1°\mathrm{C}$ and $\Delta z = 0.27R$. The same function was also defined in the y-z plane, where θ is now the angle defined from the z-axis and with $\mathbf{x}$ replacing $\mathbf{z}$.

4 Probability of the contact angle

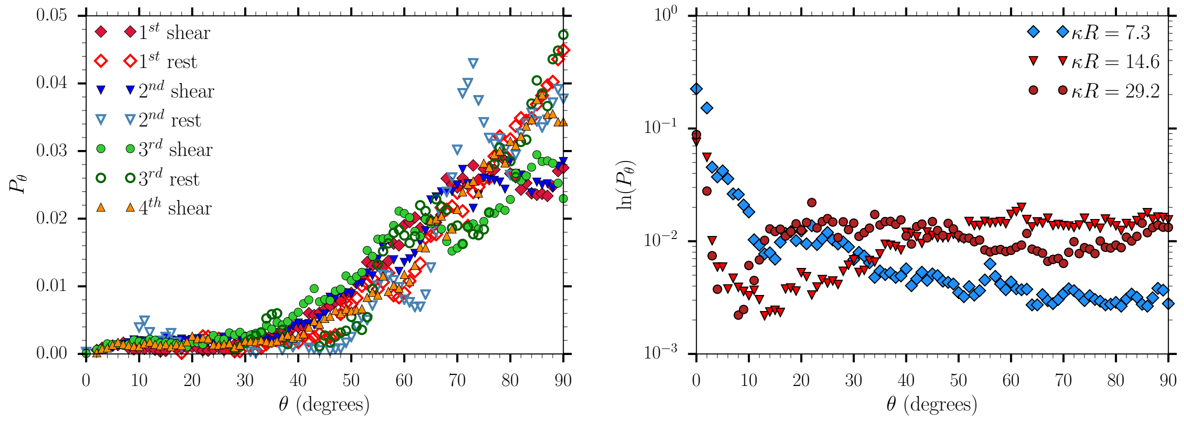

(a) $\kappa D = 14.6$ and $Ma = 1$

(b) $Ma = 4$

Figure 53: Probability of the contact angles for a transient flow at $Ma = 1$ and $\kappa D = 14.6$ (left) and under steady shear at $Ma = 4$ (right).

References

[1] Sara Jabbari-Farouji, Jean-Jacques Weis, Patrick Davidson, Pierre Levitz, and Emmanuel Trizac. Interplay of anisotropy in shape and interactions in charged platelet suspensions. *The Journal of Chemical Physics*, 141(22):224510, December 2014.

[2] Asimina Sierou. *Accelerated Stokesian dynamics development and application to sheared non-Brownian suspensions*. PhD thesis, California Institute of Technology, 2001.

Acknowledgment

Chaque thèse est unique et nécessite un dévouement complet, qui, bien que nécessaire pour avancer et atteindre ses objectifs, peut aussi devenir néfaste. C'est pourquoi il est primordial d'être correctement entouré et de remercier l'ensemble des acteurs ayant permis d'accomplir le défi entrepris plus de trois ans auparavant : l'obtention du titre de docteur.

Ce défi n'aurait pu commencer sans l'Idex de Toulouse que je remercie pour le financement de mes travaux de thèse. Ces derniers on été réalisés au sein du Laboratoire de Génie Chimique (LGC) dans le cadre de la chaire d'attractivité NEMESIS (From the Nanoscale to Eulerian Modeling: Engineering and Science In Suspensions) portée par Jeffrey Morris, directeur du Levich Institute au City College of New York. Je souhaite remercier le directeur du LGC, Pierre Aimar, de m'avoir accueilli dans le laboratoire, de m'avoir permis de siéger au conseil du laboratoire et de sa bienveillance tout au long de cette thèse.

Je tiens à remercier mes directeurs de thèse, Yannick et Martine, pour toutes les discussions que nous avons eues au cours de ces trois années et demie, au sujet de la science, du fonctionnement du laboratoire, ou tout simplement de la vie en général lors de repas au CNRS souvent très animés. Merci pour votre encadrement, je sors grandi de cette expérience.

Je souhaite remercier chaleureusement Jeffrey, qui, bien que de l'autre côté de l'Atlantique, a toujours su trouver du temps pour discuter, même si cela devait être le dimanche matin. Merci pour tout le temps passé par skype, merci de m'avoir accueilli pendant trois semaines au sein de ton institut ainsi que pour tout ce que tu as fait de sorte à m'aider à mener à terme ce projet : Thank you Jeffrey. Je remercie ensuite les personnes ayant participé au projet : Florent et Alexis. Un grand merci à Alexis qui m'a initié à l'informatique, et qui, même s'il travaillait dans un tout autre domaine, prenait le temps de faire le 'canard en plastique' bien des années après son départ du laboratoire.

Je souhaite remercier l'ensemble de mes collègues, thésards et permanents, grâce à qui l'ambiance de travail et des repas permettait de garder le sourire malgré des périodes difficiles. Un merci particulier à Martine, Yannick, Pierre et Patrice ainsi qu'aux membres de Labège Benjamin, Isaac, Emmanuel, Micheline et Kevin pour les repas. Merci à tous mes co-bureau, Cécilia, Samir, Charaf, Lisa, Arthur et Christian. Une pensée particulière pour Cécilia avec qui j'ai partagé mon bureau pendant trois années.

Au cours de cette thèse, j'ai eu l'occasion de rencontrer de bien belles personnes qui, pour certaines, sont maintenant devenues de vraies amies, ce qui démontre bien qu'une thèse, ce n'est pas seulement un travail de recherche, mais aussi une étape de la vie. Je tiens à remercier tous mes amis, qui m'ont permis de m'échapper de mon quotidien, qui m'ont épaulé, encouragé, et toujours soutenu. Merci à Romain, Dolu, Luc, Sam, Julie, Mimi, Alex, Mathilde, vous n'imaginez pas à quel point votre présence m'a rassuré et motivé.

Ensuite, je tiens à remercier toute ma famille, de sang ou de coeur, qui a suivi l'avancée des péripéties, et qui était présente le soir même de la soutenance pour fêter la délivrance. Une pensée particulière à mes grand-parents, mes parents et mes sœurs, qui sont des piliers dans ma vie, et sans qui je ne serais pas la personne que je suis devenue.

Enfin, je souhaite remercier ma compagne Lise. Tu as toujours été là pour moi, tu m'as accompagné, soutenu, tu as été mon roc, ma source de motivation. Ces trois années ont été très longues, et je tiens une nouvelle fois à te remercier pour tout ce que tu as fait pour moi.

Cette thèse aura été une aventure remplie d’émotions, positives comme négatives. Maintenant que tout est terminé et que le résultat est là, je ne peux que me rendre à l’évidence : elle m’a permis de murir. C’est pourquoi je termine ces quelques lignes en lui disant à son tour: MERCI.